TU Delft

Delft University of Technology

Ultrasound transducers for ultrafast 3D cardiovascular imaging

Simoes dos Santos, D.

DOI
10.4233/uuid:115ddae4-1b96-431b-afea-8417cb45fbc6

Publication date
2024

Document Version
Final published version

Citation (APA)
Simoes dos Santos, D. (2024). *Ultrasound transducers for ultrafast 3D cardiovascular imaging*. [Dissertation (TU Delft), Delft University of Technology]. https://doi.org/10.4233/uuid:115ddae4-1b96-431b-afea-8417cb45fbc6

Important note
To cite this publication, please use the final published version (if applicable).
Please check the document version above.

Copyright
Other than for strictly personal use, it is not permitted to download, forward or distribute the text or part of it, without the consent of the author(s) and/or copyright holder(s), unless the work is under an open content license such as Creative Commons.

Takedown policy
Please contact us and provide details if you believe this document breaches copyrights.
We will remove access to the work immediately and investigate your claim.

This work is downloaded from Delft University of Technology.
For technical reasons the number of authors shown on this cover page is limited to a maximum of 10.

Ultrasound Transducers for Ultrafast 3D Cardiovascular Imaging

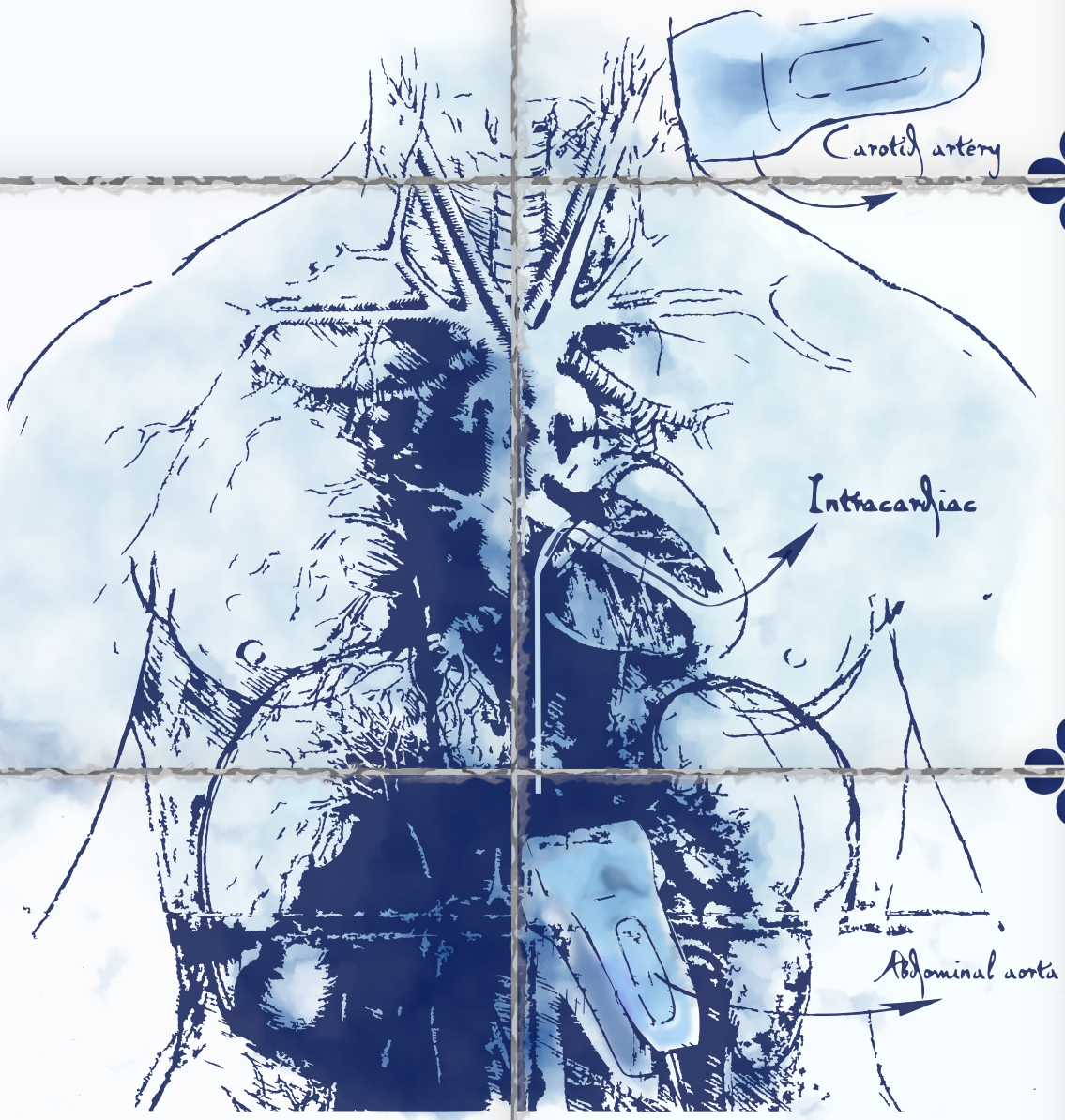

Djalma Simões dos Santos

ULTRASOUND TRANSDUCERS FOR ULTRAFAST 3D CARDIOVASCULAR IMAGING

ULTRASOUND TRANSDUCERS FOR ULTRAFAST 3D CARDIOVASCULAR IMAGING

Dissertation

for the purpose of obtaining the degree of doctor
at Delft University of Technology
by the authority of the Rector Magnificus, prof. dr. ir. T. H. J. J. van der Hagen,
chair of the Board for Doctorates
to be defended publicly on
Friday, 28 June 2024 at 12:30 o'clock

by

Djalma Simões DOS SANTOS

Master of Science in Biomedical Engineering
University of São Paulo, Brazil
born in São Paulo, Brazil

This dissertation has been approved by the promotors.

Composition of the doctoral committee:

Rector Magnificus,	chairperson
Prof. dr. ir. N. de Jong,	Delft University of Technology, promotor
Dr. ir. M. D. Verweij,	Delft University of Technology, promotor
Independent members:	
Prof. dr. ir. R. Dekker	Delft University of Technology
Dr. G. F. Pinton	University of North Carolina at Chapel Hill, USA
Dr. T. Z. Pavan	University of São Paulo, Brazil
Dr. G. McLaughlin	YorLabs, USA
Dr. T. M. L. M. da Costa	Delft University of Technology
Prof. dr. B. Rieger	Delft University of Technology, reserve member

This research is part of the **Ultra**fast Ultrasound Imaging for E**x**tended Diagnosis and **Tre**at**me**nt of Vascular Disease (**ULTRA-X-TREME**) program (project number: P17-32), which is partly financed by the Dutch Research Council (NWO).

Keywords: ultrasound imaging, matrix transducer array, 3D, high-frame-rate, application-specific integrated circuit, cardiovascular, intracardiac echocardiography, carotid artery, abdominal aorta

Printed by: Gildeprint

Cover: Designed by Djalma Simões dos Santos, inspired by two distinct sources: Delftware tiles (*Delfts blauw*), and Leonardo da Vinci's drawing *"The cardiovascular system and principal organs of a woman"*, 1509-10.

Copyright © 2024 by D. S. dos Santos

ISBN: 978-94-6384-604-2

An electronic version of this dissertation is available at
http://repository.tudelft.nl/

To Eszter and Jazmin, who drive me to focus and steer my energy towards the depths of our shared dreams.

"I, the LORD, alone probe the mind and test the heart, to reward everyone according to his ways, according to the merit of his deeds."

The Holy Bible, Jeremiah 17:10

CONTENTS

Summary xiii
Samenvatting xv
1. Introduction 1

1.1. Ultrasound in medicine 2

1.1.1. Common clinical applications 2
1.1.2. Cardiovascular diseases 4

1.2. Ultrasound probes 4

1.2.1. Operational frequency 4
1.2.2. Single element transducer 5
1.2.3. Transducer arrays 6

1.3. Three-dimensional ultrasound 6
1.4. High-frame-rate ultrasound 7
1.5. Integrated circuits for ultrasound probes 8
1.6. This thesis 9

1.6.1. Aim 9
1.6.2. Research challenges 9
1.6.3. Outline 10

1.7. References 11

Part I: Strategies for transducer characterization 17
2. Acoustic streaming-based calibration of transducers 19

2.1. Introduction 20
2.2. Theory 21
2.3. Materials and methods 23

2.3.1. Acoustic streaming measurements 23
2.3.2. Hydrophone measurements 25
2.3.3. Pulse-echo measurements 25

2.4. Results 26
2.5. Discussion 28
2.6. Conclusion 30
2.7. References 30

3. Automated characterization of transducer arrays 35

3.1. Introduction 36
3.2. Automated acoustic characterization 37

3.2.1. Alignment procedure 37
3.2.2. Transmit characterization 38
3.2.3. Receive characterization 38

3.3. Prototype matrix transducer 39

3.4. Results and discussion 39
3.5. Conclusions 42
3.6. References 43

4. Characterization of high-element-count transducers 45

4.1. Introduction 46
4.2. Theory 47

4.2.1. Translational alignment 47
4.2.2. Rotational alignment 49

4.3. Materials and methods 50

4.3.1. Experimental setup 50
4.3.2. Prototype matrix transducer 50
4.3.3. Subarrays of active elements 50
4.3.4. Pressure field characterization 51

4.4. Results 54
4.5. Discussion 56
4.6. Conclusion 57
4.7. References 58

5. The effect of subdicing on a matrix transducer 61

5.1. Introduction 62
5.2. Methods 62

5.2.1. Prototype matrix transducer 62
5.2.2. Transmit characterization 63

5.3. Results and discussion 64
5.4. Conclusions 66
5.5. References 66

Part II: Transducer design for high-frame-rate 3D imaging 69
6. Design of an ASIC for 3D carotid artery imaging 71

6.1. Introduction 72
6.2. Materials and methods 73

6.2.1. System overview 73
6.2.2. ASIC architecture 74
6.2.3. Element-level switch circuit and non-idealities 75
6.2.4. Proposed switch controller 76
6.2.5. Validation in simulation 78

6.3. Results and discussion 79

6.3.1. Experimental prototype 79
6.3.2. Electrical verification 80
6.3.3. Improvement in clock feedthrough and charge injection-induced imaging artifact 81

6.4. Conclusions 83

6.5. References 84

7. A matrix transducer for 3D carotid imaging 87

7.1. Introduction 88
7.2. Materials and methods 90

7.2.1. Design choices 90
7.2.2. Imaging scheme 91
7.2.3. ASIC design and implementation 92
7.2.4. Acoustic stack design and fabrication 93
7.2.5. Measurement setup 96

7.3. Results 99

7.3.1. Sensitivity 99
7.3.2. Time and frequency response 101
7.3.3. Directivity pattern 101
7.3.4. Dynamic range 102
7.3.5. Imaging 104

7.4. Discussion 105
7.5. Conclusions 107
7.6. Appendix A: Electrical characterization 108
7.7. Appendix B: Crosstalk analysis 109
7.8. References 111

8. A pitch-matched ASIC for high-frame-rate 3D-ICE 117

8.1. Introduction 118
8.2. System design 120

8.2.1. Overview 120
8.2.2. Architecture 121

8.3. Circuit implementation 123

8.3.1. TX Beamformer 123
8.3.2. Low-noise amplifier 126
8.3.3. Programmable gain amplifier 129
8.3.4. Datalink 131

8.4. Experimental results 134

8.4.1. Electrical measurements 135
8.4.2. Acoustic measurements 137

8.5. Conclusion 143
8.6. References 143

9. A matrix transducer for high-frame-rate 3D-ICE 147

9.1. Introduction 148
9.2. Materials and methods 150

9.2.1. Design choices 150

9.2.2. Imaging scheme 151
9.2.3. ASIC implementation 153
9.2.4. Transducer fabrication 153
9.2.5. Acoustic characterization 154
9.2.6. High frame rate 3D imaging 155
9.3. Results 156
9.3.1. Transmit characterization 156
9.3.2. Receive characterization 157
9.3.3. Pulse-echo measurements 159
9.3.4. Imaging 159
9.4. Discussion 160
9.5. Conclusions 162
9.6. References 163
10. A CMUT transducer for high-frame-rate 3D abdominal aorta imaging 167
10.1. Introduction 168
10.2. Methods 169
10.2.1. Design choices 169
10.2.2. Imaging scheme 171
10.2.3. Beam profile simulations 172
10.2.4. ASIC design 173
10.2.5. Fabrication 174
10.2.6. Pressure field characterization 174
10.2.7. High-frame-rate 3D imaging 175
10.3. Results and discussion 175
10.3.1. Simulation results 175
10.3.2. Experimental results 179
10.4. Conclusion 180
10.5. References 182
11. Discussion and conclusion 185
11.1. Overview 186
11.1.1. Transducer evaluation: calibration, automation, and performance enhancement 186
11.1.2. Advances in transducers for high-frame-rate 3D imaging 187
11.2. Recommendations and future work 188
11.2.1. Calibration of transducers using acoustic streaming 188
11.2.2. Automated characterization of matrix transducers 188
11.2.3. Fabrication process of matrix transducers 188
11.2.4. Further evaluation and imaging tests 189
11.3. Conclusion 190
11.4. References 190

Acknowledgments 193
List of publications 197
About the author 199

SUMMARY

CARDIOVASCULAR diseases stand as the leading cause of death worldwide. Cardiovascular diseases are a group of disorders of the heart and blood vessels, such as atherosclerosis, congenital heart diseases, rheumatic heart diseases, and arrhythmias. Early detection of cardiovascular issues is imperative for effective treatment, and the implementation of screening programs facilitates timely identification and intervention, ultimately reducing morbidity rates. Ultrasound imaging is a widely utilized technique for assessing cardiovascular diseases due to its portability, lack of radiation exposure, and relatively lower associated costs compared to other imaging modalities such as magnetic resonance imaging and computed tomography.

In this thesis, we detail the development of specialized ultrasound probes for three distinct cardiovascular applications: carotid artery imaging, intracardiac echocardiography, and abdominal aorta imaging. These applications necessitate high-frame-rate 3D imaging with a wide field of view, requiring ultrasound matrix transducers with a vast number of elements and integrated electronics. We outline the design, fabrication, and characterization of three probes tailored for each specific application.

Chapter 1 provides an introduction to ultrasound imaging, discussing the technology behind medical ultrasound probes and the need for enhancements for cardiovascular applications. We review available approaches for ultrafast three-dimensional ultrasound imaging and present the aims of this research project.

The thesis is divided into two parts. The first part focuses on simplifying and automating the acoustic characterization process of ultrasound transducers.

Chapter 2 introduces a novel calibration technique for ultrasound transducers utilizing acoustic streaming, in which the ultrasound wave induces local streaming in the liquid in which it propagates. The assessment involved a comparison of this method with two established techniques: hydrophone and pulse-echo measurements. At the central frequency of 5 MHz, the transmit efficiency of a standard commercial probe estimated from streaming measurements was 1.9 kPa/V. In contrast, hydrophone and pulse-echo measurements yielded transmit efficiencies of 2.1 kPa/V and 1.8 kPa/V, respectively. These findings suggest that the proposed method for estimating the transfer function of ultrasound transducers achieves a satisfactory level of accuracy.

In **Chapter 3**, we present an automated procedure for the element-level acoustic characterization of an ultrasound matrix transducer in both transmit and receive operations. To evaluate its effectiveness, we applied the pipeline to characterize a lead zirconate titanate (PZT) matrix transducer featuring 960 elements. The results demonstrate that the proposed pipeline offers a rapid and convenient approach for characterizing ultrasound transducers.

Chapter 4 introduces an automated method for measuring pressure fields in ultrasound matrix transducers with a high element count using a needle hydrophone. This approach significantly reduces measurement time compared to

traditional methods, enabling an extensive assessment of transducer performance. Validation with a prototype PZT matrix transducer consisting of 2880 elements demonstrates the effectiveness of the procedure, revealing insights into individual beam profiles, sensitivity maps, and time/frequency responses.

In **Chapter 5**, we investigated the transmit performance of a prototype PZT matrix transducer with both subdiced and non-subdiced elements. On average, subdicing led to a 25% increase in peak pressure, a 10% expansion in bandwidth, and a 25% reduction in ringing time. The findings suggest that subdicing enhances the performance of ultrasound transducers with large elements (width-to-thickness ratio greater than 0.7).

The second part of this thesis explores the design, manufacturing, characterization, and imaging of dedicated matrix transducers featuring integrated Application-Specific Integrated Circuits (ASICs).

Chapter 6 introduces an ultrasound transceiver ASIC designed for carotid artery imaging, featuring a technique to reduce switching artifacts. The enhanced switch controller effectively addresses clock feedthrough and charge injection issues observed in the first-generation ASIC, resulting in a 20 dB decrease in imaging artifacts.

Chapter 7 outlines the development of a PZT matrix transducer with integrated ASICs for carotid artery imaging. The prototype was designed to have 7680 elements on 8 × 1 tiled ASICs, but two ASICs were damaged during fabrication. On average, individual transducer elements exhibited a transmit efficiency of 30 Pa/V at 200 mm distance and a −6 dB fractional bandwidth of 45%. The receive dynamic range measured 81 dB, with a range of detectable pressure between 60 Pa and 700 kPa.

In **Chapter 8**, we introduce a transceiver ASIC designed for catheter-based high-frame-rate 3D ultrasound imaging. By employing time-division multiplexing, subarray beamforming, and a load modulation multi-level data transmission channel, we achieved an 18-fold reduction in cable count. The system can generate transmit patterns at up to 30 V, provides quick settling after the transmit phase, and has a power consumption of 1.12 mW per element in receive.

Chapter 9 details the development of a matrix transducer for high-frame-rate 3D intracardiac echocardiography. The matrix consists of 16 × 18 PZT elements with a pitch of 160 µm × 160 µm and integrates with an ASIC. We measured a transmit efficiency of 28 Pa/V at 5 cm distance per element and a bandwidth of 60%. In receive, a dynamic range of 80 dB is measured with a minimum detectable pressure of 10 Pa per element. The probe is capable of imaging at a frame rate of up to 1000 volumes/s and is intended to cover a volume of 70° × 70° × 10 cm.

Chapter 10 presents the design of a high-frame-rate 3D imaging capacitive micromachined ultrasonic transducer (CMUT) matrix comprising 64 × 128 elements for abdominal aorta imaging. The matrix is interfaced with ASICs, and we employed subarray beamforming and time-division multiplexing to obtain an 8-fold reduction in channel count. To achieve the desired frame rate, we use four diverging transmit beams. We included initial imaging experiments conducted on tissue-mimicking and needle phantoms. These results show that we successfully captured 3D images at a rate of 2000 volumes/s. The intended imaging volume is 60° × 60° × 10 cm.

Chapter 11 concludes the thesis, summarizing the main findings and providing recommendations for future research.

SAMENVATTING

HART- en vaatzieken zijn wereldwijd de belangrijkste doodsoorzaak. Cardiovasculaire ziektes zijn aandoeningen aan het hart en bloedvaten, zoals atherosclerose, aangeboren hartafwijkingen, reumatische hartziekten, en hartritmestoornissen. Voor een effectieve behandeling van deze ziekten is het noodzakelijk deze vroegtijdig op te sporen. Het opzetten van bevolkingsonderzoeken maakt vroegtijdige identificatie en interventie mogelijk, waardoor uiteindelijk het sterftecijfer omlaag wordt gebracht. Echografie is een breed gebruikte afbeeldingsmethode om hart- en vaatziekten in kaart te brengen doordat de apparatuur makkelijk verrijdbaar is, geen ioniserende straling gebruikt, en relatief goedkoop inzetbaar is in vergelijking met andere afbeeldingsmethoden zoals MRI en CT.

Deze thesis beschrijft het ontwikkelproces van gespecialiseerde ultrasone transducenten voor drie specifieke cardiovasculaire toepassingen: afbeelden van de halsslagader, intracardiale echografie en beeldvorming van de buikslagader. Deze drie toepassingen vereisen allemaal 3D-afbeeldingen met een hoge beeldfrequentie met een breed zichtveld. Om dit te kunnen doen zijn matrix transducenten benodigd die een enorm aantal elementen hebben en geïntegreerde elektronica bevatten. In dit proefschrift beschrijven we het ontwerp, de fabricage en de karakterisering van drie sondes die aangepast zijn voor elke specifieke toepassing.

Hoofdstuk 1 bevat een introductie over echografie, bediscussieerd de technologie achter de medische transducenten en de benodigde verbeteringen voor het gebruik in cardiovasculaire toepassingen. Daarnaast bekijken we de beschikbare benaderingen om ultrasnelle 3D-echografie mogelijk te maken en presenteren we de doelstellingen van dit onderzoeksproject.

Deze thesis bevat twee delen. De focus in het eerste deel is het vereenvoudigen en automatiseren van het akoestische karakteriseringsproces van ultrasone transducers.

Hoofdstuk 2 introduceert een nieuwe manier om transducers te karakteriseren door gebruik te maken van *acoustic streaming*, waarbij een geluidsgolf een lokale stroming van de vloeistof induceert. We vergeleken deze methode met twee gevestigde technieken: hydrofoon en puls-echo metingen. Bij een centrale frequentie van 5 MHz van een standaard commerciële echoprobe was de geschatte zendefficiëntie met de voorgestelde methode 1.9 kPa/V, terwijl met hydrofoon en puls-echo metingen respectievelijk 2.1 kPa/V and 1.8 kPa/V werd gemeten. Dit toont aan dat met de voorgestelde methode de overdrachtsfunctie van de transducent voldoende accuraat kan worden gekarakteriseerd.

In **Hoofdstuk 3** presenteren we een geautomatiseerd proces om elk element in een matrix te karakteriseren in zowel transmissie als ontvangst. De effectiviteit werd onderzocht door een matrix met 960 elementen te karakteriseren. De resultaten tonen aan de voorgestelde methode een snelle en handige manier is om de ultrasone transducent te karakteriseren.

Hoofdstuk 4 introduceert een geautomatiseerde manier om drukvelden van een matrix transducer te meten op basis van hydrofoonmetingen. Deze benadering

kost significant minder tijd dan gebruikelijke methodes, waardoor het mogelijk wordt om een extensief de prestaties van een probe te onderzoeken. De methode is gevalideerd doormiddel van experimenten met een PZT matrix transducer die 2880 elementen bevat. Hiermee is aangetoond dat de methode effectief is en dat het hierdoor mogelijk is om het stralingsprofiel, de zend- en ontvangst-efficiëntie, het tijdsignaal, en het frequentiespectrum van elk individueel element te meten.

In **Hoofdstuk 5** onderzochten we de zendefficiëntie van een prototype matrix transducent die elementen bevat die elk moedwillig zijn opgedeeld in twee sub-elementen. Een ander gedeelte van de elementen is intact gelaten ter referentie. Gemiddeld zorgde het opdelen voor een 25% hogere piekdruk, 10% hogere bandbreedte en 25% kortere puls duur. De resultaten laten zien dat het opdelen van elementen positief uitpakt op de prestaties van een probe die elementen heeft met een breedte-dikte verhouding groter dan 0.7.

Het tweede deel van dit proefschrift onderzoekt het ontwerp, de productie, de karakterisering en de afbeeldingskwaliteit van gespecialiseerde matrix transducenten met geïntegreerde Applicatie-Specifieke geïntegreerde circuits (ASICs).

Hoofdstuk 6 introduceert een PZT matrix transducer geïntegreerd met een verbeterde ASIC, ontworpen om de halsslagader af te beelden. In de nieuwe ASIC is de schakelcontroller verbeterd om de beeldartefacten te verminderen die werden waargenomen met een eerdere versie. De oorzaak hiervan was het niet-ideale gedrag van de transistoren. Het resultaat is een afnamen van 20 dB in beeldartefacten.

Hoofdstuk 7 beschrijft de ontwikkeling van een PZT matrix transducer met geïntegreerde ASICs voor het afbeelden van de halsslagader. Dit prototype was ontworpen om 7680 elementen te hebben op 8 × 1 ASICs in totaal, maar twee ASICs waren beschadigd geraakt tijdens de fabricatie. Gemiddeld had elk element van dit prototype een zendefficiëntie van 30Pa/V op 200 mm afstand en een -6 dB fractionele bandbreedte van 45%. In ontvangst was het dynamisch bereik 81 dB, met een minimaal en maximaal meetbare akoestische druk van respectievelijk 60 Pa en 700 kPa.

In **Hoofdstuk 8** wordt een ASIC geïntroduceerd voor het maken van ultrasnelle 3D-afbeeldingen vanuit een katheter. Door het gebruik van *time-division multiplexing*, micro-bundelvormers en een meervoudig-niveau data zend kanaal met belastingsmodulatie bereikten we een 18-voudige vermindering in het aantal benodigde kabels. De ASIC kan transmissie spanningen van maximaal 30 V genereren, kan snel schakelen tussen zenden en ontvangen en heeft een stroomverbruik van 1.12 mW per element in ontvangst.

Hoofdstuk 9 beschrijft de ontwikkeling van een matrix transducent voor intracardiale echografie die ultrasnel 3D-afbeelding kan maken. De matrix bevat 16 bij 18 PZT elementen met een hart-op-hart afstand van 160 bij 160 µm, en bevat een geïntegreerde ASIC. De zendefficiëntie van deze probe is 28 Pa/V op 5 cm afstand per element en de fractionele bandbreedte is 60%. Het dynamisch bereik in ontvangst is 80 dB, terwijl de minimaal meetbare druk 10 Pa is voor elk element afzonderlijk. Deze matrix kan afbeeldingen maken met een beeldfrequentie van 1000 volumes per seconde over een zichtveld van 70° × 70° × 10 cm.

Hoofdstuk 10 presenteert een matrix ontwerp voor het maken van ultrasnelle 3D-afbeeldingen van de buikslagader. De transducent bevat 64 × 128 capacitieve microfabricage ultrasone transducers (CMUT) elementen bovenop meerdere ASICs. In de ASIC maken we gebruik van micro-bundelvorming en *time-division multiplexing* om een 8-voudige reductie te behalen in het aantal kanalen. Om de benodigde beeldfrequentie te behalen is het plan om af te beelden met vier divergerende bundels in transmissie. Dit hoofdstuk bevat initiële afbeeldingsexperimenten op een weefsel- en een naald fantoom. De resultaten tonen aan dat het mogelijk is om af te beelden met 2000 volumes per seconde met een zichtveld van 60° × 60° × 10 cm.

In **Hoofdstuk 11** worden de belangrijkste bevindingen uit dit proefschrift samengevat en worden een aantal vervolgonderzoeken voorgesteld.

1

INTRODUCTION

1

1.1. ULTRASOUND IN MEDICINE

ULTRASOUND has profoundly benefited humanity across multiple domains, and perhaps the most prominent one is medicine [1]. Originating as a military tool employed for detecting metal flaws, the use of ultrasound for general purposes began after World War II [2]. The first ultrasonic testing apparatus, known as the supersonic reflectoscope, was developed by Firestone in 1940 [3]. This innovative device applied the pulse-echo ranging principle to identify defects in metals through a reasonably compact instrument. When commercial versions of this equipment became available, a select group of medical practitioners recognized its potential for probing the human body, sparking investigations of the use of an analogous technique for medical purposes [4].

In the early 1950s, the collaboration between Wild and Reid led to the development of techniques for detecting and imaging tumors in soft tissues, including the breast and colon [5]. This pioneering effort was paralleled by the work of Howry, who explored sound wave reflections from tissue interfaces, culminating in the production of the first two-dimensional cross-sectional images of diagnostic quality [6], [7]. These groundbreaking advancements triggered widespread interest in medical diagnostics, leading to significant technical enhancements.

The scarcity of suitable devices prompted an era of intense experimentation and adaptation, wherein surplus wartime equipment and other sonographic instruments were repurposed for medical use [4]. Nearly two decades later, significant progress was made in pulse-echo imaging systems by Somer and Bom, who respectively introduced the phased-array and linear-array transducers in 1968 [8] and 1971 [9], marking a substantial leap toward the ultrasound imaging systems commonly employed today.

1.1.1. COMMON CLINICAL APPLICATIONS

Ultrasound stands out as one of the most widely used imaging techniques worldwide [10], [11]. Its portability, lack of radiation exposure, and relatively lower costs compared to other medical imaging modalities such as magnetic resonance imaging and computed tomography, make it a preferred choice [12]. Ultrasound imaging spans a wide range of applications and is continually expanding, with new potential uses frequently proposed [1].

Conventional ultrasound excels in imaging soft tissues, allowing the visualization of morphological structures and enabling measurements of sizes and distances within organs [13]. Additionally, various ultrasound methods explore tissue elasticity, which enables the identification and characterization of pathological tissues, such as cysts and tumors. This is possible because malignant tumors are generally stiffer than the surrounding healthy tissue [14].

In obstetrics, ultrasound holds immense significance [4], serving as a crucial tool for monitoring pregnancy, enabling regular assessments of fetal development, and granting expectant parents the remarkable opportunity to “see” their baby's growth within the mother’s womb. As an example, Figure 1.1(a) depicts a typical two-dimensional (2D) ultrasound image of a fetus captured in brightness mode (B-

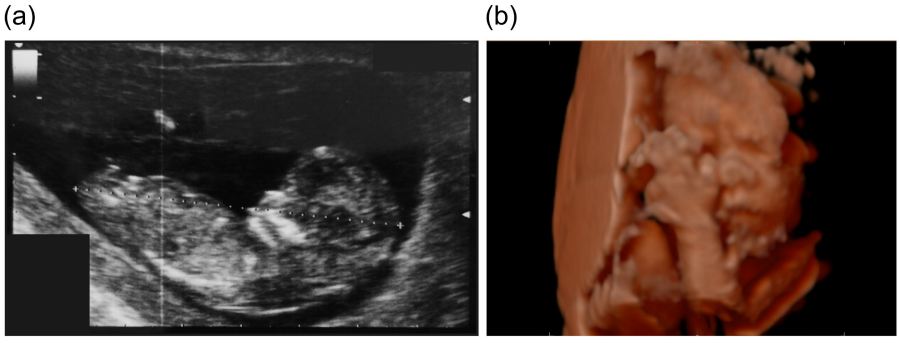

Figure 1.1: (a) 2D ultrasound image of a 12-week fetus. (b) 3D ultrasound image of a 27-week fetus.

mode). In this mode, strong reflectors are depicted as bright spots, while weak reflectors appear as darker regions [1]. Moving into three-dimensional (3D) ultrasound, such as the fetal depiction in Figure 1.1(b), depth perception enriches visualization, while four-dimensional (4D) ultrasound images go beyond by presenting these 3D images in real-time, providing live movement over time.

In cardiovascular diagnosis, ultrasound also plays a major role. Assessing the carotid artery, for example, offers predictive insights into the risk of a stroke [15]. Additionally, the Doppler effect enables the visualization of blood flow within different vessels and across the heart's valves [16]. Duplex ultrasonography combines the principles of anatomic and flow ultrasound, providing physicians with comprehensive insights [4]. Advancements in miniaturization facilitate intravascular imaging, enabling visualization not only from within the vessels [17], but also from within the heart [18].

Ultrasound also finds frequent application in physiotherapy, where it is used for warming inner tissue layers to accelerate the healing process [1]. Additionally, high-intensity focused ultrasound (HIFU) is commonly employed for non-invasive tumor treatment, known as ablation, in various organs [19]. Another significant application lies in lithotripsy, a routine clinical procedure. This method involves focusing high-intensity acoustic bursts on kidney stones, breaking them down for natural elimination through the urinary tract [20].

Further applications of ultrasound use acoustic waves to boost the permeability of both skin and internal membranes, facilitating drug delivery [21]. Moreover, studies demonstrate ultrasound's potential to introduce large molecules into cells, advancing possibilities for gene therapy [22].

Hard tissues like bones and teeth present a technical challenge due to their strong reflectivity and absorption of acoustic waves [23]. While there are a handful of commercial systems available for bone assessment and dental purposes, this sector is not dominant [1].

Finally, ultrasound imaging also spans various applications in cosmetic and post-cosmetic surgery treatments, although not all of these newer applications have undergone comprehensive clinical validation. Together, the above-mentioned

applications and innovations highlight the significant interest, remarkable advancements, and vast potential of ultrasound in medicine [24]. Despite its age (nearly a century old), ultrasound continues to evolve and thrive.

1.1.2. CARDIOVASCULAR DISEASES

Cardiovascular diseases stand as the leading cause of death globally, claiming an estimated 17.9 million lives each year according to the World Health Organization [25]. Cardiovascular diseases are a group of disorders of the heart and blood vessels, such as atherosclerosis, congenital heart diseases, rheumatic heart diseases, arrhythmias, and other conditions. Early detection of cardiovascular issues is essential for effective treatment, and the implementation of screening programs enables early identification and prompt intervention, ultimately reducing morbidity rates through timely interventions [26]. In this thesis, our focus will be on three specific cardiovascular applications: carotid artery imaging, intracardiac echography, and abdominal aorta imaging.

Carotid artery stenosis occurs when fatty deposits (plaques) obstruct the carotid artery. Such blockages in the carotid arteries are a frequent source of stroke, a medical emergency that occurs when the blood supply to the brain is interrupted or seriously reduced. Surgical removal of carotid plaques, referred to as carotid endarterectomy, is the primary treatment for stroke patients with carotid artery stenosis. The assessment of the carotid plaque state is typically performed using ultrasound imaging [27], [28].

Another significant cause of stroke is atrial fibrillation, characterized by an abnormal heart rhythm resulting from disruptions or irregularities in the electrical signals that regulate the heart's beating [29]. These irregularities can cause the heart to beat too quickly, too slowly, or in an irregular pattern, affecting its ability to pump blood effectively. While atrial fibrillation can be initially treated with drugs, some cases may require cardiac interventional procedures. Intracardiac echocardiography can serve as a valuable tool in guiding these procedures [30], [31].

Additionally, the aorta, the largest artery in the body, can also be prone to a potentially life-threatening condition known as an abdominal aortic aneurysm (AAA), which involves swelling in the aorta [32]. While most AAAs are asymptomatic initially, they pose a risk of rupture, which can have severe and even fatal consequences. With an aging population, the incidence of AAAs has surged, contributing significantly to mortality rates. Surgical intervention is typically required for AAA treatment, and healthcare providers often recommend regular ultrasound screenings for individuals at risk [33].

1.2. ULTRASOUND PROBES

1.2.1. OPERATIONAL FREQUENCY

The human ear typically perceives sound waves within the audible range of 20 Hz to 20 kHz. Sound waves beyond this upper limit, exceeding 20 kHz, are called ultrasound waves. This is the case of ultrasound medical devices, which use sound

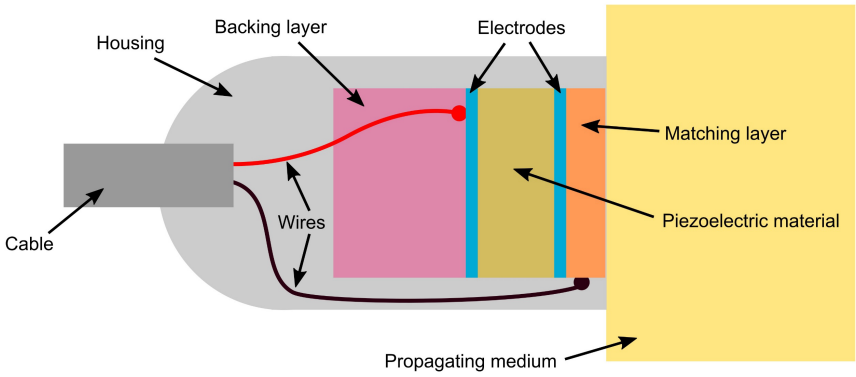

Figure 1.2: Cross-sectional illustration of a single-element transducer.

waves in the range of 1–20 MHz. Choosing the right frequency is crucial for achieving the optimal image resolution in ultrasound. High-frequency ultrasound waves (short wavelengths) produce images of exceptional axial resolution. However, these high-frequency waves experience more attenuation, particularly over long distances, making them suitable primarily for imaging superficial structures. Conversely, low-frequency waves (long wavelengths) yield lower-resolution images but excel in penetrating deeper structures due to reduced attenuation. Hence, optimal imaging involves using high-frequency transducers (within the 10–15 MHz range) for visualizing superficial structures and employing low-frequency transducers (typically 2–5 MHz) to capture images of deeper structures [4], [12].

1.2.2. SINGLE ELEMENT TRANSDUCER

At the core of every medical ultrasound imaging system lies the ultrasound transducer, which is responsible for converting electrical energy into mechanical energy and vice versa [34]. Most commonly, transducers today are made from lead zirconate titanate (PZT) [35]. However, the field is witnessing the emergence of transducers made from microelectromechanical systems (MEMS), including technologies like capacitive micromachined ultrasonic transducers (CMUTs) [36] and piezoelectric micromachined ultrasonic transducers (PMUTs) [37].

Typically, two additional layers are attached on both sides of the piezoelectric element, creating a sandwich structure shown in Figure 1.2. On the front side, facing the body, there is a matching layer, which is used to improve the energy transfer from the transducer to the tissue. The composition of this layer involves different materials to achieve the desired acoustic impedance value. On the back side of the PZT element sits the backing layer. Its role is to prevent excessive vibrations by absorbing energy transmitted to the rear of the transducer. To accomplish this, a material with a high attenuation coefficient is employed to effectively dampen mechanical oscillations [38], [39].

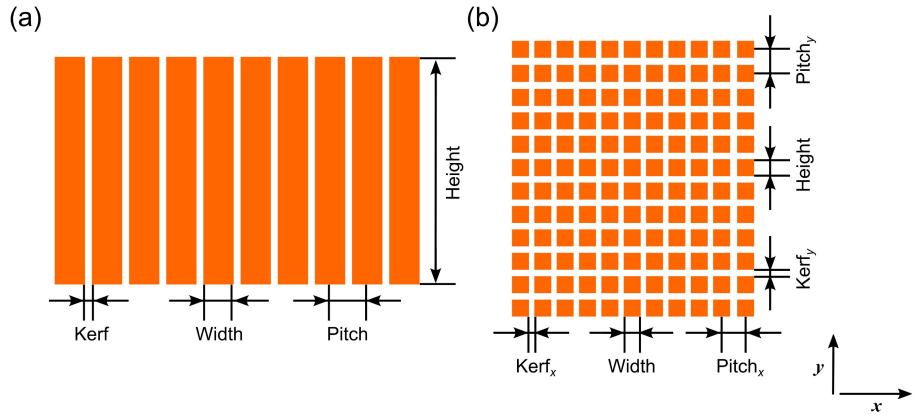

Figure 1.3: Transducer array configurations. (a) Linear array. (b) Matrix array.

1.2.3. TRANSDUCER ARRAYS

The majority of medical ultrasound transducers are array-type rather than single-element transducers. A transducer array consists of multiple small elements arranged in specific patterns. Although the shape of these elements can vary, rectangular ones are commonly chosen due to their cost-effectiveness in manufacturing [40]. These arrays can be divided into two main categories: linear (or 1D) arrays, where elements are aligned in a single line, and matrix (or 2D) arrays, where elements are arranged in a two-dimensional grid. As illustrated in Figure 1.3, the gap between two elements is called the “kerf”, while the distance between the centers of two adjacent elements is referred to as the "pitch" [41].

When an array allows electronic control over all its elements, it is called a 'phased array.' One of the significant advantages of phased arrays is their ability to electronically 'shape' the acoustic field. By electronically manipulating each element's delay and weighting, the beam can be automatically focused, steered, or shifted. This adjustment not only affects beam direction but also alters lateral resolution. Furthermore, phased arrays offer dynamic receive focusing, ensuring precise focusing across the scan depth, unlike the fixed focal lengths in single-element transducers [1], [4], [40]. A 1D phased array can focus and steer its beam through a sector-shaped region within a single plane, whereas a matrix array can focus and steer its beam through a 3D volume.

1.3. THREE-DIMENSIONAL ULTRASOUND

The most common clinical applications rely on 2D ultrasound imaging due to its capability to display cross-sectional views of the region of interest in real time. However, interpreting complex 3D structures from 2D images can be exceptionally difficult. Sonographers must mentally reconstruct these structures in three dimensions, a process highly subjective and influenced by their level of expertise. To

ensure accurate assessment of certain conditions, the use of 3D ultrasound imaging becomes crucial [28], [42].

Three main approaches are employed to generate volumetric ultrasound images: mechanical sweeping transducers, freehand scanning systems, and 2D matrix transducers. Mechanical sweeping involves physically moving a traditional 1D linear/phased array transducer using a motorized system. This movement determines both the position and orientation of the 2D images, which are later processed to reconstruct the 3D image [43].

Freehand scanning systems utilize a sensor attached to the conventional 1D array transducer. As the transducer is manipulated, the trajectory and orientation, alongside the 2D images, are recorded [44]. Both motorized and freehand scanning methods suffer from limitations in spatial resolution between imaging planes and slow scanning time. These drawbacks restrict their suitability for applications requiring high frame rates [45].

An alternative method for 3D imaging involves the use of a 2D matrix array. As mentioned earlier, a matrix array can focus and steer its beam within a 3D volume. This allows the transducer to remain stationary while electronically scanning the beam across the volume of interest [46]. Compared to the other methods, this technique overcomes the speed limitations, allowing for higher frame rates. Nevertheless, fabricating matrix transducers presents significant challenges due to the vast number of small-sized elements [47].

1.4. HIGH-FRAME-RATE ULTRASOUND

Conventional ultrasound involves sequential insonification of narrowly focused transmit beams (Figure 1.4(a)), followed by the acquisition of the backscattered echoes, which are then reconstructed line by line to form an image [48], [49]. In this process, the number of transmit events is equal to the number of scan lines N_L needed to generate an image [50]. Thus, the time required to construct a single 2D image (i.e., a frame) can be calculated as $T_f = (2N_L D/c)$, where D is the imaging depth and c is the speed of sound in the imaging medium. As a result, the frame rate FR can be determined as:

$$FR = \frac{1}{T_f} = \frac{c}{2N_L D} \tag{1.1}$$

For instance, considering an image with a depth of 5 cm and a width of 256 scan lines, it would result in a frame rate of about 60 Hz [51], [52]. While the typical frame rates achieved in conventional ultrasound imaging suffice for standard clinical assessments, they might not adequately capture short-time events that are crucial, for instance, in echocardiography [52], [53] or in scenarios demanding 3D/4D imaging with a substantial number of scan lines (typically several thousands) [51].

Therefore, it is of interest to explore techniques capable of increasing the temporal resolution of ultrasound imaging [54].

High-frame-rate ultrasound imaging can be achieved by employing unfocused transmit beams, such as plane (Figure 1.4(b)) and diverging waves (Figure 1.4(c)), along with parallel receive beamforming, also often referred to as multi-line acquisition [55], [56]. This approach removes the constraint imposed by the number of scan lines on the frame rate, thereby enabling higher frame rates:

$$FR_{ultrafast} = \frac{c}{2D} \tag{1.2}$$

Considering the same imaging scenario with a depth of 5 cm, the image could now be acquired at a frame rate of 15 kHz. However, while an unfocused transmit beam covers a wider region compared to a focused beam, it does impact image quality. Specifically, in high-frame-rate ultrasound, lateral spatial resolution and image contrast tend to be inferior to those achieved with conventional line-by-line imaging using focused transmit beams [48]. Nevertheless, image quality can be enhanced by transmitting multiple tilted plane waves or diverging waves and then coherently summing the acquired images [57].

The increased frame rates now possible in ultrasound imaging have created opportunities to measure tissue motion, blood, and contrast agents at kilohertz frequencies. This advancement has inspired the development of novel clinical applications for ultrasound, such as shear wave elastography [58], functional brain imaging [59], high-resolution vector flow imaging [60], ultrafast contrast agents imaging [61], electromechanical wave imaging [62], and more.

1.5. INTEGRATED CIRCUITS FOR ULTRASOUND PROBES

High-frame-rate 3D ultrasound imaging requires the use of a 2D matrix transducer array, which generally must have a large aperture and element pitch smaller than half the wavelength along both directions to prevent unwanted artifacts in the image

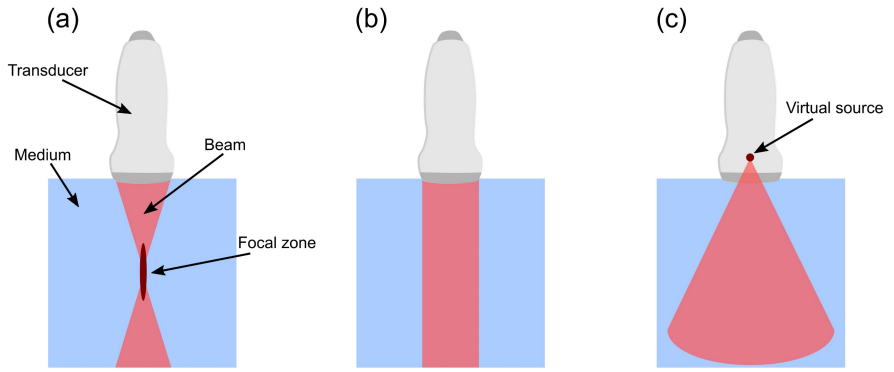

Figure 1.4: Different transmit beams. (a) Focused beam. (b) Plane wave. (c) Diverging wave.

[63]. However, the combination of small-sized elements and a wide aperture leads to a considerably large number of transducer elements, often in the order of thousands [64]. While constructing a matrix array with such an extensive element count is feasible, establishing electrical connections to all these elements becomes impractical due to limited space for accommodating cables and a shortage of channels on the ultrasound system (usually up to 256 channels).

Various methods have been proposed to simplify fully populated matrix arrays, such as sparse matrix arrays and row-column addressed matrix arrays. Sparse arrays effectively reduce channel count and electronic complexity, allowing high-frame rate 3D imaging [65]. However, they come with two primary limitations: lower signal-to-noise ratio and higher clutter levels. Row-column addressed arrays, on the other hand, decrease the number of connections from N^2 to $2N$ in an $M \times M$ matrix array. Yet, this design has its drawbacks, including more complex read-out sequences and a lower frame rate due to switching [66], [67].

Another approach involves the use of application-specific integrated circuits (ASICs), which can be integrated directly with the matrix array. This integration allows high-element-count transducers to interface with traditional 128- to 256-channel systems. To reduce channel count, different techniques can be employed, such as channel multiplexing, sub-aperture beamforming, in-probe-digitization, and time-division multiplexing [68], [69], [70]. Beyond channel reduction, ASICs offer additional advantages. For instance, they can amplify received signals, compensating for signal attenuation caused by cable loading, among other benefits [71]. These advantages make matrix arrays with in-probe integrated circuits an attractive technology for high-frame-rate 3D ultrasound imaging, although this comes at the cost of a more complex and costly developing process.

1.6. THIS THESIS

1.6.1. AIM

The overall aim of this thesis is to develop novel ultrasound probes to improve the diagnosis and treatment of cardiovascular diseases. Specifically, the research targets three specific clinical applications: carotid artery imaging, intracardiac echocardiography, and abdominal aorta imaging. These applications demand high-frame-rate 3D imaging with a relatively wide field of view, which calls for ultrasound matrix transducers with a substantial number of elements and integrated electronics. The thesis details the process of designing, fabricating, characterizing, and testing three distinct probes specifically designed for each targeted application.

1.6.2. RESEARCH CHALLENGES

1.6.2.1. PROBE DESIGN

When designing ultrasound transducers for high-frame-rate 3D imaging, several challenges arise. Primarily, these probes require thousands of elements, which present practical limitations in managing the vast number of cables within the transducer housing and connecting them to standard imaging systems. To reduce

channel count, integrating ultrasound probes with ASICs is essential, although it necessitates complex and specific architectures within a limited area. Additionally, it is crucial to explore imaging schemes capable of effectively achieving the required frame rate within the desired field of view while optimizing performance and maintaining image quality.

1.6.2.2. MANUFACTURING PROCESS

The integration of ASICs into ultrasound matrix transducers introduces complexity, impacting both the manufacturing process and the functionality of the probes. It is essential to explore methods for improving processes, minimizing costs, ensuring scalability, and maintaining optimal performance while seamlessly integrating ASICs with ultrasound probes.

1.6.2.3. CHARACTERIZATION PROCESS

Implementing a comprehensive electrical and acoustical characterization process is crucial for evaluating both the manufacturing process and probe performance. This involves conducting detailed element-level characterization in both transmit and receive operations, as well as designing measurement setups and algorithms capable of automatically executing tests, analyzing results, and identifying areas for improvement.

1.6.3. OUTLINE

Part I: Strategies for transducer characterization

The first part of this thesis focuses on strategies to simplify and automate the acoustic characterization process of ultrasound transducers. Given the recent advancements in transducer technology with complex design and technical requirements, there is also a clear need for appropriate tools to effectively characterize these transducers.

Chapter 2 introduces a novel approach for calibrating single-element ultrasound transducers using the acoustic streaming effect they generate. This alternative method achieves accuracy levels comparable to traditional pulse-echo and hydrophone measurements.

Chapter 3 presents a pipeline designed to automate the characterization process of a matrix transducer consisting of about a thousand elements. This pipeline handles the characterization for both transmit and receive operations of each single element within the transducer in a fast and convenient way.

Chapter 4 describes the process employed to characterize the pressure field of high-element-count matrix transducers (over 1000 elements) using hydrophone measurements. The procedure involves a high level of integration among different devices, measurements, and instrumentation. The outcomes provide valuable insights into the distinct acoustic outputs of individual transducer elements.

Chapter 5 presents the experimental impact of subdicing on a PZT matrix transducer with large elements (width-to-thickness ratio larger than 0.7). Within the prototype transducer, elements with and without subdicing are compared

directly under identical conditions. The results indicate superior performance among the subdiced elements compared to their non-subdiced counterparts.

Part II: Transducer design for high-frame-rate 3D imaging

The second part of this thesis explores the development, manufacturing, characterization, and imaging assessment of dedicated matrix transducers featuring integrated ASICs. These transducers are tailored for specific medical applications that require high-frame-rate 3D ultrasound imaging.

Chapter 6 presents the design of an ASIC integrated with a dedicated piezoelectric matrix transducer intended for high-frame-rate 3D carotid artery imaging. This ASIC utilizes an improved switch design specifically aimed at reducing imaging artifacts.

Chapter 7 details the design, fabrication, and tests of a dedicated PZT matrix transducer tailored specifically for high-frame-rate 3D carotid artery imaging. The transducer was designed to have over 7000 elements and is mounted on top of 8 identical tiled ASICs. The performance evaluation of the prototype involves a comprehensive series of measurements.

Chapter 8 discusses the development of an ASIC integrated with a dedicated PZT matrix designed for high-frame-rate 3D intracardiac echocardiography. This ASIC employs various techniques to achieve a reduction in cable count while simultaneously minimizing power consumption within the catheter.

Chapter 9 describes the development of a PZT matrix transducer prototype for high-frame-rate 3D intracardiac echocardiography, with a specific focus on electromechanical wave imaging. The matrix is built on top of an ASIC that generates transmission signals and digitizes the received signals. The performance of the prototype is characterized, and its functionality is fully verified.

Chapter 10 presents the development of a CMUT matrix array for high-frame-rate 3D imaging of the abdominal aorta. This transducer comprises over 8000 elements and is integrated with pitch-matched ASICs. The main design aspects are discussed, followed by initial tests to verify the functionality of the probe.

Chapter 11 concludes the thesis, summarizing the main findings and offering recommendations for future research.

1.7. REFERENCES

[1] H. Azhari, *Basics of Biomedical Ultrasounds for Engineers*. Hoboken, New Jersey: John Wiley & Sons, Inc., 2010.

[2] P. J. Dempsey, "The History of Breast Ultrasound," *Journal of Ultrasound in Medicine*, vol. 23, no. 7, pp. 887–894, Jul. 2004, doi: 10.7863/jum.2004.23.7.887.

[3] F. A. Firestone, "The Supersonic Reflectoscope, an Instrument for Inspecting the Interior of Solid Parts by Means of Sound Waves," vol. 17, no. 3, 1945.

[4] T. L. Szabo, *Diagnostic Ultrasound Imaging: Inside Out*. New York: Elsevier, 2014. doi: 10.1016/C2011-0-07261-7.

[5] J. J. Wild and J. M. Reid, "Application of Echo-Ranging Techniques to the Determination of Structure of Biological Tissues," *Science (1979)*, vol. 115, no. 2983, pp. 226–230, Feb. 1952, doi: 10.1126/science.115.2983.226.

[6] D. H. Howry, D. A. Stott, and W. R. Bliss, "The ultrasonic visualization of carcinoma of the breast and other soft-tissue structures," *Cancer*, vol. 7, no. 2, pp. 354–358, Mar. 1954, doi: 10.1002/1097-0142(195403)7:2<354::AID-CNCR2820070220>3.0.CO;2-9.

[7] J. H. Holmes, D. H. Howry, G. J. Posakony, and C. R. Cushman, "The ultrasonic visualization of soft tissue structures in the human body.," *Trans Am Clin Climatol Assoc*, vol. 66, no. C, pp. 208–25, 1954.

[8] J. C. Somer, "Electronic sector scanning for ultrasonic diagnosis," *Ultrasonics*, vol. 6, no. 3, pp. 153–159, 1968, doi: 10.1016/0041-624X(68)90277-1.

[9] N. Bom, C. T. Lancee, G. van Zwieten, F. E. Kloster, and J. Roelandt, "Multiscan echocardiography. I. Technical description," *Circulation*, vol. 48, no. 5, pp. 1066–1074, 1973, doi: 10.1161/01.CIR.48.5.1066.

[10] K. A. Kaproth-Joslin, R. Nicola, and V. S. Dogra, "The history of US: From bats and boats to the bedside and beyond," *Radiographics*, vol. 35, no. 3, pp. 960–970, 2015, doi: 10.1148/rg.2015140300.

[11] C. F. Dietrich, C. B. Sirlin, M. O'Boyle, Y. Dong, and C. Jenssen, "Editorial on the current role of ultrasound," *Applied Sciences (Switzerland)*, vol. 9, no. 17, pp. 1–9, 2019, doi: 10.3390/app9173512.

[12] S. N. Narouze, *Atlas of Ultrasound-Guided Procedures in Interventional Pain Management*. New York, NY: Springer New York, 2011. doi: 10.1007/978-1-4419-1681-5.

[13] W. Zhou, X. Ma, L. Pan, Y. Wang, and C. Zhou, "Application of conventional ultrasound coupled with virtual touch tissue imaging and quantification in the assessment of muscle strength," *Ann Palliat Med*, vol. 9, no. 5, pp. 3402–3409, Sep. 2020, doi: 10.21037/apm-20-1715.

[14] N. Frulio and H. Trillaud, "Ultrasound elastography in liver," *Diagn Interv Imaging*, vol. 94, no. 5, pp. 515–534, May 2013, doi: 10.1016/j.diii.2013.02.005.

[15] P. Kruizinga, F. Mastik, N. de Jong, A. F. W. van der Steen, and G. van Soest, "High frame rate ultrasound imaging of human carotid artery dynamics," in *2012 IEEE International Ultrasonics Symposium*, IEEE, Oct. 2012, pp. 1177–1180. doi: 10.1109/ULTSYM.2012.0293.

[16] J. Provost, C. Papadacci, C. Demene, J.-L. Gennisson, M. Tanter, and M. Pernot, "3-D ultrafast doppler imaging applied to the noninvasive mapping of blood vessels in Vivo," *IEEE Trans Ultrason Ferroelectr Freq Control*, vol. 62, no. 8, pp. 1467–1472, Aug. 2015, doi: 10.1109/TUFFC.2015.007032.

[17] H. M. Garcia-Garcia, M. A. Costa, and P. W. Serruys, "Imaging of coronary atherosclerosis: intravascular ultrasound," *Eur Heart J*, vol. 31, no. 20, pp. 2456–2469, Oct. 2010, doi: 10.1093/eurheartj/ehq280.

[18] W. Lee, S. F. Idriss, P. D. Wolf, and S. W. Smith, "A miniaturized catheter 2-D array for real-time, 3-D intracardiac echocardiography," *IEEE Trans Ultrason Ferroelectr Freq Control*, vol. 51, no. 10, pp. 1334–1346, Oct. 2004, doi: 10.1109/TUFFC.2004.1350962.

[19] F. L. Lizzi *et al.*, "Radiation-force technique to monitor lesions during ultrasonic therapy," *Ultrasound Med Biol*, vol. 29, no. 11, pp. 1593–1605, Nov. 2003, doi: 10.1016/S0301-5629(03)01052-4.

[20] A. J. Coleman and J. E. Saunders, "A review of the physical properties and biological effects of the high amplitude acoustic fields used in extracorporeal lithotripsy," *Ultrasonics*, vol. 31, no. 2, pp. 75–89, Jan. 1993, doi: 10.1016/0041-624X(93)90037-Z.

[21] K. Kooiman *et al.*, "Oil-filled polymer microcapsules for ultrasound-mediated delivery of lipophilic drugs," *Journal of Controlled Release*, vol. 133, no. 2, pp. 109–118, Jan. 2009, doi: 10.1016/J.JCONREL.2008.09.085.

[22] A. Ziadloo, J. Xie, and V. Frenkel, "Pulsed focused ultrasound exposures enhance locally administered gene therapy in a murine solid tumor model," *J Acoust Soc Am*, vol. 133, no. 3, pp. 1827–1834, Mar. 2013, doi: 10.1121/1.4789390.

[23] G. Renaud and S. Salles, "Single-Sided Ultrasound Imaging of the Bone Cortex: Anatomy, Tissue Characterization and Blood Flow," in *Advances in Experimental Medicine and Biology*, vol. 1364, Springer, 2022, pp. 197–225. doi: 10.1007/978-3-030-91979-5_10.

[24] J. Seo and Y. Kim, "Ultrasound imaging and beyond: recent advances in medical ultrasound," *Biomed Eng Lett*, vol. 7, no. 2, pp. 57–58, May 2017, doi: 10.1007/s13534-017-0030-7.

[25] World Health Organization, "Cardiovascular diseases." Accessed: Feb. 09, 2024. [Online]. Available: https://www.who.int/health-topics/cardiovascular-diseases#tab=tab_1

[26] S. M. Bierig, A. Arnold, L. C. Einbinder, E. Armbrecht, and T. Burroughs, "Cardiovascular Ultrasound Combined With Non-invasive Screening for the Detection of Undiagnosed Cardiovascular Disease: A Literature Review," *Journal of Diagnostic Medical Sonography*, vol. 34, no. 3, pp. 197–206, May 2018, doi: 10.1177/8756479317737764.

[27] H. R. Tahmasebpour, A. R. Buckley, P. L. Cooperberg, and C. H. Fix, "Sonographic Examination of the Carotid Arteries," *RadioGraphics*, vol. 25, no. 6, pp. 1561–1575, Nov. 2005, doi: 10.1148/rg.256045013.

[28] D. S. dos Santos *et al.*, "A Tiled Ultrasound Matrix Transducer for Volumetric Imaging of the Carotid Artery," *Sensors*, vol. 22, no. 24, p. 9799, Dec. 2022, doi: 10.3390/s22249799.

[29] A. S. Go *et al.*, "Prevalence of Diagnosed Atrial Fibrillation in Adults," *JAMA*, vol. 285, no. 18, p. 2370, May 2001, doi: 10.1001/jama.285.18.2370.

[30] D. S. dos Santos *et al.*, "An Ultrasound Matrix Transducer for High-Frame-Rate 3-D Intra-cardiac Echocardiography," *Ultrasound Med Biol*, vol. 50, no. 2, pp. 285–294, Feb. 2024, doi: 10.1016/j.ultrasmedbio.2023.11.001.

[31] D. Wildes *et al.*, "4-D ICE: A 2-D Array Transducer With Integrated ASIC in a 10-Fr Catheter for Real-Time 3-D Intracardiac Echocardiography," *IEEE Trans Ultrason Ferroelectr Freq Control*, vol. 63, no. 12, pp. 2159–2173, Dec. 2016, doi: 10.1109/TUFFC.2016.2615602.

[32] D. Mozaffarian *et al.*, "Executive Summary: Heart Disease and Stroke Statistics—2016 Update," *Circulation*, vol. 133, no. 4, pp. 447–454, Jan. 2016, doi: 10.1161/CIR.0000000000000366.

[33] P. Bihari *et al.*, "Strain Measurement of Abdominal Aortic Aneurysm with Real-time 3D Ultrasound Speckle Tracking," *European Journal of Vascular and Endovascular Surgery*, vol. 45, no. 4, pp. 315–323, Apr. 2013, doi: 10.1016/j.ejvs.2013.01.004.

[34] J. W. Hunt, M. Arditi, and F. S. Foster, "Ultrasound Transducers for Pulse-Echo Medical Imaging," *IEEE Trans Biomed Eng*, vol. BME-30, no. 8, pp. 453–481, Aug. 1983, doi: 10.1109/TBME.1983.325150.

[35] H. P. Savakus, K. A. Klicker, and R. E. Newnham, "PZT-epoxy piezoelectric transducers: A simplified fabrication procedure," *Mater Res Bull*, vol. 16, no. 6, pp. 677–680, Jun. 1981, doi: 10.1016/0025-5408(81)90267-1.

[36] B. T. Khuri-Yakub and Ö. Oralkan, "Capacitive micromachined ultrasonic transducers for medical imaging and therapy," *Journal of Micromechanics and Microengineering*, vol. 21, no. 5, p. 054004, May 2011, doi: 10.1088/0960-1317/21/5/054004.

[37] P. Muralt *et al.*, "Piezoelectric micromachined ultrasonic transducers based on PZT thin films," *IEEE Trans Ultrason Ferroelectr Freq Control*, vol. 52, no. 12, pp. 2276–2288, Dec. 2005, doi: 10.1109/TUFFC.2005.1563270.

[38] V. M. do Nascimento, V. L. d. S. Nantes Button, J. M. Maia, E. T. Costa, and E. J. V Oliveira, "Influence of backing and matching layers in ultrasound transducer performance," *Spie*, vol. 5035, p. 86, 2003, doi: 10.1117/12.479924.

[39] N. de Jong, N. Bom, J. Souquet, and G. Faber, "Vibration modes, matching layers and grating lobes," *Ultrasonics*, vol. 23, no. 4, pp. 176–182, Jul. 1985, doi: 10.1016/0041-624X(85)90027-7.

[40] J. D. Bronzino, *Medical Devices and Systems*. CRC Press, 2006. doi: 10.1201/9781420003864.

[41] K . Kirk Shung and J. Yen, "Array transducers and Beamformers," in *Ultrasound Imaging and Therapy*, A. Fenster and J. C. Lacefield, Eds., Boca Raton, FL: CRC Press, 2015.

[42] S. Holbek, M. J. Pihl, C. Ewertsen, M. B. Nielsen, and J. A. Jensen, "In vivo 3-D vector velocity estimation with continuous data," in *2015 IEEE International Ultrasonics Symposium (IUS)*, IEEE, Oct. 2015, pp. 1–4. doi: 10.1109/ULTSYM.2015.0235.

[43] Z. Guo and A. Fenster, "Three-dimensional power Doppler imaging: A phantom study to quantify vessel stenosis," *Ultrasound Med Biol*, vol. 22, no. 8, pp. 1059–1069, Jan. 1996, doi: 10.1016/S0301-5629(96)00125-1.

[44] J. N. Welch, J. A. Johnson, M. R. Bax, R. Badr, and R. Shahidi, "A real-time freehand 3D ultrasound system for image-guided surgery," in *2000 IEEE Ultrasonics Symposium. Proceedings. An International Symposium (Cat. No.00CH37121)*, IEEE, 2000, pp. 1601–1604. doi: 10.1109/ULTSYM.2000.921630.

[45] R. W. Prager, U. Z. Ijaz, A. H. Gee, and G. M. Treece, "Three-dimensional ultrasound imaging," *Proc Inst Mech Eng H*, vol. 224, no. 2, pp. 193–223, Feb. 2010, doi: 10.1243/09544119JEIM586.

[46] D. H. Turnbull and F. S. Foster, "Fabrication and characterization of transducer elements in two-dimensional arrays for medical ultrasound imaging," *IEEE Trans Ultrason Ferroelectr Freq Control*, vol. 39, no. 4, pp. 464–475, Jul. 1992, doi: 10.1109/58.148536.

[47] S. W. Smith, W. Lee, E. D. Light, J. T. Yen, P. Wolf, and S. Idriss, "Two dimensional arrays for 3-D ultrasound imaging," in *2002 IEEE Ultrasonics Symposium, 2002. Proceedings.*, IEEE, 2002, pp. 1545–1553. doi: 10.1109/ULTSYM.2002.1192590.

[48] H. Hasegawa, "Very high frame rate ultrasound for medical diagnostic imaging," in *AIP Conference Proceedings*, 2019, p. 020015. doi: 10.1063/1.5133930.

[49] G. M. Lanza, "Ultrasound Imaging," *Invest Radiol*, vol. 55, no. 9, pp. 573–577, Sep. 2020, doi: 10.1097/RLI.0000000000000679.

[50] T. Misaridis and J. A. Jensen, "Use of modulated excitation signals in medical ultrasound. Part I: basic concepts and expected benefits," *IEEE Trans Ultrason Ferroelectr Freq Control*, vol. 52, no. 2, pp. 177–191, Feb. 2005, doi: 10.1109/TUFFC.2005.1406545.

[51] J. Bercoff, "Ultrafast Ultrasound Imaging," in *Ultrasound Imaging - Medical Applications*, O. Minin and I. Minin, Eds., InTech, 2011. doi: 10.5772/19729.

[52] S. Afrakhteh, G. Iacca, and L. Demi, "High Frame Rate Ultrasound Imaging by Means of Tensor Completion: Application to Echocardiography," *IEEE Trans Ultrason Ferroelectr Freq Control*, vol. 70, no. 1, pp. 41–51, Jan. 2023, doi: 10.1109/TUFFC.2022.3223499.

[53] M. Cikes, L. Tong, G. R. Sutherland, and J. D'hooge, "Ultrafast Cardiac Ultrasound Imaging," *JACC Cardiovasc Imaging*, vol. 7, no. 8, pp. 812–823, Aug. 2014, doi: 10.1016/j.jcmg.2014.06.004.

[54] A. Rabinovich, Z. Friedman, and A. Feuer, "Multi-line acquisition with minimum variance beamforming in medical ultrasound imaging," *IEEE Trans Ultrason Ferroelectr Freq Control*, vol. 60, no. 12, pp. 2521–2531, Dec. 2013, doi: 10.1109/TUFFC.2013.2851.

[55] D. P. Shattuck, M. D. Weinshenker, S. W. Smith, and O. T. von Ramm, "Explososcan: A parallel processing technique for high speed ultrasound imaging with linear phased arrays," *J Acoust Soc Am*, vol. 75, no. 4, pp. 1273–1282, Apr. 1984, doi: 10.1121/1.390734.

[56] O. Senouf *et al.*, "High Frame-Rate Cardiac Ultrasound Imaging with Deep Learning," in *Lecture Notes in Computer Science (including subseries Lecture Notes in Artificial Intelligence and Lecture Notes in Bioinformatics)*, vol. 11070 LNCS, 2018, pp. 126–134. doi: 10.1007/978-3-030-00928-1_15.

[57] C. Papadacci, M. Pernot, M. Couade, M. Fink, and M. Tanter, "High-contrast ultrafast imaging of the heart," *IEEE Trans Ultrason Ferroelectr Freq Control*, vol. 61, no. 2, pp. 288–301, Feb. 2014, doi: 10.1109/TUFFC.2014.6722614.

[58] J. Bercoff, M. Tanter, and M. Fink, "Supersonic shear imaging: a new technique for soft tissue elasticity mapping," *IEEE Trans Ultrason Ferroelectr Freq Control*, vol. 51, no. 4, pp. 396–409, Apr. 2004, doi: 10.1109/TUFFC.2004.1295425.

[59] E. Macé, G. Montaldo, I. Cohen, M. Baulac, M. Fink, and M. Tanter, "Functional ultrasound imaging of the brain," *Nat Methods*, vol. 8, no. 8, pp. 662–664, Aug. 2011, doi: 10.1038/nmeth.1641.

[60] J. Udesen, F. Gran, K. Hansen, J. A. Jensen, C. Thomsen, and M. B. Nielsen, "High frame-rate blood vector velocity imaging using plane waves: Simulations and preliminary experiments," *IEEE Trans Ultrason Ferroelectr Freq Control*, vol. 55, no. 8, pp. 1729–1743, Aug. 2008, doi: 10.1109/TUFFC.2008.858.

[61] O. Couture, S. Bannouf, G. Montaldo, J.-F. Aubry, M. Fink, and M. Tanter, "Ultrafast Imaging of Ultrasound Contrast Agents," *Ultrasound Med Biol*, vol. 35, no. 11, pp. 1908–1916, Nov. 2009, doi: 10.1016/j.ultrasmedbio.2009.05.020.

[62] J. Provost, W.-N. Lee, K. Fujikura, and E. E. Konofagou, "Imaging the electromechanical activity of the heart in vivo," *Proceedings of the National Academy of Sciences*, vol. 108, no. 21, pp. 8565–8570, May 2011, doi: 10.1073/pnas.1011688108.

[63] Y. Paul, D. Barthez, R. Léveillé, V. Peter, and D. Scrivani, "Side lobes and grating lobes artifacts in ultrasound imaging," *Veterinary Radiology & Ultrasound*, vol. 38, no. 5, pp. 387–393, Sep. 1997, doi: 10.1111/j.1740-8261.1997.tb02104.x.

[64] J. Provost *et al.*, "3D ultrafast ultrasound imaging in vivo," *Phys Med Biol*, vol. 59, no. 19, pp. L1–L13, 2014, doi: 10.1088/0031-9155/59/19/L1.

[65] A. Ramalli, E. Boni, A. S. Savoia, and P. Tortoli, "Density-tapered spiral arrays for ultrasound 3-D imaging," *IEEE Trans Ultrason Ferroelectr Freq Control*, vol. 62, no. 8, pp. 1580–1588, 2015, doi: 10.1109/TUFFC.2015.007035.

[66] L. Wei *et al.*, "High Frame Rate Volumetric Imaging of Microbubbles Using a Sparse Array and Spatial Coherence Beamforming," *IEEE Trans Ultrason Ferroelectr Freq Control*, vol. 68, no. 10, pp. 3069–3081, 2021, doi: 10.1109/TUFFC.2021.3086597.

[67] M. F. Rasmussen and J. A. Jensen, "3-D ultrasound imaging performance of a row-column addressed 2-D array transducer: A measurement study," in *2013 IEEE International Ultrasonics Symposium (IUS)*, IEEE, Jul. 2013, pp. 1460–1463. doi: 10.1109/ULTSYM.2013.0370.

[68] B. Savord and R. Solomon, "Fully sampled matrix transducer for real time 3D ultrasonic imaging," in *IEEE Symposium on Ultrasonics, 2003*, IEEE, 2003, pp. 945–953. doi: 10.1109/ULTSYM.2003.1293556.

[69] C. Chen *et al.*, "A Pitch-Matched Front-End ASIC With Integrated Subarray Beamforming ADC for Miniature 3-D Ultrasound Probes," *IEEE J Solid-State Circuits*, vol. 53, no. 11, pp. 3050–3064, Nov. 2018, doi: 10.1109/JSSC.2018.2864295.

[70] T. M. Carpenter, M. W. Rashid, M. Ghovanloo, D. M. J. Cowell, S. Freear, and F. L. Degertekin, "Direct Digital Demultiplexing of Analog TDM Signals for Cable Reduction in Ultrasound Imaging Catheters," *IEEE Trans Ultrason Ferroelectr Freq Control*, vol. 63, no. 8, pp. 1078–1085, Aug. 2016, doi: 10.1109/TUFFC.2016.2557622.

[71] E. Kang *et al.*, "A Reconfigurable Ultrasound Transceiver ASIC With 24 × 40 Elements for 3-D Carotid Artery Imaging," *IEEE J Solid-State Circuits*, vol. 53, no. 7, pp. 2065–2075, Jul. 2018, doi: 10.1109/JSSC.2018.2820156.

PART I: STRATEGIES FOR TRANSDUCER CHARACTERIZATION

2

ACOUSTIC STREAMING-BASED CALIBRATION OF ULTRASOUND TRANSDUCERS[1]

[1] This chapter is based on the following publication:
dos Santos, D.S.; Baldini, L.; Vos, H.J.; Verweij, M.D.; de Jong, N.; van Neer, P.L.M.J. Acoustic Streaming-Based Calibration of Ultrasound Transducers. Applied Acoustics 2024, 217, 109863, doi:10.1016/j.apacoust.2024.109863.

2.1. INTRODUCTION

THE characterization of the pressure field transmitted by ultrasound transducers is a critical aspect of their design process. This process is crucial for validating models, optimizing design parameters, evaluating the manufacturing process, and investigating acoustic phenomena that may affect the transducer's behavior in practice [1]. Furthermore, pressure field characterization is essential to facilitate the maintenance of transducers used in various applications, particularly in the medical field. As the operating characteristics of ultrasound transducers tend to change over time and usage with an average lifespan [2], concerns may arise regarding the effectiveness and safety of these transducers [3]. Therefore, it is imperative to establish test routines to periodically evaluate the performance of ultrasound transducers and ensure their compliance with national and international standards [4].

An important aspect in assessing the performance of an ultrasound transducer is determining its transmit transfer function, also known as transmit efficiency, which is a frequency-dependent quantity defined as the ratio of the output acoustic pressure at the transducer's surface to the input voltage on its electrodes [5]. Various methods have been proposed to estimate the transmit efficiency of the transducer, with the standard approach involving the use of a calibrated hydrophone to record the time-varying acoustic pressure generated by the transducer at specified locations using an xyz-positioning stage. Although this method is convenient, it can be costly as hydrophone calibration needs to be performed annually at an accredited laboratory [6]–[8]. Another common technique for measuring the acoustic output of ultrasound transducers is the use of radiation force balances. This method measures the acoustic radiation force produced when ultrasound is incident upon an absorbing target [9]. However, this technique has its drawbacks, as it is expensive, challenging to operate, and highly sensitive to noise and vibrations [10].

Alternative methods for estimating the transducer transfer function are based on the reciprocity technique [11]. Dang et al. [12] introduced a model-based approach that employs three transducers in a pitch-catch configuration and only requires electrical measurements such as voltage and current. This method enables the determination of both the magnitude and phase of the transfer function. However, this is a relatively complex and time-consuming process that involves the use of three distinct setups, requiring careful realignments between changes in setup. Lopez-Sanchez et al. [13] proposed a simplified version of the aforementioned method, which uses a single pulse-echo setup and relies solely on electrical measurements to determine the magnitude and phase of the transfer function. However, this method has a drawback as the magnitude of the transfer function is somewhat affected by the settings of the driving source at lower frequencies. Van Neer et al. [5] proposed a method that employs a pulse-echo setup along with complex electrical impedance measurements. This method can determine the absolute transfer function with a high degree of accuracy and is relatively straightforward. However, it requires the use of an impedance analyzer, which is an expensive device that may not always be accessible. Matte et al. [7] proposed an alternative method for estimating the absolute transfer function by using an uncalibrated hydrophone together with pressure field simulations. This method

requires an iterative algorithm to match the measured levels of harmonics with the simulated harmonic distortion coefficient. A limitation of this approach is that it considers only the second harmonic in the calculations, which results in a sharp increase in estimation error at high-pressure levels.

Recently, a few studies have investigated the transmit characterization of transducers through a phenomenon called acoustic streaming. Acoustic streaming refers to the steady flow induced by the ultrasound transducer in the propagating medium [14]. By measuring the streaming velocity, which is directly related to the acoustic power emitted by the transducer, it becomes possible to estimate the acoustic pressure generated by the transducer. Hariharan et al. [15] and Slama et al. [16] utilized acoustic streaming to characterize high-intensity focused ultrasound (HIFU) transducers, while Tan et al. [17] applied it to characterize an ultrasonic thruster. To track the acoustic streaming motion and predict the intensity field of the transducer, these studies utilized particle image velocimetry (PIV). Although this approach successfully characterized the acoustic output of the transducers, it's important to note that it involves complex experimental setups and requires sophisticated algorithms to solve the seeding particle velocity.

In this paper, we introduce a streaming-based method for determining the transmit transfer function of ultrasound transducers. The key advantage of our approach is that it offers a simpler setup compared to the previous studies that utilize PIV to track streaming motion. Instead, we employ ink as a tracer and use a digital camera to measure the induced streaming velocity in water. To validate the effectiveness of the proposed method, we compared its performance with two other well-established methods: hydrophone and pulse-echo measurements [5], [18].

2.2. THEORY

Acoustic streaming refers to the consistent movement or steady flow of a fluid induced by the propagation of acoustic waves. This is a non-linear effect that can be described using the general equations of hydrodynamics, namely the continuity equation (2.1) and the Navier-Stokes equation (2.2).

$$\frac{\partial \rho}{\partial t} + \nabla \cdot \rho v = 0 \tag{2.1}$$

$$\rho\left(\frac{\partial v}{\partial t} + v \cdot \nabla v\right) = -\nabla p + \left(\zeta + \frac{4}{3}\eta\right)\nabla\nabla \cdot v - \eta \nabla \times \nabla \times v \tag{2.2}$$

where p is the pressure, ρ the density, v the velocity, and ζ and η are, respectively, the bulk and the shear viscosity coefficients of the fluid [14], [19]. By combining Eq. (2.1) and (2.2), we obtain:

$$\frac{\partial(\rho v)}{\partial t} + \rho(v \cdot \nabla)v + v\nabla \cdot \rho v = -\nabla p + \left(\zeta + \frac{4}{3}\eta\right)\nabla\nabla \cdot v - \eta \nabla \times \nabla \times v \tag{2.3}$$

The phenomenon of acoustic streaming can be divided into two components: a linear oscillation component, which is dominated by the fluid's compressibility, and a steady flow component, which is governed by the fluid's viscosity. In this context, it is assumed that the time scales of the harmonic oscillations and the steady flow differ significantly from each other [20]. To implement this idea, Nyborg [21], [22] introduced expansions of the pressure, density, and velocity in terms of successively higher-order approximations:

$$\begin{aligned} p &= p_0 + p_1 + p_2 \\ \rho &= \rho_0 + \rho_1 + \rho_2 \\ v &= 0 + v_1 + v_2 \end{aligned} \tag{2.4}$$

where the subscript 0 denotes the state of the undisturbed fluid, 1 represents the first-order approximations that oscillate in time with frequency ω, and 2 indicates the second-order approximations that are time-independent [20], [23]. The term v_2 is the streaming velocity that we seek. Using the higher-order approximations and taking the time average of Eq. (2.3), Nyborg obtained a governing equation for the acoustic streaming, which may be written as:

$$F = -\nabla p_2 + \left(\zeta + \frac{4}{3}\eta\right)\nabla\nabla v_2 - \eta\nabla \times \nabla \times v_2 \tag{2.5}$$

with

$$F = \rho_0\langle(v_1 \cdot \nabla)v_1 + v_1(\nabla \cdot v_1)\rangle \tag{2.6}$$

and the symbol $\langle X\rangle$ denotes the time average of X at a fixed point in space [19], [22]. Note that F depends only on first-order quantities and is a known function, while the right-hand side of Eq. (2.5) contains unknown second-order terms. This means that the force F is equivalent to an external force driving the second-order system.

For an exponentially attenuating plane wave, this force is called the acoustic radiation force F_{rad} and can be expressed as:

$$F_{rad} = \frac{2\alpha I_{TA}}{c} \tag{2.7}$$

where α is the absorption coefficient, I_{TA} is the local time-average acoustic intensity, and c is the longitudinal sound speed in the medium [24]–[27].

Nowicki et al. [28], [29] obtained the solution for the axial component of the streaming velocity for the case of a plane acoustic wave generated by an unfocused circular transducer, which is given by:

$$v_{2z}(0,0,z) = \frac{\alpha I_{TA} r^2}{\eta c} \int_0^{\infty} e^{-2\alpha r s} \left[\sqrt{1 + \left(\frac{z}{r} - s\right)^2} - \sqrt{1 + \left(\frac{z}{r} + s\right)^2} + \left(\frac{z}{r} + s\right) - \left|\frac{z}{r} - s\right| \right] ds \tag{2.8}$$

where r is the radius of the transducer, I_{TA} is the time-averaged intensity at the surface of the transducer, and s is the integration variable on the propagation axis z.

Eq. (2.8) establishes a relationship between the streaming velocity and the acoustic intensity at the transducer surface. Therefore, by measuring the velocity of the streaming flow along the axial axis, one can calculate the acoustic pressure generated at the surface of the transducer, provided the medium properties and the transducer effective radius are known. It is important to note that this analysis is based on the assumption that the streaming jet maintains a steady, laminar flow within an infinite medium. This implies that there is no interaction between the acoustic beam and the surrounding walls, thereby eliminating the presence of an acoustic boundary layer in the problem. Under these conditions, the flow dynamics are primarily governed by a balance between the effects of viscosity, inertia, and the acoustic radiation force [30].

2.3. MATERIALS AND METHODS

2.3.1. ACOUSTIC STREAMING MEASUREMENTS

Figure 2.1(a) depicts the experimental setup used for generating acoustic streaming, comprising a circular transducer (V309, Olympus NDT, Waltham, MA, USA), placed in a water tank labeled with a millimeter grid to enable distance measurement. The transducer used in the experiment had a center frequency of 5 MHz and an effective radius of 5.6 mm, which was determined by comparing the simulated radiation pattern of a piston model with experiments [31]. To drive the transducer, we employed an arbitrary function generator (AWG; 33521A, Agilent Technologies, Inc., Santa Clara, CA, USA), which was configured to generate a sine wave burst with a peak amplitude of 0.2 V into a 50 Ω load. This burst had a duty factor τ of 0.7 and operated at a pulse repetition frequency PRF of 100 Hz. The excitation frequency f ranged from 2 to 8 MHz, incrementing in steps of 1 MHz. The number of cycles n applied for each excitation frequency was determined by:

$$n = \tau \cdot \frac{f}{PRF} \tag{2.9}$$

The AWG output was then amplified by a 50 dB power amplifier (2100L, ENI, Inc., Rochester, NY, USA) and connected to the transducer. To measure the voltage at the transmitting transducer at various frequencies, a digital oscilloscope (DSO-X 2022A, Agilent Technologies, Inc., Santa Clara, CA, USA) was utilized.

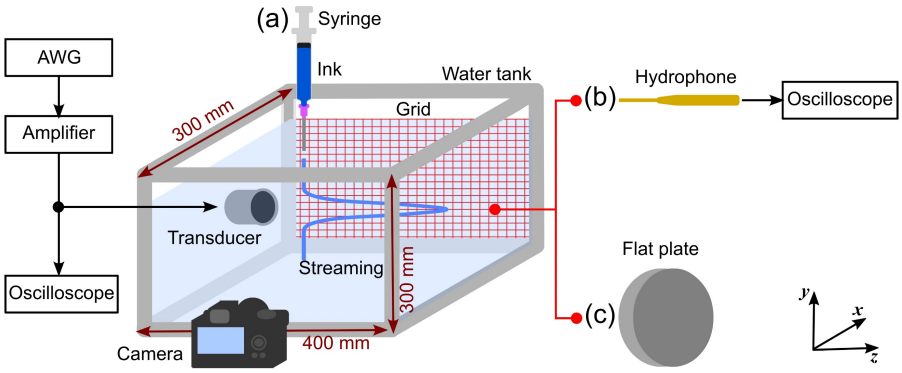

Figure 2.1: Experimental setup for transmit transfer function estimation with different methods (not drawn to scale). (a) Acoustic streaming. (b) Hydrophone measurements. (c) Pulse-echo measurements.

To track the axial streaming velocity, we injected 10 ml of ink (Quink, Parker Pen Company, Boulogne-Billancourt, France) into the water using a syringe and recorded the resulting flow using a digital camera (PowerShot SX620 HS, Canon, Inc., Ota, Japan) at a rate of 30 frames per second. Special care was taken to avoid external vibrations and to ensure that the ink jet flowed undisturbed along the axial axis of the transducer. Multiple videos were recorded at each excitation frequency to minimize variability and random errors. The recorded videos were transferred to a computer for processing, and the streaming velocity was measured by analyzing sequential frames from the videos. To account for optical refraction effects in the readout of the millimeter scale, a comparison was made between the size of the millimeter scale immersed in water and behind the water tank wall. We observed a factor of 0.56 difference between the two cases, which was then utilized to correct for refraction in the streaming velocity measurements. To prevent acoustic reflections, we placed an ultrasound absorber at the wall of the water tank, directly in front of the transducer.

The time-averaged intensity I_{TA} at the transducer surface was then calculated using Eq. (2.8) with α = 2.5×10^{-4} Np/cm/MHz^2, η = 1 mPa·s, and c = 1470 m/s for water at 20°C. Next, the peak pressure p_0 at the surface of the transducer was calculated by:

$$p_0 = \left(\sqrt{\frac{2\rho c I_{TA}}{\tau}} \right) \tag{2.10}$$

where ρ is 997 kg/m^3.

Once the peak pressure was obtained for each excitation frequency, we calculated the transmit transfer function T_t of the transducer by:

$$T_t(\omega) = \frac{p_0(\omega)}{V(\omega)} \tag{2.11}$$

where V is the peak voltage measured over the transducer.

For reciprocal transducers, the transmit and receive transfer functions are related by the complex spherical wave reciprocity [11]. Using the expression derived by van Neer et al. [5], [18], the receive transfer function T_r of a circular transducer can be expressed as:

$$\frac{T_r(\omega)}{T_t(\omega)} = \frac{2 \cdot Z(\omega) \cdot A}{\rho \cdot c} \tag{2.12}$$

where Z is the electrical impedance of the transducer and $A = \pi r^2$ is its surface area.

2.3.2. HYDROPHONE MEASUREMENTS

Figure 2.1(b) depicts the experimental setup utilized for obtaining the transmit transfer function via hydrophone measurements, which is described by van Neer et al. [5]. A calibrated hydrophone (SN3800, Precision Acoustics Ltd., Dorchester, UK) with a diameter of 0.2 mm was positioned 160 mm away from the transducer surface. An xyz-stage was used to ensure proper alignment. The transducer was excited with a 1-cycle sine wave with a peak amplitude of 5 V generated by an AWG (33250A, Agilent Technologies, Inc., Santa Clara, CA, USA) with the output impedance set to 50 Ω. Both the voltage at the transmitting transducer and the output voltage of the hydrophone were digitized by an oscilloscope (DSO-X 4054A, Agilent Technologies, Inc., Santa Clara, CA, USA) and transferred to a computer for processing. The transmit transfer function of the transducer derived from hydrophone measurements was calculated by:

$$T_t(\omega) = \frac{V_{hydr}(\omega)}{V(\omega) \cdot T_{hydr}(\omega) \cdot D(\omega) \cdot \alpha(\omega)} \tag{2.13}$$

where V_{hydr} is the Fourier transform of the voltage produced by the hydrophone, V is the Fourier transform of the voltage measured over the transducer, T_{hydr} is the transfer function of the hydrophone, D is the diffraction correction function for the transducer [32], and α is the attenuation.

2.3.3. PULSE-ECHO MEASUREMENTS

Figure 2.1(c) shows the experimental setup for deriving the transmit transfer function from pulse-echo measurements according to the method introduced by van Neer et al. [18], [33]. Prior to conducting the pulse-echo measurements, the complex electrical impedance of the transducer submerged in water was recorded using an impedance analyzer (4294A, Agilent Technologies, Inc., Santa Clara, CA, USA). As a reflector, we used a cylindrical steel plate with a diameter of 200 mm and a thickness of 80 mm placed at a distance of 160 mm from the transducer. The transducer was driven using a 1-cycle sine wave with a peak amplitude of 5 V generated by an AWG (33250A, Agilent Technologies, Inc., Santa Clara, CA, USA) with the output

impedance set to 50 Ω. Both the transmitting voltage measured over the transducer and the received echo signal were digitized by an oscilloscope (DSO-X 4054A, Agilent Technologies, Inc., Santa Clara, CA, USA) with its input impedance set to 1 MΩ. The transmit transfer function derived from pulse-echo measurements was calculated by:

$$T_t(\omega) = \sqrt{\frac{V_{open}(\omega) \cdot \rho \cdot c}{2 \cdot Z(\omega) \cdot A \cdot V(\omega) \cdot D(\omega) \cdot \alpha(\omega) \cdot R}} \tag{2.14}$$

where V_{open} is the Fourier transformed open circuit voltage over the transducer (in reception), ρ is the density of the medium, c is the sound speed in the medium, Z is the electrical impedance of the transducer, A is the area of the transducer, V is the Fourier transform of the voltage over the transducer (in transmission), D the diffraction correction function for the transmitting transducer to the flat plate and back [32], α is the attenuation, and R is the reflection coefficient of the reflector (0.94 for steel).

2.4. RESULTS

Figure 2.2(a) shows the graph just after the ink is injected into the water but before the ultrasound transducer is turned on. The ink jet is situated at a distance of 55 mm

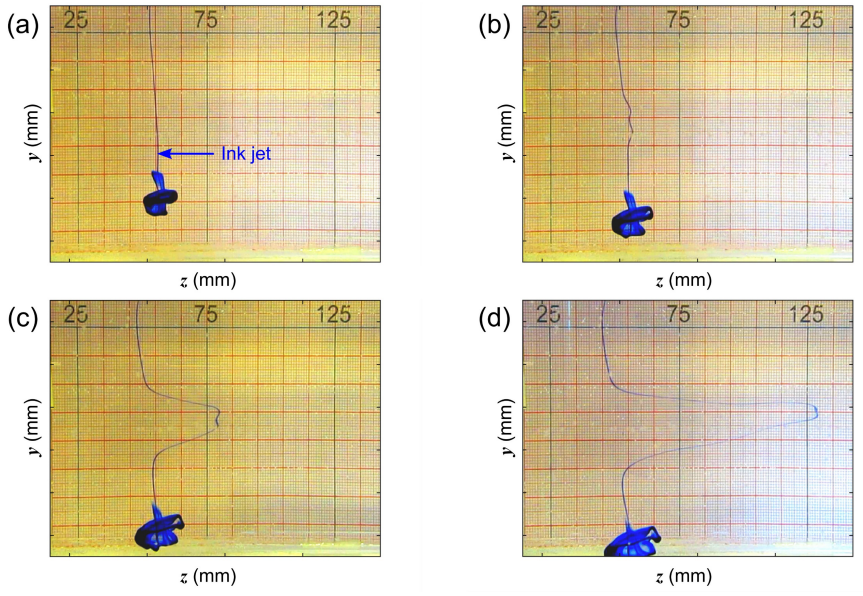

Figure 2.2: Streaming flow moving the ink jet at different instants in time with a 5 MHz excitation. (a) Time = 11.67 s. (b) Time = 13.33 s. (c) Time = 15.00 s. (d) Time = 16.67. The scale on the back indicates the axial distance from the transducer surface.

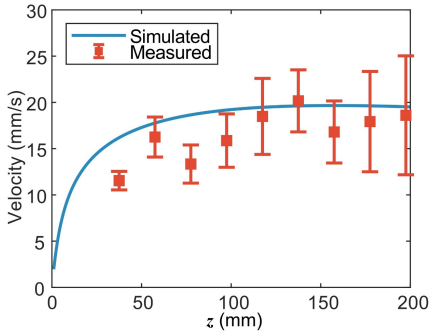

Figure 2.3: Simulated and measured streaming velocity along the axial axis with a 5 MHz excitation and a source peak pressure of 30 kPa. The error bars represent the mean values ± one standard deviation of the measured values.

from the transducer. Since no streaming is generated, the ink jet sinks to the bottom of the tank in a straight line. In Figure 2.2(b)-(d) the transducer is activated, and the acoustic streaming generated is clearly visible in the tracer. As time goes by, the wavefront of the streaming moves away from the transducer and its displacement can be easily tracked with the scale behind it. By analyzing the ink displacement at multiple frames, the instantaneous streaming velocity can be measured.

Figure 2.3 shows the comparison between the streaming velocities obtained from simulations and measurements along the axial line, utilizing a 5 MHz excitation. Based on the measured streaming velocities, we estimate a source peak pressure of about 30 kPa at the transducer surface, which was subsequently used in the simulations. Notably, the measured and simulated velocities demonstrate a good agreement within the range of 100 to 200 mm, where the velocity stabilizes. The slightly lower values measured at 40 and 80 mm are likely due to both inertia [30] and suboptimal alignment between the camera and the direction of the ink jet.

In Figure 2.4, the measured electrical impedance of the transducer when submerged in water is shown. As observed, the impedance magnitude demonstrates a gradual decrease across frequencies. A magnitude of approximately 40 Ω is measured near the center frequency of the transducer.

The transmit and the receive transfer functions of the transducer derived using the various methods are shown in Figure 2.5(a) and Figure 2.5(b), respectively. At the central frequency of 5 MHz, the transmit efficiency estimated from streaming measurements is 1.9 kPa/V. Comparatively, via hydrophone and pulse-echo measurements, we obtained transmit efficiencies of 2.1 kPa/V and 1.8 kPa/V respectively. Regarding the receive transfer function, we measured a sensitivity of 8.0 μV/Pa through streaming measurements, 9.0 μV/Pa through hydrophone measurements, and 7.7 μV/Pa through pulse-echo measurements at 5 MHz. Overall, the transfer functions obtained from acoustic streaming are in agreement with pulse-echo measurements. At lower frequencies, however, they tend to have lower values compared to hydrophone measurements.

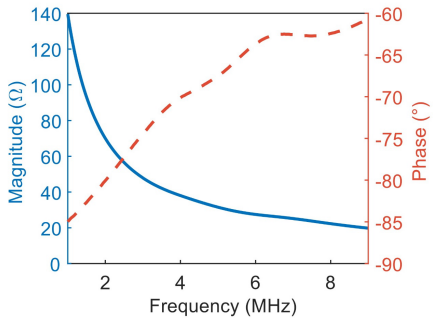

Figure 2.4: Measured electrical impedance magnitude (solid line) and phase (dashed line) of the transducer.

2.5. DISCUSSION

Hydrophone, pulse-echo measurements, and radiation force balances are standard methods for quantifying the acoustic output of ultrasound transducers. However, these approaches often come with drawbacks such as high costs, complexity, and the requirement for frequent calibration or specialized equipment. In this paper, we introduce an alternative method for evaluating the transfer function of ultrasound transducers utilizing acoustic streaming. By measuring the axial streaming velocity generated by the transducer, we can estimate its acoustic power (similar to the approach of a radiation force balance), and further provide a means to calculate its absolute transmit efficiency. By incorporating impedance measurements, we can determine the receive sensitivity of the transducer, assuming the reciprocity principle. In addition to its inherent simplicity and cost-effectiveness, the proposed method offers the potential to characterize transducers in various environments without requiring extensive modifications to the measurement setup, as long as the medium properties and the effective radius of the transducer are known.

In this study, all water parameters were based on values reported in the literature on ultrasonic waves in water [34], [35], except for the speed of sound, which was directly measured. Similar values for water properties have been used in previous studies involving acoustic streaming in water [29], [36]–[38]. Note that, it is assumed in this context that the addition of ink did not alter the inherent properties of the water. Should the experiment be conducted in a different medium, the work of Moudjed et al. may offer valuable insights into establishing a relationship between the streaming velocity in various liquids and the velocity obtained in water [30].

To obtain reliable measurements, it is important to address key aspects of the setup and minimize potential sources of error. First and foremost, external

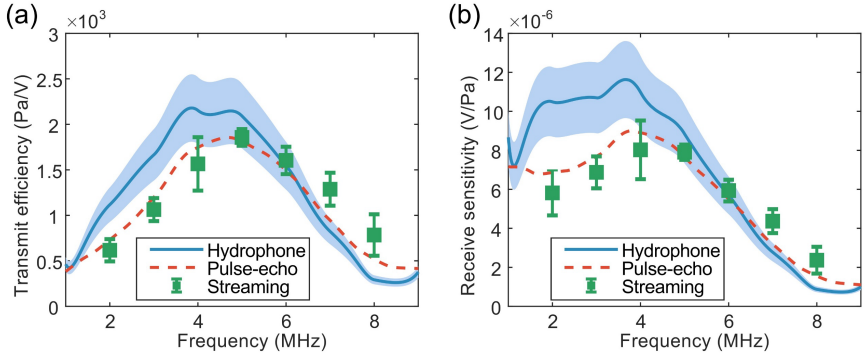

Figure 2.5: Transducer transfer function derived from different methods. (a) Transmit efficiency. (b) Receive sensitivity. The error bars represent the mean values ± one standard deviation of the streaming measurements. The shaded areas represent the uncertainty of the hydrophone calibration.

vibrations must be prevented to avoid disturbances in the water and the resulting streaming flow. Within our setup, we observed that certain devices, such as the amplifier, the AWG, and the computer, generated significant vibrations. To minimize their impact, we isolated the water tank on a separate bench, effectively reducing the influence of these vibrations. Additionally, it is crucial to acknowledge that the pumping action of the syringe inherently creates vibrations that can disrupt the streaming flow. To mitigate any unwanted displacement caused by the pumping, we secured the syringe in a holder and ensured that only the needle was submerged in the water, minimizing disturbances to the system. Another potential source of vibration is the push-button of the camera used for recording the streaming. To eliminate manual disturbances, we opted for remote triggering of the camera.

The estimation of the streaming velocity is susceptible to various types of errors. Firstly, it is essential to ensure precise alignment and propagation of the tracer along the axial axis during measurements, as the streaming velocity equation is applicable solely to the axial line. This is particularly important because the side view photos shown in Figure 2.2 do not provide information about the lateral position (along the x-direction) of the streaming flow. To address this, incorporating a camera with a top view can be highly beneficial. Secondly, it is worth noting that the approach used for velocity estimation, which involved a scale affixed to the wall of the water tank, is prone to refraction effects and parallax error. Parallax arises when there is a misalignment between the camera, the tracer, and the scale, resulting in inaccuracies. We estimated the refraction correction by measuring a ruler placed on the axial axis. To minimize parallax error, we ensured that the camera was positioned perpendicular to the grid and directly in front of the location where velocity was being estimated. If the streaming velocity is estimated at various positions along the axial line, as in Figure 2.3, it is advisable to adjust the camera position accordingly to avoid any angled perspectives. Lastly, it is important to measure the streaming velocity a few seconds after activating the ultrasound transducer. This is done to ensure that the flow reaches a steady state and to minimize the influence of inertia

on the measurements [15], [16]. Note that we conducted velocity measurements at longer intervals after activating the transducer (30 and 45 seconds) and observed no changes in streaming velocities. This suggests that the flow reached a steady state. Alternatively, the steady-state time could be predicted through numerical calculations, as presented by Hariharan et al. [15].

The performance of the proposed method was evaluated by comparing it with hydrophone and pulse-echo measurements. Overall, all three methods provide satisfactory accuracy for absolute transfer function measurements. The transfer functions shown in Figure 2.5 demonstrate a similar trend for all three methods, both in transmit and receive modes. Particularly at 5 MHz, they exhibit a relatively good level of agreement, indicating that they are interchangeable and that the selection of the method should be based on specific requirements and practical considerations. When comparing the transmit efficiency derived from streaming measurements with pulse-echo measurements at 5 MHz, an error of 5.5% is observed, while an error of 9.5% is obtained when comparing streaming with hydrophone measurements (the uncertainty of the hydrophone calibration is ±17%). At lower frequencies, the streaming and pulse-echo methods diverge slightly from the hydrophone measurements. Lower frequencies pose challenges as the streaming velocities become low and the ink dissolves in water over a long period of time, making accurate measurements difficult. At higher frequencies, the slight differences between the curves are probably caused by the inaccuracy of estimation of the attenuation coefficient.

2.6. CONCLUSION

This paper demonstrates a novel approach for estimating the absolute transfer function of an ultrasound transducer by measuring the velocity of the acoustic streaming it generates. The method was evaluated and compared with hydrophone and pulse-echo measurements. The results showed that our method yields similar outcomes, with an error of 9.5% compared to hydrophone measurements and an error of 5.5% compared to pulse-echo measurements at the center frequency. The proposed approach offers an alternative solution for characterizing ultrasound transducers and opens up possibilities for characterization in a wider range of scenarios, particularly in situations where traditional equipment is not accessible due to cost or complexity constraints. In a clinical or industrial environment, the pressure field produced by an ultrasound transducer can be estimated with nothing more than a small water tank, a ruler, and a stopwatch.

2.7. REFERENCES

[1] D. S. Dos Santos *et al.*, "Automated Characterization of Matrix Transducer Arrays using the Verasonics Imaging System," in *2022 IEEE International Ultrasonics Symposium (IUS)*, IEEE, Oct. 2022, pp. 1–4. doi: 10.1109/IUS54386.2022.9957544.

[2] C. Papageorgiou and T. Laopoulos, "Self-calibration of ultrasonic transducers in an intelligent data acquisition system," in *Proceedings of the 2nd IEEE International Workshop on Intelligent*

Data Acquisition and Advanced Computing Systems: Technology and Applications, IDAACS 2003, IEEE, 2003, pp. 2–6. doi: 10.1109/IDAACS.2003.1249504.

[3] FDA, "Marketing Clearance of Diagnostic Ultrasound Systems and Transducers," Rockville, MD, USA, 2019.

[4] Roy C. Preston, *Output Measurements for Medical Ultrasound*. London: Springer London, 1991. doi: 10.1007/978-1-4471-1883-1.

[5] P. L. M. J. van Neer, G. Matte, J. Sijl, J. M. G. Borsboom, and N. de Jong, "Transfer functions of US transducers for harmonic imaging and bubble responses," *Ultrasonics*, vol. 46, no. 4, pp. 336–340, Nov. 2007, doi: 10.1016/j.ultras.2007.05.002.

[6] IEC 62127-1:2013., "Ultrasonics – Hydrophones – Part 1: Measurement and characterization of medical ultrasonic fields up to 40 MHz," Geneva, Switzerland, 2013.

[7] G. M. Matte, J. M. G. Borsboom, P. van Neer, and N. de Jong, "Estimating Acoustic Peak Pressure Generated by Ultrasound Transducers from Harmonic Distortion Level Measurement," *Ultrasound Med Biol*, vol. 34, no. 9, pp. 1528–1532, Sep. 2008, doi: 10.1016/j.ultrasmedbio.2008.03.003.

[8] "OndaSonics. Frequently Asked Questions." Accessed: Jun. 20, 2023. [Online]. Available: https://www.ondasonics.com/applications/faqs/

[9] K. M. Swamy and F. J. Keil, "Ultrasonic power measurements in the milliwatt region by the radiation force float method," *Ultrason Sonochem*, vol. 9, no. 6, pp. 305–310, Nov. 2002, doi: 10.1016/S1350-4177(02)00087-1.

[10] J. Xing and J. Chen, "Design of a Thermoacoustic Sensor for Low Intensity Ultrasound Measurements Based on an Artificial Neural Network," *Sensors*, vol. 15, no. 6, pp. 14788–14808, Jun. 2015, doi: 10.3390/s150614788.

[11] R. J. Bobber, "General Reciprocity Parameter," *J Acoust Soc Am*, vol. 39, no. 4, pp. 680–687, Apr. 1966, doi: 10.1121/1.1909941.

[12] C. Dang, L. W. Schmerr Jr., and A. Sedov, "Ultrasonic Transducer Sensitivity and Model-Based Transducer Characterization," *Research in Nondestructive Evaluation*, vol. 14, no. 4, pp. 203–228, 2003, doi: 10.1007/s00164-002-0006-5.

[13] A. Lopez-sanchez and L. Schmerr, "Determination of an ultrasonic transducer's sensitivity and impedance in a pulse-echo setup," *IEEE Trans Ultrason Ferroelectr Freq Control*, vol. 53, no. 11, pp. 2101–2112, Nov. 2006, doi: 10.1109/TUFFC.2006.150.

[14] C. Eckart, "Vortices and streams caused by sound waves," *Physical Review*, vol. 73, no. 1, pp. 68–76, 1948, doi: 10.1103/PhysRev.73.68.

[15] P. Hariharan, M. R. Myers, R. A. Robinson, S. H. Maruvada, J. Sliwa, and R. K. Banerjee, "Characterization of high intensity focused ultrasound transducers using acoustic streaming," *J Acoust Soc Am*, vol. 123, no. 3, pp. 1706–1719, Mar. 2008, doi: 10.1121/1.2835662.

[16] R. B. H. Slama, B. Gilles, M. Ben Chiekh, and J. C. Bera, "Characterization of focused-ultrasound-induced acoustic streaming," *Exp Therm Fluid Sci*, vol. 101, no. March 2018, pp. 37–47, Jan. 2019, doi: 10.1016/j.expthermflusci.2018.10.001.

[17] A. C. H. Tan and F. S. Hover, "Correlating the Ultrasonic Thrust force with acoustic streaming Velocity," in *2009 IEEE International Ultrasonics Symposium*, IEEE, Sep. 2009, pp. 2627–2630. doi: 10.1109/ULTSYM.2009.5442075.

[18] P. L. M. J. van Neer, H. J. Vos, and N. de Jong, "Reflector-based phase calibration of ultrasound transducers," *Ultrasonics*, vol. 51, no. 1, pp. 1–6, Jan. 2011, doi: 10.1016/j.ultras.2010.05.001.

[19] Robert T. Beyer, *Nonlinear Acoustics*. United States. Naval Ship Systems Command, 1974.

[20] D. Möller, T. Hilsdorf, J. Wang, and J. Dual, "Acoustic streaming used to move particles in a circular flow in a plastic chamber," in *AIP Conference Proceedings*, 2012, pp. 775–778. doi: 10.1063/1.3703295.

[21] W. L. M. NYBORG, "Acoustic Streaming," 1965, pp. 265–331. doi: 10.1016/B978-0-12-395662-0.50015-1.

[22] W. L. Nyborg, "Acoustic Streaming due to Attenuated Plane Waves," *J Acoust Soc Am*, vol. 25, no. 1, pp. 68–75, 1953, doi: 10.1121/1.1907010.

[23] J. Wu and G. Du, "Acoustic streaming generated by a focused Gaussian beam and finite amplitude tonebursts," *Ultrasound Med Biol*, vol. 19, no. 2, pp. 167–176, Jan. 1993, doi: 10.1016/0301-5629(93)90008-C.

[24] J. Doherty, G. Trahey, K. Nightingale, and M. Palmeri, "Acoustic Radiation Force Elasticity Imaging in Diagnostic Ultrasound," *IEEE Trans Ultrason Ferroelectr Freq Control*, vol. 60, no. 4, pp. 685–701, 2013, doi: 10.1109/TUFFC.2013.2617.

[25] M. Palmeri, A. Sharma, R. Bouchard, R. Nightingale, and K. Nightingale, "A Finite-Element Method Model of Soft Tissue Response to Impulsive Acoustic Radiation Force," *IEEE Trans Ultrason Ferroelectr Freq Control*, vol. 13, no. 14–15, pp. 1133–1145, 2005, doi: 10.1016/j.micinf.2011.07.011.

[26] J. Bercoff, M. Tanter, and M. Fink, "Supersonic shear imaging: a new technique for soft tissue elasticity mapping," *IEEE Trans Ultrason Ferroelectr Freq Control*, vol. 51, no. 4, pp. 396–409, Apr. 2004, doi: 10.1109/TUFFC.2004.1295425.

[27] D. S. dos Santos, F. M. Cardoso, and S. S. Furuie, "Two-dimensional ultrasonic transducer array for shear wave elastography in deep tissues: a preliminary study," *Research on Biomedical Engineering*, vol. 36, no. 3, pp. 277–289, Sep. 2020, doi: 10.1007/s42600-020-00068-6.

[28] A. Nowicki, T. Kowalewski, W. Secomski, and J. Wójcik, "Estimation of acoustical streaming: theoretical model, Doppler measurements and optical visualisation," *European Journal of Ultrasound*, vol. 7, no. 1, pp. 73–81, Feb. 1998, doi: 10.1016/S0929-8266(98)00020-2.

[29] A. Nowicki, W. Secomski, and J. Wójcik, "Acoustic streaming: Comparison of low-amplitude linear model with streaming velocities measured by 32-MHz Doppler," *Ultrasound Med Biol*, vol. 23, no. 5, pp. 783–791, Jan. 1997, doi: 10.1016/S0301-5629(97)00005-7.

[30] B. Moudjed, V. Botton, D. Henry, H. Ben Hadid, and J.-P. Garandet, "Scaling and dimensional analysis of acoustic streaming jets," *Physics of Fluids*, vol. 26, no. 9, Sep. 2014, doi: 10.1063/1.4895518.

[31] L. W. Schmerr, "FUNDAMENTAL MODELS AND MEASUREMENTS FOR ULTRASONIC NONDESTRUCTIVE EVALUATION SYSTEMS," in *Ultrasonic and Advanced Methods for Nondestructive Testing and Material Characterization*, WORLD SCIENTIFIC, 2007, pp. 3–31. doi: 10.1142/9789812770943_0001.

[32] A. Goldstein, D. R. Gandhi, and W. D. O'Brien, "Diffraction effects in hydrophone measurements," *IEEE Trans Ultrason Ferroelectr Freq Control*, vol. 45, no. 4, pp. 972–979, 1998, doi: 10.1109/58.710571.

[33] P. L. M. J. van Neer, H. J. Vos, M. G. Danilouchkine, and N. de Jong, "Simple method for measuring phase transfer functions of transducers," in *2010 IEEE International Ultrasonics Symposium*, IEEE, Oct. 2010, pp. 1454–1457. doi: 10.1109/ULTSYM.2010.5935890.

[34] J. M. M. Pinkerton, "The Absorption of Ultrasonic Waves in Liquids and its Relation to Molecular Constitution," *Proceedings of the Physical Society. Section B*, vol. 62, no. 2, pp. 129–141, Feb. 1949, doi: 10.1088/0370-1301/62/2/307.

[35] L. N. Liebermann, "The Second Viscosity of Liquids," *Physical Review*, vol. 75, no. 9, pp. 1415–1422, May 1949, doi: 10.1103/PhysRev.75.1415.

[36] T. Kamakura, T. Sudo, K. Matsuda, and Y. Kumamoto, "Time evolution of acoustic streaming from a planar ultrasound source," *J Acoust Soc Am*, vol. 100, no. 1, pp. 132–138, Jul. 1996, doi: 10.1121/1.415948.

[37] H. Mitome, "The mechanism of generation of acoustic streaming," *Electronics and Communications in Japan (Part III: Fundamental Electronic Science)*, vol. 81, no. 10, pp. 1–8, Oct. 1998, doi: 10.1002/(SICI)1520-6440(199810)81:10<1::AID-ECJC1>3.0.CO;2-9.

[38] V. Frenkel, R. Gurka, A. Liberzon, U. Shavit, and E. Kimmel, "Preliminary investigations of ultrasound induced acoustic streaming using particle image velocimetry," *Ultrasonics*, vol. 39, no. 3, pp. 153–156, Apr. 2001, doi: 10.1016/S0041-624X(00)00064-0.

3

AUTOMATED CHARACTERIZATION OF MATRIX TRANSDUCER ARRAYS USING THE VERASONICS IMAGING SYSTEM[1]

[1] This chapter is based on the following publication:
dos Santos, D.S.; Fool, F.; Kim, T.; Noothout, E.; Rozsa, N.; Vos, H.J.; Bosch, J.G.; Pertijs, M.A.P.; Verweij, M.D.; de Jong, N. Automated Characterization of Matrix Transducer Arrays Using the Verasonics Imaging System. In Proceedings of the 2022 IEEE International Ultrasonics Symposium (IUS); IEEE, October 10 2022; Vol. 2022-Octob, pp. 1–4

3.1. INTRODUCTION

OVER the past decades, ultrasound imaging has made considerable progress. Novel approaches and breakthroughs in diagnostic and therapeutic ultrasound together with the continuous improvement in electronics have prompted quick and significant advancements in imaging systems and transducer technology [1], [2]. With the need for cutting-edge transducer arrays with complex designs and ambitious technical requirements (e.g., reduced size, increased number of elements, improved sensitivity, and wide bandwidth), there is also a need for suitable tools to characterize, test, and evaluate such transducers [3].

The acoustic characterization is a crucial process in the design of ultrasound transducer arrays [4], [5]. This process is necessary to validate models, analyze variations between transducer elements, evaluate the manufacturing process, and investigate various acoustic phenomena that influence the transducer's behavior in practice [6], [7]. Thus, to develop new and better probes, it is very important to have a good knowledge of the performance of the prototyped transducers experimentally [8].

Another essential role of acoustic characterization is to provide means for the maintenance of transducers available for clinical use. It is well known that the operating characteristics of an ultrasound transducer tend to change with time and usage with an average life expectancy, which is sometimes limited to a few months of continuous use. Besides, the transducer might suffer from severe degradation depending on the environment [3]. These aspects might raise concerns with regard to the effectiveness and safety of the transducer for a specific clinical application [9]. Therefore, test routines must be established to periodically evaluate the performance/operation of medical transducers and to check their conformance with national and international standards [10].

Despite the importance of the acoustic characterization process and the great advances in transducer technology, little has been reported on describing the setup needed for the characterization of these novel transducers. Without appropriate tools, the characterization process of highly complex prototype transducers might involve various manual steps, which can be laborious, time-consuming, and subject to errors [11]. This might discourage a complete characterization of the transducer (especially if it has a large number of elements) leading to an under-representation or inadequate evaluation of the prototype (e.g., assessing the performance of the transducer only in terms of a pulse-echo test [12]). To come to an extensive, high-quality evaluation of a prototype transducer, an element-level characterization of both transmit and receive operations is indispensable. In this paper, we present a pipeline to automatically perform the acoustic characterization of each individual element of a matrix transducer using a research imaging system. The performance of the proposed pipeline is tested on a prototype matrix transducer consisting of 960 elements.

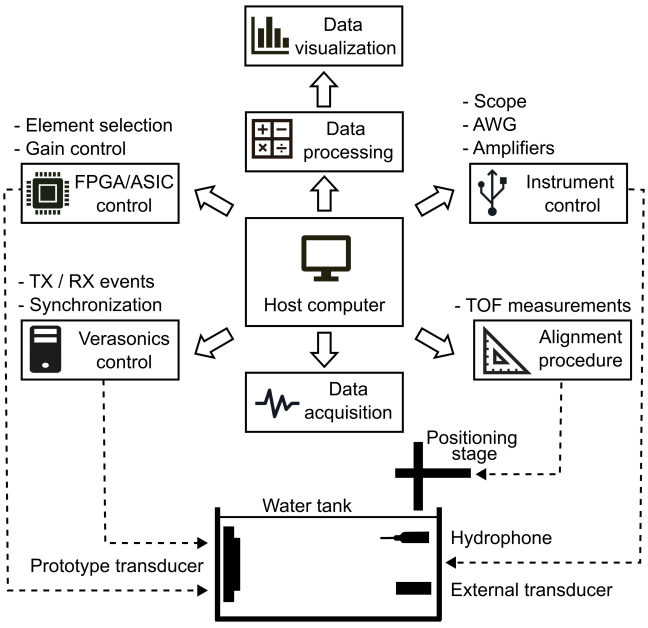

Figure 3.1: Experimental setup for the automated characterization.

3.2. AUTOMATED ACOUSTIC CHARACTERIZATION

The experimental setup for the automated characterization of the prototype transducer is schematized in Figure 3.1. As seen, multiple instrumentation devices are integrated to perform different measurement tasks, which are controlled and synchronized by the host computer of the Verasonics imaging system (V1, Verasonics, Inc., Kirkland, WA, USA) via MATLAB interface (2014b, The MathWorks, Inc., Natick, MA, USA) using external functions. The proposed pipeline can be divided into three main parts:

3.2.1. ALIGNMENT PROCEDURE

The alignment procedure is used to align the prototype transducer with a needle hydrophone prior to the transmit characterization. This is required to reduce the influence of the hydrophone directivity in the measurements. The flowchart of the procedure is shown in Figure 3.2. First, the user selects the element to be aligned with the hydrophone and defines the acquisition settings. Then, the Verasonics (indicated as “VSX” in the flowchart) drives a group of elements individually and sends a trigger to the oscilloscope (“Scope”). For each transmit event, the hydrophone signal is digitized by the oscilloscope and transferred to the computer. Next, the time-of-flight (TOF) of the hydrophone signal is measured and used to estimate the relative distance between the hydrophone and the element under alignment. Finally, the calculated coordinates are sent to the *xyz*-positioning stage to

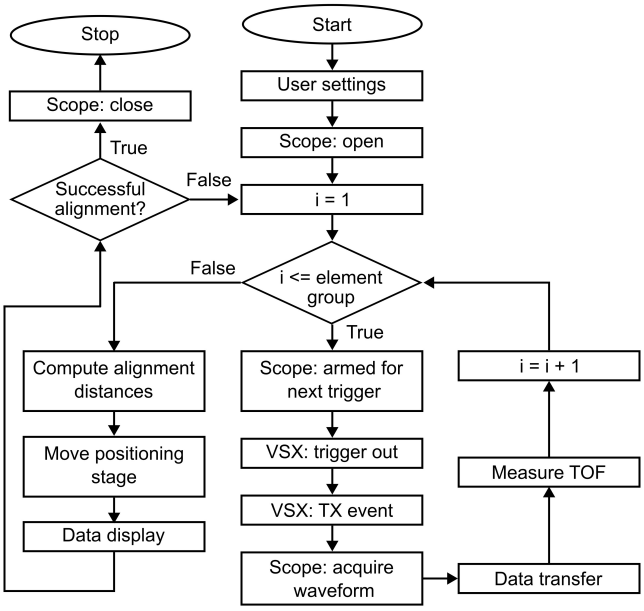

Figure 3.2: Flowchart of the alignment procedure.

move the hydrophone to the aligned position. The performance of the alignment procedure is displayed to the user in real time for evaluation.

3.2.2. TRANSMIT CHARACTERIZATION

The flowchart of the transmit (TX) characterization is shown in Figure 3.3. The process starts with the acquisition settings defined by the user. Then, the Verasonics drives the transducer elements individually. For each transmit event, the hydrophone signal is digitized by the oscilloscope and transferred to the computer, where data is processed and displayed in real time. When the acquisition is complete, the user can visualize the variation in transmit efficiency across the transducer elements, as well as the time and frequency response parameters of all individual elements. Furthermore, this setup can be utilized to measure the directivity pattern of individual elements. For this, the hydrophone is automatically rotated between the transmit events.

3.2.3. RECEIVE CHARACTERIZATION

The flowchart of the receive (RX) characterization is shown in Figure 3.4. For this process, a calibrated external transducer is used as a transmitter. First, the user defines the receive gain settings, which include the prototype in-probe amplifiers (indicated as “Gain” in the flowchart) and the Verasonics time-gain compensation (TGC). The user also selects the voltage range of the arbitrary waveform generator

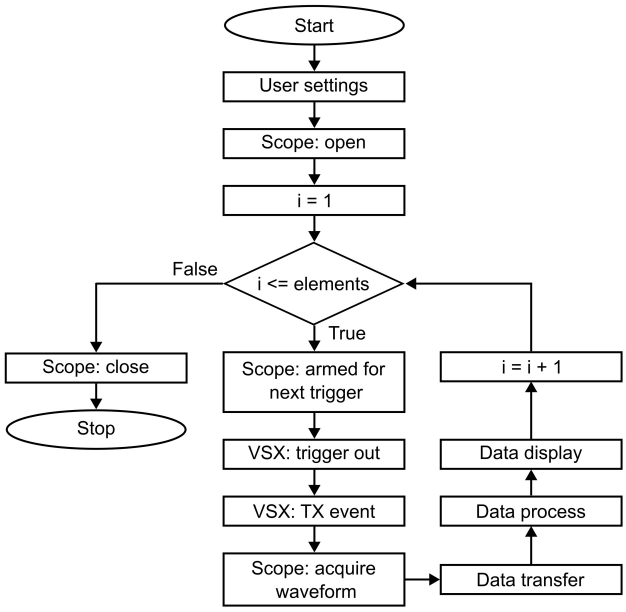

Figure 3.3: Flowchart of the automated transmit characterization.

(AWG) to drive the external transducer. Next, the Verasonics sweeps through the range of gains and output voltages. For each iteration, the received signal of individual elements is recorded and the variation in receive sensitivity across all elements is displayed in real-time. When the acquisition is complete, the overall dynamic range (i.e., the relationship between received acoustic pressure and output voltage) is displayed to the user.

3.3. PROTOTYPE MATRIX TRANSDUCER

We have fabricated a prototype matrix transducer array made of lead zirconate titanate (PZT) that operates at 7.5 MHz and consists of 960 elements with a pitch of 300 µm × 150 µm. The PZT matrix was mounted on top of an application-specific integrated circuit (ASIC) whose element-level circuits match the pitch of the array. The prototype transducer interfaces with the Verasonics imaging system using a custom-designed printed circuit board (PCB). More details about the design of the prototype transducer can be found in our previous publications [13]–[15].

3.4. RESULTS AND DISCUSSION

Figure 3.5(a) and Figure 3.5(b) show the sensitivity variation across all elements of the prototype transducer obtained from the automated transmit and receive characterization, respectively. As seen, the majority of the elements are working

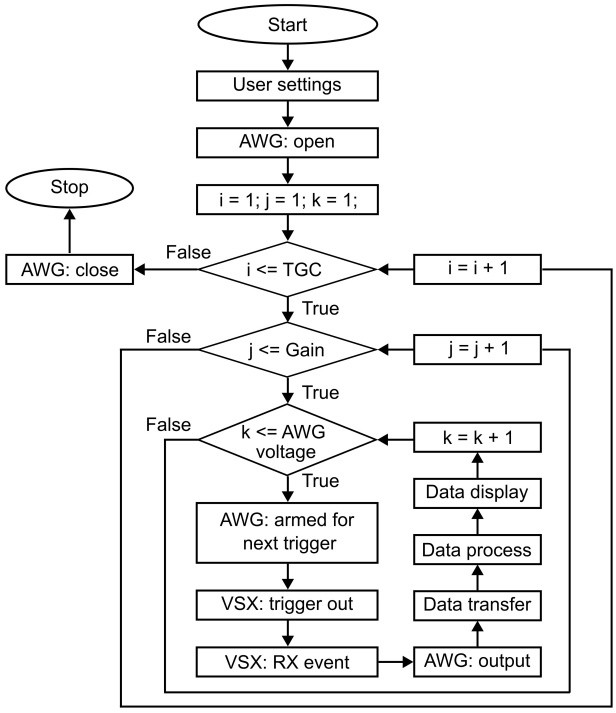

Figure 3.4: Flowchart of the automated receive characterization.

within the 0 dB to -6 dB level in both transmit and receive. Note however that rows 10 and 20 are defective in receive.

After the alignment procedure, the transmit sensitivity characterization takes about 10 minutes to be carried out. This means that, for each element, it takes approximately 0.6 seconds for the acquisition of the hydrophone signal, data transfer, and processing. The receive sensitivity characterization of the entire prototype is much quicker: it is complete in just a few seconds. However, note that the alignment procedure for the receive characterization is not yet automated. Currently, the real-time sensitivity map, as the one shown in Figure 3.5(b), is used as a guide for the alignment (i.e., the user manually finds the position of maximum acoustic pressure from the external transducer).

The center frequency and -6 dB bandwidth derived from the transmit characterization are shown in Figure 3.6(a) and Figure 3.6(b), respectively. Most of the elements exhibit a center frequency between 7.5 and 8 MHz, in accordance with the acoustic design. The majority of the elements show a bandwidth of around 3.5 MHz, which represents approximately 45%.

Figure 3.7 shows the directivity pattern in transmit for nine arbitrarily selected elements. As seen, all elements exhibit a -6 dB beam width of about 32 degrees and a sharp peak at 0 degrees (we believe that this bump is due to electrical crosstalk, but further investigation is needed). At the beginning of each set of scans, the

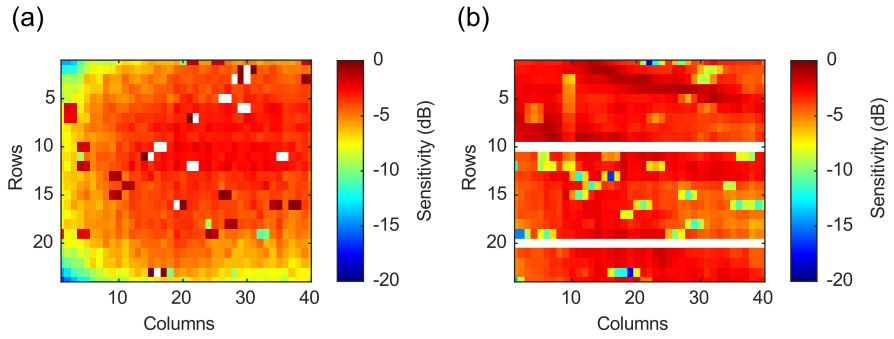

Figure 3.5: (a) Transmit efficiency. (b) Receive sensitivity. The elements shown in white are faulty.

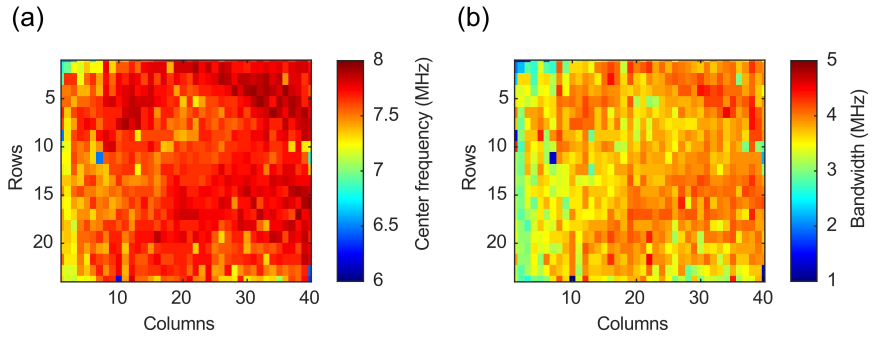

Figure 3.6: (a) Center frequency. (b) Bandwidth (-6 dB).

hydrophone was automatically aligned with the selected element. Since a very good agreement is observed between the different elements, we can imply that the alignment procedure was successfully performed with low variability. The alignment procedure takes about 2 minutes to be conducted.

Figure 3.8 shows the relation between the received pressure at the transducer surface and the corresponding output voltage for different gain settings. The plotted values represent the average over the 960 transducer elements. The minimum detectable pressure is about 60 Pa, whereas the maximum measured pressure is about 40 kPa. Thus, the measured dynamic range is 56 dB. The dynamic range characterization takes about 15 minutes to be carried out.

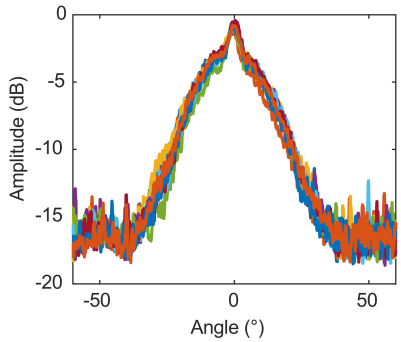

Figure 3.7: Directivity pattern of a few elements.

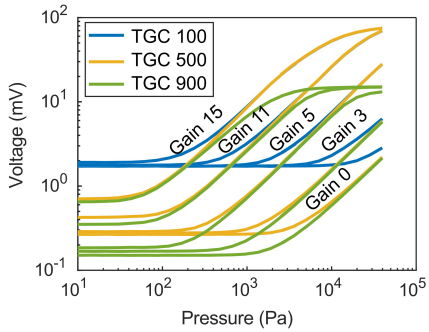

Figure 3.8: Relation between the received pressure at the transducer surface and the corresponding output voltage for different gain settings.

3.5. CONCLUSIONS

In this paper, a pipeline for the automated acoustic characterization of an ultrasound matrix transducer is presented. The implemented workflow, which is controlled by the host computer of the Verasonics imaging system, consists of an alignment procedure based on TOF measurements, followed by the transmit characterization with a hydrophone, and the receive characterization for different gain settings using an external transducer. The performance of the pipeline was evaluated on a prototype PZT matrix transducer consisting of 960 elements. The results demonstrate that the proposed pipeline can be used as a rapid and convenient method to perform the element-level characterization of a matrix transducer. Compared to manual characterization, the proposed pipeline can significantly enhance the quality of the characterization process of prototype transducers and hence lead to an improved probe design. Future work will include a process to measure the acoustic crosstalk between the transducer elements.

3.6. REFERENCES

[1] J. Seo and Y. Kim, "Ultrasound imaging and beyond: recent advances in medical ultrasound," *Biomed Eng Lett*, vol. 7, no. 2, pp. 57–58, May 2017, doi: 10.1007/s13534-017-0030-7.

[2] T. L. Szabo, *Diagnostic Ultrasound Imaging: Inside Out*. New York: Elsevier, 2014. doi: 10.1016/C2011-0-07261-7.

[3] C. Papageorgiou and T. Laopoulos, "Self-calibration of ultrasonic transducers in an intelligent data acquisition system," in *Proceedings of the 2nd IEEE International Workshop on Intelligent Data Acquisition and Advanced Computing Systems: Technology and Applications, IDAACS 2003*, IEEE, 2003, pp. 2–6. doi: 10.1109/IDAACS.2003.1249504.

[4] M. T. Burgess and E. E. Konofagou, "Fast qualitative two-dimensional mapping of ultrasound fields with acoustic cavitation-enhanced ultrasound imaging," *J Acoust Soc Am*, vol. 146, no. 2, pp. EL158–EL164, 2019, doi: 10.1121/1.5122194.

[5] Y. Yu, G. Shen, Y. Zhou, J. Bai, and Y. Chen, "Quantitative Assessment of Acoustic Intensity in the Focused Ultrasound Field Using Hydrophone and Infrared Imaging," *Ultrasound Med Biol*, vol. 39, no. 11, pp. 2021–2033, Nov. 2013, doi: 10.1016/j.ultrasmedbio.2013.05.004.

[6] V. Daeichin *et al.*, "Acoustic characterization of a miniature matrix transducer for pediatric 3D transesophageal echocardiography," *Ultrasound Med Biol*, vol. 44, no. 10, pp. 2143–2154, Oct. 2018, doi: 10.1016/j.ultrasmedbio.2018.06.009.

[7] M. Shabanimotlagh *et al.*, "Optimizing the directivity of piezoelectric matrix transducer elements mounted on an ASIC," *IEEE International Ultrasonics Symposium, IUS*, pp. 5–8, 2017, doi: 10.1109/ULTSYM.2017.8091752.

[8] B. Cugnet, J. Assaad, and A.-C. Hladky-Hennion, "Characterization of matched piezoelectric transducer bars," *J Acoust Soc Am*, vol. 115, no. 6, pp. 2904–2913, Jun. 2004, doi: 10.1121/1.1739486.

[9] FDA, "Marketing Clearance of Diagnostic Ultrasound Systems and Transducers," Rockville, MD, USA, 2019.

[10] Roy C. Preston, *Output Measurements for Medical Ultrasound*. London: Springer London, 1991. doi: 10.1007/978-1-4471-1883-1.

[11] A. Pulkkinen, J. J. Leskinen, and A. Tiihonen, "Ultrasound field characterization using synthetic schlieren tomography," *J Acoust Soc Am*, vol. 141, no. 6, pp. 4600–4609, Jun. 2017, doi: 10.1121/1.4986623.

[12] F. Bertocci, A. Grandoni, L. Francalanci, and A. Fabbrizzi, "Design of Robot-based Measurement System for the Quality Assessment of Ultrasound Probes for Medical Imaging," in *2020 IEEE International Symposium on Medical Measurements and Applications (MeMeA)*, IEEE, Jun. 2020, pp. 1–6. doi: 10.1109/MeMeA49120.2020.9137326.

[13] T. Kim *et al.*, "Design of an Ultrasound Transceiver ASIC with a Switching-Artifact Reduction Technique for 3D Carotid Artery Imaging," *Sensors*, vol. 21, no. 1, p. 150, Dec. 2020, doi: 10.3390/s21010150.

[14] D. S. dos Santos *et al.*, "Experimental Investigation of the Effect of Subdicing on an Ultrasound Matrix Transducer," in *2021 IEEE International Ultrasonics Symposium (IUS)*, IEEE, Sep. 2021, pp. 1–3. doi: 10.1109/ius52206.2021.9593315.

[15] E. Kang *et al.*, "A Reconfigurable Ultrasound Transceiver ASIC With 24 × 40 Elements for 3-D Carotid Artery Imaging," *IEEE J Solid-State Circuits*, vol. 53, no. 7, pp. 2065–2075, Jul. 2018, doi: 10.1109/JSSC.2018.2820156.

4

CHARACTERIZATION OF PRESSURE FIELDS IN HIGH-ELEMENT-COUNT ULTRASOUND MATRIX TRANSDUCERS [1]

[1] In preparation.

4.1. INTRODUCTION

IN recent decades, there has been remarkable progress in ultrasound imaging. Novel techniques and breakthroughs in diagnostic and therapeutic ultrasound, together with ongoing improvements in electronics have led to rapid and substantial advancements in both imaging systems and transducer technology [1], [2]. With the increasing demand for cutting-edge transducer arrays with complex designs and ambitious technical requirements, such as reduced size, increased element count, improved sensitivity, and wide bandwidth, the need for suitable tools to characterize, test, and evaluate these transducers has become evident. To come to a comprehensive and high-quality evaluation of transducer arrays, it is vital to conduct a detailed characterization of their performance at the element level [3], [4].

The characterization of the pressure field produced by ultrasound transducers is an essential component in their design process [5], [6]. This is important for verifying models, optimizing design parameters, assessing the manufacturing process, and exploring acoustic phenomena that might influence the transducer's behavior [7], [8], [9]. Thus, in order to develop new and better probes, it is crucial to have a solid understanding of the acoustic output of the prototyped transducers [4], [10]. In addition to this, acoustic characterization is necessary for the maintenance of transducers utilized in a wide range of applications, especially in the medical field. Given that the operating characteristics of ultrasound transducers tend to change over time and usage with an average lifespan [3], concerns may arise regarding their effectiveness and safety [11]. Hence, it becomes imperative to establish regular test routines to assess the performance of ultrasound transducers periodically and verify their compliance with national and international standards [12].

The pressure field characterization is commonly performed using a needle hydrophone, which records the time-varying acoustic pressure generated by the transducer at any spatial location of interest [13], [14], [15], [16]. During hydrophone measurements, the positioning of the hydrophone with regard to the transducer is of utmost importance and requires careful attention [17], [18], [19]. A small error in positioning can lead to misinterpretations of the measured pressure field, hindering the determination of important beam parameters, such as the focal length, beam width, steering angle, and side lobes [14]. In addition, hydrophone alignment is necessary to minimize the influence of the hydrophone's directivity on the measurements. Hence, achieving and maintaining a correct alignment is crucial for obtaining reliable information from hydrophone measurements.

A simple way for aligning the hydrophone with a transducer involves visually positioning the hydrophone perpendicular to the center of the transducer surface. This approach is particularly straightforward when dealing with transducers that are sufficiently large and easily visible to the operator, such as single-element transducers. However, when dealing with transducer arrays, which typically consist of smaller elements, visual alignment becomes more challenging and less accurate, particularly for elements located towards the periphery of the transducer [14]. Note that this alignment method assumes that the optical axis of the transducer coincides with its acoustic axis, which may not always be true, for instance, when the transducer's housing is angled [20], [21].

The most widely used method for aligning the hydrophone with a transducer element is by conducting hydrophone scans to determine the position of maximum pressure, which corresponds to the acoustic axis of the transducer. Although this method offers high spatial accuracy, achieving the desired level of precision typically involves multiple iterations with finer scans [21], [22], resulting in a laborious and time-consuming process [5], [6], [23]. Unfortunately, the limitations associated with hydrophone scans might discourage a complete characterization of transducer arrays, particularly when dealing with matrices consisting of a large number of elements. These limitations can lead to an inadequate evaluation or an under-representation of the transducer's performance [4], which is not desirable when prototyping a transducer device. Therefore, it is crucial to explore alternative methods that can facilitate hydrophone measurements and ensure a comprehensive assessment of all transducer elements.

This paper presents a procedure for characterizing the pressure field of ultrasound matrix transducers with a large number of elements. This method automates the alignment of the hydrophone with the transducer elements, as well as data acquisition and processing. The hydrophone alignment relies on time-of-flight (TOF) measurements from a selected subset of elements. These TOF values combined with a priori knowledge of the transducer's geometry and the properties of the medium, provide enough information to perform the alignment between the hydrophone and each individual transducer element. To demonstrate the proposed characterization process, we applied it to evaluate a prototype matrix transducer consisting of 2880 elements [24], [25], [26].

4.2. THEORY

In this section, we describe how to perform the hydrophone alignment procedure using TOF measurements. This procedure includes both translational and rotational alignments.

4.2.1. TRANSLATIONAL ALIGNMENT

Figure 4.1(a) shows a hydrophone tip positioned at point H(x, y, z) alongside a matrix array $A_{i,j}$ of size $n \times m$. Here, the indices $i = 1, 2, \dots, n$ and $j = 1, 2, \dots, m$ represent the number of transducer elements in the x and y directions, respectively. The central element of the array (highlighted in blue in the figure) is denoted by $a_{\bar{n},\bar{m}}$, where $\bar{n} = (n + 1)/2$ and $\bar{m} = (m + 1)/2$ for an odd number of elements in both directions. To perform the alignment of the hydrophone with the central element, we need to determine the distances d_x and d_y required to translate the hydrophone to the desired position.

We begin by calculating the acoustic ray path $r_{\bar{n},\bar{m}}$, which is the distance from the centroid of the central element to the hydrophone tip. This is done by measuring the time-of-flight $\Delta t_{\bar{n},\bar{m}}$, which is the time taken for an ultrasound wave to propagate from the surface of the central element to the hydrophone:

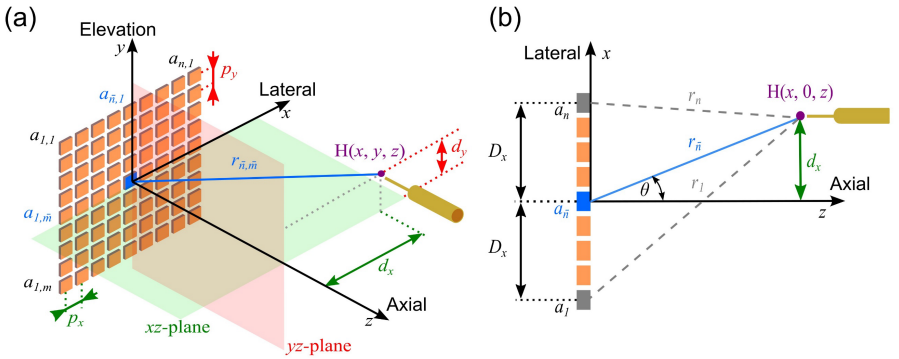

Figure 4.1: Geometry and coordinate system for translational alignment. (a) 3D view. (b) 2D view on the *xz*-plane.

$$r_{\bar{n},\bar{m}} = c\Delta t_{\bar{n},\bar{m}} \tag{4.1}$$

where c is the sound speed in the medium.

To simplify, let us focus on a two-dimensional scenario within the xz-plane, shown in Figure 4.1(b). The distance between the midpoints of the central element of the array ($a_{\bar{n}}$) and the nth element (a_n) is:

$$D_x = \left(\frac{2a_n - 1 - n}{2}\right) p_x \tag{4.2}$$

where p_x is the pitch of the array in the x-direction.

Assuming that the first element (a_1) and the last element (a_n) are equidistant from the central element, we can use the law of cosines to calculate the lengths of the ray paths r_1 and r_n:

$$r_1 = \sqrt{r_{\bar{n}}{}^2 + D_x^2 + 2r_{\bar{n}} D_x \sin\theta} \tag{4.3}$$

$$r_n = \sqrt{r_{\bar{n}}{}^2 + D_x^2 - 2r_{\bar{n}} D_x \sin\theta} \tag{4.4}$$

where θ is the angle between the normal of the element $a_{\bar{n}}$ and its ray path $r_{\bar{n}}$.

Therefore, the required translation distance is:

$$d_x = r_{\bar{n}} \sin\theta = \left(\frac{r_1^2 - r_{\bar{n}}{}^2 - D_x^2}{2D_x}\right) = -\left(\frac{r_n^2 - r_{\bar{n}}{}^2 - D_x^2}{2D_x}\right) \tag{4.5}$$

Thus, by measuring the TOF of three equidistant elements along one axis, we can align the hydrophone with the central element. For a matrix transducer, the same procedure is applied in the yz-plane.

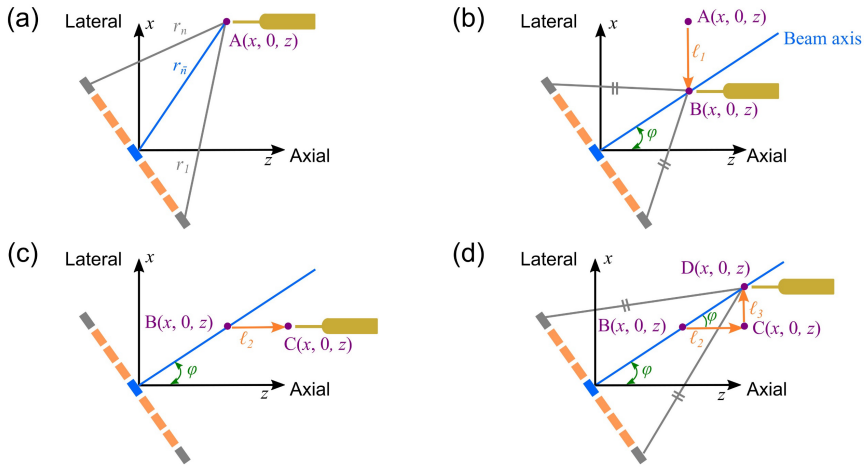

Figure 4.2: Rotational alignment on the *xz*-plane. (a) Initial position. (b) First translational alignment. (c) Displacement of the hydrophone in the *z* direction. (d) Second translational alignment.

4.2.2. ROTATIONAL ALIGNMENT

In Figure 4.2(a), the transducer surface is not perpendicular to the z axis. The hydrophone is initially located at point $\mathrm{A}(x, 0, z)$. To perform the angular alignment of the hydrophone with the central element, we need to determine the angle φ required to rotate the array, making its surface normal to the z axis. The procedure starts with a translational alignment of the hydrophone with the central element, as described earlier. This moves the hydrophone from $\mathrm{A}(x, 0, z)$ to $\mathrm{B}(x, 0, z)$ by a distance ℓ_1. Note that, $\mathrm{B}(x, 0, z)$ lies on the axial axis of the central element, as shown in Figure 4.2(b). Next, the hydrophone is moved along the z axis towards point $\mathrm{C}(x, 0, z)$, located at a known distance ℓ_2 away from $\mathrm{B}(x, 0, z)$, as depicted in Figure 4.2(c). At $\mathrm{C}(x, 0, z)$, a second translational alignment is conducted, displacing the hydrophone to $\mathrm{D}(x, 0, z)$ by a known distance ℓ_3, as shown in Figure 4.2(d). The required angle is then determined by:

$$\varphi = \tan^{-1}\left(\frac{\ell_3}{\ell_2}\right) \tag{4.6}$$

For a matrix transducer, the rotational alignment is also performed on the *yz*-plane. Note that, this procedure does not involve rotation around the z-axis. This is because standard setups for ultrasound measurements typically provide only five degrees of freedom (three translations and two rotations) and exclude rotation around the z-axis [12].

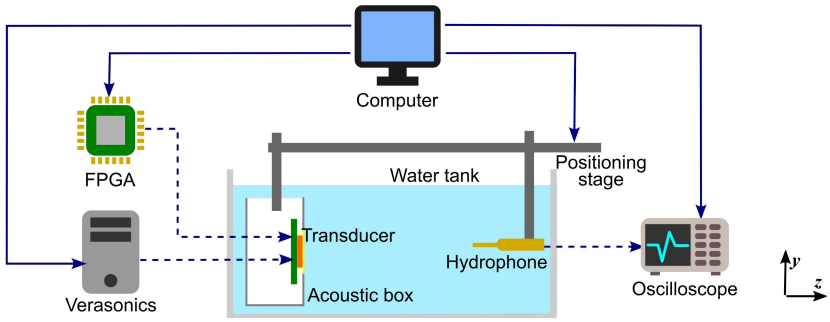

Figure 4.3: Experimental setup for pressure field characterization.

4.3. MATERIALS AND METHODS

4.3.1. EXPERIMENTAL SETUP

The setup utilized for performing the pressure field characterization of a matrix ultrasound transducer is schematized in Figure 4.3. Placed at one extremity of the water tank, a 0.2 mm needle hydrophone (PVDF, Precision Acoustics Ltd., Dorchester, UK) is affixed to a rod that can be translated along three orthogonal directions. At the opposing side of the tank, a prototype matrix transducer is mounted to a rod that allows rotation around the y-axis. To capture the hydrophone signals, an oscilloscope (DSO-X 4024A, Agilent Technologies, Santa Clara, CA, USA) is utilized, while a research imaging system (V1, Verasonics, Inc., Kirkland, WA, USA) is employed to drive the transducer. All these devices and instruments are controlled by the host computer of the Verasonics system.

4.3.2. PROTOTYPE MATRIX TRANSDUCER

The prototype matrix transducer has a center frequency of 7.5 MHz with a pitch of 150 µm × 300 µm and it is made from lead zirconate titanate (PZT). The matrix array is constructed directly over 1×10 identical application-specific integrated circuits (ASICs), whose element-level circuits are matched to the pitch of the array (Figure 4.4). For this study, three ASICs of the prototype were connected (red regions in the figure), which means that 2880 elements of the matrix can be individually addressed. More details about the prototype transducer can be found in our previous publications [25], [26].

4.3.3. SUBARRAYS OF ACTIVE ELEMENTS

Ideally, aligning a hydrophone with a matrix transducer in the x and y directions would require TOF measurements from just five elements – the central element and four elements around it. In practice, however, the actual success of this alignment depends on the transducer's performance and element yield. It is well known that

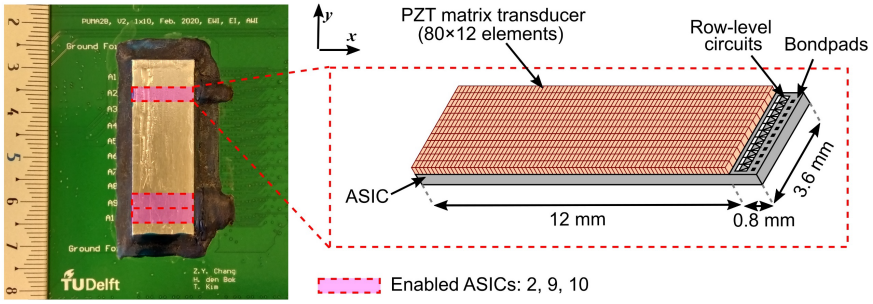

Figure 4.4: Photograph of the prototype transducer and schematic drawing of a single ASIC on top of the PZT matrix.

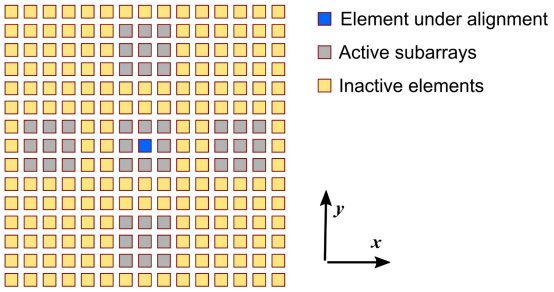

Figure 4.5: A matrix array with active subarrays of size 3 × 3.

PZT transducers are susceptible to imperfections, such as crystal depolarization, open circuits, or short circuits, which can impact their functionality and consequently the alignment procedure.

To address these potential issues, we took a different approach. Instead of relying solely on five individual elements, we divided the transducer into five subarrays of active elements, as shown in Figure 4.5. Within each subarray, we calculated the average TOF value to minimize the impact of defective elements on TOF measurements. Additionally, we applied an amplitude threshold set above the noise floor to confirm the functionality of active elements. If an element did not reach this threshold, its TOF contribution within the subarray was disregarded.

4.3.4. PRESSURE FIELD CHARACTERIZATION

We have designed a graphical user interface (GUI) software to assist in the pressure field characterization of the prototype matrix transducer. Figure 4.6 illustrates the flowchart of this application, which was developed using MATLAB (2014b, The

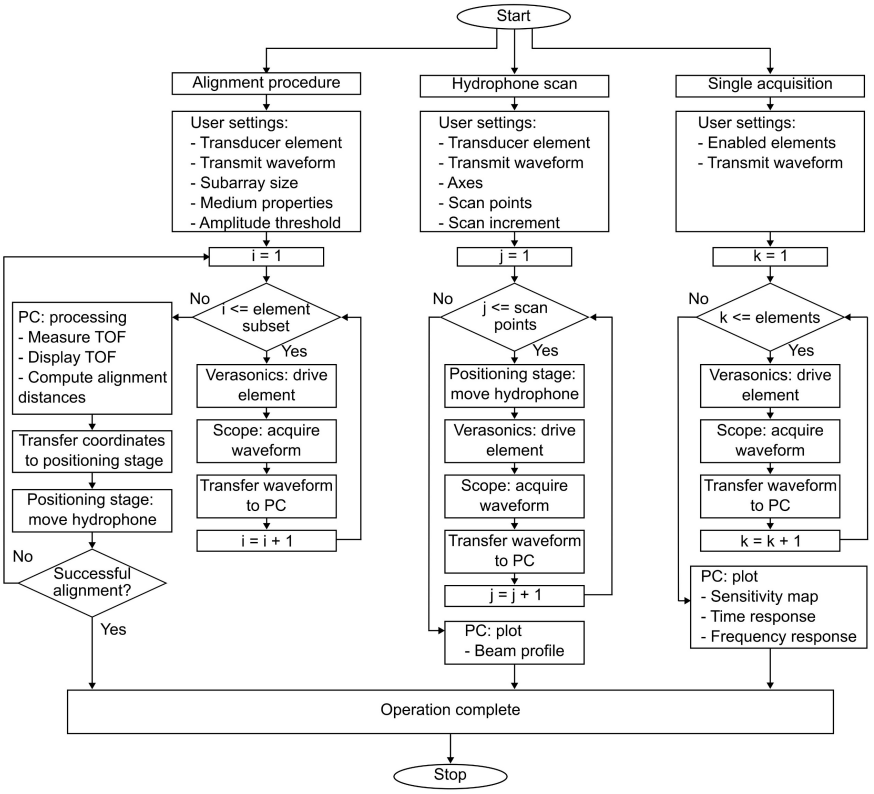

Figure 4.6: Flowchart of the designed GUI for pressure field characterization.

MathWorks, Inc., Natick, MA, USA). The GUI provides three distinct modes of operation: alignment procedure, hydrophone scan, and single acquisition mode.

In alignment mode, the user selects the element to align with the hydrophone and sets key parameters for the alignment procedure (e.g., medium properties, subarray size, amplitude threshold, etc.). Then, the Verasonics drives each active element, and during each transmission, the hydrophone's signal is digitized and sent to the computer for processing. After data acquisition, the computer determines alignment distances and directs the positioning stage to move the hydrophone to the appropriate position. Real-time feedback allows the user to immediately assess the alignment procedure.

In hydrophone scan mode, the user can perform standard linear and planar scans to evaluate important transducer characteristics like beam profile, directivity pattern, and transmit beamforming capabilities. As input, the user specifies scan parameters such as the number of scan points, increment, and scan axes. Once the operation begins, the transducer is excited and the scan is executed. At each spatial point, hydrophone signals are acquired and transferred to the computer. The measured beam profile is then displayed to the user in real time as the acquisition progresses.

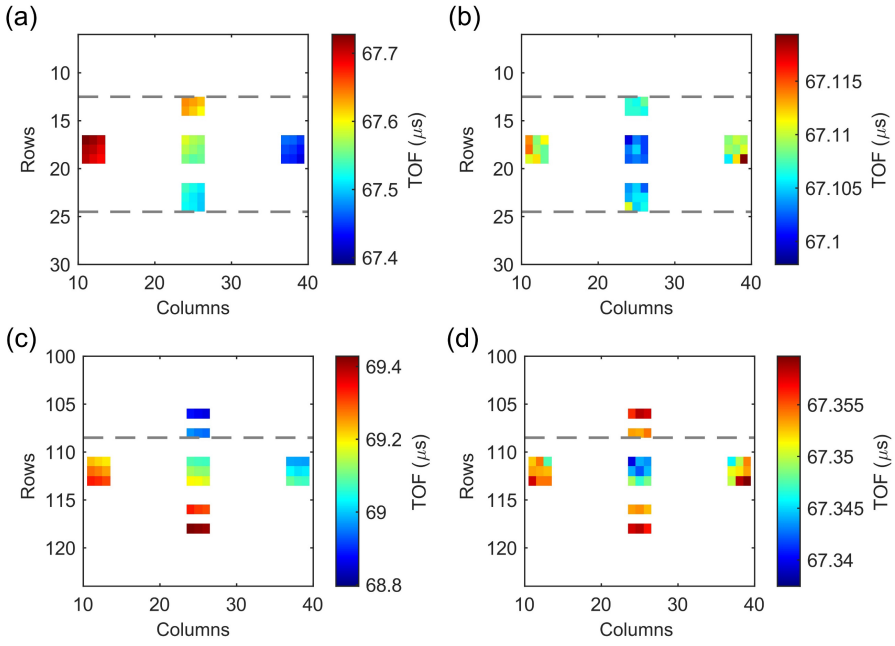

Figure 4.7: Measured TOF values. (a) Before and (b) after alignment with element $a_{25,18}$. (c) Before and (d) after alignment with element $a_{25,112}$.

In single acquisition mode, the hydrophone remains stationary at a fixed position while the Verasonics sequentially activates each individual element of the transducer. During each transmit event, the hydrophone captures signals, which are then transferred to the computer for processing. This mode of operation is valuable for assessing variations among individual elements and offers a quick, comprehensive overview for evaluating the manufacturing process.

In order to demonstrate the capabilities of the designed software, we systematically tested each mode of operation. To evaluate the alignment procedure, we aligned the hydrophone with two arbitrarily selected elements of the transducer. Initially, we aligned it with element $a_{25,18}$, located within ASIC 2, and subsequently with element $a_{25,112}$, located within ASIC 10. Prior to the alignment process, the hydrophone was positioned randomly and underwent translations and rotations.

Table 4.1: Measured TOF values for various active subarrays after alignment.

Element	Left (µs)	Right (µs)	Error (ns)	Top (µs)	Bottom (µs)	Error (ns)
$a_{25,18}$	67.1107	67.1104	0.3	67.1069	67.1054	1.5
$a_{25,112}$	67.3534	67.3526	0.8	67.3555	67.3554	0.1

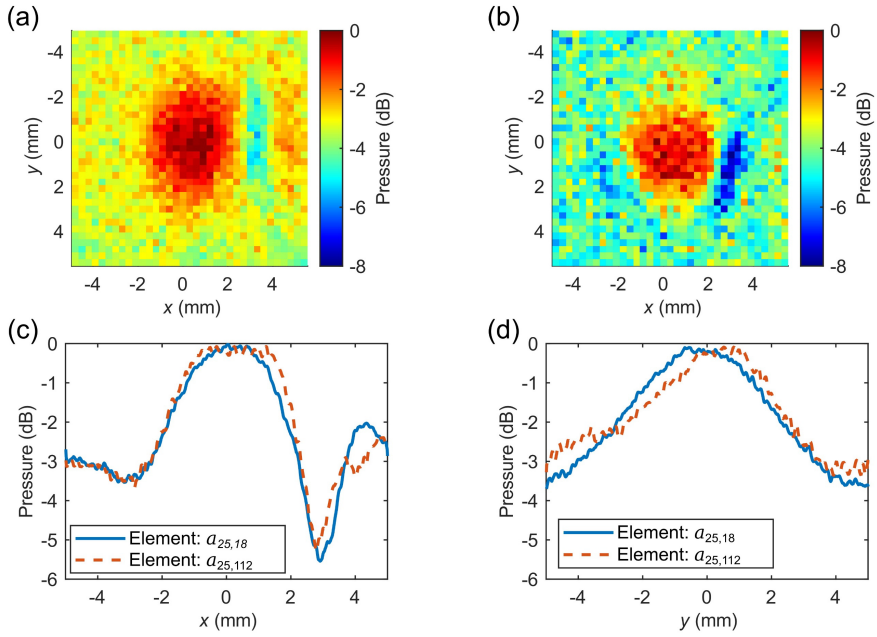

Figure 4.8: 2D beam profile of (a) element $a_{25,18}$ and (b) element $a_{25,112}$. 1D beam profile (a) along the *x* axis and (d) along the *y* axis.

For the alignment process, we employed active subarrays of size 3 × 3, which was determined through simulations using the ultrasound simulator FOCUS [27]. An amplitude threshold of 30 mV was applied, and the measured speed of sound in water was 1484 m/s at a temperature of 22 °C. After the alignment, we performed hydrophone scans to characterize the beam profiles of the two elements under test. Lastly, we performed single acquisitions for all individual elements, positioning the hydrophone at the two different locations, in order to assess the influence of hydrophone directivity on the measurements.

4.4. RESULTS

The measured TOF for all active subarrays of the prototype transducer before and after the alignment is shown in Figure 4.7. Table 4.1 presents the averaged TOF values obtained after the alignment procedure, together with the absolute error calculated between the left-right and top-bottom active subarrays. After the alignment procedure, it is evident that the TOF values exhibit greater symmetry with respect to the central subarray, with an absolute error smaller than 1 ns between the symmetrical subarrays. This indicates successful alignment of the hydrophone tip with the axial axis of the central element.

Note that a few elements within the active subarrays, specifically from rows 12, 107, and 118, did not exceed the noise threshold and were consequently excluded

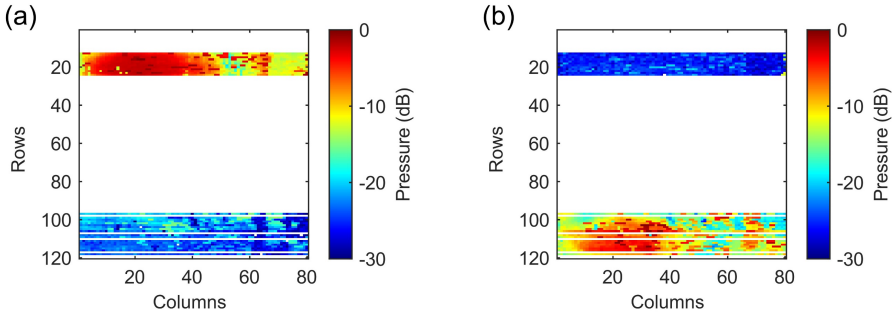

Figure 4.9: Transmit peak pressure for each individual transducer element. (a) Hydrophone aligned with element $a_{25,18}$. (b) Hydrophone aligned with element $a_{25,112}$.

from the calculations of the alignment distances. The entire process, including recording the TOF for all active subarrays (comprising 45 active elements), data transfer and processing, and positioning the hydrophone, can be accomplished in about one minute.

The measured 2D and 1D beam profiles for the two elements under evaluation are illustrated in Figure 4.8. Each planar scan required approximately 15 minutes to complete, while the linear scans were accomplished in about 12 minutes. The planar scans reveal that the acoustic beams from both elements are centered at the origin of the coordinate system, confirming the success of the alignment procedure. From the linear scans, it is clear that both elements exhibit similar trends in both directions, although the measured beam profile is not symmetrical. In the x direction, we measured a -3 dB beamwidth of approximately 4 mm, with a noticeable dip is observed at 3 mm. In the y direction, the -3 dB beamwidth is about 6 mm.

In Figure 4.9, we present the peak pressure for each individual element of the transducer, which we obtained by aligning the hydrophone with the elements within ASIC 2 and ASIC 10. To generate these maps, it took approximately seven minutes to acquire and process hydrophone data from all 2880 elements. When we align the hydrophone with element $a_{25,18}$, which is within ASIC 2, we observed that approximately 400 elements exhibit a transmit efficiency falling within the range of 0 dB to -6 dB, accounting for 14 % of the elements. Conversely, when aligned with element $a_{25,112}$, which is within ASIC 10, roughly 200 elements show a transmit efficiency within the 0 dB to – 6 dB range, representing 7 % of the elements. Thus, it is clear that the number elements falling within the -6 dB range changes dramatically depending on the alignment of the hydrophone.

Figure 4.10 shows 2D histogram of the time and frequency responses for all individual elements of the prototype transducer after correcting for the hydrophone directivity. In the time domain response, the measured peak pressure averaged across all elements is about 1.9 kPa, with a -20 dB ringing time of about 0.2 µs. In the frequency domain, the prototype exhibits an average center frequency of 7.5 MHz, with a bandwidth of approximately 45 %.

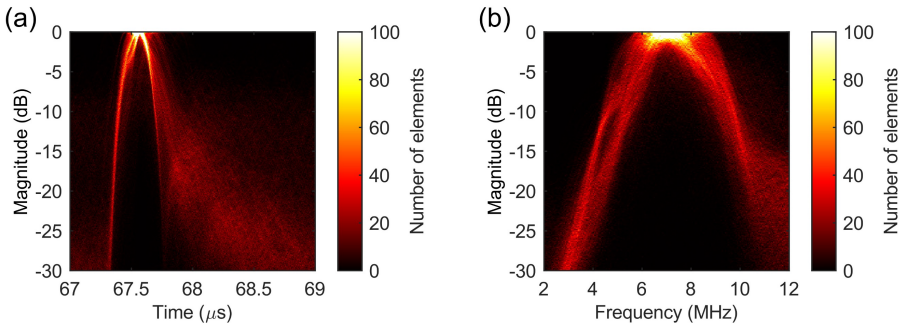

Figure 4.10: Time and frequency domain responses for all transducer elements.
(a) Envelope of the time signals after correcting for time delays between the signals using cross-correlation. (b) Frequency spectrum.

4.5. DISCUSSION

This paper presents an automated procedure to characterize the pressure field of an ultrasound matrix transducer consisting of thousands of individual elements using hydrophone measurements. The procedure starts with the alignment of the hydrophone with the element under test using TOF measurements, followed by the beam profile characterization of the transducer elements, the generation of sensitivity maps, and an evaluation of the time and frequency responses for each element. This automated approach facilitates a comprehensive analysis and accelerates the iterative process of designing dedicated PZT matrix transducers with a substantial number of elements and integrated electronics.

The alignment of the hydrophone with the transducer elements is typically one of the slowest and most cumbersome steps in the characterization process. This is because it often requires multiple scans to locate the maximum of the acoustic beam for the element under test. In our proposed method, we speed up the alignment process by utilizing TOF measurements from five active subarrays. This approach can be completed in approximately a minute if the entire measurement setup is automated, requiring only a single iteration for a specific element. Compared to hydrophone scans, which usually take more than five minutes and might require multiple iterations, our method offers significant advantages. The primary factor influencing measurement time in our approach is the size of the subarrays. While larger subarrays help smooth out poor signals from defective elements, they also result in slower measurement times. Note that the alignment procedure presented here is not intended to be conducted for every individual element, as this would consume a significant amount of time. Rather, it should target a few key elements within the array. In our previous work [26], we showed that aligning the hydrophone at just two locations per ASIC was sufficient to characterize this prototype transducer minimizing the influence of the hydrophone directivity.

The TOF maps depicted in Figure 4.7 illustrate that the TOF values exhibit symmetry around the element under test upon completion of the alignment procedure, suggesting that the hydrophone is accurately positioned on the acoustic

beam of the desired element. Table 4.1 shows that the averaged TOF values within symmetrical subarrays are nearly identical, with an absolute error of about 1 ns between them.

The successful completion of the alignment procedure is further confirmed by the beam profiles depicted in Figure 4.8, which are appropriately centered at the origin of the coordinate system. This positioning enables the beam profile to be evaluated locally (i.e., in a smaller region) with a finer spatial resolution, thereby reducing measurement time and improving the quality of the characterization. Note that the observed dip at 3 mm in the x direction is likely due to acoustic crosstalk between elements, a phenomenon we have previously investigated [26].

The maps presented in Figure 4.9 reveal that the sensitivity of the transducer elements varies significantly depending on the position of the hydrophone. This variation is caused by the directivity pattern (from both the element and the hydrophone) and can lead to measurement errors, bias, and misinterpretation of the transducer performance. To mitigate these issues, it is crucial to minimize the angle between the acoustic axis of the elements under test and the normal to the hydrophone surface, ideally keeping it as close to zero as possible.

Figure 4.10 shows that the time and frequency responses of the individual transducer elements closely match. Furthermore, the probe's specifications, including center frequency and bandwidth, align with the design parameters. After proper hydrophone alignment and directivity correction, 70% of the elements exhibits a peak pressure within the -6dB range. Based on the measured peak pressure (1.9 kPa) and a transmit voltage of 40 V peak, we estimated an average transmit efficiency of approximately 50 Pa/V at 100 mm. These results are consistent with our previous designs [24], [26].

The procedure herein presented involves a high level of integration of various devices, measurements, and instrumentation, which may not be straightforward for average users. Implementing this solution may require some time and effort, but it is valuable in an environment of continuous design and testing of ultrasound transducers with a high element count. Once the system is implemented, it can be readily adapted for different probes. While the primary focus of this work is on matrix arrays, it is worth noting that the described procedure can also be applied, to some extent, to characterize the pressure field of different types of transducers.

4.6. CONCLUSION

In this paper, we introduce an automated technique designed to analyze pressure fields within high-element count ultrasound matrix transducers. Compared to conventional methods, this approach substantially reduces measurement time, enabling a faster and more comprehensive evaluation of transducer performance. Through experimental validation using a prototype matrix transducer comprising 2880 elements, we demonstrate the effectiveness of this automated procedure. It provides valuable insights into beam profiles, sensitivity maps, and the time/frequency responses of individual elements. Ultimately, this procedure represents a significant advancement in the characterization of ultrasound

transducers, leading to enhancements in their design, manufacturing, and safety evaluation.

4.7. REFERENCES

[1] J. Seo and Y. Kim, "Ultrasound imaging and beyond: recent advances in medical ultrasound," *Biomed Eng Lett*, vol. 7, no. 2, pp. 57–58, May 2017, doi: 10.1007/s13534-017-0030-7.

[2] T. L. Szabo, *Diagnostic Ultrasound Imaging: Inside Out*. New York: Elsevier, 2014. doi: 10.1016/C2011-0-07261-7.

[3] C. Papageorgiou and T. Laopoulos, "Self-calibration of ultrasonic transducers in an intelligent data acquisition system," in *Proceedings of the 2nd IEEE International Workshop on Intelligent Data Acquisition and Advanced Computing Systems: Technology and Applications, IDAACS 2003*, IEEE, 2003, pp. 2–6. doi: 10.1109/IDAACS.2003.1249504.

[4] D. S. Dos Santos *et al.*, "Automated Characterization of Matrix Transducer Arrays using the Verasonics Imaging System," in *2022 IEEE International Ultrasonics Symposium (IUS)*, IEEE, Oct. 2022, pp. 1–4. doi: 10.1109/IUS54386.2022.9957544.

[5] M. T. Burgess and E. E. Konofagou, "Fast qualitative two-dimensional mapping of ultrasound fields with acoustic cavitation-enhanced ultrasound imaging," *J Acoust Soc Am*, vol. 146, no. 2, pp. EL158–EL164, 2019, doi: 10.1121/1.5122194.

[6] Y. Yu, G. Shen, Y. Zhou, J. Bai, and Y. Chen, "Quantitative Assessment of Acoustic Intensity in the Focused Ultrasound Field Using Hydrophone and Infrared Imaging," *Ultrasound Med Biol*, vol. 39, no. 11, pp. 2021–2033, Nov. 2013, doi: 10.1016/j.ultrasmedbio.2013.05.004.

[7] V. Daeichin *et al.*, "Acoustic characterization of a miniature matrix transducer for pediatric 3D transesophageal echocardiography," *Ultrasound Med Biol*, vol. 44, no. 10, pp. 2143–2154, Oct. 2018, doi: 10.1016/j.ultrasmedbio.2018.06.009.

[8] M. Shabanimotlagh *et al.*, "Optimizing the directivity of piezoelectric matrix transducer elements mounted on an ASIC," *IEEE International Ultrasonics Symposium, IUS*, pp. 5–8, 2017, doi: 10.1109/ULTSYM.2017.8091752.

[9] D. S. dos Santos, L. Baldini, H. J. Vos, M. D. Verweij, N. de Jong, and P. L. M. J. van Neer, "Acoustic streaming-based calibration of ultrasound transducers," *Applied Acoustics*, vol. 217, p. 109863, Feb. 2024, doi: 10.1016/j.apacoust.2024.109863.

[10] B. Cugnet, J. Assaad, and A.-C. Hladky-Hennion, "Characterization of matched piezoelectric transducer bars," *J Acoust Soc Am*, vol. 115, no. 6, pp. 2904–2913, Jun. 2004, doi: 10.1121/1.1739486.

[11] FDA, "Marketing Clearance of Diagnostic Ultrasound Systems and Transducers," Rockville, MD, USA, 2019.

[12] Roy C. Preston, *Output Measurements for Medical Ultrasound*. London: Springer London, 1991. doi: 10.1007/978-1-4471-1883-1.

[13] M. A. Ghanem *et al.*, "Field Characterization and Compensation of Vibrational Nonuniformity for a 256-Element Focused Ultrasound Phased Array," *IEEE Trans Ultrason Ferroelectr Freq Control*, vol. 65, no. 9, pp. 1618–1630, 2018, doi: 10.1109/TUFFC.2018.2851188.

[14] A. Hurrell and F. Duck, "A two-dimensional hydrophone array using piezoelectric PVDF," *IEEE Trans Ultrason Ferroelectr Freq Control*, vol. 47, no. 6, pp. 1345–1353, Nov. 2000, doi: 10.1109/58.883523.

[15] T. Marhenke, S. J. Sanabria, B. R. Chintada, R. Furrer, J. Neuenschwander, and O. Goksel, "Acoustic field characterization of medical array transducers based on unfocused transmits and single-plane hydrophone measurements," *Sensors (Switzerland)*, vol. 19, no. 4, pp. 1–17, 2019, doi: 10.3390/s19040863.

[16] ASTM E1065/E1065M-14, "Standard Guide for Evaluating Characteristics of Ultrasonic Search Units." 2014. doi: 10.1520/E1065_E1065M-14.

[17] Y. Q. Wu, P. M. Shankar, and P. A. Lewin, "Characterization of ultrasonic transducers using a fiberoptic sensor," *Ultrasound Med Biol*, vol. 20, no. 7, pp. 645–653, Jan. 1994, doi: 10.1016/0301-5629(94)90113-9.

[18] E. G. Radulescu, P. A. Lewin, A. Nowicki, and W. A. Berger, "Hydrophones' effective diameter measurements as a quasi-continuous function of frequency," *Ultrasonics*, vol. 41, no. 8, pp. 635–641, 2003, doi: 10.1016/S0041-624X(03)00180-X.

[19] J. Adach, R. C. Chivers, and L. W. Anson, "Ultrasonic propagation, scattering, and defocusing in suspensions," *Journal of the Acoustical Society of America*, vol. 93, no. 6, pp. 3208–3219, 1993, doi: 10.1121/1.405705.

[20] P. Ramaekers, M. de Greef, R. Berriet, C. T. W. Moonen, and M. Ries, "Evaluation of a novel therapeutic focused ultrasound transducer based on Fermat's spiral," *Phys Med Biol*, vol. 62, no. 12, pp. 5021–5045, Jun. 2017, doi: 10.1088/1361-6560/aa716c.

[21] M. E. Schafer and P. A. Lewin, "A computerized system for measuring the acoustic output from diagnostic ultrasound equipment," *IEEE Trans Ultrason Ferroelectr Freq Control*, vol. 35, no. 2, pp. 102–109, Mar. 1988, doi: 10.1109/58.4160.

[22] S. Rajagopal and B. T. Cox, "100 MHz bandwidth planar laser-generated ultrasound source for hydrophone calibration," *Ultrasonics*, vol. 108, no. July, p. 106218, 2020, doi: 10.1016/j.ultras.2020.106218.

[23] A. Pulkkinen, J. J. Leskinen, and A. Tiihonen, "Ultrasound field characterization using synthetic schlieren tomography," *J Acoust Soc Am*, vol. 141, no. 6, pp. 4600–4609, Jun. 2017, doi: 10.1121/1.4986623.

[24] D. S. dos Santos *et al.*, "Experimental Investigation of the Effect of Subdicing on an Ultrasound Matrix Transducer," in *2021 IEEE International Ultrasonics Symposium (IUS)*, IEEE, Sep. 2021, pp. 1–3. doi: 10.1109/IUS52206.2021.9593315.

[25] T. Kim *et al.*, "Design of an Ultrasound Transceiver ASIC with a Switching-Artifact Reduction Technique for 3D Carotid Artery Imaging," *Sensors*, vol. 21, no. 1, p. 150, Dec. 2020, doi: 10.3390/s21010150.

[26] D. S. dos Santos *et al.*, "A Tiled Ultrasound Matrix Transducer for Volumetric Imaging of the Carotid Artery," *Sensors*, vol. 22, no. 24, p. 9799, Dec. 2022, doi: 10.3390/s22249799.

[27] R. J. McGough, "Rapid calculations of time-harmonic nearfield pressures produced by rectangular pistons," *J Acoust Soc Am*, vol. 115, no. 5, pp. 1934–1941, May 2004, doi: 10.1121/1.1694991.

5

EXPERIMENTAL INVESTIGATION OF THE EFFECT OF SUBDICING ON AN ULTRASOUND MATRIX TRANSDUCER[1]

[1] This chapter is based on the following publication:
dos Santos, D.S.; Fool, F.; Kim, T.; Noothout, E.; Vos, H.J.; Bosch, J.G.; Pertijs, M.A.P.; Verweij, M.D.; de Jong, N. Experimental Investigation of the Effect of Subdicing on an Ultrasound Matrix Transducer. In Proceedings of the 2021 IEEE International Ultrasonics Symposium (IUS); IEEE, September 11 2021; pp. 1–3.

5.1. INTRODUCTION

MEDICAL ultrasound is an indispensable imaging modality due to its flexibility and non-invasive character [1]. Over the past decades, real-time three-dimensional (3D) ultrasound has attracted much attention since it enables clinicians to diagnose more accurately than with conventional two-dimensional (2D) ultrasound imaging [2]. A common way to generate real-time 3D images is by using a matrix transducer that contains many elements (in the order of thousands) of very small pitch (in the order of hundreds of micrometers). It is a great challenge to build a matrix array with such a vast number of elements because it requires thousands of electrical connections between the matrix array and the imaging system, which is impractical if not impossible. One of the approaches to overcome this issue is by manufacturing the transducer matrix directly on top of an application-specific integrated circuit (ASIC) to reduce the number of cables [3]–[5].

Most of the clinically available ultrasound probes are made of a piezoelectric material (PZT). The performance of a PZT transducer is directly related to its geometry, which affects the mode of vibration of the elements [6], [7]. If the width-to-thickness ratio of the element is smaller than 0.7, the element will mainly vibrate in the thickness mode, which is more efficient due to the piston-like motion. If the width-to-thickness ratio is greater than 0.7, unwanted vibration modes will reduce the efficiency of the transducer. Since the wavelength in PZT is about twice the wavelength in water (λ), we can say that thickness vibration is obtained when the width of the element is well below 0.7λ [5]–[9]. Thus, elements with a small width are preferred to achieve high efficiency. On the other hand, to radiate more power into the medium, the element should be as large as possible. This leads to a contradiction that can be solved by subdicing, which means cutting each transducer element into smaller sub-elements with non-through cuts [7].

The influence of subdicing on a matrix transducer integrated with an ASIC has been previously investigated through simulations in [5]. In this paper, we investigate the effect of subdicing experimentally. For this purpose, we build a prototype PZT matrix (on top of ASICs) having subdiced and non-subdiced elements, so they can be directly compared. We analyze the transmit performance of all individual elements in the time and frequency domain, and we also compare the directivity pattern of subdiced and non-subdiced elements.

5.2. METHODS

5.2.1. PROTOTYPE MATRIX TRANSDUCER

We have fabricated a prototype PZT matrix transducer that operates at 7.5 MHz and consists of 48×80 elements with a pitch of 300 μm × 150 μm (1.5λ × 0.75λ). Along the 300 μm pitch direction, the matrix alternates between subdiced, yielding sub-elements of 150 μm × 150 μm, and non-subdiced elements every 6 rows, as shown in Figure 5.1. In this way, it is possible to directly compare subdiced with non-subdiced elements under the same conditions. The PZT matrix was mounted on top of 4×1 tiled ASICs whose element-level circuits match the pitch of the array. The

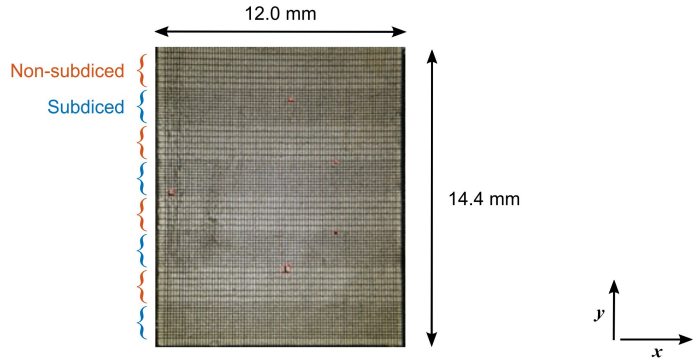

Figure 5.1. A photograph of the fabricated PZT matrix with subdiced and non-subdiced rows.

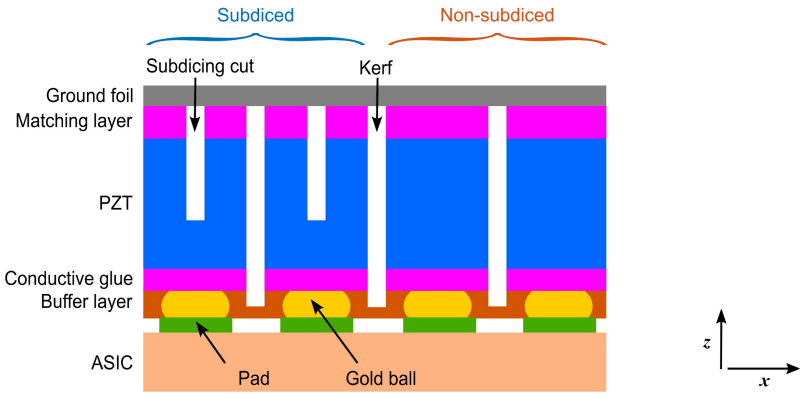

Figure 5.2: Acoustic stack of the prototype matrix transducer (not drawn to scale).

prototype transducer interfaces with a Verasonics V1 imaging system (Verasonics, Inc., Kirkland, WA, USA) using a custom-designed motherboard PCB [3], [10]. The geometry and the composition of the acoustic stack are shown in Figure 5.2. For subdiced elements, one single cut was applied with a cutting depth of 70% of the total element thickness, i.e., the thickness of the PZT and the matching layer. According to [7], a cutting depth of 70% is sufficient to reduce spurious vibration modes while providing mechanical stability to the elements.

5.2.2. TRANSMIT CHARACTERIZATION

The transmit characterization was performed with a 1 mm calibrated needle hydrophone (SN 2082, Precision Acoustics Ltd., Dorchester, UK) placed at 100 mm away from the transducer surface. The Verasonics V1 was used to drive each array element individually with a 30 V unipolar pulse. The hydrophone signals were

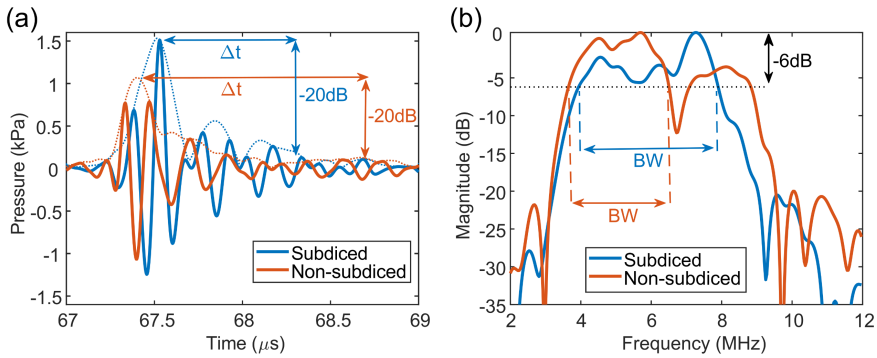

Figure 5.3: (a) Time and (b) frequency domain responses of a non-subdiced and a subdiced element.

amplified by a 60 dB amplifier (AU-1519, Miteq, Inc., Hauppauge, NY, USA), digitized by an oscilloscope (DSO-X 4024A, Agilent Technologies, Santa Clara, CA, USA), and transferred to a computer automatically.

To evaluate the directivity pattern of the elements, a 0.2 mm calibrated needle hydrophone (SN 1688, Precision Acoustics Ltd., Dorchester, UK) was placed at 50 mm away from the transducer surface and rotated from 0 to 60 degrees. Before measuring the directivity of each evaluated element, the hydrophone was aligned by finding the maximum acoustic pressure.

5.3. RESULTS AND DISCUSSION

In Figure 5.3(a), the time domain responses, plotted in solid lines, of a non-subdiced and a subdiced element are shown. The envelope of the pulse is plotted in dotted lines. The measured peak pressure (i.e., envelope peak) of this subdiced element is about 1.5 times higher than for the non-subdiced one. Another parameter obtained from the time response is the ringing time $\Delta t_{\text{-20dB}}$, defined as the time interval for the envelope amplitude to decrease below -20 dB of its corresponding peak. The ringing time of the subdiced element is about 0.8 μs. For the non-subdiced element, this is about 1.32 μs.

The frequency domain responses of the subdiced and non-subdiced elements are depicted in Figure 5.3(b). The non-subdiced element shows an unwanted dip at around 7 MHz, reducing its -6 dB bandwidth ($BW_{\text{-6dB}}$). For the subdiced element, the unwanted dip is shifted to higher frequencies, yielding a higher bandwidth. This indicates that subdicing reduces spurious vibration modes, as expected.

The relative peak pressure across all elements of the matrix is shown in Figure 5.4. It is visible that the subdiced rows are, in general, more efficient than the non-subdiced ones. As seen, the majority of the array elements are functioning, but some elements are defective. Rows 2 and 48 do not transmit possibly due to defective (or

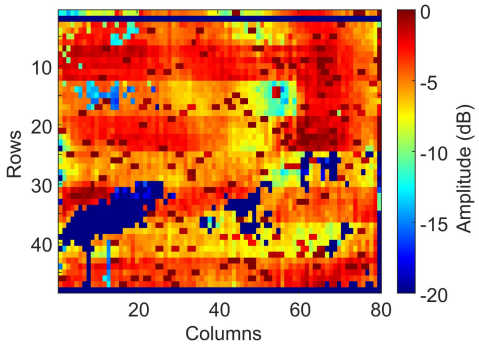

Figure 5.4: Relative peak pressure of all transducer elements (corrected for the hydrophone directivity).

missing) bond wires. The remaining defective elements were likely damaged during the fabrication process.

The directivity pattern of a subdiced and a non-subdiced element is shown in Figure 5.5. The analytical curve of an ideal piston in a rigid planar baffle is also plotted for comparison [11]. The beam width of the prototype matrix (for both subdiced and non-subdiced elements) is considerably narrower than the ideal one. For the non-subdiced element, extra peaks occur at around 40 degrees, where a dip is expected. The cause of these peaks has not yet been identified as this is not observed in simulations [4], [7]. The directivity pattern of the subdiced element agrees better with the analytical curve.

The overall performance of the prototype transducer matrix is summarized in Table 5.1. The listed values represent the average over 1920 array elements. An exception to this is the value of the beam width, which was obtained by averaging the results over 12 elements. The measured peak pressure of subdiced elements is 25% higher than the non-subdiced ones. This confirms that subdicing increases the transmit efficiency even though the surface area of the element is reduced. Besides, subdiced elements have a shorter pulse duration with a ringing time that is 25% smaller. The peak frequency of subdiced elements was raised by 1 MHz and the bandwidth by 10% when compared to non-subdiced elements.

Table 5.1: Comparison between non-subdiced and subdiced elements.

Parameter	**Non-subdiced**	**Subdiced**
Peak pressure (kPa)	1.2 ± 0.2	1.5 ± 0.4
Ringing $\Delta t_{\text{-20dB}}$ (µs)	1.4 ± 0.1	1.1 ± 0.3
Peak frequency (MHz)	5.2 ± 0.2	6.1 ± 0.2
Bandwidth $_{\text{-6dB}}$ (%)	32 ± 4	42 ± 9
Beam width $_{\text{-6dB}}$ (°)	22.0 ± 2	29.0 ± 2

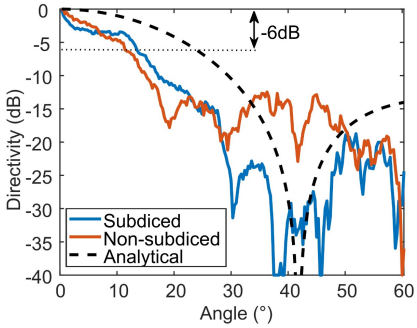

Figure 5.5: Directivity pattern of a non-subdiced and a subdiced element.

5

5.4. CONCLUSIONS

In this paper, the performance of a prototype matrix transducer built on ASICs and consisting of subdiced and non-subdiced elements was analyzed in transmit. On average, subdicing increases the peak pressure by 25%, raises the bandwidth by 10%, and reduces the ringing time by 25%. In addition, the directivity pattern of subdiced elements is more similar to the analytical curve. The results indicate that subdicing improves the performance of the transducer with large elements (width-to-thickness ratio larger than 0.7).

5.5. REFERENCES

[1] A. Fenster, D. B. Downey, and H. N. Cardinal, "Three-dimensional ultrasound imaging," *Phys Med Biol*, vol. 46, no. 5, pp. R67–R99, May 2001, doi: 10.1088/0031-9155/46/5/201.

[2] Q. Huang and Z. Zeng, "A Review on Real-Time 3D Ultrasound Imaging Technology," *Biomed Res Int*, vol. 2017, 2017, doi: 10.1155/2017/6027029.

[3] T. Kim *et al.*, "Design of an Ultrasound Transceiver ASIC with a Switching-Artifact Reduction Technique for 3D Carotid Artery Imaging," *Sensors*, vol. 21, no. 1, p. 150, Dec. 2020, doi: 10.3390/s21010150.

[4] M. Shabanimotlagh *et al.*, "Optimizing the directivity of piezoelectric matrix transducer elements mounted on an ASIC," *IEEE International Ultrasonics Symposium, IUS*, pp. 5–8, 2017, doi: 10.1109/ULTSYM.2017.8091752.

[5] M. Shabanimotlagh, J. Janjic, S. Raghunathan, M. A. P. Pertijs, N. de Jong, and M. Verweij, "The role of sub-dicing in the acoustical design of an ultrasound matrix transducer for carotid arteries imaging," in *2016 IEEE International Ultrasonics Symposium (IUS)*, IEEE, Sep. 2016, pp. 1–4. doi: 10.1109/ULTSYM.2016.7728470.

[6] N. de Jong, N. Bom, J. Souquet, and G. Faber, "Vibration modes, matching layers and grating lobes," *Ultrasonics*, vol. 23, no. 4, pp. 176–182, Jul. 1985, doi: 10.1016/0041-624X(85)90027-7.

[7] J. Janjic, M. Shabanimotlagh, G. van Soest, A. F. W. van der Steen, N. de Jong, and M. D. Verweij, "Improving the Performance of a 1-D Ultrasound Transducer Array by Subdicing," *IEEE Trans Ultrason Ferroelectr Freq Control*, vol. 63, no. 8, pp. 1161–1171, Aug. 2016, doi: 10.1109/TUFFC.2016.2561935.

[8] J. Janjic, M. Shabanimotlagh, M. D. Verweij, G. van Soest, A. F. W. van der Steen, and N. de Jong, "Quantifying the effect of subdicing on element vibration in ultrasound transducers," in *2015 IEEE International Ultrasonics Symposium (IUS)*, IEEE, Oct. 2015, pp. 1–4. doi: 10.1109/ULTSYM.2015.0553.

[9] D. H. Cortes, S. K. Datta, and O. M. Mukdadi, "Effect of subdicing on the dispersion and resonance behavior of elastic guided waves in 1D array ultrasound transducers," in *Medical Imaging 2009: Physics of Medical Imaging*, E. Samei and J. Hsieh, Eds., Feb. 2009, p. 72584L. doi: 10.1117/12.811606.

[10] E. Kang *et al.*, "A Reconfigurable Ultrasound Transceiver ASIC With 24 × 40 Elements for 3-D Carotid Artery Imaging," *IEEE J Solid-State Circuits*, vol. 53, no. 7, pp. 2065–2075, Jul. 2018, doi: 10.1109/JSSC.2018.2820156.

[11] L. W. Schmerr, "Fundamentals of Ultrasonic Phased Arrays," in *Solid Mechanics and Its Applications*, J. R. Barber and Anders Klarbring, Eds., Cham, Switzerland: Springer, 2015.

PART II: TRANSDUCER DESIGN FOR HIGH-FRAME-RATE 3D IMAGING

6

DESIGN OF AN ULTRASOUND TRANSCEIVER ASIC WITH A SWITCHING-ARTIFACT REDUCTION TECHNIQUE FOR 3D CAROTID ARTERY IMAGING[1]

[1] This chapter is based on the following publication:
Kim, T.; Fool, F.; **dos Santos, D.S.**; Chang, Z.-Y.; Noothout, E.; Vos, H.J.; Bosch, J.G.; Verweij, M.D.; de Jong, N.; Pertijs, M.A.P. Design of an Ultrasound Transceiver ASIC with a Switching-Artifact Reduction Technique for 3D Carotid Artery Imaging. Sensors 2020, 21, 150, doi:10.3390/s21010150.

6.1. INTRODUCTION

REAL-TIME 3D ultrasound imaging is an essential technique for the accurate assessment of carotid artery disease by measuring blood flow, plaque deformation, and pulse wave velocity [1,2,3,4]. To realize this, the next generation of ultrasound probes require matrix transducer arrays with thousands of elements to cover a sufficiently large aperture (>400 mm^2). It is possible to build a matrix array with such a high number of elements, but making electrical connections to all the elements is highly challenging since conventional imaging systems have a limited number of channels.

This issue can be addressed by integrating application-specific integrated circuits (ASICs) into the probe to reduce the number of electrical connections via cables to the imaging system. Various approaches to interface such large-aperture matrix transducer arrays using a reduced number of cables have been reported, such as receive sub-array beamforming [5,6,7,8], programmable high-voltage (HV) pulsers [9,10,11,12,13,14], switch matrices [15,16], row-by-row scanning schemes [12,14], and row- or column-parallel connection schemes [13].

We previously reported a first-generation transceiver ASIC with a row-level architecture for both receive (RX) and transmit (TX) channels [17]. This ASIC consists of 24 × 40 element-level HV switches and control logic that allows selected transducer elements in each row to be connected to a TX and RX channel of an imaging system. The element-level circuits are laid out in a pitch-matched fashion and connect directly via bondpads to transducer elements stacked on top of the chip. Although the functionality of this ASIC has been successfully demonstrated in a 3D imaging experiment, noticeable imaging artifacts associated with parasitic transmissions generated by HV switch actuation at the TX to RX transition and vice versa were found. In particular, thousands of switches actuate simultaneously in a full-aperture selection for plane wave transmission, making this problem more serious. The parasitic transmissions originate from non-idealities of the HV MOSFETs in the switch circuits, i.e., clock feedthrough and charge injection, generating switching transients on the transducer elements.

Charge injection and clock feedthrough in low-voltage analog complementary metal–oxide–semiconductor (CMOS) circuits have been discussed extensively in the literature [18], and several techniques to cancel their effects have been reported, such as dummy transistor compensation [19,20] and differential clock feedthrough attenuation [21]. However, these techniques are not directly applicable in this design because the HV laterally diffused metal oxide semiconductor (LDMOS) transistors used for HV switches are much larger than low-voltage transistors. As a result, these solutions, which rely on additional transistors, would make die area occupied by the element-level switch circuit too large in comparison to the size of the transducer elements. Recently, one approach, linearized control of the gate voltage of a HV MOSFET, has been reported to address this issue in an ASIC design with large aperture transducer arrays for ultrasound imaging applications [22].

In this work, as an alternative, we propose a second-generation transceiver ASIC focusing on minimizing the effects due to non-idealities of the HV MOSFETs, the root cause of the mentioned imaging artifacts. To achieve this, we propose a new HV switch controller that generates control signals for the HV switches with improved

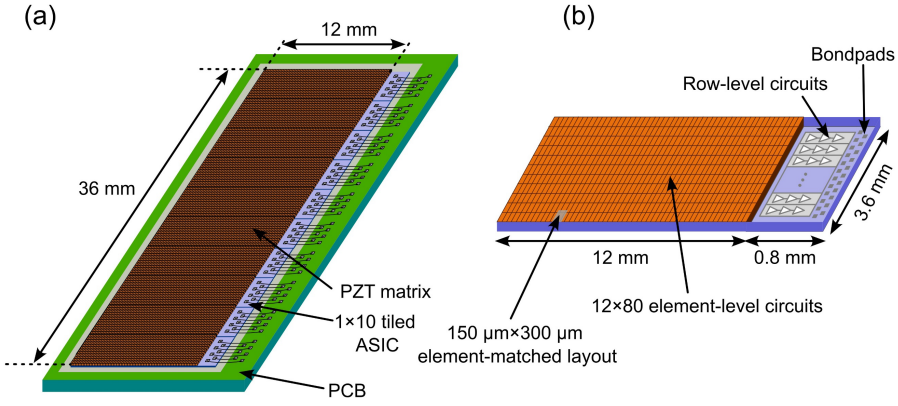

Figure 6.1: (a) Overview of the proposed matrix transducer on tiled application-specific integrated circuits (ASICs). (b) Overview of a single tile consisting of 12 × 80 transducer elements on top of an ASIC with 12 × 80 element-level switches and row-level circuits.

timing to alleviate the effects of their non-idealities. In this design, a current discharging path from the transducer element to the ground is created at the TX and RX switching moments. Consequently, this leads to significantly reduced peak-to-peak amplitudes of the switching transients.

6.2. MATERIALS AND METHODS

6.2.1. SYSTEM OVERVIEW

The size of the matrix transducer to cover an aperture sufficiently large enough for carotid artery imaging is 36 × 12 mm^2. To facilitate the realization of a full-sized array, we designed the second-generation ASIC via a MLM (multi-layer mask) full-wafer fabrication process. Compared to our previous work [17], the row pitch was increased from 150 to 300 µm while keeping the center frequency as it was. Thus, the number of rows in the ASIC was reduced from 24 to 12 so that the density of the wire bonds that electrically connect the ASIC to a printed circuit board (PCB) was also significantly reduced. This modification of physical dimensions enabled us to wire bond more reliably, which is one of the main challenges of the first-generation ASIC. On the other hand, the number of columns per ASIC increased from 40 to 80, which allowed us to implement the targeted aperture by tiling 1 × 10 ASICs, as shown in Figure 6.1(a). This increased number of columns provided an important additional advantage compared to the previous work with 2 × 10 ASICs tiled, since wire-bond connections only have to be made on one side of the tiled array.

As shown in Figure 6.1(b), each of the ASICs had a die size of 3.6 × 12.8 mm^2, and interfaced with an array of 12 × 80 (rows × columns) transducer elements through element-level and row-level circuits. Each pitch-matched element-level circuit was connected to the corresponding transducer element via a bondpad.

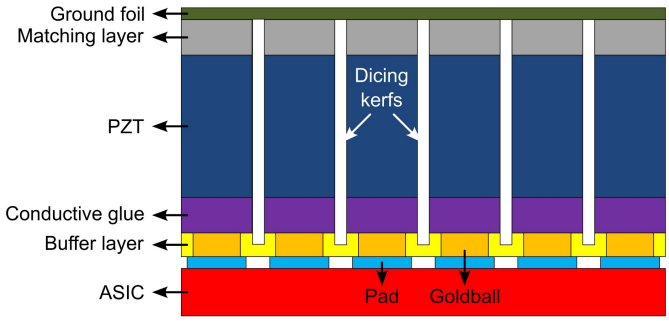

Figure 6.2: Cross-sectional view of the transducer array mounted on top of the ASIC.

Bondpads on the periphery of each ASIC were arranged in two columns. The inner column connected row-level TX and RX signals to an imaging system. Bondpads of the outer column made connections for digital control signals as well as analog and digital power supplies.

In the same way as the first-generation ASIC, the piezoelectric layer (PZT)-on-CMOS integration scheme illustrated in Figure 6.2 [23] was adopted to build the transducer array on top of the ASICs. To electrically connect the circuitry on the ASIC to the transducer elements, we formed gold bumps on top of the ASIC bondpads using a wire-bonding tool. This was done in a matrix pattern with the same pitch as the transducer array. A nonconductive epoxy buffer layer was then deposited, filling the gaps between the gold. After this, the buffer layer was ground down to expose the gold, thus providing reliable electrical contacts for the transducer elements. On top of the epoxy layer, the acoustic stack consisting of a PZT and a matching layer was constructed. The conductive glue layer created the electrical connection between contacts and the electrode on the back-side of the piezoelectric ceramic. After that, the stack was diced into the desired 150 × 300 µm pitch array pattern using a diamond saw. The dicing kerfs were air-filled to minimize the crosstalk between elements. Finally, the array was covered with an aluminum foil that formed the elements' common ground electrode.

6.2.2. ASIC ARCHITECTURE

Figure 6.3 shows the top-level architecture of the second-generation ASIC. The 80 elements in each row of the matrix shared a row-level RX and TX bus to reduce channel count by a factor of 80. Even with 1 × 10 tiled ASICs, the total number of RX and TX channels was 240, which could be managed by an imaging system. Each transducer element was connected to the RX bus or the TX bus through a programmable element-level circuit. The RX bus was associated with a shared row-level circuit, which amplified the received echo signals, filtered out-of-band noise, and drove the connection to the imaging system.

Ahead of starting successive transmit/receive cycles, we needed to program the ASIC. Row-level logic was used to select one of the various element-selection modes

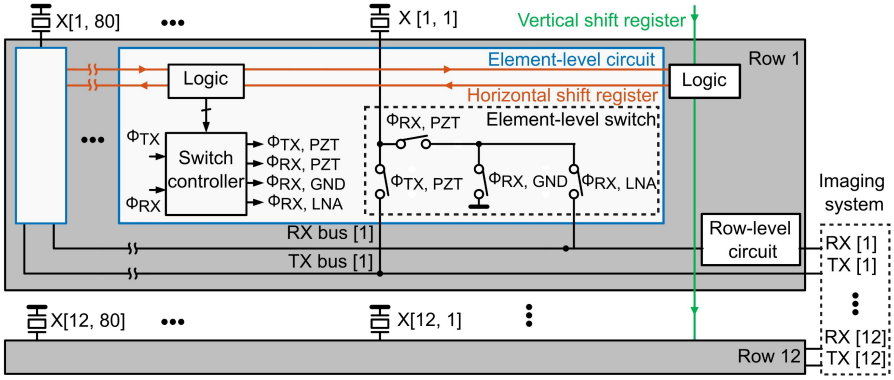

Figure 6.3: Block diagram of the second-generation ASIC.

supported by the ASIC to implement a specific imaging scheme and set the gain of the row-level circuit. This logic was programmed through a vertical shift registers (VSR) that was loaded during the programming phase. Each element was associated with logic allowing us to change rapidly between transmit/receive cycles the selection of active elements for a specific transmit and/or receive cycle. This element-level logic was pre-loaded through a horizontal shift register (HSR) during the programming phase. The switch controller received low-voltage digital signals (Φ_{TX} and Φ_{RX}) from a field-programmable gain array (FPGA) and generated 5-V control signals ($\Phi_{TX,PZT}$, $\Phi_{RX,PZT}$, $\Phi_{RX,GND}$, and $\Phi_{RX,LNA}$), according to the pre-loaded data, to drive the element-level switch circuit. In this design, the switch controller was implemented using a non-overlapping clock generator to minimize the non-idealities of HV devices introduced above in the switch circuit.

6.2.3. ELEMENT-LEVEL SWITCH CIRCUIT AND NON-IDEALITIES

Figure 6.4 shows the circuit diagram of the element-level switches implemented in the first-generation ASIC. The HV switches were needed to enable HV pulse transmission while keeping a more compact implementation and less power consumption. The control signals were generated by simple combinational logic from the TX/RX phases (Φ_{TX} and Φ_{RX}) and three enable bits (ELE_EN[i, j], TX_EN[i, j], and RX_EN[i, j]), which were pre-loaded via the HSR in the programming phase. The ELE_EN bit determined whether an element was enabled (high) or disabled (low). If a certain element was disabled, it was excluded from participating in imaging and connected to the ground via transistors M5 and M6. This helped to prevent the signal of disabled elements from coupling to the RX bus and capacitive coupling from the TX bus to the disabled elements in the TX phase Φ_{TX}. For the enabled elements, the remaining two bits, TX_EN and RX_EN, determined whether they participate in transmission and/or reception.

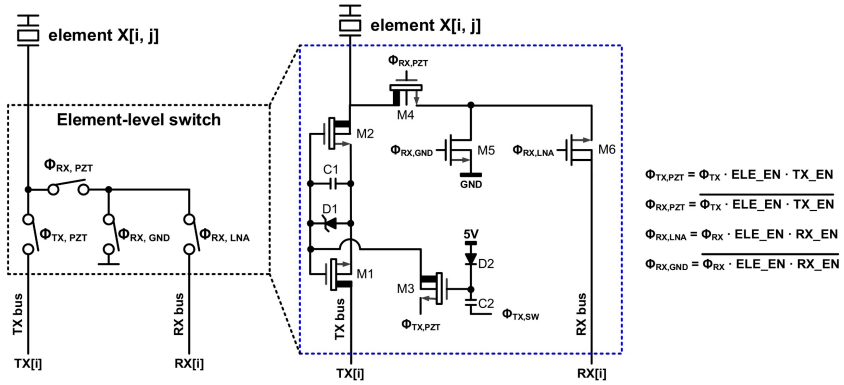

Figure 6.4: Simplified circuit diagram of the element-level switch and the combinational logic equation, implemented as the switch controller, proposed in [17].

During the TX phase Φ_{TX}, the row-level TX bus, TX[i] was connected to the element if ELE_EN[i, j] and TX_EN[i, j] were high. Two back-to-back n-type HV LDMOS transistors (M1 and M2), driven by $\Phi_{TX,\,PZT}$, allowed an external imaging system to send a unipolar pulse with a peak value up to 65 V. To turn on M1 and M2, we charged a bootstrap capacitor C1 connected between their source and gate through M3 by making $\Phi_{TX,SW}$ high at the beginning of Φ_{TX}. Soon after that, $\Phi_{TX,SW}$ went low to turn off M3, keeping M1 and M2 on and allowing them to swing up with the transmit HV pulses on the TX bus. To provide a sufficiently high gate voltage to turn on M1 and M2, we gave the bootstrap capacitor C1 a relatively large value of 7.2 pF in this design. At the end of Φ_{TX}, C1 was discharged by pulling down the source of M3 so that M1 and M2 were turned off. During the RX phase Φ_{RX}, transistors M4 and M6 connected the element to the RX bus if ELE_EN[i, j] and RX_EN[i, j] were high.

As described earlier, an important consideration in this design is minimizing the impact of non-idealities, clock feedthrough, and charge injection of the HV switches, which generate switching glitches on the transducer element at the TX to RX transition and vice versa. This problem eventually leads to visible imaging artifacts. Figure 6.5(a) shows simulated waveforms of the control signals driving the element-level switch transistors. Even without a transmitted pulse, noticeable switching glitches appear on the element, as shown in Figure 6.5(b). The peak amplitudes of these undesired glitches at the RX to TX transition and vice versa were 2.19 V and −0.64 V, respectively. This amplitude, in the volt range, led to visible imaging artifacts, even when applying a high-voltage transmit pulse with an amplitude of tens of volts.

6.2.4. PROPOSED SWITCH CONTROLLER

To minimize the switching transients discussed in the previous section, we proposed a new timing diagram, shown in Figure 6.6(a), of the switch control signals. At the transition from RX to TX, the RX bus was first disconnected from the element by

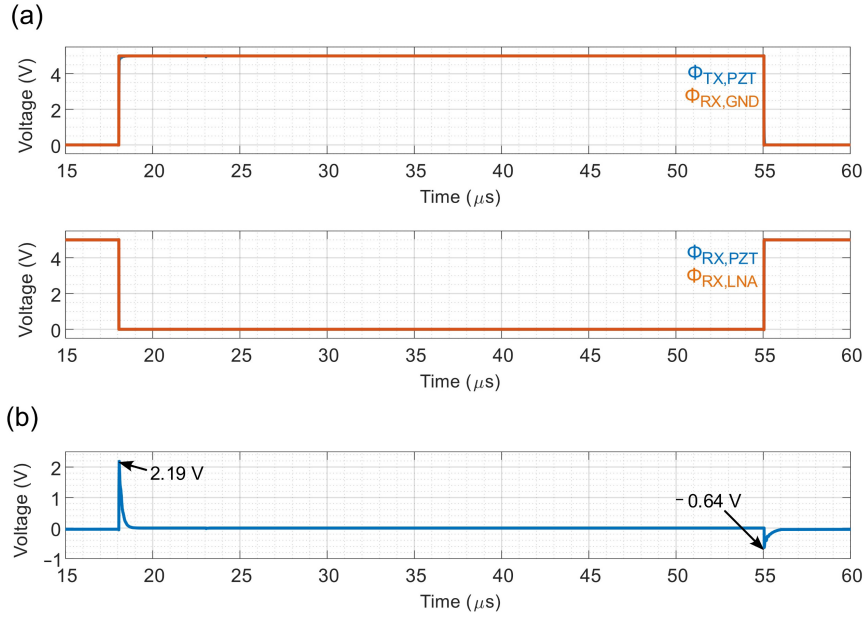

Figure 6.5: Simulated waveforms of the element-level circuit implemented in the first-generation ASIC. (a) Control signals driving the element-level switch circuit. (b) Switching transients on the transducer element.

making $\Phi_{RX,\,LNA}$ low while $\Phi_{RX,\,PZT}$ remained high. Subsequently, M5 was turned on by making $\Phi_{RX,\,GND}$ high; thus, a low-impedance discharging path from the element to the ground was created before actuating M1 and M2 associated with the HV TX switch. Thus, when $\Phi_{TX,\,PZT}$ was made high, the clock feedthrough-induced current could flow to the ground through transistor M5 instead of to the element. Finally, when $\Phi_{RX,\,PZT}$ was made low, the charge injection error from M4 could be absorbed to both ground and the low-impedance output of the pulser. This switching sequence reduced the peak amplitude of the switching transients significantly at the transition of RX to TX. Although M6, a 5 V device, was switching without a discharging path to the ground, the associated transient was not critical because M6 was much smaller than the high-voltage devices.

Conversely, at the transition of TX to RX, transistor M4 was activated first to create a discharging path again from the element to the ground. At the transition of $\Phi_{TX,\,PZT}$, a significant error could be generated due to charge injection related to M1 and M2. However, the resulting voltage transient on the element was minimized because the associated charge could flow via M4 and M5 to the ground.

Figure 6.6(b) shows the switch controller's design with cascaded non-overlapping clock generators to generate the control signals presented in Figure 6.6(a). Each stage employed delay unit cells in which metal–oxide–semiconductor (MOS) capacitors were used to make sufficient delay (>100 ns) between the signals.

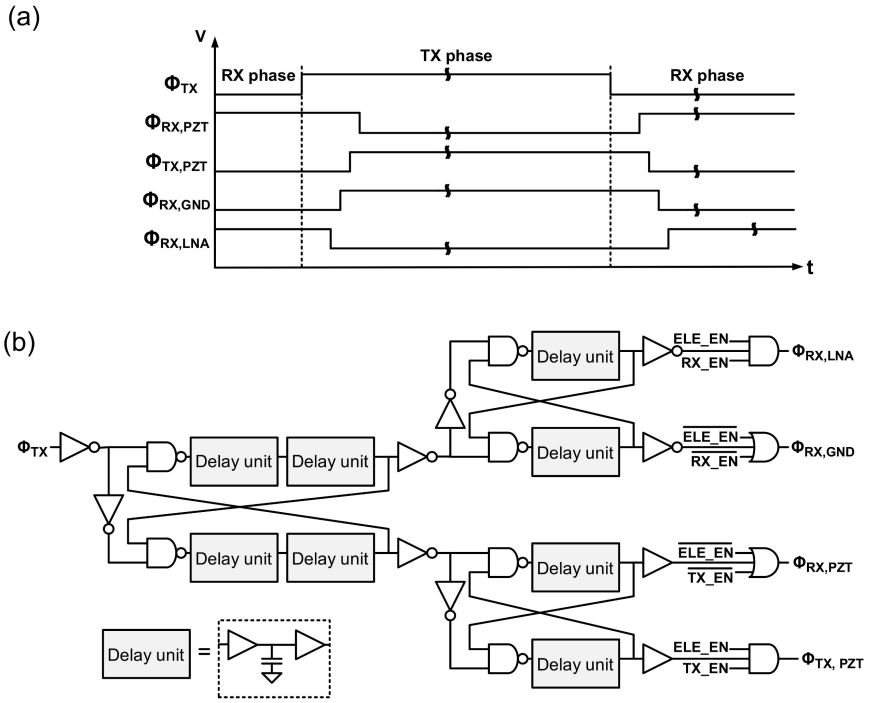

Figure 6.6: (a) The proposed timing diagram of the control signals to minimize the switching transients and (b) implementation of the switch controller to generate such signals.

6.2.5. VALIDATION IN SIMULATION

The proposed switch controller was simulated to validate the reduction of the switching transients. Figure 6.7 shows the simulation results of the control signals generated by the controller, the voltage on the element, and the current flowing through M5 in Figure 6.4 at the switching moments for the TX to RX transition and vice versa. Figure 6.7(a) shows the transition of the signals at the switching moment from RX to TX, with the peak-to-peak amplitude of switching transients being 139.2 mV, as shown in Figure 6.7(b). Figure 6.7(c) shows that the current flows through M5 at the switching moments of high-voltage transistors M1, M2, and M4, resulting in the reduction of the switching transients. Figure 6.7(d) shows waveforms of the control signals at the transition from TX to RX, with the peak-to-peak amplitude being 207.3 mV, as shown in Figure 6.7(e). In particular, the largest peak value of −118.8 mV, associated with the falling edge of $\Phi_{TX,\,PZT}$, was caused by the charge injection effect of M1 and M2. This amplitude was significantly reduced because the charge-injection-induced current was also absorbed into the ground via M5, as is confirmed in Figure 6.7(f). Consequently, compared to 2.19 V in the first-generation

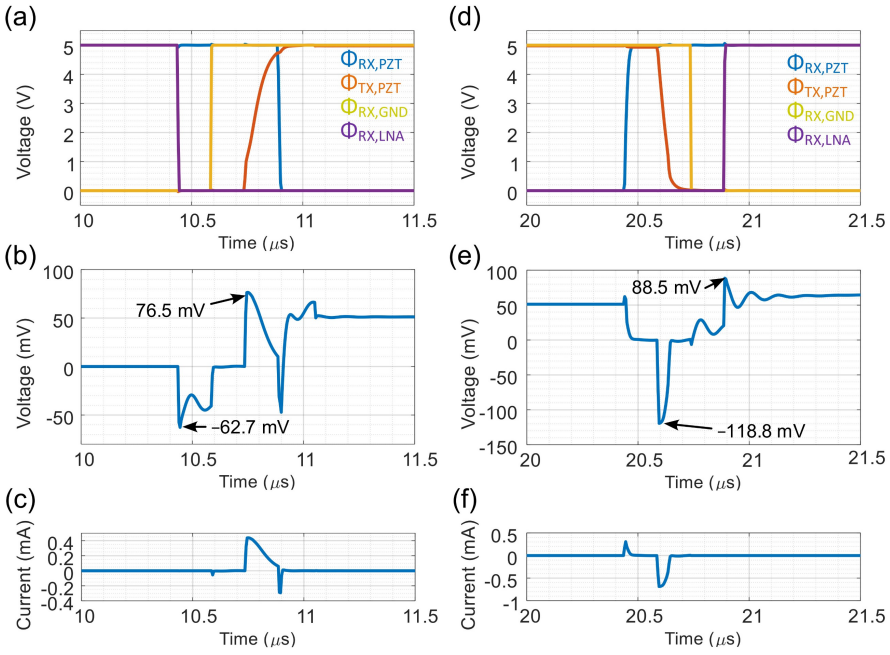

Figure 6.7: Simulated waveforms with the proposed switch controller at the transition of RX to TX (a–c) and vice versa (d–f). (a,d) Control signals driving the element-level switch circuit, (b,e) the switching transients on the transducer element, and (c,f) the drain current flowing via M5.

ASIC simulation, the peak-to-peak amplitude of the switching transients with the newly designed switch controller was reduced by around 20 dB.

6.3. RESULTS AND DISCUSSION

6.3.1. EXPERIMENTAL PROTOTYPE

The ASIC was fabricated in a 0.18-µm HVBCD process. Figure 6.8(a) and Figure 6.8(b) show a photograph of a bare die and a plot of the layout of the element-level TX and RX circuits, respectively. The area of the element-level circuit was matched to the 150 × 300 µm^2 transducer element size. In the prototype shown in Figure 6.8(c), four ASICs were mounted on a test PCB and wire-bonded for RX and TX channels as well as for power and control signals. A piezo-electric transducer array was built on top of the ASICs using the process described in [23]. The prototype was covered by a ground foil, the common ground electrode of the transducer elements, and by a moisture protection layer.

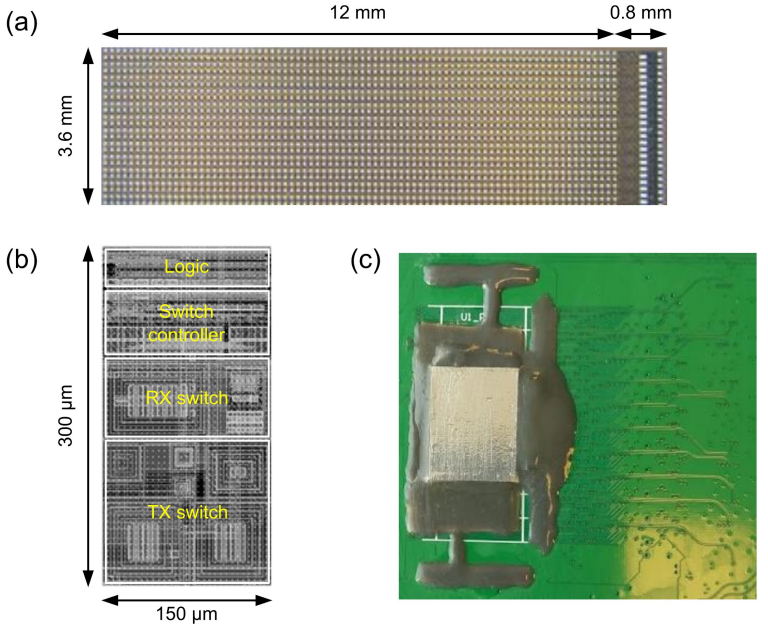

Figure 6.8: (a) Chip photograph of the ASIC. (b) Layout of the pitch-matched element-level circuit. (c) Test printed circuit board (PCB) with transducer array on top of the ASICs.

6.3.2. ELECTRICAL VERIFICATION

In the electrical characterization, an ASIC die without a transducer array was used, on which selected transducer pads were wire-bonded to the test board to observe the switching transients. Without applying a high-voltage TX pulse, residual switching transients were visible, as shown in Figure 6.9. Their peak-to-peak amplitudes at the TX to RX transition and vice versa were 100 mV_{PP} and 30 mV_{PP}, respectively. Compared to the simulation results with the first-generation ASIC shown in Figure 6.5, the peak-to-peak values were reduced by factors of 6 and 70. Compared to the simulation results shown in Figure 6.7, the measured peak-to-peak amplitudes were a factor of 2 and 5 lower. This was likely due to the effects of the wire-bonded connection, the bondpad on the PCB, and the probe capacitance in the test setup, which resulted in a higher capacitance, and hence a smaller transient voltage than in the simulation. Taking this loading effect into account, the results were consistent with the expected reduction of 20 dB derived earlier.

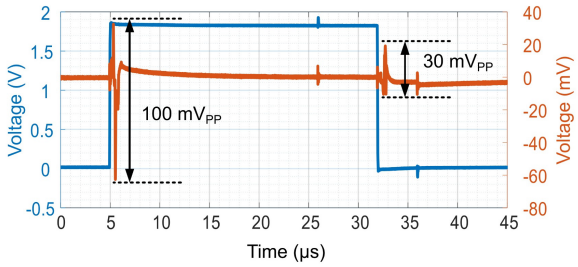

Figure 6.9: Measured waveforms of the RX phase (blue) and the switching transient observed on the element X [6, 41] (orange).

6.3.3. IMPROVEMENT IN CLOCK FEEDTHROUGH AND CHARGE INJECTION-INDUCED IMAGING ARTIFACT

The test-bench for acoustic experiments to validate the reduced switching artifacts is shown in Figure 6.10. A Verasonics V1 imaging system (Verasonics, Kirkland, WA, USA) was used to generate the HV TX signals. To interface the TX and RX signals between the Verasonics and the test PCB, we designed a motherboard PCB. On the transmit paths, a matching circuit was implemented to guarantee a unipolar excitation pulse. The received signals were buffered with unity-gain operational amplifiers on the motherboard before being fed into the Verasonics. The motherboard also included low-dropout regulators (LDOs) to generate supply voltages for analog, digital, and 5 V circuitry. Moreover, the board contained digital buffers to transfer the signals from the field-programmable gate array (FPGA) board. These digital signals consisted of clock and data for programming the ASICs and their control signals.

Pulse-echo measurements were performed to obtain imaging results using a quartz plate as a reflector located at a depth of 13 mm. The TX signal was a unipolar half-cycle 7.5 MHz pulse with a peak value of 1 V. All elements were enabled to send a plane wave on the full-aperture in TX, and echo signals were received in a column-by-column fashion. The reason for using a relatively small 1 V pulse was to better bring out the switching artifacts compared to the 60 V pulse used in normal operation. To record the switching glitches at the transitions of both TX to RX and vice versa, we applied two successive RX phases, as shown in Figure 6.11. During the first RX phase, the echo signal from the transmitted 1 V pulse and the switching transients from the first transition from TX to RX (the first rising edge) can be recorded. In the second cycle, the switching transients from the first transition from RX to TX (the first falling edge) and from the second transition from TX to RX (the second rising edge) were recorded.

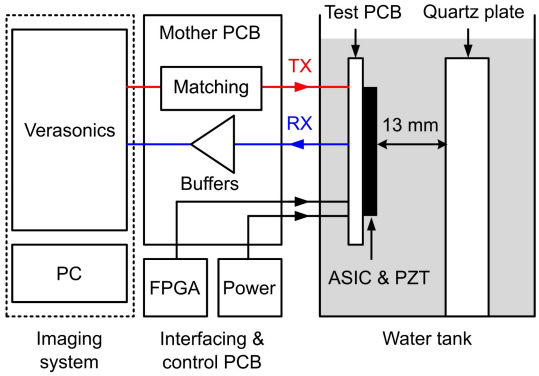

Figure 6.10: Overview of the measurement setup used for demonstrating the effect of the switching transients for the first- and the second-generation ASICs.

Figure 6.12 demonstrates how the switching transients affected the image and how much imaging artifacts were improved with the proposed switch controller circuit. Figure 6.12(a) and Figure 6.12(b) show the RF signal for a single channel captured by the Verasonics and the imaging result, respectively, with the first-generation ASIC. As can be seen in Figure 6.12(a), the peak-to-peak amplitude of the RX to TX switching transients located at a depth of 38 mm was considerably larger than the echo signal from the transmitted 1 V pulse. Even if the largest pulse amplitude supported by the ASIC of 65 V would be used, these switching transients would give significant artifacts in the image. On the other hand, the amplitude of the RX to TX switching transients was reduced by a factor of 20 dB in Figure 6.12(c) and Figure 6.12(d) for the second-generation ASIC. This reduced amplitude corresponded to a parasitic transmitted pulse with an amplitude of only 0.3 V. If the maximum pulse amplitude of 65 V were to be used, the echo signals from the switching would be 46.7 dB smaller than the echoes from the intended pulse, making their impact on the image much less significant. This result demonstrated that the switching artifact reduction scheme with the proposed switch controller improved image quality significantly.

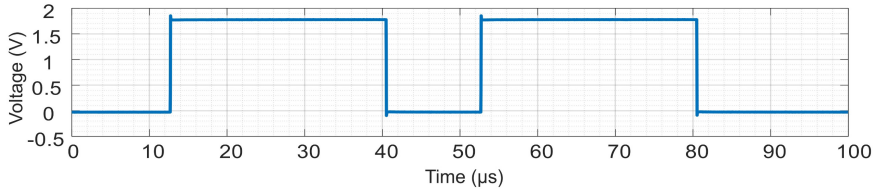

Figure 6.11: The waveform of the RX phase with two cycles used in the pulse-echo measurement to record the switching glitches at both TX to RX transition and vice versa.

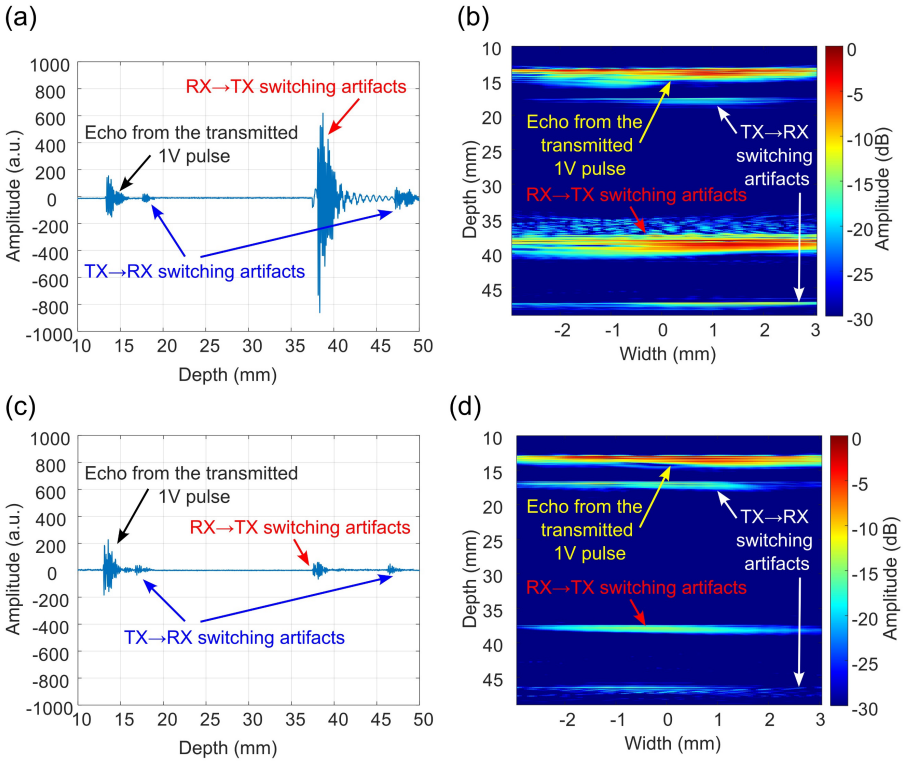

Figure 6.12: Comparison of switching transients for the first- and second-generation ASICs. (a) Time-domain plot of the received RX output data for a single channel and (b) B-Mode imaging result with the first-generation ASIC. (c) Time-domain plot for the second-generation ASIC with the same test conditions and (d) its imaging result.

6.4. CONCLUSIONS

We present an ultrasound transceiver ASIC design with a switching artifact reduction technique, designed for 3D volumetric imaging of the carotid artery. We have previously reported a first-generation ASIC design [17] that demonstrated the 3D imaging capability; however, we observed noticeable ghost echoes in the experiment. We have identified that this issue originates from clock feedthrough and charge injection of the HV MOSFETs in the element-level switch circuits, generating switching transients on the transducer elements that lead to parasitic pulse transmission. The improved switch controller proposed in this paper generates control signals of HV switches such that a discharge path to ground is created at the critical switching moments, strongly reducing the transients on the transducer

element. Measured results demonstrate a 20 dB reduction in imaging artifacts compared to our previous ASIC.

6.5. REFERENCES

[1] M. Couade *et al.*, "Ultrafast imaging of the arterial pulse wave," *IRBM*, vol. 32, no. 2, pp. 106–108, Apr. 2011, doi: 10.1016/j.irbm.2011.01.012.

[2] H. Hasegawa, K. Hongo, and H. Kanai, "Measurement of regional pulse wave velocity using very high frame rate ultrasound," *Journal of Medical Ultrasonics*, vol. 40, no. 2, pp. 91–98, 2013, doi: 10.1007/s10396-012-0400-9.

[3] P. Kruizinga *et al.*, "High-Definition Imaging of Carotid Artery Wall Dynamics," *Ultrasound Med Biol*, vol. 40, no. 10, pp. 2392–2403, Oct. 2014, doi: 10.1016/j.ultrasmedbio.2014.03.009.

[4] J. Provost *et al.*, "3D ultrafast ultrasound imaging in vivo," *Phys Med Biol*, vol. 59, no. 19, pp. L1–L13, 2014, doi: 10.1088/0031-9155/59/19/L1.

[5] B. Savord and R. Solomon, "Fully sampled matrix transducer for real time 3D ultrasonic imaging," in *IEEE Symposium on Ultrasonics, 2003*, IEEE, 2003, pp. 945–953. doi: 10.1109/ULTSYM.2003.1293556.

[6] C. Chen *et al.*, "A Front-End ASIC With Receive Sub-array Beamforming Integrated With a 32 × 32 PZT Matrix Transducer for 3-D Transesophageal Echocardiography," *IEEE J Solid-State Circuits*, vol. 52, no. 4, pp. 994–1006, Apr. 2017, doi: 10.1109/JSSC.2016.2638433.

[7] T. Kim, S. Shin, and S. Kim, "An 80.2 dB DR 23.25 mW/Channel 8-Channel Ultrasound Receiver With a Beamforming Embedded SAR ADC," *IEEE Transactions on Circuits and Systems II: Express Briefs*, vol. 66, no. 9, pp. 1487–1491, Sep. 2019, doi: 10.1109/TCSII.2018.2889810.

[8] Y. Igarashi *et al.*, "Single-Chip 3072-Element-Channel Transceiver/128-Subarray-Channel 2-D Array IC With Analog RX and All-Digital TX Beamformer for Echocardiography," *IEEE J Solid-State Circuits*, vol. 54, no. 9, pp. 2555–2567, Sep. 2019, doi: 10.1109/JSSC.2019.2921697.

[9] I. O. Wygant *et al.*, "An integrated circuit with transmit beamforming flip-chip bonded to a 2-D CMUT array for 3-D ultrasound imaging," *IEEE Trans Ultrason Ferroelectr Freq Control*, vol. 56, no. 10, pp. 2145–2156, Oct. 2009, doi: 10.1109/TUFFC.2009.1297.

[10] A. Bhuyan *et al.*, "Integrated Circuits for Volumetric Ultrasound Imaging With 2-D CMUT Arrays," *IEEE Trans Biomed Circuits Syst*, vol. 7, no. 6, pp. 796–804, Dec. 2013, doi: 10.1109/TBCAS.2014.2298197.

[11] K. Chen, H.-S. Lee, A. P. Chandrakasan, and C. G. Sodini, "Ultrasonic Imaging Transceiver Design for CMUT: A Three-Level 30-Vpp Pulse-Shaping Pulser With Improved Efficiency and a Noise-Optimized Receiver," *IEEE J Solid-State Circuits*, vol. 48, no. 11, pp. 2734–2745, Nov. 2013, doi: 10.1109/JSSC.2013.2274895.

[12] B. H. Kim, Y. Kim, S. Lee, K. Cho, and J. Song, "Design and test of a fully controllable 64×128 2-D CMUT array integrated with reconfigurable frontend ASICs for volumetric ultrasound imaging," *IEEE International Ultrasonics Symposium, IUS*, pp. 77–80, 2012, doi: 10.1109/ULTSYM.2012.0019.

[13] K. Chen, H. S. Lee, and C. G. Sodini, "A Column-Row-Parallel ASIC Architecture for 3-D Portable Medical Ultrasonic Imaging," *IEEE J Solid-State Circuits*, vol. 51, no. 3, pp. 738–751, Mar. 2016, doi: 10.1109/JSSC.2015.2505714.

[14] S.-J. Jung, J.-K. Song, and O.-K. Kwon, "Three-Side Buttable Integrated Ultrasound Chip With a 16 × 16 Reconfigurable Transceiver and Capacitive Micromachined Ultrasonic Transducer Array for 3-D Ultrasound Imaging Systems," *IEEE Trans Electron Devices*, vol. 60, no. 10, pp. 3562–3569, Oct. 2013, doi: 10.1109/TED.2013.2278441.

[15] S. Tamano, T. Kobayashi, S. Sano, K. Hara, J. Sakano, and T. Azuma, "3D ultrasound imaging system using fresnel ring array & high voltage multiplexer IC," in *IEEE Ultrasonics Symposium, 2004*, IEEE, 2004, pp. 782–785. doi: 10.1109/ULTSYM.2004.1417838.

[16] R. Fisher *et al.*, "Reconfigurable arrays for portable ultrasound," in *IEEE Ultrasonics Symposium, 2005.*, IEEE, 2005, pp. 495–499. doi: 10.1109/ULTSYM.2005.1602899.

[17] E. Kang *et al.*, "A reconfigurable ultrasound transceiver ASIC with 24 × 40 elements for 3-D carotid artery imaging," *IEEE J Solid-State Circuits*, vol. 53, no. 7, pp. 2065–2075, Jul. 2018, doi: 10.1109/JSSC.2018.2820156.

[18] C. C. Enz and G. C. Temes, "Circuit techniques for reducing the effects of op-amp imperfections: autozeroing, correlated double sampling, and chopper stabilization," *Proceedings of the IEEE*, vol. 84, no. 11, pp. 1584–1614, 1996, doi: 10.1109/5.542410.

[19] C. Eichenberger and W. Guggenbuhl, "Dummy transistor compensation of analog MOS switches," *IEEE J Solid-State Circuits*, vol. 24, no. 4, pp. 1143–1146, 1989, doi: 10.1109/4.34103.

[20] C. Eichenberger and W. Guggenbuhl, "On charge injection in analog MOS switches and dummy switch compensation techniques," *IEEE Trans Circuits Syst*, vol. 37, no. 2, pp. 256–264, 1990, doi: 10.1109/31.45719.

[21] Chung-Yu Wu, Chih-Cheng Chen, and Jyh-Jer Cho, "Precise CMOS current sample/hold circuits using differential clock feedthrough attenuation techniques," *IEEE J Solid-State Circuits*, vol. 30, no. 1, pp. 76–80, 1995, doi: 10.1109/4.350189.

[22] R. Wodnicki *et al.*, "Tiled Large Element 1.75D Aperture with Dual Array Modules by Adjacent Integration of PIN-PMN-PT Transducers and Custom High Voltage Switching ASICs," in *2019 IEEE International Ultrasonics Symposium (IUS)*, IEEE, Oct. 2019, pp. 1955–1958. doi: 10.1109/ULTSYM.2019.8925552.

[23] C. Chen *et al.*, "A prototype PZT matrix transducer with low-power integrated receive ASIC for 3-D transesophageal echocardiography," *IEEE Trans Ultrason Ferroelectr Freq Control*, vol. 63, no. 1, pp. 47–59, 2016, doi: 10.1109/TUFFC.2015.2496580.

7

A TILED ULTRASOUND MATRIX TRANSDUCER FOR VOLUMETRIC IMAGING OF THE CAROTID ARTERY[1]

[1] This chapter is based on the following publication:
dos Santos, D.S.; Fool, F.; Mozaffarzadeh, M.; Shabanimotlagh, M.; Noothout, E.; Kim, T.; Rozsa, N.; Vos, H.J.; Bosch, J.G.; Pertijs, M.A.P.; et al. A Tiled Ultrasound Matrix Transducer for Volumetric Imaging of the Carotid Artery. Sensors 2022, 22, 9799, doi:10.3390/s22249799.

7.1. INTRODUCTION

CAROTID arteries are major blood vessels located on both sides of the neck that supply the head and brain with oxygen and nutrients. Carotid artery disease, which is referred to as atherosclerosis or stenosis, occurs when fatty deposits (plaques) clog the carotid artery [1]. The blockage of the carotid arteries is a frequent source of stroke, a medical emergency that occurs when the blood supply to the brain is interrupted or seriously reduced [2]. Assessing the progression of atherosclerosis in the carotid artery is very useful for risk stratification, evaluation of patient response to medical interventions, evaluation of new risk factors, genetic research, and quantification of the effects of new therapies [3], [4]. The assessment of the carotid plaque state is commonly performed with ultrasound imaging for the purpose of medical diagnosis [5].

With conventional two-dimensional (2D) ultrasound imaging, the assessment of the plaque is based on multiple 2D images, which are mentally combined by the operator to form a subjective impression of the three-dimensional (3D) vessel structure. Using this approach, accurate assessment of the plaque progress is difficult and highly dependent on the skills and experience of the sonographer [6]. This requires the reproduction of the same imaging plane at later times, which is difficult and sometimes impossible due to the restrictions imposed by the patient's anatomy or position. Moreover, quantitative estimation of the plaque volume from a 2D ultrasound is based on measurements of height, width, and length in different orthogonal views for ideal shapes (e.g., ellipsoidal), which are prone to error [7]. A 3D ultrasound has the potential for accurate quantitative monitoring of the changes in plaque volume and might be vital for therapy assessment [2], [4], [8], [9]. In carotid artery diagnosis, measurement of blood flow and plaque surface motion are important parameters [10]. For accurate analysis of the dynamics of the blood flow, 3D vector velocities at a high frame rate are necessary. Two-dimensional methods do not provide a realistic picture of the actual flow and do not provide information about the out-of-plane velocity component [11]. Thus, these 3D phenomena can only be assessed correctly with high frame rate 3D ultrasound imaging.

Going from 2D to 3D high-frame-rate ultrasound imaging is challenging. While mechanically swept or free-hand scanning techniques using a linear (i.e., one-dimensional) transducer array might suffice for low-frame rate applications, a 2D matrix transducer array is necessary for high-frame-rate applications [7]. This matrix transducer should cover a sufficiently large aperture (>400 mm^2) and its element pitch should preferably be smaller than half of the wavelength (λ) in both directions to avoid grating lobes. The combination of small elements and a large aperture results in a very large number of transducer elements (in the order of thousands) [12]–[14]. It is possible to build a matrix array with such a vast number of elements, but making electrical connections to all the elements is a great challenge [15]. Various techniques have been proposed to reduce the complexity of fully populated matrix arrays, such as sparse matrix arrays and row-column addressed matrix arrays. Sparse arrays can effectively reduce channel count and electronic complexity, and can perform high-frame rate volumetric imaging [16]–[19]. However, this type of array has two fundamental limitations, which are the lower signal-to-noise ratio (SNR) and higher clutter levels [20]–[22]. Row-column

addressed arrays, on the other hand, can reduce the number of connections from N^2 to $2N$ in a matrix array consisting of N × N elements [23]–[25]. However, the inherent drawbacks of this transducer are the more complex read-out sequences and the lower frame rate, which is limited due to switching [21].

As an alternative, application-specific integrated circuits (ASICs) can be directly integrated with the matrix array to reduce the number of electrical connections, allowing large-element-count transducers to be used with traditional 128- to 256-channel systems and probe cables [26], [27]. With this approach, the channel reduction can be done in multiple ways depending on the intended application, for example by channel multiplexing, sub-aperture beamforming, in-probe-digitization, or time-division multiplexing [28]–[30]. Besides channel reduction, an ASIC can also perform amplification of the received signals to prevent attenuation due to the loading of the cables connecting the ASIC to the imaging system [31], [32]. These advantages make matrix arrays with in-probe electronics an attractive technology for 3D high-frame rate ultrasound imaging, although this comes at the cost of a more complex and costly developing process. Examples of commercially available matrix array probes with a large element count and integrated ASIC include the xMATRIX technology from Philips [33], the iQ+ technology from Butterfly [34], [35], and the 4G CMUT technology from Fujifilm [36].

We have previously presented a first-generation matrix transducer array made of lead zirconate titanate (PZT), designed for high-frame rate, 3D imaging of the carotid arteries that was built directly on top of an ASIC [14], [31]. Since building one single ASIC large enough to cover the carotid bifurcation is very challenging and expensive, we opted for a tiling approach in which multiple small identical ASICs were tiled together in both the lateral and elevation direction to form a larger array. A single ASIC contained 24 × 40 element-level circuits that consisted of transmit (TX) switches, receive (RX) switches, and control logic. The ASIC architecture could accommodate nine arbitrary TX/RX patterns in the provided memories. The architecture allowed the matrix to operate like an electronically translatable array and we have previously shown how to achieve a high frame rate with such a transducer [37]. The layout of element-level circuits was matched to the element pitch of the matrix array, which was 150 μm in both directions. By using 10 × 2 tiled ASICs, a probe with an aperture of 36 mm × 12 mm consisting of 19,200 elements (240 rows and 80 columns) could be constructed; however, at that time, we only presented a 4 × 2 tiled design, which was too small for carotid artery imaging. Although the functionality of this matrix transducer was successfully demonstrated in a 3D imaging experiment [14], the probe had limitations in terms of transmit voltage, cable count, and the number of pre-programmed patterns, which needed to be tackled in the next generation of the probe.

In the second generation of the transducer, presented in this paper, we have developed a prototype to resolve the limitations present in the previous design. The new version contains 12 × 80 elements per ASIC that interface with a PZT matrix array of 300 μm × 150 μm. Due to this, we only need to tile the ASICs in one direction instead of two directions, which makes the alignment during manufacturing much easier. In addition, the larger pitch overcomes electronics space limitations in the pitch-matched configuration, which allows increasing the TX pulse voltage from 30 V to 65 V. Additionally, the number of pre-programmed arbitrary patterns is

increased to 20. Finally, undesired transmit signals that originated from the TX-to-RX mode switching (and vice versa) are significantly reduced in the new version of the ASIC [15].

This paper describes the development of the prototype tiled matrix transducer that is based on the second-generation ASIC described above. The goal of this work is to demonstrate the feasibility of using the tiling approach to build a sufficiently large aperture, and to evaluate the potential of using the prototype for 3D imaging of the carotid artery. In so doing, we will discuss the design, fabrication process, and extensive characterization of the transducer that was targeted to have 7680 piezo elements built on top of 8 × 1 tiled ASICs. We also performed volumetric imaging of a wire phantom to demonstrate the imaging capabilities of the prototype.

7.2. MATERIALS AND METHODS

7.2.1. DESIGN CHOICES

Volumetric imaging currently cannot attain the same frame rate, resolution, and image quality as in 2D, at least not all at the same time. The main issue is that with a large fully populated matrix array there are too many elements to control and read out at once. Therefore, trade-offs exist between frame rate, resolution, and image quality, which are different for the various types of matrix arrays discussed in the introduction. We have opted to use an ASIC to have a large field of view while still maintaining high frame rates. In this section, we discuss our design choices.

The matrix transducer is designed for imaging of the carotid bifurcation. We have chosen a center frequency of 7.5 MHz as this is recommended for carotid imaging applications [38]. For the aperture size, we aimed at about 40 mm × 15 mm as the carotid bifurcation is easily accessible and therefore allows for larger apertures. However, manufacturing such a large ASIC in one piece would be very expensive [39]. Thus, we opted to employ a tiled approach where we place multiple smaller and identical ASICs next to each other to create a larger aperture. The final aperture will be 36 mm × 12 mm, which consists of an array of 10 × 1 tiled ASICs of 3.6 mm × 12 mm each. A schematic drawing is shown in Figure 7.1.

A large aperture requires a large number of elements, but the number of available channels on an ultrasound system is limited. Research scanners like the ULA-OP [40] and the Verasonics Vantage [41] nowadays contain up to 256 channels. Our ASIC design requires separated TX and RX channels; therefore, we opted to limit ourselves to 128 transmit and 128 receive channels. However, since filling the total aperture with square elements with a pitch of 0.5 λ would require over 40,000 elements, and thus, over 40,000 channels, a significant degree of channel reduction is required.

As we are using ASICs, there are various ways to reduce the channel count. In our design, we make use of the fact that the fastest flow velocities in the carotid bifurcation are achieved along the long axis of the vessel, corresponding to the long side of the probe aperture (y-direction in Figure 7.1) and that the velocities in the direction of the short side (x-direction) are in comparison much slower. We can therefore use an asymmetric design where each row of the probe has a single

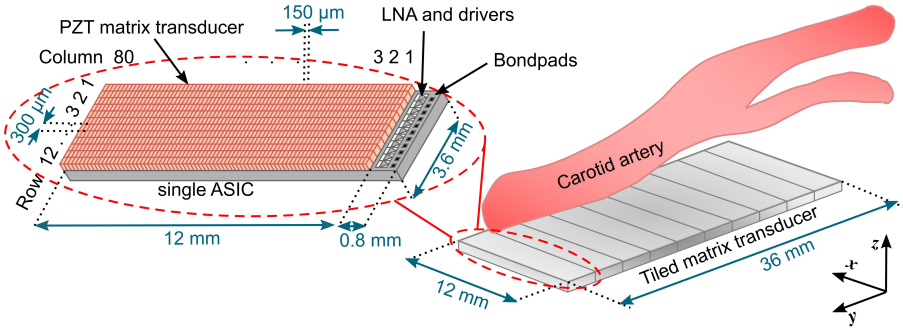

Figure 7.1: Schematic drawing of the envisioned full matrix transducer (right), together with a single ASIC transducer with PZT elements mounted on top (left).

transmit and receive channel and the columns can be enabled or disabled at will. This design represents an electronically translatable 1D array (translatable in the *x*-direction). Using this approach, assuming a pitch of 0.5 λ, the channel count could be reduced to 360 transmit and 360 receive channels, which would still be too high for contemporary research scanners. A way to further reduce the channel count is by increasing the element pitch in the *y*-direction to 300 µm, which corresponds to 1.5 λ. Such a large pitch can result in grating lobes and limited steering capability, yet it could be acceptable as we have chosen to make the aperture very large, and therefore high steering angles are not necessary. Another downside of having larger PZT elements is that they will not vibrate like a piston because the element width is much larger than 1.5 λ [42]. Instead, unwanted vibration modes will be generated, which significantly reduce the efficiency of the transducer [42], [43]. Fortunately, the performance of elements having a width greater than 0.7 λ can be improved by subdicing the elements, as we have previously investigated through simulations [43] and experiments [44]. With the proposed pitch of 300 µm in the *y*-direction, only 120 TX and 120 RX channels are necessary, which satisfies our requirements.

7.2.2. IMAGING SCHEME

Each imaging modality requires a different trade-off between spatial and temporal resolution: conventional B-mode requires the highest spatial resolution possible, Doppler imaging needs the best temporal resolution [25], [45], and pulse wave imaging (i.e., wall motion imaging during the pulse wave in the blood vessels) requires a bit of both [3]. The designed ASIC allows for an arbitrary element group selection and thus supports different element configurations for different imaging purposes [31]. A few examples are outlined in Figure 7.2. For high-resolution B-mode imaging, the whole aperture can be used for transmission, while reception can take place column by column. For high-frame rate flow imaging, the transducer can operate like an electronically translatable fully addressable 1D array where a subset of the columns is used in transmit and receive, and these columns are translated

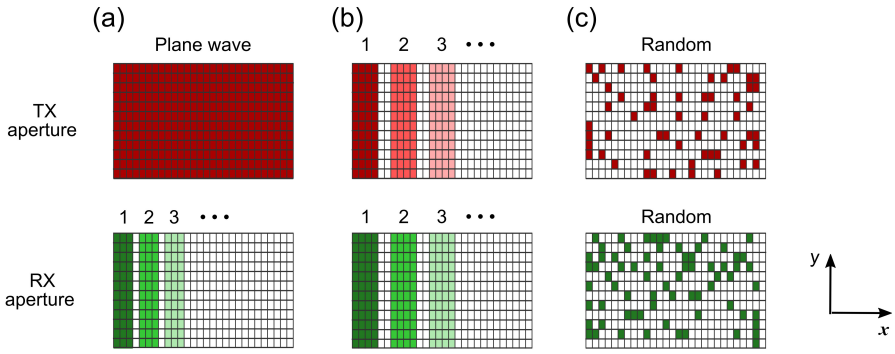

Figure 7.2: Example imaging schemes determined by different transmit and receive element configurations. (a) Plane-wave imaging. (b) Dynamic linear array. (c) Random pattern imaging.

between each TX/RX event. For other purposes, specific patterns or even pseudo-random selection are possible [31], [46].

7.2.3. ASIC DESIGN AND IMPLEMENTATION

7

Figure 7.3 shows the top-level architecture of the second-generation ASIC. Each row of the matrix has 80 elements that share row-level TX and RX buses to reduce the channel count by a factor of 80. Each transducer element has a programmable switching circuit that allows the element to be connected to the TX bus, the RX bus, both TX and RX buses (i.e., pulse-echo operation), or to the ground (i.e., disabled). The element-level circuitry fits in the 300 µm × 150 µm area occupied by the transducer element, allowing the PZT matrix to be integrated directly on top of the ASIC.

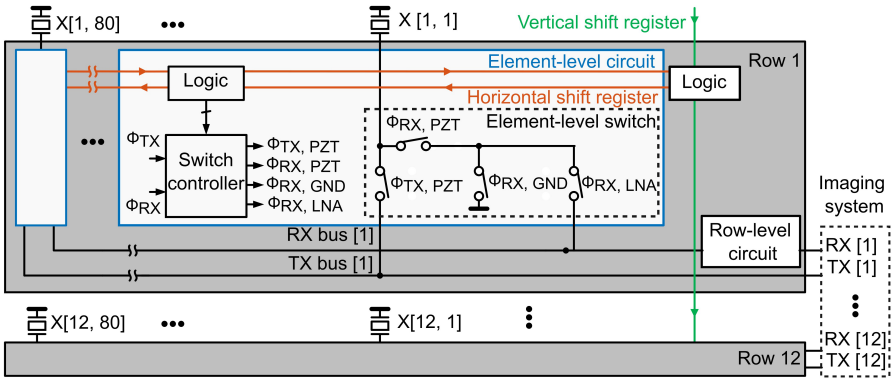

Figure 7.3: Block diagram of the architecture of a single ASIC.

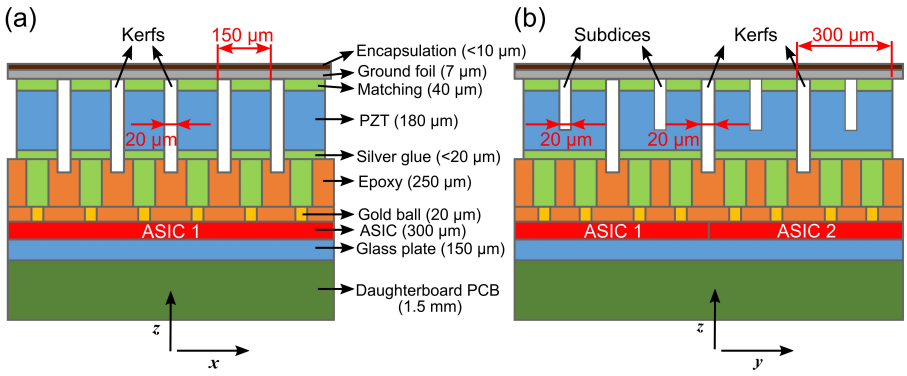

Figure 7.4: Overview of the acoustic stack (not drawn to scale). (a) Front view. (b) Side view. The numbers in parenthesis indicate the dimension in the z-direction (i.e., thickness).

Each RX bus is associated with a shared row-level circuit consisting of a low-noise amplifier (LNA), a programmable gain amplifier (PGA), and a cable driver, which connects the output signal to a receive channel of the imaging system. The various combinations of LNA/PGA gain settings allow the achievement of a programmable gain ranging from −8.6 dB to 32.7 dB with an average step of 2.75 dB. The gain can be changed during the receive phase to make sure the signal level stays within the dynamic range of the ASIC. Each TX bus receives an externally generated high voltage transmit unipolar pulse with an amplitude of tens of volts. The control logic, which is programmed through horizontal and vertical shift registers, determines whether an element participates in a given TX/RX cycle; selects the element configuration for a specific imaging scheme; and sets the gain of the row-level circuit. More details about the current ASIC design can be found in our previous publication [15].

7.2.4. ACOUSTIC STACK DESIGN AND FABRICATION

7.2.4.1. STACK DESIGN

Our stack design was similar to what we have used previously for matrix transducers in our lab [3], [14], [31], [37], [47] and consisted of a PZT array built on top of an ASIC, a single matching layer, an aluminum ground foil, and a top protective layer. At the bottom of the PZT, there was a buffer layer that allowed for tolerances in dicing depths and electrically isolated neighboring elements. A major issue in the previous designs was the fact that the acoustic stack was mounted only through thin layers on top of the ASIC. This made fabrication easier, but due to the lack of damping between the PZT and the ASIC, a significant amount of energy was transmitted into the ASIC, which hardly attenuates the waves. This resulted in two effects: reflections from layers beneath the ASIC; and cross-talk between elements due to the propagation of lamb waves, which can be visible as extra peaks in the directivity pattern [47]. There are various approaches to reducing the effect of the ASIC on acoustic performance. Shabanimothlag et al. proposed to either lap down the thickness of the ASIC and

place a standard acoustic backing behind the ASIC, or dice deep cuts into the ASIC [47]. These approaches work in simulation, but are difficult to realize in practice as the ASIC mainly consists of silicon, which is brittle and hence hard to process. All alternative methods use an interfacing surface layer such as epoxy between the ASIC and PZT to induce a quarter-wavelength mode and direct most of the acoustic energy from the PZT forward [48]. Wildes et al. proposed a high-impedance “dematching” layer (DML) that reduced the need for a high-attenuation backing layer [27]. They used anisotropic conductive adhesive and flex circuits to attach the acoustic stack to the ASIC. The disadvantage of this approach is that the dicing depth must be carefully controlled to cut through the DML and fully isolate the elements while not cutting through the flex circuit, which would damage the circuit traces. Wodnicki et al. proposed the use of an interposer conductive backing of pillars to connect the acoustic stack to the surface of the ASIC [49]. The interposer consisted of a 3D-printed acrylic frame that was filled with conducting and acoustically absorbing silver epoxy material. The thickness of the interposer backing was considerably large (4 mm) to ensure great attenuation. The downside of this approach is that the assembly of the interposer to the ASIC is a potential source of failures in electrical connections, and the size of the acrylic wall is limited by the resolution of the 3D printer.

In the current design, we have opted for an interposer layer that consists of pillars of silver glue and an epoxy material with high attenuation. The composite layer consists of a small channel of silver glue that electrically connects the PZT material to the ASIC and an epoxy that we previously used as a backing and has high attenuation. The thickness of the interposer was chosen such that it dampens the

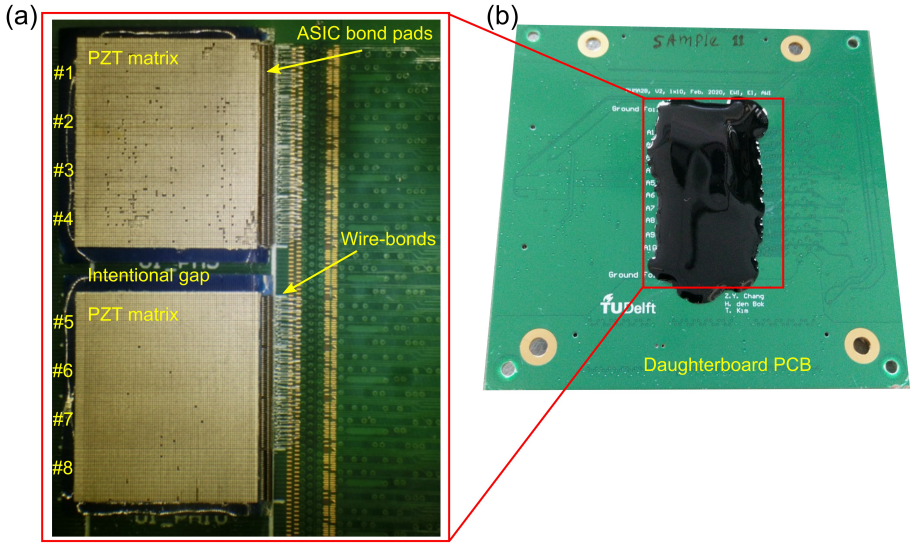

Figure 7.5: Photograph of the prototype transducer. (a) Fabrication of the PZT matrix with 96 × 80 (rows × columns) elements on top of 8×1 tiled ASICs. (b) The finished transducer on the daughterboard.

waves significantly, but not completely, as in the work of Wodnicki et al. With the chosen thickness, the interposer can be manufactured using conventional dice-and-fill methods. A schematic drawing of the designed acoustic stack with material information is presented in Figure 7.4. As seen, the interposer layer also serves as a buffer layer, which provides a margin for the dicing.

7.2.4.2. STACK FABRICATION

In our previous work [44], in which we investigated the effect of subdicing on a PZT matrix built on top of ASICs, we limited ourselves to the fabrication of a matrix transducer consisting of 4 × 1 tiled ASICs. The main difficulty lay in maintaining a flat surface of the stack over the whole area. The flatness of the stack surface is crucial for the dicing process because the dicing kerfs should be deep enough to guarantee the electrical and acoustical isolation between the elements, but shallow enough to not cut into the ASICs. Unfortunately, ASIC damage during the dicing process was a recurrent problem encountered in our previous attempts to fabricate the matrix.

In the current work, in order to minimize the risk of ASIC damage when dicing, we opted to manufacture a sample consisting of 8 × 1 tiled ASICs with a gap of one ASIC in the middle, i.e., the acoustic stack consists of two times 4 × 1 tiled ASICs with a gap of one ASIC in between the two. This is not the final version of the matrix transducer; however, this prototype is certainly relevant to verify the reliability of our manufacturing process, and to evaluate the functionality and performance of a prototype twice as large as our previous ones.

The transducer fabrication process starts with gluing the ASIC tiles onto a glass plate, which acts as a flat surface to guide the alignment of the ASICs and ensure that the ASICs have the same surface height. After this, gold balls are deposited on the ASIC pads (two bond pads are available per element to improve the connection stability). The gaps between the gold balls are filled with an electrically isolating epoxy material, which is then ground down until the gold balls are again exposed. The main role of this layer is to establish a mechanical buffer for dicing the interposer layer and to electrically isolate neighboring elements from each other. This buffer layer also provides the electrical connections from the ASIC bond pads to the interposer layer.

Next, the interposer is built by first depositing a thick layer of the non-conductive epoxy material. A 50 µm dicing blade is used to dice in one direction to expose the gold balls. These grooves are then filled with conductive glue and afterward, the excess material is ground away. Then, the dicing blade is used to dice in the other direction in between the gold balls, and these grooves are filled again by the non-conducting buffer material. Excess material is again ground away so that we end up with a flat top layer.

Next in the process, a matching layer made of conductive glue is applied on top of the piezoelectric material (3203HD, CTS Corporation, Lisle, IL, EUA). Then, the stack consisting of PZT and the matching layer is glued on top of the interposer. After this, the acoustical stack is diced. Two types of cuts are used. The through-cuts are made to separate the PZT elements with 300 × 150 µm pitch, and they may partially extend into the interposer layer (see Figure 7.4). The subdicing cuts, on the other

hand, only extend to about 70% of the pillar thickness. All the dicing/subdicing cuts are made using a 20 μm thick diamond blade and the dicing kerfs are not re-filled with any material, to minimize the acoustical crosstalk between the elements.

To finalize the matrix, a common ground electrode is made by gluing a 7 μm thick aluminum foil on top of the whole matrix array. Afterward, a thin layer of encapsulation material (AptFlex F7, Precision Acoustics Ltd., Dorchester, UK) is placed on top to prevent moisture from infiltrating the acoustic stack and thereby damaging the array. Photographs taken during and after the fabrication of the matrix transducer are shown in Figure 7.5.

7.2.4.3. ELECTRICAL CONNECTIONS

A daughterboard (see Figure 7.5(b)) was designed to hold the matrix transducer, and to provide the transmit, receive, power, and control signals to the ASIC. The electrical connections from the ASIC bond pads to the daughterboard bond pads were made with a bonding machine using 18 μm thick aluminum wire bonds. Ultraviolet curing glob top epoxy was applied over the bonding wires for protection.

The daughterboard is connected to a motherboard by micro coaxial cable assemblies (Samtec, New Albany, IN, USA) to transfer the TX and RX data. The motherboard interfaces with a Verasonics imaging system (V1, Verasonics, Inc., Kirkland, WA, USA) via two connectors (DLM5-260PW6A, ITT Corporation, White Plains, NY, USA) such that it can be mounted directly on the Verasonics machine. An electronic matching network is provided in the transmit paths to minimize overshoot and undershoot of the transmission signal, to guarantee the unipolar character of the excitation generated from the Verasonics. On the other hand, to compensate for the cable load effect and to minimize the losses of the transmission line, the receive paths are buffered with unity gain operational amplifiers on the motherboard to provide impedance matching between the output of the ASIC and the Verasonics. The power and control signals are transferred via a flat ribbon cable from the motherboard to the daughterboard. An external FPGA (DE2-115, Altera Corp., San Jose, CA, USA) generates the control data to program the ASIC, and an external power supply provides the power for the daughterboard and the motherboard. The Verasonics computer controls the overall operation of the whole system through MATLAB (2014b, The MathWorks, Inc., Natick, MA, USA).

7.2.5. MEASUREMENT SETUP

7.2.5.1. ELECTRICAL CHARACTERIZATION

The electrical performance of the ASIC and the whole signal chain from the ASIC to the Verasonics, including the cables and the motherboard, was evaluated by a test sample ASIC without the acoustic stack. Randomly selected element bond pads on the ASIC were wire-bonded to an externally accessible test pad on the daughterboard. The transmit, receive, power, and control bond pads on the ASIC were wire bonded to the daughterboard in the usual way. After programming the ASIC, we used an arbitrary waveform generator (AWG; 33250A, Agilent Technologies, Santa Clara, CA, USA) to apply a 50-cycle sinusoidal signal of 7.5 MHz

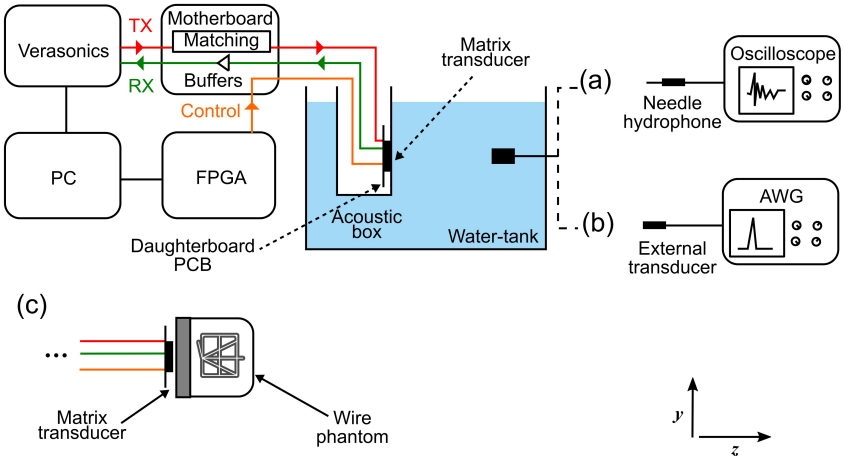

Figure 7.6: Acoustical measurement setup. (a) Transmit characterization. (b) Receive characterization. (c) Imaging using a CIRS phantom.

to the test bond pad as a test signal. The corresponding output signals were recorded at three different locations: at the input of the buffer on the motherboard; at the output of the buffer on the motherboard (i.e., at the input of the Verasonics); and at the output of the analog-to-digital converter of the Verasonics. We present the electrical performance of the signal chain in Appendix A.

7

7.2.5.2. ACOUSTICAL CHARACTERIZATION

Figure 7.6 shows a schematic diagram of the setup for the acoustical evaluation of the prototype transducer. For this purpose, the transducer was mounted in a box with an acoustical window made of 25 µm thick polyimide. The whole setup was submerged in a tank filled with deionized water.

For the transmit characterization (see option (a) in Figure 7.6), each element was driven individually with a 20 V unipolar pulse provided by the Verasonics imaging system. The acoustic pressure generated by the elements was detected by a calibrated 1 mm needle hydrophone (SN2082, Precision Acoustics Ltd., Dorchester, UK) positioned at a distance of 200 mm away from the transducer in the z-direction. On the xy-plane, the hydrophone was placed in front of the active elements in order to reduce the influence of its directivity, as follows. In the y-direction, we aligned the hydrophone with a central row of the ASIC under testing, whereas in the x-direction, the hydrophone was aligned at two different positions: at column 20 for measuring elements located on the left-hand side (i.e., columns 1 to 40) of the matrix shown in Figure 7.5(a); and at column 60 for measuring elements at the right-hand side (columns 41 to 80). The hydrophone output was amplified by a 60 dB amplifier (AU-1519, Miteq, Inc., Hauppauge, NY, USA), digitized by an oscilloscope (DSO-X 4024A, Agilent Technologies, Santa Clara, CA, USA), and automatically transferred to the Verasonics computer. Lastly, the recorded signals were bandpass filtered with cutoff

Table 7.1: Parameters for the directivity pattern simulation.

Parameter	Value
Element center frequency	7.5 MHz
Element size	300 µm × 150 µm
Excitation type	Hanning weighted pulse
Number of cycles	1
Sound speed	1480 m/s

frequencies of 4 and 12 MHz to eliminate noise from lower and higher frequency sources.

The directivity pattern of nine arbitrarily selected elements was characterized in the *x*- and *y*-directions with hydrophone scans. For this purpose, we used a calibrated 0.2 mm needle hydrophone (SN2385, Precision Acoustics Ltd., Dorchester, UK) located 50 mm away from the transducer in the *z*-direction. The hydrophone output was amplified and recorded as detailed in the previous paragraph. For comparison, we have also simulated the directivity pattern of an equivalent rectangular piston using the ultrasound simulator FOCUS [50]. The relevant simulation parameters are given in Table 7.1.

To evaluate the receive performance (see option (b) in Figure 7.6), an external transducer was utilized as a transmitter and excited with a 3-cycle sinusoidal burst generated by an AWG. We used a pre-calibrated 1 mm circular single-element transducer (PA865, Precision Acoustics Ltd., Dorchester, UK), which was placed at the center of the matrix's surface (i.e., at the origin of the *xy*-plane) at a distance z = 300 mm. The received signals of each individual element were acquired with the Verasonics.

Using the same setup described in the previous paragraph, we have also measured the overall dynamic range, which is defined as the difference between the highest and the lowest detectable pressures. With input pressures ranging from about 1 Pa to 50 kPa, we recorded the received signals for different gain settings of the Verasonics time-gain-compensation (TGC) and the ASIC gain (i.e., the combinations of LNA/PGA gain settings). For the ASIC gains, we used gain levels of 0, 3, 7, 11, and 15, which in decibels correspond to −8.6 dB, 0 dB, 12.1 dB, 23.5 dB, and 32.7 dB, respectively.

7.2.5.3. IMAGING

To test the imaging capabilities of the transducer prototype (see option (c) n Figure 7.6), we imaged a commercial ultrasound phantom for 3D evaluation (model: 055, CIRS, Inc., Norfolk, VA, USA), which contains wires with a diameter of 100 µm. For this test, only the top ASICs (i.e., ASICs 1 to 4) of the prototype were active, which means about 3800 active elements. All the active elements were excited simultaneously to generate a plane wave. In reception, the echoed wavefronts were recorded column-by-column. This necessitates 80 transmit events for recording the data detected by all elements. The raw echo data was filtered using a 50th-order

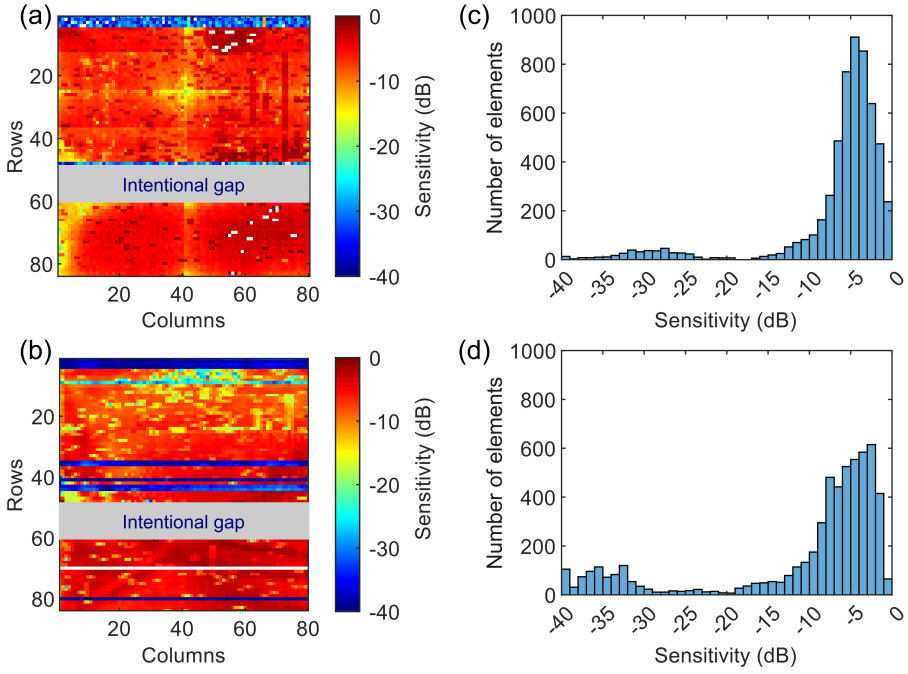

Figure 7.7: Sensitivity variation across the transducer elements. (a) Transmit sensitivity. (b) Receive sensitivity. (c) Transmit sensitivity histogram. (d) Receive sensitivity histogram.

bandpass finite impulse response (FIR) filter with cut-off frequencies of 5 and 9 MHz. The sound speed value used for the reconstruction was 1540 m/s.

A 3D volume with a lateral/elevation size of about 14 mm covering a depth ranging from 5 to 35 mm was discretized with a pixel size of 100 µm and reconstructed with a delay-and-sum beamforming technique. The reconstruction was conducted using a GPU code developed based on the direct sampling concept [51], [52]. The beamformed echo data were first normalized, then log-compressed, and finally, shown with a dynamic range of 50 dB and 30 dB for 3D and 2D representation, respectively. The 3D volumetric image rendering was performed with MATLAB. For quantitative evaluation, the full width at half-maximum (FWHM) of the point spread function (PSF) from wire reflections in the lateral and axial directions was calculated in different elevation planes (from −3 mm to 3 mm, with a spacing of 1 mm) to evaluate the variability of resolution.

7.3. RESULTS

7.3.1. SENSITIVITY

The normalized sensitivity map across all elements of the matrix transducer in transmit and receive are presented in Figure 7.7(a) and Figure 7.7(b), respectively. The plotted values represent the envelope peak of the time domain signals

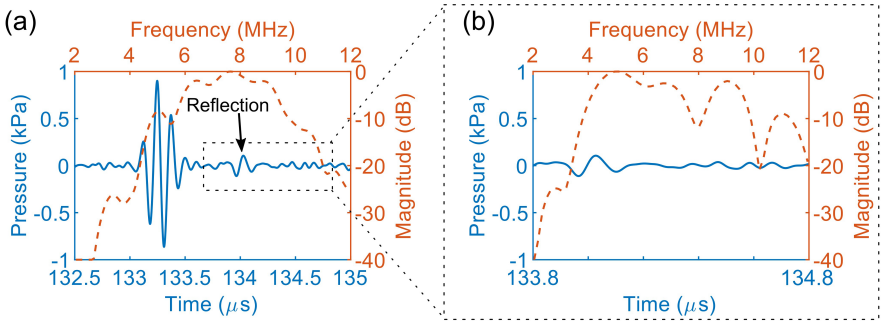

Figure 7.8: (a) Time and frequency domain response for a single element. (b) Close-up look at the second pulse.

expressed in decibels (relative to the maximum). Note that some elements (shown in white) have been omitted from the map because they exhibit a considerably higher amplitude (10 dB higher than the mean amplitude over all elements), which hinders the visualization of the variation across the remaining elements. Note also that ASICs 7 and 8 have suffered damages during the fabrication process and have been disconnected from the daughterboard. Due to this, we cannot include these ASICs in the overall evaluation of the prototype transducer, and we have omitted them in all figures presented in this section.

The sensitivity variation is somewhat similar in transmit and receive, but there are noticeable differences between them. In transmit, the elements located at the left bottom corner of the matrix (i.e., near columns 1 to 4 from ASICs 4 to 6) and also the ones located near the vertical centerline (i.e., near column 40 from ASICs 1 to 6) exhibit a lower efficiency, which is below −10 dB. The measurements for these elements were likely affected by the directivity of the hydrophone, as this effect is not seen in the receive map. In total, five rows are not functioning in transmit: rows 1 to 4, and row 48. This means that 400 elements are defective in transmit, which corresponds to 7% of the elements if we consider only elements from ASICs 1 to 6. In receive, however, there are significantly more defective rows: 12 in total. This represents 960 elements, i.e., 17% of the elements from ASICs 1 to 6. Besides the defective rows, many elements in ASICS 1 and 2 show a lower sensitivity (below −10 dB) in receive. Further observations regarding defective elements will be presented later in the discussion.

Figure 7.7(c) shows the histogram of transmit sensitivity. As can be seen, about 3900 elements are within the 0 dB to −6 dB level. This represents 72% of the elements if we consider only functioning elements (i.e., elements located in defective/missing rows are not counted). In receive, as shown in the histogram in Figure 7.7(d), about 2800 elements have a sensitivity above −6 dB. This represents 58% of the functioning elements.

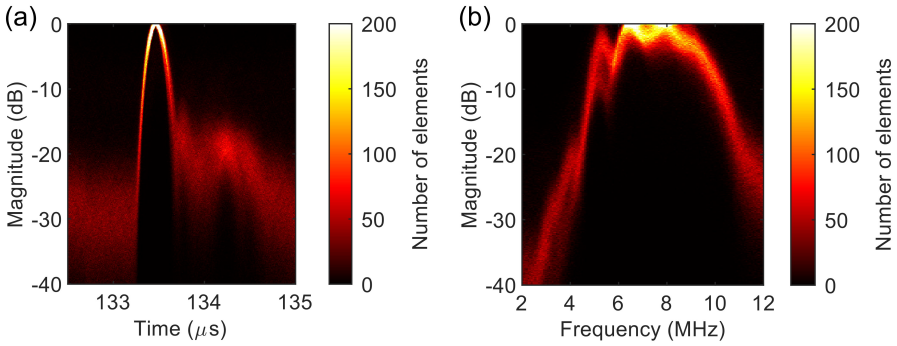

Figure 7.9: Time and frequency domain responses for all elements. (a) Envelope of the time signals. (b) Frequency spectrum.

7.3.2. TIME AND FREQUENCY RESPONSE

Figure 7.8(a) shows the transmit pressure wave for a single transducer element (blue solid line), recorded with the hydrophone at z = 200 mm, together with its fast Fourier transform (red dashed line). Note that there is a second pulse present in the time domain response, with a delay of about 1.5 µs from the main pulse (see black arrow in the figure). This is likely due to reflections from the back side of the ASIC. The second pulse exhibits a peak frequency of about 5 MHz, as seen in the frequency spectrum in Figure 7.8(b).

In Figure 7.9, the time and frequency responses for all working elements of the transducer are presented. In the figure, the color of each pixel represents the count of the number of occurrences in that pixel. In the time domain response shown in Figure 7.9(a), the time delays between the signals have been corrected using cross-correlation.

The transmit performance of the transducer is summarized in Table 7.2 in terms of peak pressure, center frequency, −6 dB bandwidth, and ringing time, which is defined as the time interval for the envelope amplitude to decrease below −20 dB of its corresponding peak. The listed values represent the mean and standard deviation over the working elements (i.e., rows 1–4 and 48 are neglected in the calculations).

7.3.3. DIRECTIVITY PATTERN

Figure 7.10 shows the measured directivity pattern of nine arbitrarily selected elements in transmit together with the corresponding averaged directivity pattern (black solid line) and the simulated result (blue dashed line). The measured directivity pattern differs somewhat from the simulated one in both directions. As indicated in the figure, the measurements show a sharp peak with an amplitude of 2.5 dB higher than in simulation at zero degrees. Ignoring this sharp peak, the directivity pattern along the *x*-direction exhibits a −6 dB beam width of about 70 and 105 degrees in measurements and simulations, respectively. This difference is due to the presence of a dip at ±40 seen in the measurements. In addition, an extra dip

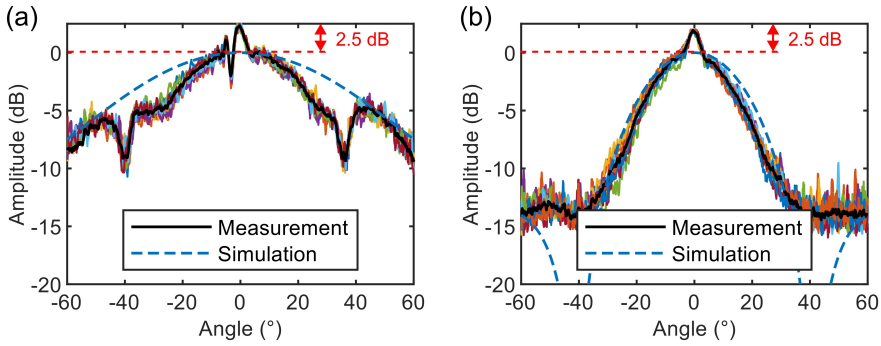

Figure 7.10: Measured and simulated directivity pattern in transmit. (a) Along the x-direction. (b) Along the y-direction.

at −4 degrees is also present in the measurements. Along the *y*-direction, the measured directivity pattern shows a −6 dB beam width of about 42 degrees, which agrees well with the simulated one. The dips observed in the simulation at ±40 degrees are not present in the measurements due to the noise floor, which is about −14 dB.

7

7.3.4. DYNAMIC RANGE

Figure 7.11 shows the relation between the received pressure at the transducer surface and the corresponding ASIC RX output voltage for different TGC and ASIC gain settings. The plotted values represent the average over all the functioning elements. The received signal amplitudes were converted from Verasonics output units back to millivolts at the Verasonics channel input using the results obtained from the electrical characterization (see Appendix A). Note that the values ranging from 50 kPa to 1 MPa (the gray region in the figure) were extrapolated based on the trend before and the observed saturation limits. This was done because we did not apply pressures above 50 kPa to avoid damage to the transmitting transducer.

It can be seen that the relationship between received pressure and the output voltage is characterized by both linear and non-linear regimes. In the mid-range, where the curves are nearly linear, we observed an average difference of about 3 dB between most of the adjacent ASIC gain steps. For the lowest gain, we measured a

Table 7.2: Transmit performance of the prototype transducer.

Parameter	Value
Peak pressure (kPa)	0.6 ± 0.2
Center frequency (MHz)	7.5 ± 0.6
Bandwidth $_{-6\,dB}$ (%)	46 ± 14
Ringing time $_{-20\,dB}$ (µs)	0.3 ± 0.15

receive sensitivity of approximately 55 nV/Pa, whereas for the highest gain the receive sensitivity is about 9 μV/Pa. This corresponds to a total gain range of 44 dB.

In the low range, the curves are dominated by the noise floor of both the Verasonics and the ASIC, as indicated in the figure. It is noticeable that the noise floor varies for different TGC and ASIC gain settings. As can be seen, the noise floor for higher ASIC gain levels (gains 11 and 15) remains approximately the same regardless of the TGC changes. From this perspective, we can conclude that the noise floor for higher ASIC gain levels is determined exclusively by the ASIC gain. On the other hand, for lower ASIC gain levels (gains 0 to 7), the noise floor remains basically the same regardless of the ASIC gain changes. Therefore, we can say that the noise floor for this gain setting is determined by the Verasonics only. Note that TGC 500 exhibits a slightly higher noise floor than TGC 700 and 900, possibly because the noise floor is significantly determined by both the ASIC and the Verasonics.

In the high range, the curves are dominated by the saturation levels of the Verasonics and the ASIC. As noticed in the figure, the saturation level for TGC 900 is about 15 mV, whereas for TGC 700 it is 60 mV. This is in agreement with the corresponding saturation levels presented in Appendix A. However, for TGC 500 we did not observe a saturation at about 80 mV in the electrical characterization (see Figure A1 in Appendix A). Therefore, the saturation observed in Figure 7.11 for TGC 500 actually corresponds to the saturation level of the ASIC (note that the saturation level of the ASIC is irrespective of the ASIC gain). Because of the observed saturation values for both the ASIC and Verasonics, we were able to extrapolate the results above 50 kPa.

The receive performance of the prototype transducer for different gain settings is summarized in Table 7.3. Here, the minimum detectable pressure is defined as the pressure level at which the SNR becomes 0 dB, whereas the maximum detectable pressure is defined as the pressure level at which the 1 dB compression is reached.

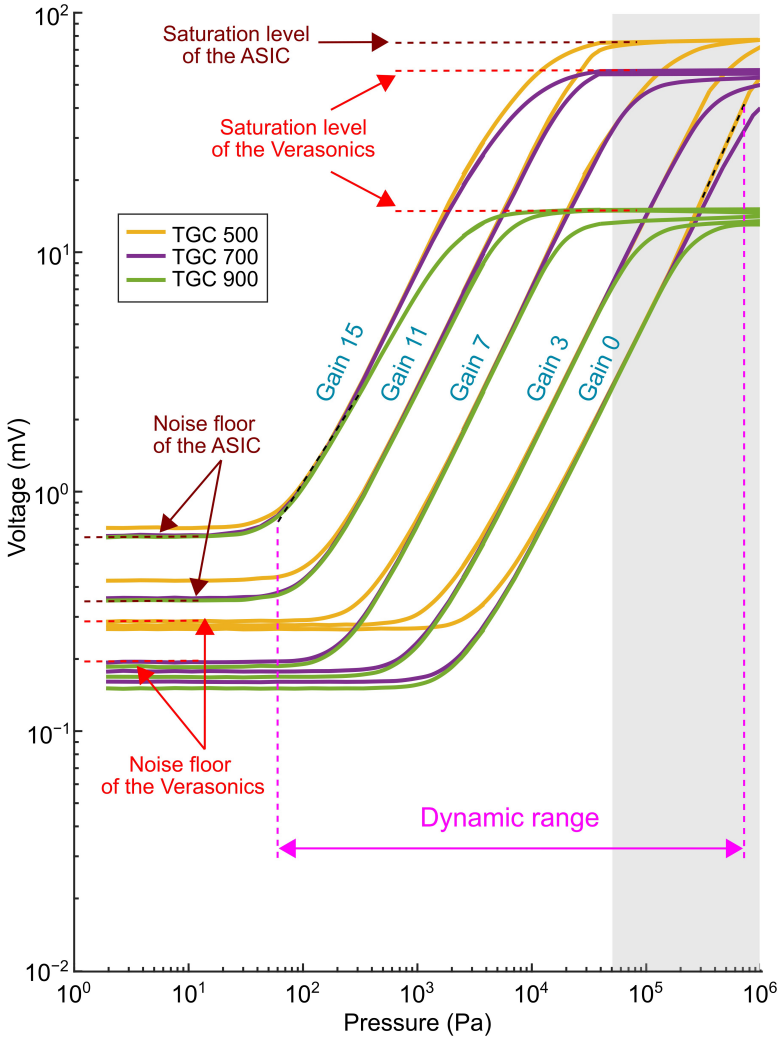

Figure 7.11: The relation between the received pressure and ASIC output voltage for different gain settings.

7.3.5. IMAGING

Figure 7.12 shows the schematic representation of the wire phantom together with the reconstructed 2D and 3D images (the 2D image is one slice of the 3D image). As can be seen, the wires numbered 1 to 6 and 11 are clearly detectable in both the 2D and 3D images. Wires 7, 8, and 10 were not detected though, and wire 9 was barely detectable. This could be due to the small effective aperture (contribution of a low number of elements) in reconstructing the pixels on the edge of the image. The trend

Table 7.3: Receive performance for different gain settings.

ASIC Gain	Minimum Pressure (kPa)	Maximum Pressure (kPa)	Receive Sensitivity (µV/Pa)
0	30	700 *	0.06
3	2	200 *	0.15
7	0.3	70 *	0.72
11	0.2	20	2.73
15	0.06	4	8.79

* Extrapolated values.

of lateral FWHM in Figure 7.13 indicates that the lateral resolution degrades when the imaging depth increases. The range of lateral and axial FWHM is almost the same for all the wires except wires 9 and 11, which are positioned at larger z values.

7.4. DISCUSSION

In this work, we have presented a 7.5 MHz prototype transducer for 3D imaging of the carotid artery. We have built an array of 8 × 1 tiled ASIC integrated with a PZT matrix consisting of 7680 elements. We have opted to leave a gap in the middle of the array to reduce the risk of mechanical damage to the ASICs during the manufacturing process due to misalignment. The current size of the gap is one full ASIC due to the current design of the daughterboard PCB layout, but if building a large aperture in parts remains necessary, a redesigned PCB can reduce the gap to a single row. Unfortunately, two ASICs still were malfunctioning due to electrical issues: in ASIC 8, we observed a short in one of the power supplies to the ASIC during

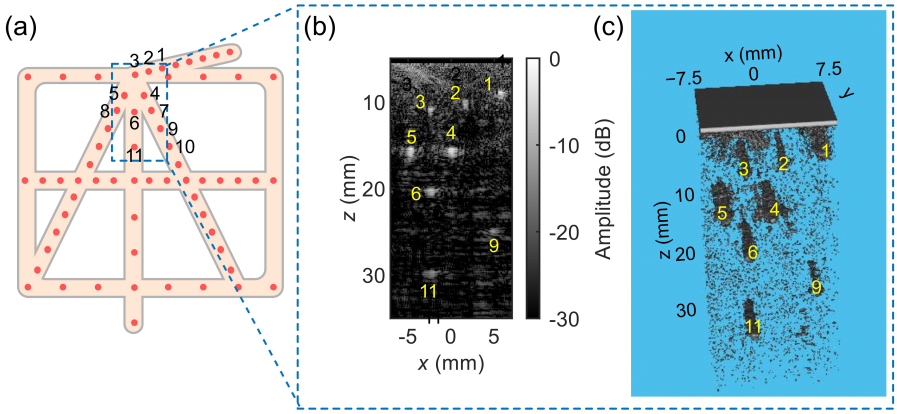

Figure 7.12: (a) Scheme of the wire phantom and numbered wires (the dashed rectangle depicts the field of view of the transducer). The reconstructed (b) 2D and (c) 3D images.

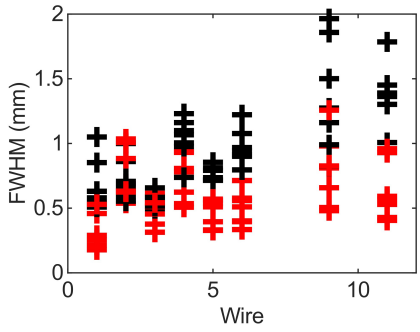

Figure 7.13: The axial and lateral FWHM for different wires in different elevation planes.

manufacturing and decided not to use this ASIC further. In ASIC 7, we found a short during the final check before finishing the fabrication and decided to remove the bond wires for this ASIC. We are currently investigating ways to minimize damage to the ASICs (both mechanical and electrical) during the fabrication process and increase the element yield. One potential approach is to prefabricate the acoustic stack (i.e., the PZT matrix, matching layer, and interposer) separately and attach it to the ASIC pads (or gold balls) at a later time. The procedure of bonding the acoustic stack to the ASIC could be accomplished by using an anisotropic conductive film, as described in [39]. In addition, the risk of electrical damage, such as caused by electrostatic discharge (ESD) events, could be significantly reduced if we are able to effectively ground leakage paths during the assembly of the acoustic stack on the ASICs. We will explore these possibilities in our future work.

The maps presented in Figure 7.7 show that 72% and 58% of the working elements exhibit sensitivity variation within the −6 dB range in transmit and receive, respectively. On the one hand, the achieved element yield is sufficient to demonstrate the technology employed in the prototype transducer, allowing us to evaluate features and test the functionality of the current design. On the other hand, for imaging purposes or mass production, the element yield must be improved to avoid defective rows. This is a major problem that needs to be tackled in our manufacturing process. Regarding rows 1 to 4, which do not work in both transmit or receive, we found afterward that this was caused by a damaged cable in our measurement setup. Regarding the rows that do not work only in receive (mostly from ASIC 4), we believe this is due to faulty wire bonds or damage to the motherboard components. Besides defective rows, many elements in ASICs 1 and 2 show a lower sensitivity (below −10 dB) in receive. These elements probably suffered damage/degradation during or after the transmit experiments (the transmit and receive measurements were performed in an interval of one week). The degree of degradation might be verified by repeating the transmit characterization and comparing it with the previous measurements. Regarding the omitted elements in the map (shown in white), we think that they exhibit a considerably higher amplitude due to a short in the acoustic stack between multiple elements.

Figure 7.8 and Figure 7.9 show that the time and frequency responses of different transducer elements are quite similar (based on the number of overlapped

pixels in Figure 7.9) and behave as expected. Based on the measured peak pressure (0.6 kPa) and the transmit voltage (20 V peak amplitude), we estimate an average transmit efficiency of approximately 30 Pa/V at 200 mm. This value is comparable with our previous prototype with subdiced elements [44]. On average, the elements have a center frequency of 7.5 MHz and a −6 dB single-way bandwidth of about 45%. However, we have observed that many elements exhibit a sharp peak at 5 MHz and a dip at 6 MHz, which reduces their bandwidth significantly. This is likely caused by the effect of reflections and standing waves from the bottom side of the transducer, i.e., from the ASICs.

The measured directivity pattern shown in Figure 7.10 follows the trend of the simulated one in both directions but deviates significantly at specific points. These deviations can be explained by a combination of both electrical and acoustical crosstalk (see Appendix B for details). The electrical crosstalk in our case means that all elements of a row are somewhat excited when an electrical pulse is sent to the transmit bus of that row. This is likely the cause of the sharp peak of 2.5 dB at 0 degrees. Since this type of crosstalk only happens in transmit, the sharp peak will be absent in the receive directivity pattern. Furthermore, because we intend to use at least half of the elements on a row in transmit, the peak will not affect the images generated by this probe. Along the x-direction, the dips observed at ±40 degrees are likely caused by acoustical crosstalk. Since the prototype transducer was designed to operate with low steering angles, these dips are not considered to be important. Previously, in the design without an interposer layer, we also observed peaks at ±20 degrees in the directivity pattern. With the interposer, there is now an attenuating medium in between the elements and the ASIC and due to that, these peaks do not show up anymore. This suggests that the employed interposer layer helps to reduce the crosstalk due to the propagation of Lamb waves in the ASIC.

As seen in Figure 7.11, the minimum detectable pressure of 60 Pa is limited by the noise floor of the ASIC for gain 15. On the other hand, the maximum detectable pressure is about 700 kPa, which is limited by the saturation level of the ASIC for gain 0 and TGC 500. Therefore, the overall dynamic range of the prototype transducer is about 81 dB, which is sufficient for carotid imaging applications [53].

The performance of the prototype transducer was tested by imaging a commercial wire phantom, as shown in Figure 7.12 and Figure 7.13, which proves the applicability of the prototype for plane wave 3D imaging. Future work should include further evaluation of beamforming image quality and in vitro and in vivo experiments.

7.5. CONCLUSIONS

We have demonstrated the design, fabrication, and characterization of a PZT matrix transducer with integrated electronics. The ASIC architecture together with the subdicing of the piezo elements allowed us to effectively reduce the channel count to 120 transmit and 120 receive channels. The prototype transducer was targeted to have 7680 elements built on top of 8 × 1 tiled ASICs; however, two ASICs were damaged during the fabrication process. On average, the individual elements of the transducer exhibited a transmit efficiency of 30 Pa/V at 200 mm and a −6 dB

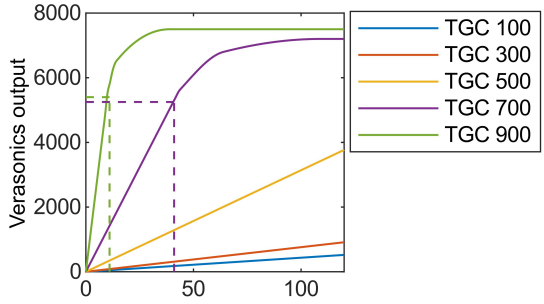

Figure A1: Relation between the input and output of the Verasonics V1 system for several TGC gains at 7.5 MHz.

bandwidth of 45%. The receive dynamic range is 81 dB with a minimum and maximum detectable pressure of 60 Pa and 700 kPa, respectively. Overall, the characterization results are promising and encourage us to pursue further up-scaling by fabricating a larger PZT matrix transducer on 10 × 1 tiled ASICs with an increased element yield. In this way, we expect to realize a fully populated matrix consisting of about 10,000 elements in the near future.

7.6. APPENDIX A: ELECTRICAL CHARACTERIZATION

Figure A1 shows the relationship between the output voltage of the ASIC (connected to the Verasonics input channel) and the output of the Verasonics for different TGC settings. The curves show that for TGC levels of 100, 300, and 500, the Verasonics signals are always linear in the range evaluated. However, with TGC levels of 700 and 900, nonlinear deformation of the signal is observed above 5500 units (shown by the dashed lines) due to the saturation of the Verasonics output. Table A1 presents the maximum acceptable input voltage (determined using the 1 dB compression point), the corresponding Verasonics output, and the gain in the linear range at each TGC setting. By increasing the TGC, the Verasonics gain is increased; however, the maximum acceptable input voltage in the linear regime is decreased.

Table A1: Characterization of the Verasonics V1 system for different TGC settings.

TGC	Maximum Input (mV)	Verasonics Output	Slope (1/mV)
100	310	1245	4.1
300	310	2315	7.6
500	185	5497	31.4
700	45	5514	129.3
900	11	5602	543.3

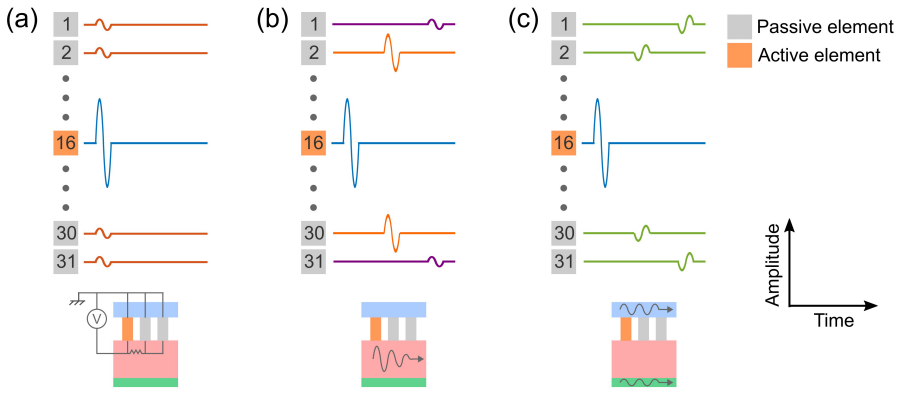

Figure B1: Assumptions for crosstalk simulations. (a) Electrical crosstalk. (b) Acoustical crosstalk via an attenuating medium. (c) Acoustical crosstalk via a non-attenuating medium.

7.7. APPENDIX B: CROSSTALK ANALYSIS

Herein, we investigate whether the differences observed between the simulated and experimental directivity patterns could be explained by interelement crosstalk present in the prototype transducer. Since our measurement setup and transducer configuration do not allow us to measure the crosstalk directly, we analyzed the possible effects of both electrical and acoustical crosstalk on the directivity pattern via simulations. For this, we used the ultrasound simulator FOCUS, as explained previously (see Table 7.1), to simulate the directivity pattern of the transducer elements excited with different amplitudes and time delays to mimic the crosstalk [54], [55]. In all simulations, we used an array of 31 elements with the active element being the central one.

For the electrical crosstalk simulations, the neighboring passive array elements were excited simultaneously with an equal amplitude between them but a lower amplitude as compared to the active element, as shown in Figure B1(a). With regard to the acoustical crosstalk, we hypothesized that there were two different kinds of acoustical crosstalk happening. First, we assumed that the vibration of the active element will generate wave propagation through the interposer layer that will induce a vibration in the neighboring elements. To simulate this, the passive elements were excited with amplitudes and delays based on the distance from the active element, as shown in Figure B1(b). Second, we hypothesized that there will also be crosstalk via a non-attenuating medium such as the ASIC. Here the delays are again based on the distance from the active elements, but the amplitude of the passive elements is the same, as shown in Figure B1(c). The crosstalk analysis was performed only along the *x*-direction.

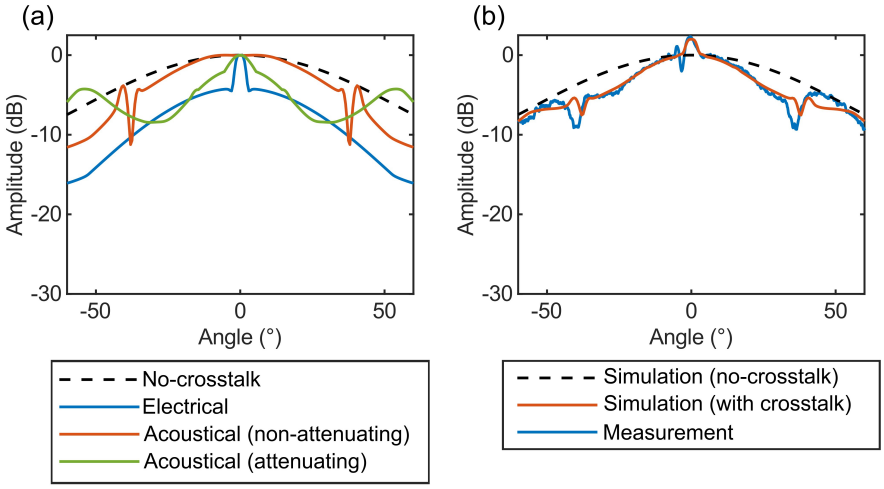

Figure B2: Directivity pattern along the x-direction. (a) Effect of individual crosstalks. (b) Effect of the combined crosstalk.

Figure B2(a) shows the effect of each simulated crosstalk on the directivity pattern. As can be seen, the electrical crosstalk introduces a sharp peak at zero degrees. We observed that the magnitude of the sharp peak is determined by the amplitude of the passive elements. Regarding the acoustical crosstalk via the interposer, the beam is narrowed and two bumps appear, whose position is determined by the velocity of the medium. Finally, the acoustical crosstalk via the non-attenuating material generates two dips or peaks, depending on the phase.

To investigate the combination of electrical and acoustical crosstalk, we swept through different values of amplitudes and time delays in order to fit the simulated data to the experimental one. Figure B2(b) shows the result of the fitting procedure and Table B1 lists the values of amplitudes, time delays, and propagation speeds used to fit the curve. As seen, the trend of the simulated directivity pattern with crosstalk follows the experimental curve. This result suggests that the extra peak and dips observed in the measured directivity pattern could be caused by a combination of electrical and the two types of acoustical crosstalk. Note, however, that the value of propagation speed in the non-attenuating medium differs

Table B1: Parameters for crosstalk simulations.

	Electrical	**Acoustical (non-attenuating)**	**Acoustical (attenuating)**
Amplitude	-30 dB	−20 dB	−3.5 dB *
Time delay*	-	0.0612 µs	0.0833 µs
Propagation speed	-	2450 m/s	1800 m/s

* Between adjacent elements.

significantly from the propagation speed of Lamb waves in the ASIC [47], which suggests that this kind of crosstalk goes via another layer.

For our purposes, this brief analysis suffices to represent the contribution of different types of crosstalk in the directivity pattern. An in-depth simulation study of crosstalk is left for later work as this is beyond the scope of this paper.

7.8. REFERENCES

[1] K. K. Dakok, M. Z. Matjafri, N. Suardi, A. A. Oglat, and S. E. Nabasu, "A review of carotid artery phantoms for doppler ultrasound applications," *J Med Ultrasound*, vol. 29, no. 3, pp. 157–166, 2021, doi: 10.4103/JMU.JMU_164_20.

[2] A. Delcker and C. Tegeler, "Influence of ECG-Triggered Data Acquisition on Reliability for Carotid Plaque Volume Measurements with a Magnetic Sensor Three-Dimensional Ultrasound System," *Ultrasound Med Biol*, vol. 24, no. 4, pp. 601–605, May 1998, doi: 10.1016/S0301-5629(98)00012-X.

[3] P. Kruizinga, F. Mastik, N. de Jong, A. F. W. van der Steen, and G. van Soest, "High frame rate ultrasound imaging of human carotid artery dynamics," in *2012 IEEE International Ultrasonics Symposium*, IEEE, Oct. 2012, pp. 1177–1180. doi: 10.1109/ULTSYM.2012.0293.

[4] A. Landry, J. D. Spence, and A. Fenster, "Measurement of Carotid Plaque Volume by 3-Dimensional Ultrasound," *Stroke*, vol. 35, no. 4, pp. 864–869, Apr. 2004, doi: 10.1161/01.STR.0000121161.61324.ab.

[5] J. D. Spence, M. Eliasziw, M. DiCicco, D. G. Hackam, R. Galil, and T. Lohmann, "Carotid Plaque Area," *Stroke*, vol. 33, no. 12, pp. 2916–2922, Dec. 2002, doi: 10.1161/01.STR.0000042207.16156.B9.

[6] A. Fenster, D. B. Downey, and H. N. Cardinal, "Three-dimensional ultrasound imaging," *Phys Med Biol*, vol. 46, no. 5, pp. R67–R99, May 2001, doi: 10.1088/0031-9155/46/5/201.

[7] R. W. Prager, U. Z. Ijaz, A. H. Gee, and G. M. Treece, "Three-dimensional ultrasound imaging," *Proc Inst Mech Eng H*, vol. 224, no. 2, pp. 193–223, Feb. 2010, doi: 10.1243/09544119JEIM586.

[8] U. Schminke, L. Motsch, B. Griewing, M. Gaull, and C. Kessler, "Three-dimensional power-mode ultrasound for quantification of the progression of carotid artery atherosclerosis," *J Neurol*, vol. 247, no. 2, pp. 106–111, Feb. 2000, doi: 10.1007/PL00007790.

[9] A. Delcker and H. C. Diener, "Quantification of atherosclerotic plaques in carotid arteries by three-dimensional ultrasound," *Br J Radiol*, vol. 67, no. 799, pp. 672–678, Jul. 1994, doi: 10.1259/0007-1285-67-799-672.

[10] A. Harloff, "Carotid Plaque Hemodynamics," *Interv Neurol*, vol. 1, no. 1, pp. 44–54, 2012, doi: 10.1159/000338360.

[11] S. Holbek, M. J. Pihl, C. Ewertsen, M. B. Nielsen, and J. A. Jensen, "In vivo 3-D vector velocity estimation with continuous data," in *2015 IEEE International Ultrasonics Symposium (IUS)*, IEEE, Oct. 2015, pp. 1–4. doi: 10.1109/ULTSYM.2015.0235.

[12] J. Provost *et al.*, "3D ultrafast ultrasound imaging in vivo," *Phys Med Biol*, vol. 59, no. 19, pp. L1–L13, Oct. 2014, doi: 10.1088/0031-9155/59/19/L1.

[13] B. Heiles *et al.*, "Ultrafast 3D Ultrasound Localization Microscopy Using a 32 × 32 Matrix Array," *IEEE Trans Med Imaging*, vol. 38, no. 9, pp. 2005–2015, 2019, doi: 10.1109/TMI.2018.2890358.

[14] M. Mozaffarzadeh *et al.*, "Receive/Transmit Aperture Selection for 3D Ultrasound Imaging with a 2D Matrix Transducer," *Applied Sciences*, vol. 10, no. 15, p. 5300, Jul. 2020, doi: 10.3390/app10155300.

[15] T. Kim *et al.*, "Design of an Ultrasound Transceiver ASIC with a Switching-Artifact Reduction Technique for 3D Carotid Artery Imaging," *Sensors*, vol. 21, no. 1, p. 150, Dec. 2020, doi: 10.3390/s21010150.

[16] E. Roux, A. Ramalli, M. Robini, H. Liebgott, C. Cachard, and P. Tortoli, "Spiral array inspired multi-depth cost function for 2D sparse array optimization," in *2015 IEEE International Ultrasonics Symposium (IUS)*, IEEE, Oct. 2015, pp. 1–4. doi: 10.1109/ULTSYM.2015.0096.

[17] N. Ellens, A. Pulkkinen, J. Song, and K. Hynynen, "The utility of sparse 2D fully electronically steerable focused ultrasound phased arrays for thermal surgery: a simulation study," *Phys Med Biol*, vol. 56, no. 15, pp. 4913–4932, Aug. 2011, doi: 10.1088/0031-9155/56/15/017.

[18] P. Ramaekers, M. de Greef, R. Berriet, C. T. W. Moonen, and M. Ries, "Evaluation of a novel therapeutic focused ultrasound transducer based on Fermat's spiral," *Phys Med Biol*, vol. 62, no. 12, pp. 5021–5045, Jun. 2017, doi: 10.1088/1361-6560/aa716c.

[19] A. Ramalli, E. Boni, A. S. Savoia, and P. Tortoli, "Density-tapered spiral arrays for ultrasound 3-D imaging," *IEEE Trans Ultrason Ferroelectr Freq Control*, vol. 62, no. 8, pp. 1580–1588, 2015, doi: 10.1109/TUFFC.2015.007035.

[20] I. O. Wygant *et al.*, "An integrated circuit with transmit beamforming flip-chip bonded to a 2-D CMUT array for 3-D ultrasound imaging," *IEEE Trans Ultrason Ferroelectr Freq Control*, vol. 56, no. 10, pp. 2145–2156, Oct. 2009, doi: 10.1109/TUFFC.2009.1297.

[21] L. Wei *et al.*, "High Frame Rate Volumetric Imaging of Microbubbles Using a Sparse Array and Spatial Coherence Beamforming," *IEEE Trans Ultrason Ferroelectr Freq Control*, vol. 68, no. 10, pp. 3069–3081, 2021, doi: 10.1109/TUFFC.2021.3086597.

[22] E. Roux, F. Varray, L. Petrusca, C. Cachard, P. Tortoli, and H. Liebgott, "Experimental 3-D Ultrasound Imaging with 2-D Sparse Arrays using Focused and Diverging Waves," *Sci Rep*, vol. 8, no. 1, pp. 1–12, 2018, doi: 10.1038/s41598-018-27490-2.

[23] M. F. Rasmussen and J. A. Jensen, "3-D ultrasound imaging performance of a row-column addressed 2-D array transducer: A measurement study," in *2013 IEEE International Ultrasonics Symposium (IUS)*, IEEE, Jul. 2013, pp. 1460–1463. doi: 10.1109/ULTSYM.2013.0370.

[24] K. Chen, H. S. Lee, and C. G. Sodini, "A Column-Row-Parallel ASIC Architecture for 3-D Portable Medical Ultrasonic Imaging," *IEEE J Solid-State Circuits*, vol. 51, no. 3, pp. 738–751, Mar. 2016, doi: 10.1109/JSSC.2015.2505714.

[25] M. Flesch *et al.*, "4D in vivo ultrafast ultrasound imaging using a row-column addressed matrix and coherently-compounded orthogonal plane waves," *Phys Med Biol*, vol. 62, no. 11, pp. 4571–4588, Jun. 2017, doi: 10.1088/1361-6560/aa63d9.

[26] J. Janjic *et al.*, "A 2-D Ultrasound Transducer With Front-End ASIC and Low Cable Count for 3-D Forward-Looking Intravascular Imaging: Performance and Characterization," *IEEE Trans Ultrason Ferroelectr Freq Control*, vol. 65, no. 10, pp. 1832–1844, 2018, doi: 10.1109/TUFFC.2018.2859824.

[27] D. Wildes *et al.*, "4-D ICE: A 2-D Array Transducer With Integrated ASIC in a 10-Fr Catheter for Real-Time 3-D Intracardiac Echocardiography," *IEEE Trans Ultrason Ferroelectr Freq Control*, vol. 63, no. 12, pp. 2159–2173, Dec. 2016, doi: 10.1109/TUFFC.2016.2615602.

[28] B. Savord and R. Solomon, "Fully sampled matrix transducer for real time 3D ultrasonic imaging," *Proceedings of the IEEE Ultrasonics Symposium*, vol. 1, no. c, pp. 945–953, 2003, doi: 10.1109/ultsym.2003.1293556.

[29] C. Chen *et al.*, "A Pitch-Matched Front-End ASIC With Integrated Subarray Beamforming ADC for Miniature 3-D Ultrasound Probes," *IEEE J Solid-State Circuits*, vol. 53, no. 11, pp. 3050–3064, Nov. 2018, doi: 10.1109/JSSC.2018.2864295.

[30] T. M. Carpenter, M. W. Rashid, M. Ghovanloo, D. M. J. Cowell, S. Freear, and F. L. Degertekin, "Direct Digital Demultiplexing of Analog TDM Signals for Cable Reduction in Ultrasound Imaging Catheters," *IEEE Trans Ultrason Ferroelectr Freq Control*, vol. 63, no. 8, pp. 1078–1085, Aug. 2016, doi: 10.1109/TUFFC.2016.2557622.

[31] E. Kang *et al.*, "A Reconfigurable Ultrasound Transceiver ASIC With 24 × 40 Elements for 3-D Carotid Artery Imaging," *IEEE J Solid-State Circuits*, vol. 53, no. 7, pp. 2065–2075, Jul. 2018, doi: 10.1109/JSSC.2018.2820156.

[32] C. Chen *et al.*, "A Front-End ASIC with Receive Sub-array Beamforming Integrated with a 32 × 32 PZT Matrix Transducer for 3-D Transesophageal Echocardiography," *IEEE J Solid-State Circuits*, vol. 52, no. 4, pp. 994–1006, Apr. 2017, doi: 10.1109/JSSC.2016.2638433.

[33] "Philips. The xMATRIX Transducer Technology." Accessed: Jul. 28, 2022. [Online]. Available: https://www.usa.philips.com/healthcare/resources/feature-detail/xmatrix/

[34] "Butterfly. New Butterfly iQ+." Accessed: Sep. 14, 2022. [Online]. Available: https://www.butterflynetwork.eu/

[35] J. M. Rothberg *et al.*, "Ultrasound-on-chip platform for medical imaging, analysis, and collective intelligence," *Proceedings of the National Academy of Sciences*, vol. 118, no. 27, Jul. 2021, doi: 10.1073/pnas.2019339118.

[36] "Fujifilm. Technologies." Accessed: Sep. 14, 2022. [Online]. Available: https://hce.fujifilm.com/products/ultrasound/technologies.html

[37] F. Fool *et al.*, "3D high frame rate flow measurement using a prototype matrix transducer for carotid imaging," in *2019 IEEE International Ultrasonics Symposium (IUS)*, IEEE, Oct. 2019, pp. 2242–2245. doi: 10.1109/ULTSYM.2019.8925780.

[38] H. R. Tahmasebpour, A. R. Buckley, P. L. Cooperberg, and C. H. Fix, "Sonographic examination of the carotid arteries," *Radiographics*, vol. 25, no. 6, pp. 1561–1575, 2005, doi: 10.1148/rg.256045013.

[39] H.-V. Nguyen, T. Eggen, B. Sten-Nilsen, K. Imenes, and K. E. Aasmundtveit, "Assembly of multiple chips on flexible substrate using anisotropie conductive film for medical imaging applications," in *2014 IEEE 64th Electronic Components and Technology Conference (ECTC)*, IEEE, May 2014, pp. 498–503. doi: 10.1109/ECTC.2014.6897330.

[40] E. Boni *et al.*, "ULA-OP 256: A 256-Channel Open Scanner for Development and Real-Time Implementation of New Ultrasound Methods," *IEEE Trans Ultrason Ferroelectr Freq Control*, vol. 63, no. 10, pp. 1488–1495, 2016, doi: 10.1109/TUFFC.2016.2566920.

[41] "Verasonics. The Vantage System." Accessed: May 05, 2022. [Online]. Available: https://verasonics.com/the-vantage-advantage/

[42] N. de Jong, N. Bom, J. Souquet, and G. Faber, "Vibration modes, matching layers and grating lobes," *Ultrasonics*, vol. 23, no. 4, pp. 176–182, Jul. 1985, doi: 10.1016/0041-624X(85)90027-7.

[43] J. Janjic, M. Shabanimotlagh, G. van Soest, A. F. W. van der Steen, N. de Jong, and M. D. Verweij, "Improving the Performance of a 1-D Ultrasound Transducer Array by Subdicing," *IEEE Trans Ultrason Ferroelectr Freq Control*, vol. 63, no. 8, pp. 1161–1171, Aug. 2016, doi: 10.1109/TUFFC.2016.2561935.

[44] D. S. dos Santos *et al.*, "Experimental Investigation of the Effect of Subdicing on an Ultrasound Matrix Transducer," in *2021 IEEE International Ultrasonics Symposium (IUS)*, IEEE, Sep. 2021, pp. 1–3. doi: 10.1109/ius52206.2021.9593315.

[45] P. Tortoli, M. Lenge, D. Righi, G. Ciuti, H. Liebgott, and S. Ricci, "Comparison of Carotid Artery Blood Velocity Measurements by Vector and Standard Doppler Approaches," *Ultrasound Med Biol*, vol. 41, no. 5, pp. 1354–1362, May 2015, doi: 10.1016/j.ultrasmedbio.2015.01.008.

[46] P. Kruizinga *et al.*, "Towards 3D ultrasound imaging of the carotid artery using a programmable and tileable matrix array," in *2017 IEEE International Ultrasonics Symposium (IUS)*, IEEE, Sep. 2017, pp. 1–3. doi: 10.1109/ULTSYM.2017.8091570.

[47] M. Shabanimotlagh *et al.*, "Optimizing the directivity of piezoelectric matrix transducer elements mounted on an ASIC," *IEEE International Ultrasonics Symposium, IUS*, pp. 5–8, 2017, doi: 10.1109/ULTSYM.2017.8091752.

[48] S. Lee, K. Choi, K. Lee, Y. Kim, and S. Park, "A quarter-wavelength vibration mode transducer using clamped boundary backing layer," *Advances in Civil, Environmental and Materials Research*, pp. 1634–1639, 2012.

[49] R. Wodnicki *et al.*, "Co-Integrated PIN-PMN-PT 2-D Array and Transceiver Electronics by Direct Assembly Using a 3-D Printed Interposer Grid Frame," *IEEE Trans Ultrason Ferroelectr Freq Control*, vol. 67, no. 2, pp. 387–401, Feb. 2020, doi: 10.1109/TUFFC.2019.2944668.

[50] R. J. McGough, "Rapid calculations of time-harmonic nearfield pressures produced by rectangular pistons," *J Acoust Soc Am*, vol. 115, no. 5, pp. 1934–1941, May 2004, doi: 10.1121/1.1694991.

[51] K. Ranganathan, M. K. Santy, T. N. Blalock, J. A. Hossack, and W. F. Walker, "Direct sampled I/Q beamforming for compact and very low-cost ultrasound imaging," *IEEE Trans Ultrason Ferroelectr Freq Control*, vol. 51, no. 9, pp. 1082–1094, 2004, doi: 10.1109/TUFFC.2004.1334841.

[52] M. Mozaffarzadeh, E. Verschuur, M. D. Verweij, N. De Jong, and G. Renaud, "Accelerated 2D Real-Time Refraction-Corrected Transcranial Ultrasound Imaging," 2022, doi: 10.1109/TUFFC.2022.3189600.

[53] D. Lynser, C. Daniala, A. Y. Khan, E. Marbaniang, and I. Thangkhiew, "Effects of dynamic range variations on the Doppler flow velocities of common carotid arteries," *Artery Res*, vol. 22, no. C, p. 18, 2018, doi: 10.1016/j.artres.2018.02.001.

[54] M. Celmer and K. J. Opieliński, "Research and Modeling of Mechanical Crosstalk in Linear Arrays of Ultrasonic Transducers," *Archives of Acoustics*, vol. 41, no. 3, pp. 599–612, Sep. 2016, doi: 10.1515/aoa-2016-0058.

[55] A. Bybi, D. Khouili, C. Granger, M. Garoum, A. Mzerd, and A.-C. Hladky-Hennion, "Experimental Characterization of A Piezoelectric Transducer Array Taking into Account Crosstalk

Phenomenon," *International Journal of Engineering and Technology Innovation*, vol. 10, no. 1, pp. 01–14, Jan. 2020, doi: 10.46604/ijeti.2020.4348.

8

A PITCH-MATCHED HIGH-FRAME-RATE ULTRASOUND IMAGING ASIC FOR CATHETER-BASED 3D PROBES[1]

[1] This chapter is based on the following publication:
Hopf, Y.M.; **dos Santos, D.S.**; Ossenkoppele, B.W.; Soozande, M.; Noothout, E.; Chang, Z.-Y.; Chen, C.; Vos, H.J.; Bosch, J.G.; Verweij, M.D.; et al. A Pitch-Matched High-Frame-Rate Ultrasound Imaging ASIC for Catheter-Based 3-D Probes. IEEE J Solid-State Circuits 2024, 59, 476–491, doi:10.1109/JSSC.2023.3299749.

8.1. INTRODUCTION

ULTRASOUND imaging is a popular tool in medical treatments due to its relatively safe nature, cost-effectiveness, and compatibility with minimally invasive interventions [1], [2]. A special class of imaging devices used for the latter are catheter-based probes. These enable high-resolution images taken directly next to the area of interest in the body. The probes are disposable and purpose-built for their application in procedures such as intravascular ultrasound (IVUS) [3] or intracardiac echocardiography (ICE) [4], [5]. While IVUS is commonly used in procedures such as plaque detection in the vascular system and can typically work with a smaller imaging array [6], [7], [8], ICE is applied in a variety of cardiovascular interventions with more demanding requirements on the imaging depth and resolution [9], [10].

Particularly in upcoming 3D probes with 2D transducer arrays, these requirements lead to significant challenges in the design of ICE catheters. While 2D imagers with 1D transducer arrays commonly apply passive probes with direct element connection to the imaging system [11], [12], the higher cable count, crosstalk, and attenuation across thinner cables for 2D transducer matrices lead to the application of application-specific integrated circuits (ASICs) in ultrasound imaging catheters [9], [13]. The basic functionality of the electronics includes ultrasound transmission (TX) and reception (RX) on each array element to maximize the imaging aperture in the limited space of the catheter, amplification of the received echoes for robust signal transmission, and communication with an imaging system outside the body [14], [15]. For 3D imaging, the transducer pitch in the azimuthal and elevation direction has to be designed for low impact on image quality [10]. As a result, there is little space for circuitry that is matched to the pitch of the transducer. A pitchmatched design is a requirement for scalability to the about 1000 elements of a full 3D ICE design [9], [10] but leads to a high requirement on the integration density of the circuits. Prior 3D ICE designs have thus been limited to a subset of the desirable functionality as they could not integrate transmit beamforming [15], only low-voltage (LV) transmission [16], no transmit functionality at all [17], [18], or had to strongly limit the achievable volume acquisition rate [9].

High-frame-rate imaging is required in order to accommodate imaging modes such as blood flow Doppler or electromechanical wave imaging [19]. However, with the pulse repetition frequency (PRF) being limited by the imaging depth, a high frame rate implies fewer acquisitions per reconstructed volume and additional requirements on the circuit design [10].

One of the main challenges in the transition to high-framerate 3D probes is posed by the communication with the imaging system. Catheters with a diameter of around 3 mm have to accommodate all TX and RX signals next to common connections such as power and additional controls [9]. To reduce the number of TX cables, pulses are often generated on the ASIC. The configuration data can be provided via a serial link into local registers [20], [21], [22] or an efficient shift register (SR) [14], [23] before the next TX phase and delays for TX beamforming (TX BF) can be generated with local counters. However, this leads to large registers and counter cells for a dense array with a large number of delay steps. An alternative is

to implement TX control in a row/column (R/C) approach [24], [25], [26], [27]. This minimizes the amount of associated circuitry underneath the element but, in turn, limits the amount of possible TX patterns for application in a 3D ICE probe. A similar challenge is faced when externally generated pulses are only passed or blocked on the chip instead of local pulse generation [8], [26], [28].

Reduction of RX cables in the catheter has previously been achieved by multiplexing of transducer signals on fewer connections over multiple transmit/receive (T/R) cycles [28], [29]. To avoid the associated loss in frame rate, other designs have made use of the wider bandwidth of the channel compared to the imaging frequency. In these, several RX signals are multiplexed on a single connection within one T/R cycle [30], [31], [32]. When applied for sensitive analog signals, crosstalk can become an issue [33]. Digital signaling, on the other hand, has been shown to be possible with a low impact on signal integrity [15]. Nevertheless, the achievable channel count reduction by both analog and digital multiplexing methods is limited by the small bandwidth across the thin cables in the catheter.

Another approach is to apply subarray beamforming, also known as micro-beamforming (μBF) [34]. This shifts part of the RX beamforming into the catheter by delaying and summing the received signals of a subarray of elements. However, it comes at the cost of less raw data being available in the final image reconstruction and reduced frame rate as multiple acquisitions are required per reconstructed volume [35]. Both disadvantages can be mitigated while achieving significant cable-count reduction by a combination of subarray beamforming and digital time-division multiplexing (TDM). This has been shown with element-level digitization with subsequent digital beamforming [36], [37], digitization of the output of analog beamformers [15], [18], [38], and mixed schemes [39]. However, even more can be gained from the digital transmission as ultrasound imaging can tolerate higher bit error rates (BERs) than most communication links [40]. While current digital probe designs commonly rely on conventional LV differential signaling (LVDS) [15], [17], [18], [41] with relatively low BER, BER could potentially be traded to reduce the circuit area and power consumption. Moreover, it could allow for a lower cable count by dividing the total output data bandwidth across fewer channels with a higher transmission rate.

An additional aspect to consider in the design of ASICs for arrays with a large number of elements, particularly for high-frame-rate designs with little opportunity for averaging, is the common-mode interference across the channels. With decreasing size, the noise level of the transducer increases [42], [43]. The noise of each front-end amplifier can thus generally be higher before limiting the global performance. The uncorrelated noise can then still reveal weaker signals after beamforming in the imaging system with an SNR gain of $\sqrt{N}$ for N combined signals [44]. As more elements are summed for a smaller pitch, the final signal-to-noise ratio is, to first order, equal for different element sizes in a transducer array of a given size [45]. However, correlated noise between channels effectively reduces the maximum gain achievable through beamforming, meaning that it should remain well below the noise floor despite the larger number of channels.

In this article, a pitch-matched ASIC with a co-integrated transducer array with a pitch of 160 × 160 μm is presented. This article builds on our previous work [15], extending it with an integrated TX beamformer and a novel low-power load-

modulation datalink, implemented in a prototype with a 4 × larger transducer array, scalable to a full 3D ICE probe. On-chip TX control is implemented by a compact combination of an R/C and an SR approach that offers all required beam patterns. Additional area savings are achieved by encoding the delay of the TX beamformer as the difference from its neighbor, similar to [22], and re-using the shift-register cells as counters for delay generation. Local biasing schemes for the transducer and analog front-end (AFE) amplifiers enable quick settling of the input after the TX phase and a lower impact of correlated noise on the final image. In addition, a multilevel pulse amplitude modulation (PAM) channel combined with TDM and µBF achieves an RX cable-count reduction of 18 while still enabling a high frame rate of 1000 volumes/s. To reduce the heating of tissue in the patient, the driver is implemented as a load modulation (LM) architecture.

8.2. SYSTEM DESIGN

8.2.1. OVERVIEW

Figure 8.1(b) shows an overview of the developed system. A matrix of 16 × 18 transducer elements is designed for directly interfacing the presented ASIC, as shown in Figure 8.1(a). The 160-µm-pitch transducer stack is a revised version of the concept shown in [46]. The circuitry interfaces with the PZT elements through individual connections made with a gold contact on the bottom side and a common aluminum ground foil on the top.

On the side of the chip, implementation in a 0.18-µm BCD technology offers a trade-off between the ability to integrate high-voltage (HV) TX-related structures and LV logic as well as RX-related structures. Each element is connected to individual TX and RX paths to efficiently use the space inside the catheter. An isolating T/R switch between the two paths protects the receiver from HV breakdown during transmission. The receiver also implements time gain compensation (TGC) to manage the dynamic range (DR) requirement of ICE. While imaging is often done with a range of only 40 dB, ultrasound attenuation inside the human body can lead to a total DR in the order of 100 dB within one T/R cycle [15]. However, as the attenuation is time-dependent, TGC can still reduce the DR to the following components by complementing it with a time-varying gain [13]. The matrix is further grouped into subarrays of three elements each and subgroups of two subarrays each. To enable a front-end layout matched to the pitch of the transducer element, all backend circuitries, such as the datalinks and data output drivers, are pushed to the periphery. This enables the design of subgroups as unit cells that can be replicated to create a larger aperture. The periphery-level circuitry is designed in units as well and only occupies two sides, the top serving the upper and the bottom serving the lower half of the matrix, to allow scaling along one direction.

This design serves as a prototype to evaluate the architecture and shows techniques for application in a full ICE probe. While all of the functionality required for the realization of the 64 × 18-element imaging scheme presented in [10] is included, only one-fourth of the aperture in the azimuth direction is accommodated in this step. To characterize the performance of the 1D subarray beamformer in the

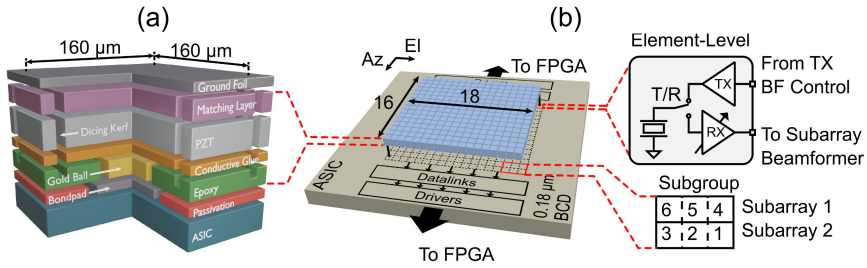

Figure 8.1: (a) Conceptual drawing of transducer stack. (b) Overview of chip assembly with details on the matrix organization.

elevation direction and the imaging approach, the full aperture is implemented along that axis. The beamformer of just three elements enables a high frame rate as only a few acquisitions are required per volume. The full probe targets a 10-cm imaging depth and thus operates at a PRF of 7.7 kHz considering the speed of sound in human tissue. Being able to image with just seven fan-shaped beams per frame, this results in a total frame rate of up to 1000 volumes/s. The seven steps employ a TX beam with 10.7° divergence in the elevation and 70° divergence in the azimuth direction and steer the subarray beamformer in a ±30° window in the elevation direction accordingly to achieve a field of view of 70° × 70° × 10 cm [10].

8.2.2. ARCHITECTURE

Figure 8.2 shows the architecture implemented in the presented design. The topology is building on what has been discussed in [15] and the TX part is based on the unipolar pulser with embedded T/R switch introduced in [47]. Compared to [47], the TX voltage was reduced from 65 to 30 V to allow for additional guard rings in the layout. Higher TX voltages could be achieved with the same architecture by adopting a silicon-on-insulator technology with deep-trench isolation. In this design, the control of the TX BF is realized with per-element digital delay cells that are configured in a mixed scheme. While global steering information is provided on the level of rows or columns of elements to save area, individual control is supplied by an SR spanning the whole matrix. To minimize the number of connections inside the catheter, the SR is also used to load the row and column data as well as all global configuration settings. The entire SR content of about 1.5 kb can be loaded in around 15 µs at a clock frequency of 100 MHz. The SR is updated during the RX period and thus forms an upper limit to the PRF at about 66 kHz, irrespective of the imaging depth.

On the receiver side, each element is individually connected to a low-noise amplifier (LNA), followed by a second-stage programmable gain amplifier (PGA) that also acts as a singleended-to-differential converter. The LNA can be discretely switched in steps of 18 dB from −12 to 24 dB and the second stage can be configured in steps of 6 dB from 6 to 24 dB. The global step size of 6 dB enables TGC with a range of 54 dB in ten steps from −6 to 48 dB with a compact implementation. The LNA

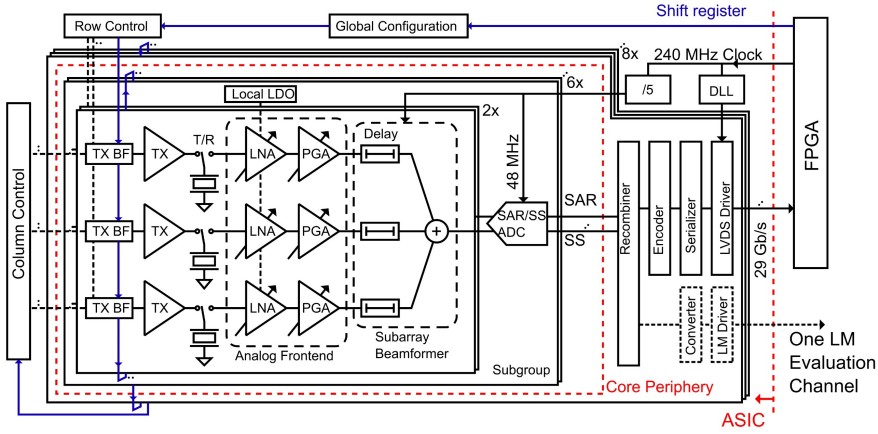

Figure 8.2: Architecture overview showing how element-level circuitry, subarray beamformers, and a shared ADC structure per subgroup are combined. The arrangement of the SR and R/C approach is sketched and a global view of the data management and clocking is provided.

architecture is a modified version of the design in [48] and was employed in [15] to enable operation with HV transmitters and seamless gain switching during echo reception in a single T/R cycle. As the received signal is most sensitive at this point, a local regulator for the LNA supplies is installed on the subgroup level here as well to reduce the effect of common interference across the whole array. The PGA is based on [18] and [49], was employed in [15], and is again adapted to get full TGC range within one T/R cycle and thus full frame rate.

The digitization from [15] is adopted with the same parameters in this design since both implementations target the same application. Three elements are combined in the elevation direction for analog subarray beamforming in the charge domain. Two neighboring subarrays are combined for layout with a shared hybrid beamforming analog-to-digital converter (ADC) in a subgroup. The ADC combines a successive approximation register (SAR) first stage and single-slope (SS) second stage and operates at 24 MS/s per channel with a resolution of 10 bits. To allocate all hardware in the core, the SAR and SS outputs are individually transferred to the periphery.

On the periphery, two datalink configurations have been included. The regular one features recombination of the SAR and SS output to 10-bit words, 8b10b encoding [50], and serialization to conventional LVDS drivers. In the process, fourfold TDM is applied, leading to a rate of 1.2 Gb/s per channel and, together with threefold subarray beamforming and considering the differential nature of the signals, a total cable-count reduction factor of 6. The second setup only serves one channel and provides a parallel path from the recombination to a multi-level encoder and an LM driver. This enables conventional access via field-programmable gate arrays (FPGAs) [51] to the whole array for convenient imaging while providing

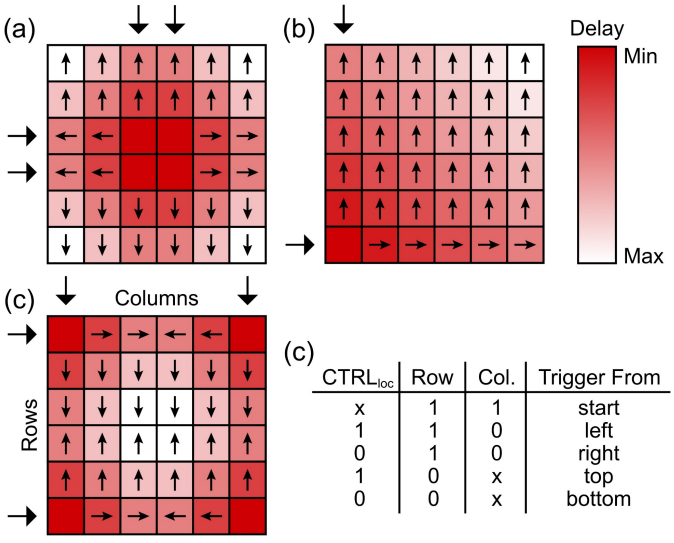

(c)

$CTRL_{loc}$	Row	Col.	Trigger From
x	1	1	start
1	1	0	left
0	1	0	right
1	0	x	top
0	0	x	bottom

Figure 8.3: Examples of TX beamformer delay patterns with arrows indicating the delay propagation for a 6 × 6 array. (a) Centered diverging wave. (b) Diagonal plane wave. (c) Focused wave. (d) Decision table for the delay propagation based on SR and R/C input.

an evaluation platform for the novel datalinks discussed in a later section. The periphery and core are timed by shared dividers and delay-locked loops (DLLs) working on a 240-MHz clock provided by the FPGA.

8.3. CIRCUIT IMPLEMENTATION

8.3.1. TX BEAMFORMER

To achieve a compact TX BF implementation, the system operates by passing a single trigger signal through the entire array based on relative delays between neighboring elements. This reduces the required delay depth per element and associated counting steps. For further area savings while still enabling the creation of all required beam patterns, the control of the propagation direction is done from the R/C level but also with one local bit from the SR, $CTRL_{loc}$. Figure 8.3 shows the examples of TX patterns that can be generated with the presented method. The targeted imaging scheme [10] relies on diverging waves that are generated by propagating a delay from the center outwards as shown in Figure 8.3(a). However, it is also possible to create other common patterns, such as the angled plane waves in Figure 8.3(b) or focused waves in Figure 8.3(c). The graphs also demonstrate how these patterns are created by indicating the starting position and R/C control with arrows along the side of the matrix. Arrows in the matrix are pointing from the element that the trigger signal was received from and Figure 8.3(d) presents the complete element-level logic table.

The circuit of an SR BF cell is shown in Figure 8.4. The local relative delay value is loaded into three flip-flops (FFs) as part of the SR with the SR input, IN_{SR}, and clock,

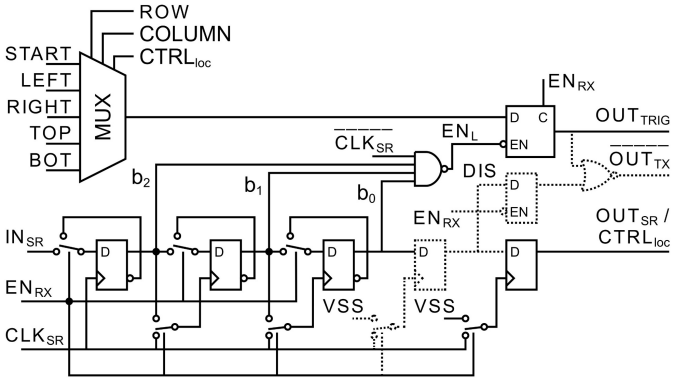

Figure 8.4: Circuit details of a TX beamformer cell with additional local pulse disabling in dashed lines.

CLK_{SR}. As the delay information is only required during the TX phase, loading of the delay cells in the SR is done during RX without additional hold cells. Moreover, an area-efficient implementation is reached by repurposing the unused SR cells to counters during TX based on the T/R control signal, EN_{RX}. The reconfiguration is achieved by switching the FF data inputs to an inverting feedback loop around the cell and using the data output of lower order bits as the clock input of higher order bits, leading to only a few switches as overhead instead of more FFs. The number of delay steps equals 2^N, N being the number of counter cells, and the actual delay is determined by the frequency of CLK_{SR} during TX as it remains connected to the least-significant bit (LSB), b_0. In this design, the 100-MHz SR clock is maintained during TX and there are three counter cells per element, leading to a total of eight steps from 0 to 70 ns.

The counter rotation is converted to an enable signal for a latch, EN_L, by detecting its highest value with a negative-AND (NAND) gate. All counters are continuously active during TX, but only when the dedicated neighbor has previously received the external trigger, it is copied further with the relative delay. Including an inverted version of CLK_{SR} can block any glitches in the asynchronous counter and clearing the latch during RX with EN_{RX} prevents any TX triggers in the wrong phase. Selection of the latch input is made with a multiplexer (MUX) controlled by the R/C signals and the output of the last element-level SR cell that serves as $CTRL_{loc}$ but also as the output to the SR of the next element, OUT_{SR}. Five different input triggers can be selected, LEFT to BOT indicating the output triggers, OUT_{TRIG}, of all neighboring elements and START being the initial external trigger. Figure 8.5 shows, as an example, the operation of three neighboring elements in a row. In Figure 8.5(a), the state at the beginning of the TX cycle is shown. The middle element is configured as a starting point. The left and right elements are configured to receive their trigger from the middle element (i.e., their right and left neighbors, respectively). The timing diagram of the whole procedure from the end of the SR operation in RX to the actual output triggers is shown in Figure 8.5(b). The output triggers are directly used to control the pulsers and a diverging wave, steered to the left, is created.

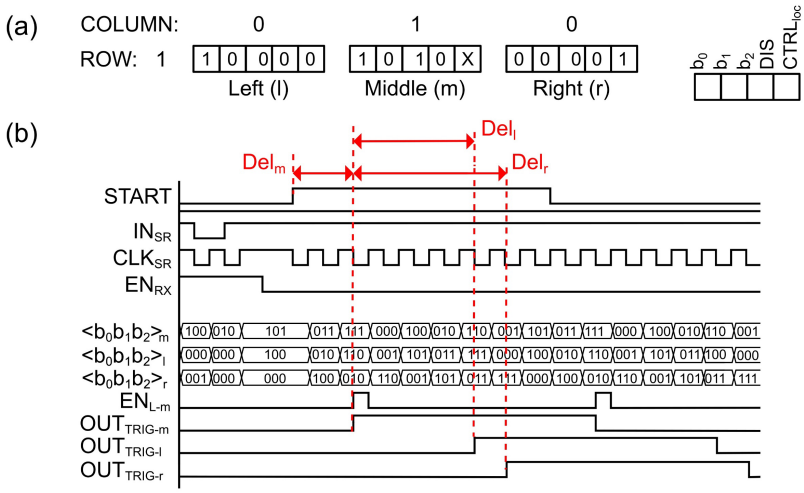

Figure 8.5: (a) Example of the status of three neighboring cells at the start of the TX period. (b) Timing diagram showing the SR loading of the TX beamformer cell, subsequent pulsing based on the delay from the START trigger, and further propagation to neighboring cells.

The dashed circuitry in Figure 8.4 is optional and has been included to support additional debugging by excluding single elements from the entire imaging operation. The implementation adds 1 bit in the local SR to receive a disable signal, DIS, and latches it such that it is also available during the RX phase. By not directly using OUT_{TRIG} to control the pulser but manipulating it with a negative-OR (NOR) gate to OUT_{TX}, elements can be permanently connected to the HV supply. At the same time, the rest of the array can function as usual as the trigger is still being passed.

Next to a compact design, TX BF by shifting an LV trigger signal through the system also has the benefit of being able to dynamically change the number of pulses and even pulse frequency if required. One potential drawback for some applications is that only delays smaller than the pulse width can be generated as EN_L needs to latch during the active interval. However, this is commonly no issue for ultrasound imaging as is analyzed in the following. Typical ultrasound imager arrays remain at a pitch of half of the center transmit wavelength, λ, as that moves grating lobes out of the picture [52]. As the relative difference in distance, D, from a virtual source (VS) between neighboring elements can at most be equal to the element pitch, it can be

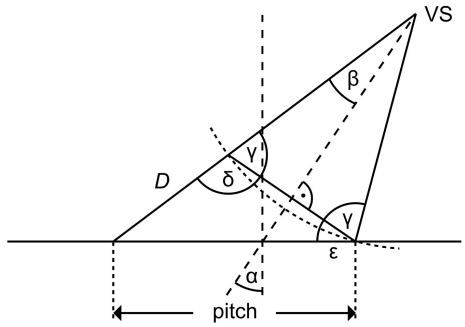

Figure 8.6: Drawing showing the difference D in excitation of two elements with a certain pitch in order to create a steered diverging wave.

shown that the maximum possible delay for these devices is half of the pulse period and thus in the coverable range

$$t_d = \frac{D}{c} = \frac{\frac{\lambda}{2}}{\lambda \cdot f} = \frac{T}{2} \tag{8.1}$$

where t_d is the required delay between elements, c is the speed of sound, f is the center frequency, and T is the pulse period. A way to determine the delay between neighbors for any pitch is shown using the diagram in Figure 8.6. The relative distance from the VS can be calculated with

$$D = \frac{\sin(\alpha)}{\cos(\beta)} \cdot \text{pitch} \tag{8.2}$$

where α is a known angle determining beam steering and β is a known angle determining beam divergence. The equation is found by applying the law of sines on the lower triangle based on angles δ and ε, found with trigonometric equations, and can be used to derive the required delay by DEL = D/c. Although the pitch is slightly above half of λ, this results in maximum delays in the order of 70% of the 80-ns pulse width for the shown design with the intended 10° divergence and maximum steering angle of 30° [10].

8.3.2. LOW-NOISE AMPLIFIER

The LNA architecture is based on the design presented in [35] but has been extended to enable co-integration with TX and high-frame-rate operation. Figure 8.7(a) shows a simplified schematic of the prior design with a direct connection of the input node, V_{IN}, to the transducer element and input biasing to V_{ref} through a high-impedance path, R_{IN}. A compact implementation is reached by a split capacitor feedback network [53], an efficient inverter-based amplifier core, and dynamic biasing to

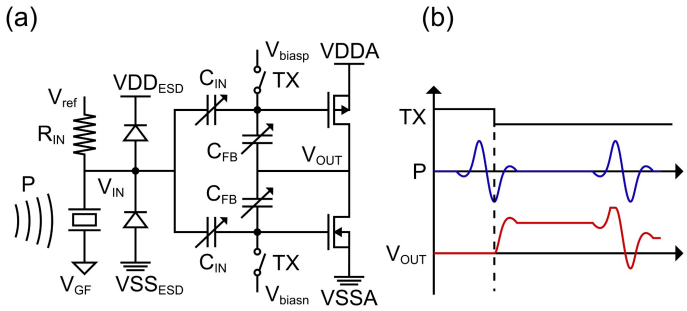

Figure 8.7: (a) Simplified schematic of an inverter-based amplifier with split capacitor feedback and dynamic biasing. (b) Illustration of how the initial transducer state and forward biasing diodes due to large inputs can lead to offset issues with dynamic biasing.

potentials V_{biasx}. Discrete TGC is achieved by reconfiguration of the capacitor network comprised of C_{IN} and C_{FB} between receive cycles.

While the shown techniques have led to a receiver with state-of-the-art power and area efficiency, there are several concerns in the transition to a high-frame-rate imaging system with TX and RX on each element. To illustrate this, Figure 8.7(b) shows two common problems that can be experienced in a transducer front end with incoming pressure waves, P, and dynamic biasing. To achieve quick settling following TX, the dynamic biasing is synchronized to the T/R cycle and active until shortly after TX is completed. The first issue is that, since echoes start returning immediately after the ultrasound transmission, the switching can never be guaranteed to take place at a moment in which no signal is present. As pulsing and dynamic biasing in a short-time window require a reference with a relatively low impedance, the final direct current (dc) operating point will be signal-dependent and can lead to a large offset. The second issue is that strong incoming signals, which often occur shortly after TX due to low initial attenuation in the medium, can lead to clipping due to the electrostatic discharge (ESD) protection diodes or the internal rails. This would change the dc operating point even during active RX, with no possibility to recover in a pure dynamic biasing implementation.

Irrespective of these external effects, the limitation to biasing in a short-time interval before reception also leads to issues if one would switch through all gain levels of the discrete TGC scheme due to non-ideal switching procedures. Finally, the transducer needs to be biased to a reference, V_{ref}, being, e.g., just the dc level of a bipolar pulser [14] or a mid-rail reference if the pulsing goes all the way to the negative rail [54]. Since this would need to happen in a short-time interval after TX, it cannot be covered by the high-impedance connection with R_{IN} for a design with TX and RX on the same element.

Figure 8.8 shows the implemented design with the proposed changes. The LNA is still applying dynamic biasing to quickly settle all critical nodes in a short-time window after the possibly high disturbance of HV TX. To target the issues discussed above, this is assisted by the connection of the transducer to a mid-rail potential, V_{CM}, via resistors. The switches are controlled with RST_{LNA} and $RST_{LNA\text{-}DEL}$ to always close at the beginning of an RX period. $R1$ is used to raise the transducer top plate from its

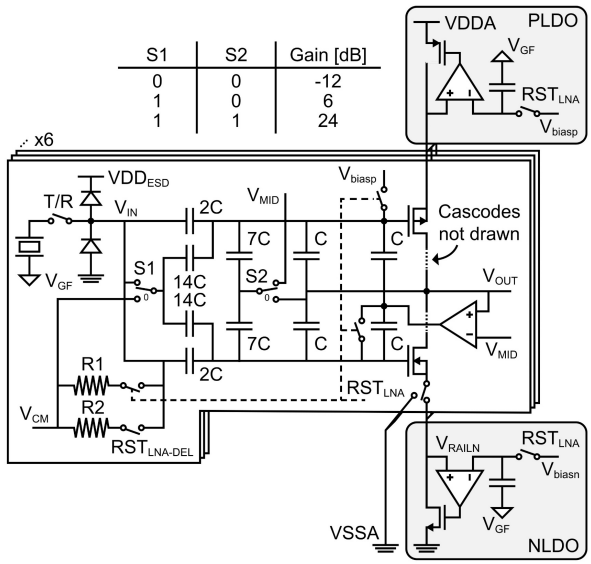

Figure 8.8: Conceptual schematic of the inverter-based LNA showing gain switching, transducer biasing, and supply regulators.

initial state of 0 V after pulsing to V_{CM}. The resistance is in the order of 50 kΩ to allow settling in 100s of ns, not losing too much RX time but also not causing a second transmission. $R2$ is around 1 MΩ and connected longer, in the order of microseconds, to settle any offset due to large inputs received shortly after TX but then also disconnected as it is a potential source of noise and interference from other channels.

Next to the added resistive components, the biasing has also been modified compared to [35] by adjusting the way in which the inverter transistors are operated. During initial dynamic biasing, the upper transistor is still directly connected to a biasing voltage, V_{biasp}, and the lower transistor is still driven by an amplifier in a feedback loop to force the LNA output voltage, V_{OUT}, to a local mid-rail potential, V_{MID}. However, this amplifier is not switched out and shorted after that but instead connected to two capacitors in parallel with the feedback capacitors of the LNA. This gives the structure a low-frequency path to correct for effects such as disturbances from gain switching or residual issues in the transducer biasing. Due to the low bandwidth of the additional amplifier and the capacitive attenuation toward the output, its noise contribution in the signal bandwidth as well as the power and area are negligible compared to the entire LNA.

The capacitor ratios and unit cells, C, of 45 fF are the same as in [35]. The input capacitors are held at the same potential the transducer is biased to, V_{CM}, before being switched in to minimize introduced disturbance in the RX period. Similarly, the feedback capacitors are connected to the same potential V_{out} that is driven to via the low-bandwidth loop after being switched out. After these capacitors are settled,

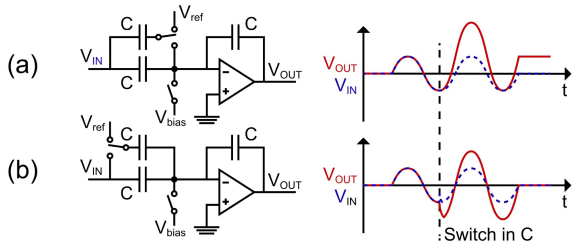

Figure 8.9: Impact of switching the gain of an amplifier in a dynamically biased capacitive feedback in active operation from (a) back and (b) front.

there is also the option of removing them from V_{MID} in order to remove the noise from that source.

To mitigate the low power supply rejection ratio (PSRR) of the inverter-based topology [55], the LNA employs the local regulators [56] as in [35] and [48]. In this design, they are shared on the subgroup level and it can be chosen to switch to the analog ground, VSSA, instead of the negative low-dropout regulator (LDO) to investigate differences. In addition, the dynamically set references of both LDOs are capacitively coupled to the ground foil node of the transducer, V_{GF}. This enables the architecture to also reject variations of the ground foil node that would otherwise be amplified with the signal. Combined with the improved PSRR, this aims to reduce the common-mode interference across channels and thus maximize the possible gain from RX beamforming.

8

8.3.3. PROGRAMMABLE GAIN AMPLIFIER

The circuit implementation of the PGA is based on the compact architecture shown in [18] but modified as the original structure cannot support high-frame-rate operation and has a limited output swing. The main issue with volume acquisition at a high rate is presented in Figure 8.9. The prior design is similar to Figure 8.9(a) and achieves gain switching by adding a capacitor to the virtual ground of an amplifier in a capacitive feedback configuration. While the constant load presented to the driving stage of this setup is beneficial, this switching alters the operating point of the setup and leads to an offset if done during active operation. As the system is dynamically biased with V_{bias}, it cannot recover over time and even with a low-bandwidth correction path, and the possibly large step could lead to a significant loss of image information.

With the approach shown in Figure 8.9(b), on the other hand, this can be avoided since the virtual ground node is not affected when the capacitor is switched from the input. The input experiences a short settling depending on the driver but then continues operation without an offset. In the proposed design, the configuration of Figure 8.9(b) is adopted to enable gain switching during echo reception. This enables full TGC in one T/R cycle, rather than having to combine repeated T/R cycles with different gain settings, thus facilitating high-framerate

(a)

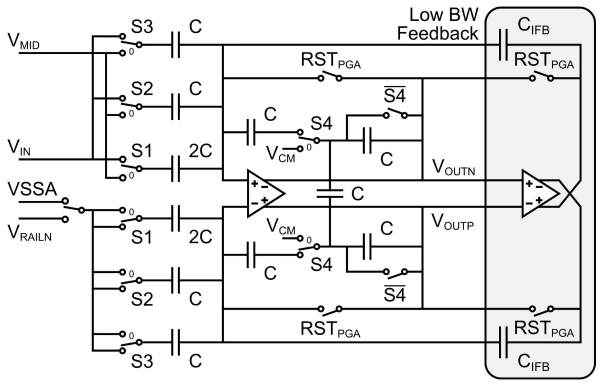

(b)

S1	S2	S3	S4	Gain [dB]
0	1	1	0	6
0	1	0	1	12
0	1	1	1	18
1	1	1	1	24

Figure 8.10: (a) Sketch of the PGA displaying gain switching and the implementation of a low-bandwidth feedback amplifier. (b) Logic table to determine the gain.

operation. Figure 8.10(a) shows the schematic implementation with compact T-type feedback [49] and Figure 8.10(b) presents the associated logic table to determine the gain depending on the switch settings. During one RX phase, the PGA will cycle through the settings three times to complement the three LNA gain switches to the full TGC range. To minimize the disturbance from gain switching, the input capacitors are connected to the output dc level of the LNA and the feedback capacitors are connected to a mid-rail potential, V_{CM}, when not in the loop. The LNA has sufficient phase margin and bandwidth to operate with the switching capacitance at its output and achieve quick settling.

Similar to [18], the structure is held in reset during TX to enable quick settling of the operating point after HV pulsing, but in addition to that, a low-bandwidth feedback path has been introduced. This enables the correction of any remaining disturbance caused by switching during one T/R cycle while adding little area and power consumption compared to that of the entire PGA. As they are not part of determining the signal gain, the capacitors of the low-bandwidth path can be adjusted in a tradeoff between attenuation of additional noise and achievable correction range. In this design, the unit capacitance, C, is 33 fF and the additional capacitors, C_{IFB}, are 9 fF. Combined with the low bandwidth of the feedback amplifier, the noise contribution to the signal path is negligible. Similarly, the mismatch between C and C_{IFB} will have a low impact on the overall noise performance of the PGA.

The configuration as a single-ended-to-differential converter from the prior design is kept to enable differential operation of the ADC and dummy switches are placed in the bottom branch of the feedback network as well to balance the design. However, instead of connecting to a mid-rail supply, the bottom branch is driven relative to the reference of the single-ended input. This ensures that no interferers

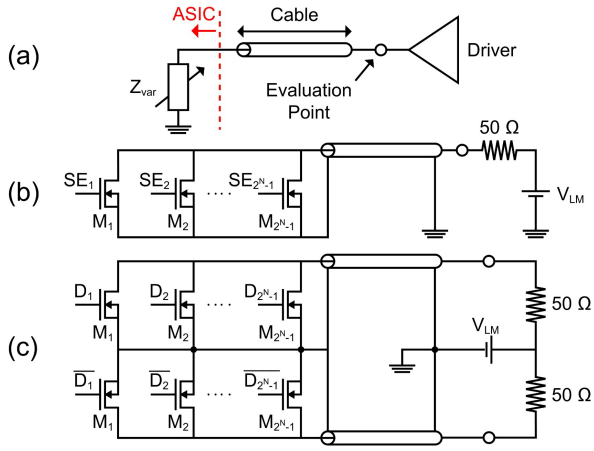

Figure 8.11: (a) Block diagram summarizing the idea of LM. (b) Example of a single-ended LM implementation. (c) Example of a differential LM implementation.

are unintentionally amplified with the received signal and is realized by mirroring the negative rail connection of the LNA. The telescopic amplifier has moreover been replaced by a two-stage miller-compensated differential amplifier with an auxiliary amplifier to provide common-mode feedback [57]. The division in a first gain stage and a high-swing output stage can show bandwidth and power consumption similar to [18] while providing a larger output swing for the ADC and not leading to gain deviation.

8

8.3.4. DATALINK

To explore possibilities to reduce the RX-related cables in the catheter, this design leverages the relatively relaxed BER requirement of ultrasound imaging [40]. By applying a multi-level PAM driver, several bits are transmitted in one symbol, allowing for a higher throughput without increasing the symbol rate that would cause limitations due to the low bandwidth of the thin cables [58] and applied process node. To reduce the power consumption associated with data transmission at the tip of the catheter, where heating must be limited to ensure safe operation in the human body [59], the driver has moreover been implemented based on LM [28]. Instead of direct driving, this only switches a variable load impedance, Z_{var}, on the chip with a driver on the other end of the cable, as shown in Figure 8.11(a). This enables measurements at an evaluation point outside the body with part of the power consumption shifted to the system side where heating is not an issue.

In this design, single-ended and differential multi-level LM implementations are investigated. Figure 8.11(b) gives an overview of the single-ended setup with the variable load being implemented by 2^N - 1 transistors with scaled widths M_X, where N is the number of bits per symbol. The array is controlled with a thermometer code

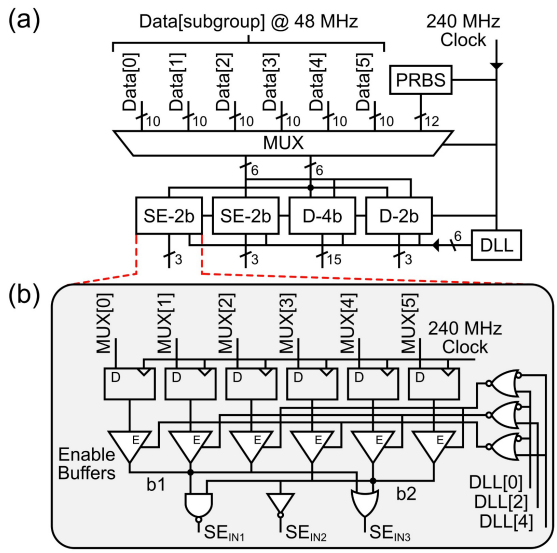

Figure 8.12: (a) Overview of the data and control configuration for the multi-level signaling. (b) Details of a single-ended implementation with 2 bits/symbol.

in SE_X and forms a divider with the termination resistance to a power supply, V_{LM}, on the system side. The differential configuration in Figure 8.11(c) relies on the same mechanism but introduces a second, inverted path with the same scaling via a second cable. For 2 bits/symbol, the switches are designed from about 15 to 130 Ω, and for 4 bits/symbol, they are designed from about 10 to 850 Ω. While a differential channel takes an additional cable, more power consumption, and circuit area, the gained rejection of common interference compared to the single-ended structure can be beneficial in a narrow catheter with multiple parallel connections. In addition, the shared return current in the ASIC will be constant to the first order, reducing possible crosstalk between channels, and the differential signal swing is twice as high for the same supply. This potentially enables a higher bandwidth per channel at the same BER as the single-ended setup and makes differential signaling an interesting part of this study.

Figure 8.12(a) gives an overview of the realized test setups in this design and their control. The 60 recombined data bits from six ADC pairs operating at 48 MHz are multiplexed into 12-bit words at 240 MHz. Based on this input, three different configurations are being analyzed in parallel: a differential driver with 2 bits/symbol at 1.44 GS/s (D-2b), a differential driver with 4 bits/symbol at 0.72 GS/s (D-4b), and two single-ended drivers with 2 bits/symbol at 0.72 GS/s that share the total data input (SE-2b). All of these achieve the targeted RX data cable reduction of 18 to ultimately arrive at a total of 64 data connections for the full probe [10] and enable the direct comparison of all schemes. The timing is provided by a DLL that creates six phases out of the input clock to accommodate the highest transmit frequency.

The internal structure of the control blocks is shown by the example of a single-ended cell in Figure 8.12(b). After synchronization of the recombined and

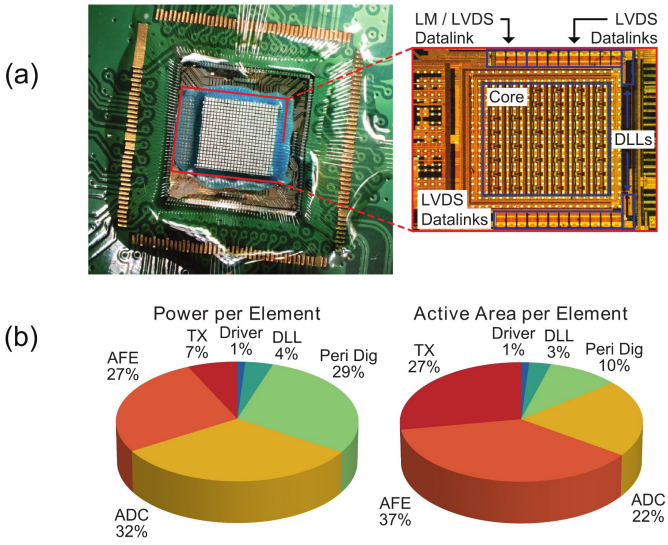

Figure 8.13: (a) Micrograph of a chip with transducer stack on its surface and an inset showing the global floorplan below. (b) Power and active area per element divided among major contributors.

multiplexed ADC outputs to the input clock, an array of buffers is used to drive two outputs, b1 and b2. The buffers can be disabled to have a high output impedance and effectively multiplex onto one output based on the overlap of phases from the DLL. Local generation of the overlap avoids the need for distributing a high-frequency clock and is done with one layer of logic gates. For the single-ended setup, only every second DLL output phase is required to realize the 0.72-GS/s output stream. In the last stage, the binary signal is converted to a thermometer representation for the LM driver based on logic gates.

The system also provides a second path with a pseudorandom bit sequence (PRBS) generator to be able to investigate the BER. It is implemented as a linear-feedback SR (LFSR) of 20 cells with 12-bit parallel output [60].

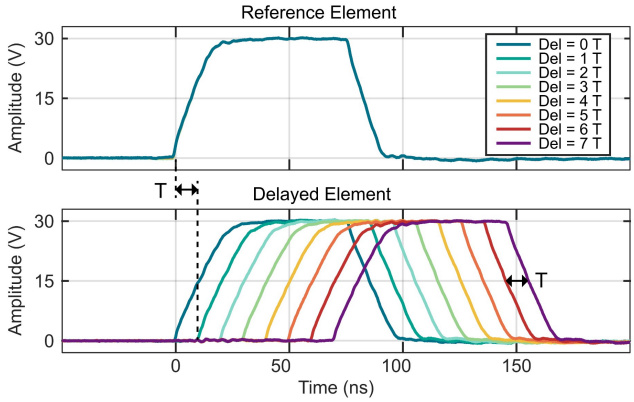

Figure 8.14: Measurement of the transmit delay between two neighboring elements with configurations from the minimum to the maximum setting.

8.4. EXPERIMENTAL RESULTS

An overview of the manufactured device is given in Figure 8.13(a). The ASIC has been fabricated in a 180-nm HV BCD technology and a transducer stack with a 160-μm pitch, 6-MHz center frequency, and 50% bandwidth has been manufactured on its surface. The 16 × 18 element matrix is complemented by two rows of dummy transducer elements to reduce edge effects and the ASIC measures a total of 7 × 7 mm in order to ease manufacturing of the prototype transducer. In the inset, the global floorplan shows a separation in two halves with datalinks on the top and bottom, enabling further scaling of the unit-cell-based structure along the horizontal axis. On the TX side, the circuit operates on a 30-V supply for the pulsers, a 5-V supply for driving the pulsers, and a 1.8-V supply for digital operations. The receiver is powered from a separate analog 1.8-V supply with an additional 1.2-V supply for the DLL delay cells and a 2.3-V supply for parts of the ADC [15].

Figure 8.13(b) presents the system-wide power and active area distribution per element. All displayed power consumption is based on measured supplies during active operation and labeled with the most dominant contributor of the relevant segment. The total power consumption of 1.2 mW per element is dominated by the RX path with 27% being primarily associated with the AFE including LDOs, 32% to the ADC, and 29% to the digital periphery blocks realizing recombination and conversion for LM signaling. The DLLs just account for about 4% of the total power as they are heavily shared across the array and the LM driver can achieve a share of only approximately 1% per element. The TX power consumption is highly dependent on the imaging mode but is generally a minor contributor due to the duty-cycled nature of ultrasound imaging. The displayed values are obtained with a three-pulse excitation of all elements at the maximum transmit voltage and 10-cm imaging depth, such as used for the creation of the b-mode images shown in this article. In the total active area of 0.03 mm^2 per element, the TX-related structures take a larger share of 27% due to area-intense HV isolation in the BCD technology. On the RX side,

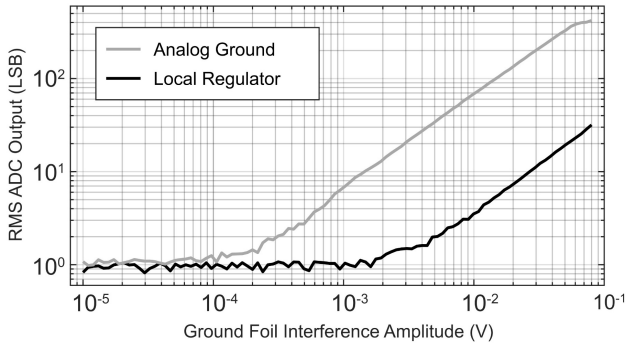

Figure 8.15: Measured ADC output relative to the amplitude of an interfering signal applied to the ground foil node in the case of LNA connection to the shared analog ground or local negative supply regulator.

the AFE is the main contributor with 37%, while the remainder is shared between about 22% for ADC-related structures, 10% for the digital periphery blocks, 3% for the DLLs, and 1% for the LM driver.

To evaluate the effectiveness of the implemented techniques, electrical and acoustic experiments have been conducted. The two configurations are each assembled with an individual daughter board to facilitate their specific requirements. Electrical test boards offer direct wire bonding to element-level bondpads, while acoustic samples are assembled with a prototype transducer matrix. A custom mother board is designed to be compatible with both, and interfaces with a computer for data processing through commercial FPGAs [51].

8.4.1. ELECTRICAL MEASUREMENTS

Figure 8.14 shows the electrical characterization of the tansmit beamformer. Two neighboring elements are each connected with a capacitor to mimic the capacitive load of a single transducer element of about 2 pF. The delay between them is swept through all the configurations from zero to seven unit time periods, *T*. The interval is determined by the clock frequency of the time reference and is in this case approximately 10 ns. The waveforms exhibit the targeted slewing and extend to the maximum transmit amplitude of 30 V.

To investigate the implemented scheme for common-mode interference rejection around the first-stage amplifier, an experiment with an intentionally injected interferer is carried out. Figure 8.15 shows the root-mean-square (rms) ADC output caused by an amplitude sweep of a 6-MHz sinusoidal signal driven onto the ground foil node with the LNA input being connected to it in the highest gain setting. To study the effects, the two configurations of the negative supply connection of the LNA, either to the shared analog ground node or the local negative supply

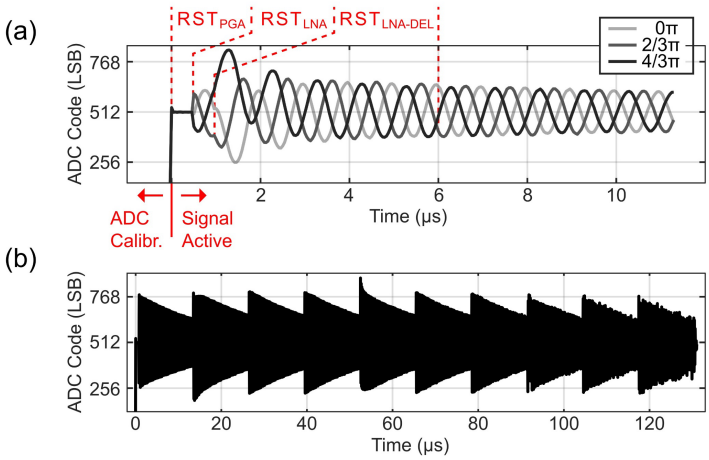

Figure 8.16: (a) Initial converter output settling for an exponentially decaying sinusoidal input with three different phases and indicated amplifier biasing times. (b) Converter output showing settling during a full T/R cycle with TGC and an exponentially decaying sinusoidal input.

regulator, are compared. The larger ground foil interference required to elevate the output code from the noise floor in the case of LNA connection to the local regulator shows the effectiveness of the suppression.

The settling of biasing points in the presence of input signals is studied with a 2-pF capacitor, modeling the capacitive component of the transducer element, in series with an arbitrary waveform generator (AWG). Figure 8.16(a) shows the ADC output at the beginning of a receive phase with three different phases of an exponentially decaying 1-MHz sinusoidal input in the lowest gain setting. The signal is active before the dynamic biasing is completed and shows the response to different initial states of the high-impedance input node when actual reception is started. Typically, $\mathrm{RST_{PGA}}$ would be asserted longer than $\mathrm{RST_{LNA}}$ to optimize settling, but it is in this case disabled earlier as it would otherwise mask the output signals needed to study the behavior. In this example, $\mathrm{RST_{PGA}}$ is active 500 ns after the start of input signaling with $\mathrm{RST_{LNA}}$ and $\mathrm{RST_{LNA\text{-}DEL}}$ being asserted 500 ns and 5 μs longer, respectively. The recorded outputs show a signal-dependent offset introduced after the completion of dynamic biasing and subsequent recovery provided by the resistive input biasing and the low-bandwidth amplifier feedback paths. Figure 8.16(b) additionally shows the ADC output during a full T/R cycle with an exponentially decaying 6-MHz input from an AWG. TGC is used from the lowest to the highest gain setting to maintain the output code level and it can be observed how non-ideal steps in the gain are compensated by the implemented biasing techniques.

To evaluate potential power savings from the implementation of a multi-level LM driver, Figure 8.17 shows a measurement of the obtained BER for a sweep of the LM supply voltage, V_{LM}, for all investigated configurations. All results are obtained using the PRBS generated on the chip and with an assembly of 42-AWG micro-coaxial

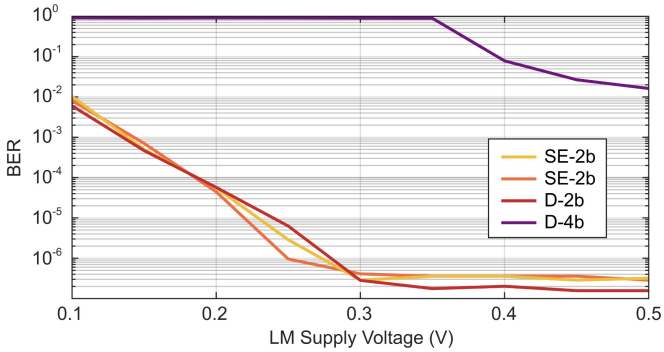

Figure 8.17: BER measured for all implemented multi-level datalinks in a sweep of the LM supply voltage.

cables with a 50-Ω characteristic impedance and a length of 1 m. The transmitted sequence is directly obtained by an oscilloscope and compared to the expected pattern after a decision feedback equalization step to determine the error rate. Due to the maximum memory depth of the oscilloscope, there is a minimum measurable BER at about $3e^{-7}$ for the SE-2b and D-4b configuration as well as half of that for the D-2b configuration. The acquired results show that even for an LM supply of about 0.27 V, all datalinks with 2 bits/symbol can achieve the targeted BER of $1e^{-6}$ to have negligible degradation of ultrasound images [40]. The significantly worse performance of the PAM-16 approach is attributed to the higher sensitivity to non-idealities in the transmitter circuit design, receiver, and equalizer when the spacing between signal levels reduces.

Out of all implemented setups, the differential transmitter with 2 bits/symbol is considered the most attractive option out of this experiment. It has a competitive performance compared to its single-ended counterparts with the same number of cables while offering more resistance to common interference. Further improvements are expected when replacing the two micro-coaxial cables for differential signaling with a differential cable. The total power spent in the D-2b setup for V_{LM} of 0.27 V is 1.2 mW, of which about 52% is spent on the chip and the rest in the 50-Ω termination and 9 Ω of the cable. Given the resulting 17-μW on-chip power consumption per element of the multi-level LM approach compared to the 260 μW per element for the implemented LVDS scheme, the designed topology shows great potential to trade surplus BER for lower power and cable count.

8.4.2. ACOUSTIC MEASUREMENTS

The characterization of the TX BF functionality is shown in Figure 8.18, following the example patterns shown in Figure 8.3. The measurements are obtained with the chip assembly being submerged in water and facing a 1 mm needle hydrophone (SN2082, Precision Acoustics Ltd., Dorchester, UK). By translation of the hydrophone with an *x yz*-stage during repeated transmission from the prototype, *C*-planes in parallel to

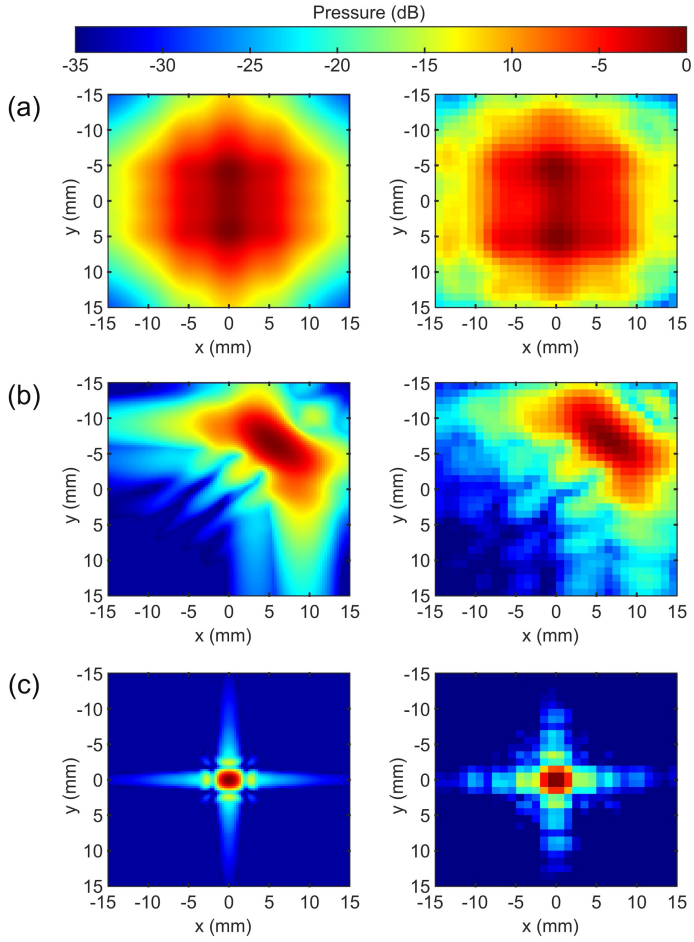

Figure 8.18: Comparison of simulated *C*-planes on the left and corresponding measured *C*-planes on the right for (a) diverging beam at 5 cm from the array, (b) plane wave steered to the northeast at 5 cm from the array, and (c) focused beam at 2 cm from the array.

the transducer surface are captured. These evaluate the maximum peak pressure at each position and are compared to simulations [61] based on the same set of delays. Figure 8.18(a) shows the simulated pressure profile at a 5-cm distance from the array for the transmission of a diverging wave on the left and the corresponding hydrophone measurement on the right. Figure 8.18(b) similarly shows the results for a plane wave angled at 10° to the northeast at a distance of 5 cm from the array and Figure 8.18(c) shows a plane 2 cm from the array with the TX BF focusing at its center. Good agreement between the measured and simulated profiles in all cases verifies the capability of creating the most common transmit-beamforming patterns applied in ultrasound imaging.

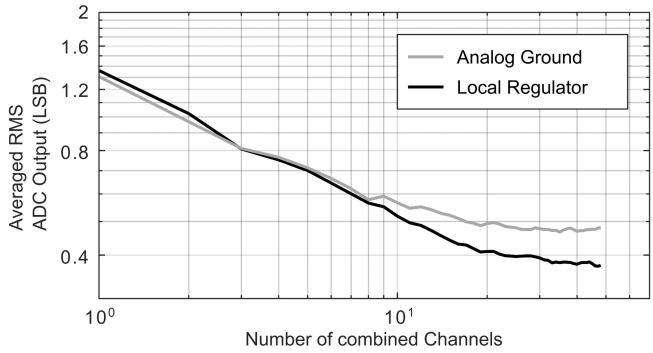

Figure 8.19: Investigation of the noise output of the array as a function of the number of combined channels with the LNAs being connected to the shared analog ground or local negative supply regulators.

An experiment investigating the noise behavior of the array is presented in Figure 8.19. In this experiment, a varying number of output channels of the chip were averaged to mimic the averaging operation associated with beamforming and the associated expected noise reduction. The measurements were done on a sample with transducer elements loaded with water and were recorded in the highest gain setting without an input signal. To study the effect on the noise floor, the experiment is conducted with the negative rail of the LNA being connected to the shared analog ground or local supply regulators. Figure 8.19 shows the rms value of the averaged outputs, as a function of the number of channels being combined. For both connections of the negative rail, there first is an exponential reduction in the amplitude before the two curves flatten off at different effective array sizes. The initial decline is close to the anticipated $\sqrt{N}$ improvement of uncorrelated noise for N combined signals [44] but gets limited by the presence of correlated interference between channels. The reduction in common interference and, thus, improvement of potential beamforming gain for the LNA connection to the local regulator compared to the direct analog ground connection can be explained with an enhanced PSRR. Noise on the shared power rails appears common to all elements and can, even in this reduced-size prototype and without active input, pose a limit to the beamforming gain.

To verify imaging functionality, a commercial 3D wire test phantom (model: 055, CIRS, Inc., Norfolk, VA, USA) has been studied with the setup shown in Figure 8.20(a). The ASIC is mounted on a custom daughterboard that faces the surface of the phantom. The daughterboard provides local decoupling and connects to a motherboard with active components for supply regulation and signal conditioning via 1-m cables. The acquired receive data from the 24 LVDS channels is captured and stored by commercially available FPGA boards [51] in real time. Each FPGA board offers eight high-speed transceivers and three boards are thus used in parallel, while one of them additionally acts as a control host for the ASIC configuration per T/R cycle. The acquired data are downloaded to a computer that initiates measurement routines and performs image processing.

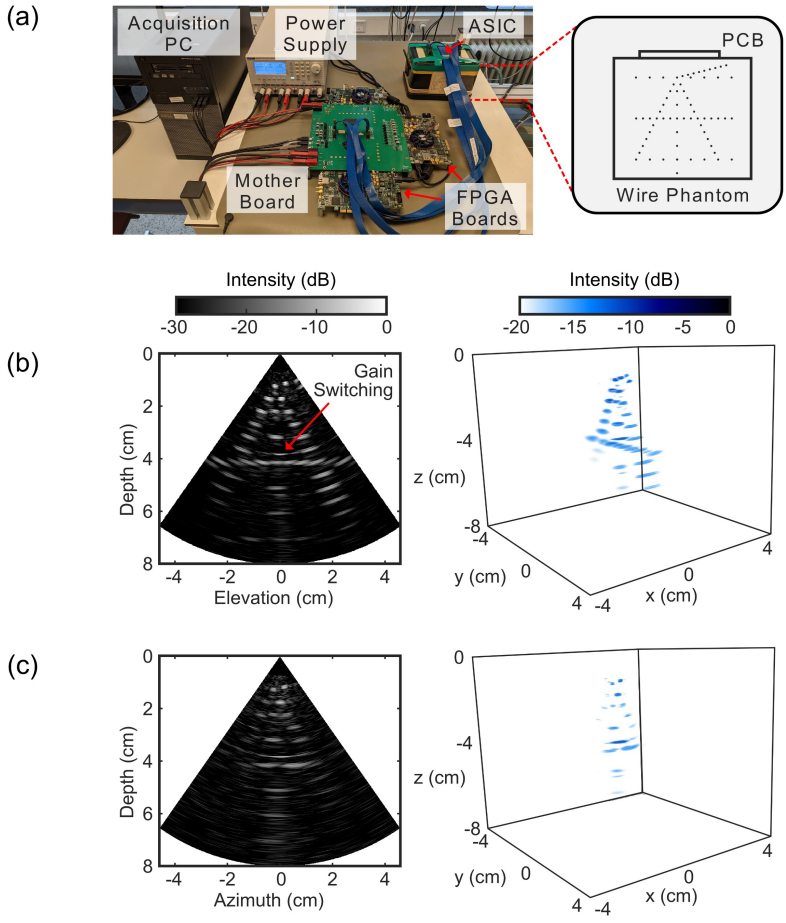

Figure 8.20: (a) Measurement setup used for imaging verification with details of the 3D wire phantom. (b) Reconstructed image plane in the elevation direction with 3D render. (c) Reconstructed image plane in the azimuth direction with 3D render.

Figure 8.20(b) shows a reconstructed image with the wires aligned in the azimuthal direction of the array so that they show up as point scatterers in the elevation plane. The upper seven gain settings of the TGC have been applied in each T/R cycle to maintain a suitable DR in the signal path across the attenuating phantom. A switching artifact can be observed when the LNA transitions to its highest gain setting while the PGA gain steps are barely noticeable. The artifact is caused by non-ideal switching resulting in a step in the RX signal and appears at a 0° azimuth and elevation angle after RX beamforming as the entire array is switching simultaneously. Given its deterministic nature, the artifact does not inherently harm the imaging and can potentially be compensated for during data processing.

As off-axis reflections do not propagate back to the transducer, the wire targets appear almost as points rather than lines in the 3D plot. The behavior along the other

dimension is thus evaluated by rotating the chip to align with the azimuth direction, as shown in Figure 8.20(c). The lower opening angle in the azimuth render is caused by the application of the imaging scheme described in [10]. This scans a volume of 70° × 70° × 10 cm at 1000 volumes/s with seven fan-shaped
beams with little divergence in the elevation direction and large divergence in the azimuth direction. As this prototype implements the full intended aperture in the elevation direction, the functionality of the 1D subarray beamformer and TX BF can be fully verified. By choosing to realize a beamwidth in the elevation direction that is the same as in the intended imaging scheme while having an aperture that is 4× smaller than the intended final size in the azimuth direction, the resulting azimuthal opening angle is approximately equal to the 20° opening angle in the elevation direction, for this approximately square array.

Table 8.1 summarizes the system and gives a comparison to the prior art in catheter-based ultrasound imagers. The system complements our earlier design described in [15] with an integrated TX beamformer and a novel multi-level LM while still providing the highest reported frame rate. This completes the architecture and shows a similar peak SNR in a 4× larger array.

Table 8.1: Comparison with the prior art in catheter-based ultrasound imagers.

	This work	JSSC'22 [15]	JSSC'21 [16]	VLSI'19 [17]	JSSC'18 [18]	TUFFC'16 [9]
Technology	**180 nm BCD**	180 nm BCD	180 nm	180 nm	180 nm	N/A
Transducer	**2D PZT**	2D PZT	2D PMUT	2D PZT	2D PZT	2D PZT
Array Size	**16 x 18**	8 x 9	6 x 6	4 x 4	6 x 24	60 x 14
Center Frequency	**6 MHz**	6 MHz	5 MHz	5 MHz	5 MHz	5.6 MHz
Pitch-matched	✓	✓	✕[†]	✓	✓	✓
Element Pitch	**160 µm x 160 µm**	160 µm x 160 µm	250 µm x 250 µm	150 µm x 150 µm	150 µm x 150 µm	110 µm x 180 µm
Included TX	**30 V**	65 V	13.2 V	✕	✕	40 V
TX Beamforming	**integrated**	external	integrated	✕	✕	integrated
Digitization	✓	✓	✓	✓	✓	✕
RX architecture	**AFE + µBF + ADC + Datalink**	AFE + µBF + ADC + Datalink	AFE + ADC	AFE + ADC	AFE + µBF + ADC + Datalink	AFE + µBF
El. / RX Cable	**18**[§]	6	0.5	0.5	18	15 to 20
Data transmission	**PAM-4 LM**[§]	LVDS	N/A	LVDS	LVDS	analog
Supported Frame-Rate	**1000 vol/s**	1000 vol/s	N/A	N/A	200 vol/s	50 vol/s
Active Area / El.	**0.030 mm²**[§]	0.032 mm²[§]	0.063 mm²	0.023 mm²	0.026 mm²[§]	N/A
RX power / El.	**1.12 mW**[§]	1.23 mW[§]	1.14 mW	1.54 mW	0.91 mW[§]	< 0.12 mW
Peak SNR	**52.2 dB**	52.3 dB	57.8 dB[‡]	49.8 dB	52.8 dB	N/A

[†] Scalability limited by a non-integrated transducer array and its connection outside of the pitch.
[§] With the proposed Datalink and drivers.
[‡] ADC only, excluding AFE.

8.5. CONCLUSION

A transceiver ASIC implementing a comprehensive architecture for catheter-based high-frame-rate 3D ultrasound imaging probes has been presented. A compact on-chip transmit beamformer design that can provide all required beam patterns is achieved by the combination of an area-efficient R/C architecture and a flexible SR approach. The impact of common interference and settling in the AFE have been investigated, and mitigation methods have been presented. The application of TDM, subarray beamforming, and an LM, multi-level data transmission channel, has led to a high cable-count reduction while reducing the power consumed on the chip and still offering a high frame rate. A prototype chip has been manufactured and successfully applied in a high-frame-rate, 3D imaging experiment to verify the functionality.

8.6. REFERENCES

[1] S. M. Bierig and A. Jones, "Accuracy and Cost Comparison of Ultrasound Versus Alternative Imaging Modalities, Including CT, MR, PET, and Angiography," *Journal of Diagnostic Medical Sonography*, vol. 25, no. 3, pp. 138–144, May 2009, doi: 10.1177/8756479309336240.

[2] Z. M. Hijazi, K. Shivkumar, and D. J. Sahn, "Intracardiac Echocardiography During Interventional and Electrophysiological Cardiac Catheterization," *Circulation*, vol. 119, no. 4, pp. 587–596, Feb. 2009, doi: 10.1161/CIRCULATIONAHA.107.753046.

[3] H. M. Garcia-Garcia, M. A. Costa, and P. W. Serruys, "Imaging of coronary atherosclerosis: intravascular ultrasound," *Eur Heart J*, vol. 31, no. 20, pp. 2456–2469, Oct. 2010, doi: 10.1093/eurheartj/ehq280.

[4] S. S. Kim, Z. M. Hijazi, R. M. Lang, and B. P. Knight, "The Use of Intracardiac Echocardiography and Other Intracardiac Imaging Tools to Guide Noncoronary Cardiac Interventions," *J Am Coll Cardiol*, vol. 53, no. 23, pp. 2117–2128, Jun. 2009, doi: 10.1016/j.jacc.2009.01.071.

[5] A. Enriquez *et al.*, "Use of intracardiac echocardiography in interventional cardiology working with the anatomy rather than fighting it," *Circulation*, vol. 137, no. 21, pp. 2278–2294, 2018, doi: 10.1161/CIRCULATIONAHA.117.031343/-/DC1.

[6] G. Gurun *et al.*, "Single-chip CMUT-on-CMOS front-end system for real-time volumetric IVUS and ICE imaging," *IEEE Trans Ultrason Ferroelectr Freq Control*, vol. 61, no. 2, pp. 239–250, Feb. 2014, doi: 10.1109/TUFFC.2014.6722610.

[7] J. Lim, C. Tekes, E. F. Arkan, A. Rezvanitabar, F. L. Degertekin, and M. Ghovanloo, "Highly Integrated Guidewire Ultrasound Imaging System-on-a-Chip," *IEEE J Solid-State Circuits*, vol. 55, no. 5, pp. 1310–1323, May 2020, doi: 10.1109/JSSC.2020.2967551.

[8] D. M. van Willigen *et al.*, "A Transceiver ASIC for a Single-Cable 64-Element Intra-Vascular Ultrasound Probe," *IEEE J Solid-State Circuits*, vol. 56, no. 10, pp. 3157–3166, Oct. 2021, doi: 10.1109/JSSC.2021.3083217.

[9] D. Wildes *et al.*, "4-D ICE: A 2-D Array Transducer With Integrated ASIC in a 10-Fr Catheter for Real-Time 3-D Intracardiac Echocardiography," *IEEE Trans Ultrason Ferroelectr Freq Control*, vol. 63, no. 12, pp. 2159–2173, Dec. 2016, doi: 10.1109/TUFFC.2016.2615602.

[10] M. Soozande *et al.*, "Imaging Scheme for 3-D High-Frame-Rate Intracardiac Echography: A Simulation Study," *IEEE Trans Ultrason Ferroelectr Freq Control*, vol. 69, no. 10, pp. 2862–2874, Oct. 2022, doi: 10.1109/TUFFC.2022.3186487.

[11] "ViewFlex™ Xtra ICE Catheter Positioning Reference Manual," St. Paul, MN, USA, 2012.

[12] T. L. Proulx, D. Tasker, and J. Bartlett-Roberto, "Advances in catheter-based ultrasound imaging Intracardiac Echocardiography and the ACUSON AcuNavTM Ultrasound Catheter," in *IEEE Ultrasonics Symposium, 2005.*, IEEE, 2005, pp. 669–678. doi: 10.1109/ULTSYM.2005.1602941.

[13] E. Kang *et al.*, "A Variable-Gain Low-Noise Transimpedance Amplifier for Miniature Ultrasound Probes," *IEEE J Solid-State Circuits*, vol. 55, no. 12, pp. 3157–3168, Dec. 2020, doi: 10.1109/JSSC.2020.3023618.

[14] M. Tan *et al.*, "A 64-Channel Transmit Beamformer With ±30-V Bipolar High-Voltage Pulsers for Catheter-Based Ultrasound Probes," *IEEE J Solid-State Circuits*, vol. 55, no. 7, pp. 1796–1806, Jul. 2020, doi: 10.1109/JSSC.2020.2987719.

[15] Y. M. Hopf *et al.*, "A Pitch-Matched Transceiver ASIC With Shared Hybrid Beamforming ADC for High-Frame-Rate 3-D Intracardiac Echocardiography," *IEEE J Solid-State Circuits*, vol. 57, no. 11, pp. 3228–3242, Nov. 2022, doi: 10.1109/JSSC.2022.3201758.

[16] J. Lee *et al.*, "A 36-Channel Auto-Calibrated Front-End ASIC for a pMUT-Based Miniaturized 3-D Ultrasound System," *IEEE J Solid-State Circuits*, vol. 56, no. 6, pp. 1910–1923, Jun. 2021, doi: 10.1109/JSSC.2021.3049560.

[17] J. Li *et al.*, "A 1.54mW/Element 150µm-Pitch-Matched Receiver ASIC with Element-Level SAR/Shared-Single-Slope Hybrid ADCs for Miniature 3D Ultrasound Probes," in *2019 Symposium on VLSI Circuits*, IEEE, Jun. 2019, pp. C220–C221. doi: 10.23919/VLSIC.2019.8778200.

[18] C. Chen *et al.*, "A Pitch-Matched Front-End ASIC With Integrated Subarray Beamforming ADC for Miniature 3-D Ultrasound Probes," *IEEE J Solid-State Circuits*, vol. 53, no. 11, pp. 3050–3064, Nov. 2018, doi: 10.1109/JSSC.2018.2864295.

[19] O. Villemain *et al.*, "Ultrafast Ultrasound Imaging in Pediatric and Adult Cardiology," *JACC Cardiovasc Imaging*, vol. 13, no. 8, pp. 1771–1791, Aug. 2020, doi: 10.1016/j.jcmg.2019.09.019.

[20] J. Kang *et al.*, "A System-on-Chip Solution for Point-of-Care Ultrasound Imaging Systems: Architecture and ASIC Implementation," *IEEE Trans Biomed Circuits Syst*, vol. 10, no. 2, pp. 412–423, Apr. 2016, doi: 10.1109/TBCAS.2015.2431272.

[21] Y. Igarashi *et al.*, "Single-Chip 3072-Element-Channel Transceiver/128-Subarray-Channel 2-D Array IC With Analog RX and All-Digital TX Beamformer for Echocardiography," *IEEE J Solid-State Circuits*, vol. 54, no. 9, pp. 2555–2567, Sep. 2019, doi: 10.1109/JSSC.2019.2921697.

[22] J. M. Rothberg *et al.*, "Ultrasound-on-chip platform for medical imaging, analysis, and collective intelligence," *Proc Natl Acad Sci U S A*, vol. 118, no. 27, p. e2019339118, Jul. 2021, doi: 10.1073/PNAS.2019339118/SUPPL_FILE/PNAS.2019339118.SM14.MOV.

[23] G. Jung *et al.*, "A Reduced-Wire ICE Catheter ASIC With Tx Beamforming and Rx Time-Division Multiplexing," *IEEE Trans Biomed Circuits Syst*, vol. 12, no. 6, pp. 1246–1255, Dec. 2018, doi: 10.1109/TBCAS.2018.2881909.

[24] K. Chen, H. S. Lee, and C. G. Sodini, "A Column-Row-Parallel ASIC Architecture for 3-D Portable Medical Ultrasonic Imaging," *IEEE J Solid-State Circuits*, vol. 51, no. 3, pp. 738–751, Mar. 2016, doi: 10.1109/JSSC.2015.2505714.

[25] K. Chen, B. C. Lee, K. E. Thomenius, B. T. Khuri-Yakub, H.-S. Lee, and C. G. Sodini, "A Column-Row-Parallel Ultrasound Imaging Architecture for 3-D Plane-Wave Imaging and Tx Second-Order Harmonic Distortion Reduction," *IEEE Trans Ultrason Ferroelectr Freq Control*, vol. 65, no. 5, pp. 828–843, May 2018, doi: 10.1109/TUFFC.2018.2811393.

[26] E. Kang *et al.*, "A Reconfigurable Ultrasound Transceiver ASIC With 24 × 40 Elements for 3-D Carotid Artery Imaging," *IEEE J Solid-State Circuits*, vol. 53, no. 7, pp. 2065–2075, Jul. 2018, doi: 10.1109/JSSC.2018.2820156.

[27] P. Guo *et al.*, "A 1.2mW/channel 100µm-Pitch-Matched Transceiver ASIC with Boxcar-Integration-Based RX Micro-Beamformer for High-Resolution 3D Ultrasound Imaging," in *2022 IEEE International Solid- State Circuits Conference (ISSCC)*, IEEE, Feb. 2022, pp. 496–498. doi: 10.1109/ISSCC42614.2022.9731784.

[28] M. Tan *et al.*, "A Front-End ASIC With High-Voltage Transmit Switching and Receive Digitization for 3-D Forward-Looking Intravascular Ultrasound Imaging," *IEEE J Solid-State Circuits*, vol. 53, no. 8, pp. 2284–2297, Aug. 2018, doi: 10.1109/JSSC.2018.2828826.

[29] I. O. Wygant *et al.*, "Integration of 2D CMUT arrays with front-end electronics for volumetric ultrasound imaging," *IEEE Trans Ultrason Ferroelectr Freq Control*, vol. 55, no. 2, pp. 327–342, Feb. 2008, doi: 10.1109/TUFFC.2008.652.

[30] P. Wagner, C. Daft, S. Panda, and I. Ladabaum, "5G-1 Two Approaches to Electronically Scanned 3D Imaging Using cMUTs," in *2006 IEEE Ultrasonics Symposium*, IEEE, 2006, pp. 685–688. doi: 10.1109/ULTSYM.2006.185.

[31] M. W. Rashid, C. Tekes, M. Ghovanloo, and F. L. Degertekin, "Design of frequency-division multiplexing front-end receiver electronics for CMUT-on-CMOS based intracardiac echocardiography," in *2014 IEEE International Ultrasonics Symposium*, IEEE, Sep. 2014, pp. 1540–1543. doi: 10.1109/ULTSYM.2014.0381.

[32] T. M. Carpenter, M. W. Rashid, M. Ghovanloo, D. M. J. Cowell, S. Freear, and F. L. Degertekin, "Direct Digital Demultiplexing of Analog TDM Signals for Cable Reduction in Ultrasound Imaging

Catheters," *IEEE Trans Ultrason Ferroelectr Freq Control*, vol. 63, no. 8, pp. 1078–1085, Aug. 2016, doi: 10.1109/TUFFC.2016.2557622.

[33] Qilong Liu, Chao Chen, Z. Chang, C. Prins, and M. A. P. Pertijs, "A mixed-signal multiplexing system for cable-count reduction in ultrasound probes," in *2015 IEEE International Ultrasonics Symposium (IUS)*, IEEE, Oct. 2015, pp. 1–4. doi: 10.1109/ULTSYM.2015.0141.

[34] B. Savord and R. Solomon, "Fully sampled matrix transducer for real time 3D ultrasonic imaging," in *IEEE Symposium on Ultrasonics, 2003*, IEEE, 2003, pp. 945–953. doi: 10.1109/ULTSYM.2003.1293556.

[35] C. Chen *et al.*, "A Front-End ASIC With Receive Sub-array Beamforming Integrated With a 32 × 32 PZT Matrix Transducer for 3-D Transesophageal Echocardiography," *IEEE J Solid-State Circuits*, vol. 52, no. 4, pp. 994–1006, Apr. 2017, doi: 10.1109/JSSC.2016.2638433.

[36] Y.-J. Kim *et al.*, "A Single-Chip 64-Channel Ultrasound RX-Beamformer Including Analog Front-End and an LUT for Non-Uniform ADC-Sample-Clock Generation," *IEEE Trans Biomed Circuits Syst*, vol. 11, no. 1, pp. 87–97, Feb. 2017, doi: 10.1109/TBCAS.2016.2571739.

[37] M.-C. Chen *et al.*, "A Pixel Pitch-Matched Ultrasound Receiver for 3-D Photoacoustic Imaging With Integrated Delta-Sigma Beamformer in 28-nm UTBB FD-SOI," *IEEE J Solid-State Circuits*, vol. 52, no. 11, pp. 1–14, Nov. 2017, doi: 10.1109/JSSC.2017.2749425.

[38] T. Kim, S. Shin, and S. Kim, "An 80.2 dB DR 23.25 mW/Channel 8-Channel Ultrasound Receiver With a Beamforming Embedded SAR ADC," *IEEE Transactions on Circuits and Systems II: Express Briefs*, vol. 66, no. 9, pp. 1487–1491, Sep. 2019, doi: 10.1109/TCSII.2018.2889810.

[39] J.-Y. Um *et al.*, "An Analog-Digital Hybrid RX Beamformer Chip With Non-Uniform Sampling for Ultrasound Medical Imaging With 2D CMUT Array," *IEEE Trans Biomed Circuits Syst*, vol. 8, no. 6, pp. 799–809, Dec. 2014, doi: 10.1109/TBCAS.2014.2375958.

[40] Z. Chen *et al.*, "Impact of Bit Errors in Digitized RF Data on Ultrasound Image Quality," *IEEE Trans Ultrason Ferroelectr Freq Control*, vol. 67, no. 1, pp. 13–24, Jan. 2020, doi: 10.1109/TUFFC.2019.2937462.

[41] M. D'Urbino *et al.*, "An Element-Matched Electromechanical ΔΣ ADC for Ultrasound Imaging," *IEEE J Solid-State Circuits*, vol. 53, no. 10, pp. 2795–2805, Oct. 2018, doi: 10.1109/JSSC.2018.2859961.

[42] I. Ladabaum, Xuecheng Jin, H. T. Soh, A. Atalar, and B. t. Khuri-Yakub, "Surface micromachined capacitive ultrasonic transducers," *IEEE Trans Ultrason Ferroelectr Freq Control*, vol. 45, no. 3, pp. 678–690, May 1998, doi: 10.1109/58.677612.

[43] A. Arnau and D. Soares, "Fundamentals of piezoelectricity," *Piezoelectric Transducers and Applications*, pp. 1–38, 2008, doi: 10.1007/978-3-540-77508-9_1/COVER.

[44] K. E. Thomenius, "Evolution of ultrasound beamformers," in *1996 IEEE Ultrasonics Symposium. Proceedings*, IEEE, 1996, pp. 1615–1622. doi: 10.1109/ULTSYM.1996.584398.

[45] C. G. Oakley, "Calculation of ultrasonic transducer signal-to-noise ratios using the KLM model," *IEEE Trans Ultrason Ferroelectr Freq Control*, vol. 44, no. 5, pp. 1018–1026, Sep. 1997, doi: 10.1109/58.655627.

[46] C. Chen *et al.*, "A Prototype PZT Matrix Transducer With Low-Power Integrated Receive ASIC for 3-D Transesophageal Echocardiography," *IEEE Trans Ultrason Ferroelectr Freq Control*, vol. 63, no. 1, pp. 47–59, Jan. 2016, doi: 10.1109/TUFFC.2015.2496580.

[47] Y. M. Hopf *et al.*, "A Compact Integrated High-Voltage Pulser Insensitive to Supply Transients for 3-D Miniature Ultrasound Probes," *IEEE Solid State Circuits Lett*, vol. 5, pp. 166–169, 2022, doi: 10.1109/LSSC.2022.3180071.

[48] C. Chen, Z. Chen, Z. Chang, and M. A. P. Pertijs, "A compact 0.135-mW/channel LNA array for piezoelectric ultrasound transducers," in *ESSCIRC Conference 2015 - 41st European Solid-State Circuits Conference (ESSCIRC)*, IEEE, Sep. 2015, pp. 404–407. doi: 10.1109/ESSCIRC.2015.7313913.

[49] K. A. Ng and Yong Ping Xu, "A Compact, Low Input Capacitance Neural Recording Amplifier," *IEEE Trans Biomed Circuits Syst*, vol. 7, no. 5, pp. 610–620, Oct. 2013, doi: 10.1109/TBCAS.2013.2280066.

[50] A. X. Widmer and P. A. Franaszek, "A DC-Balanced, Partitioned-Block, 8B/10B Transmission Code," *IBM J Res Dev*, vol. 27, no. 5, pp. 440–451, Sep. 1983, doi: 10.1147/rd.275.0440.

[51] "Cyclone V Device Datasheet." Accessed: Dec. 19, 2023. [Online]. Available: https://www.intel.com/content/www/us/en/docs/programmable/683801/current/cyclone-v-device-datasheet.html

[52] T. L. Szabo, *Diagnostic Ultrasound Imaging: Inside Out*. New York: Elsevier, 2014. doi: 10.1016/C2011-0-07261-7.

[53] M. S. Akter, R. Sehgal, F. van der Goes, K. A. A. Makinwa, and K. Bult, "A 66-dB SNDR Pipelined Split-ADC in 40-nm CMOS Using a Class-AB Residue Amplifier," *IEEE J Solid-State Circuits*, vol. 53, no. 10, pp. 2939–2950, Oct. 2018, doi: 10.1109/JSSC.2018.2859415.

[54] M. Sautto, A. S. Savoia, F. Quaglia, G. Caliano, and A. Mazzanti, "A Comparative Analysis of CMUT Receiving Architectures for the Design Optimization of Integrated Transceiver Front Ends," *IEEE Trans Ultrason Ferroelectr Freq Control*, vol. 64, no. 5, pp. 826–838, May 2017, doi: 10.1109/TUFFC.2017.2668769.

[55] Y. Chae and G. Han, "Low Voltage, Low Power, Inverter-Based Switched-Capacitor Delta-Sigma Modulator," *IEEE J Solid-State Circuits*, vol. 44, no. 2, pp. 458–472, Feb. 2009, doi: 10.1109/JSSC.2008.2010973.

[56] T. Christen, "A 15-bit 140-µW scalable-bandwidth inverter-based ΔΣ modulator for a MEMS microphone with digital output," *IEEE J Solid-State Circuits*, vol. 48, no. 7, pp. 1605–1614, Jul. 2013, doi: 10.1109/JSSC.2013.2253232.

[57] J. Huijsing, "Design Examples," in *Operational Amplifiers*, Boston, MA: Springer US, 2001, pp. 261–363. doi: 10.1007/978-1-4757-3341-9_7.

[58] J. T. Stonick, Gu-Yeon Wei, J. L. Sonntag, and D. K. Weinlader, "An adaptive pam-4 5-Gb/s backplane transceiver in 0.25-µm CMOS," *IEEE J Solid-State Circuits*, vol. 38, no. 3, pp. 436–443, Mar. 2003, doi: 10.1109/JSSC.2002.808282.

[59] FDA, "Marketing Clearance of Diagnostic Ultrasound Systems and Transducers," Rockville, MD, USA, 2019.

[60] J. J. O'Reilly, "Series-parallel generation of m-sequences," *Radio and Electronic Engineer*, vol. 45, no. 4, pp. 171–176, 1975, doi: 10.1049/REE.1975.0033/CITE/REFWORKS.

[61] R. J. McGough, "Rapid calculations of time-harmonic nearfield pressures produced by rectangular pistons," *J Acoust Soc Am*, vol. 115, no. 5, pp. 1934–1941, May 2004, doi: 10.1121/1.1694991.

9

AN ULTRASOUND MATRIX TRANSDUCER FOR HIGH-FRAME-RATE 3D INTRACARDIAC ECHOCARDIOGRAPHY[1]

[1] This chapter is based on the following publication:
dos Santos, D.S.; Ossenkoppele, B.; Hopf, Y.M.; Soozande, M.; Noothout, E.; Vos, H.J.; Bosch, J.G.; Pertijs, M.A.P.; Verweij, M.D.; de Jong, N. An Ultrasound Matrix Transducer for High-Frame-Rate 3-D Intra-Cardiac Echocardiography. Ultrasound Med Biol 2024, 50, 285–294, doi:10.1016/j.ultrasmedbio.2023.11.001.

9.1. INTRODUCTION

ARRHYTHMIA is an abnormal rhythm of the heart that results from disruptions or irregularities in the electrical signals that regulate the heart's beating. These disruptions can cause the heart to beat too fast, too slow, or in an irregular pattern, which can affect the heart's ability to pump blood effectively. The most frequently occurring arrhythmia is atrial fibrillation, which is the major cardiac cause of stroke [1]. According to estimates, more than 5.6 million people will experience this condition in the United States by 2050 [2], while in the European Union, the number is expected to reach 17.9 million by 2060 [3]. Atrial fibrillation can initially be treated with drugs, but in some cases, catheter ablation may be necessary [4]. Ablation is a procedure that uses heat, cold, or radiofrequency waves to create small scars on the heart tissue, disrupting the abnormal electrical signals responsible for an irregular heartbeat, and restoring the normal rhythm and activation patterns of the heart [5].

Since the inception of ablation procedures, X-ray fluoroscopy has been employed to provide guidance because of its large field of view and ability to clearly visualize catheters and other devices. However, fluoroscopy also has significant disadvantages. First, ionizing radiation exposure has potentially harmful effects on the practitioner and the patient and hence imaging time is severely limited. Second, fluoroscopy provides limited visualization of atrial tissues, which can make it difficult to identify and target specific areas of interest. To overcome this limitation, the practitioner must rely on the combination of visual landmarks and subtle catheter sensations [6]. However, this approach can increase the risk of incomplete ablation or damage to surrounding tissues, leading to complications or the need for additional procedures [7].

As an alternative to relying solely on fluoroscopy, intracardiac ultrasound imaging can be used in combination with fluoroscopy to provide complementary imaging guidance, leading to improved accuracy and safety during interventional procedures [6]. In intracardiac echocardiography (ICE), a catheter containing a miniature ultrasound transducer is inserted into the cardiac cavities during the ablation procedure. This enables the practitioner to navigate the ablation catheter and visualize cardiac structures from an intracardiac perspective [8]–[10]. Integrating ICE into ablation procedures for atrial fibrillation reduces both fluoroscopy time and the occurrence of major complications significantly [7], [11]. In addition to serving as a visualization tool of the cardiac structure, ultrasound can be used for electromechanical wave imaging (EWI), which is a novel ultrasound-based modality for mapping the electromechanical wave (EW), that is, the transient tissue deformations occurring in immediate response to the electrical activation [12]–[14]. Several studies have reported a high correlation between cardiac electrical activity and the consequent EW for healthy and arrhythmic cases in both simulation [15] and *in vivo* data [12]–[14], [16], [17]. Therefore, by using EW mapping, the origin of the arrhythmia can be detected, and subsequently, ablation can be carried out on the source to terminate the arrhythmia effectively [17].

At present, EWI is primarily performed using a transthoracic transducer, which is placed on the surface of the chest. One limitation of that approach is that it is more prone to generate reflections on high-impedance materials, such as the rib cage and

the pacemaker leads, leading to a poor acoustic window [14], [17]. In addition, the transthoracic transducer is limited in its ability to provide high-quality imaging of certain regions of the heart that are difficult to access from the surface of the chest. To overcome these limitations and obtain a more comprehensive and accurate EW mapping, ICE imaging might be essential. An ICE device can provide both imaging guidance during interventional procedures and a map of the cardiac electromechanical activation. Furthermore, because of its proximity to the heart, ICE imaging enables the use of higher central frequencies, resulting in better axial resolution compared with transthoracic imaging [8].

As EWs move with velocities ranging from 0.5 to 2 m/s, a high frame rate is necessary to capture their rapid movement [8]. Additionally, volumetric imaging is necessary for fully visualizing the complex patterns of EW propagation. This is because the waves propagate throughout the entire heart in three dimensions, and their precise patterns of activation and conduction can be difficult to interpret from 2D images alone [17]. Furthermore, as the activation patterns in atrial fibrillation are irregular in time and space [18], [19], the EW propagation needs to be visualized within a heartbeat rather than through the combination of acquisitions across subsequent heartbeats [17], [20]. Therefore, an ICE device that offers a high-frame-rate 3D imaging capability is critical for effective visualization of EW propagation [8].

Intracardiac echocardiography technology currently faces challenges in meeting the demands of high-frame-rate 3D imaging. Designing ICE catheters that can handle these requirements is difficult because it requires using a 2D matrix array with a sufficiently large aperture and a large number of elements. However, the diameter of the catheter limits the size of the aperture and the number of cables that can fit inside the shaft. To address the latter limitation, application-specific integrated circuits (ASICs) can be used in ICE probes, and the cable reduction can be achieved in various ways, including subarray beamforming, in-probe digitization, and time-division multiplexing [21]–[23]. In addition to reducing the number of channels, an ASIC can also amplify received signals to prevent attenuation caused by cable loading between the acoustic elements and the imaging system [24], [25]. However, recent 3D ICE designs are limited in functionality by the integration challenge. This expresses itself in the lack of integration of a transmit beamformer [26], inadequate signal-to-noise ratio (SNR) resulting from low-voltage transmit [27], receive-only architectures [6], [22], [28], or lower frame rates [6]. Examples of commercially available ICE catheters include the Verisight Pro from Philips [29], the ACUSON AcuNav from Siemens [30], and the NUVISION from Biosense Webster [31], which operates using GE Healthcare Vivid ultrasound systems. Although these probes offer 2D and 3D live imaging guidance, their frame rates are relatively low for EWI.

We have recently conducted a simulation study in which we proposed a novel imaging scheme for high-frame-rate 3D ICE imaging using a side-looking matrix composed of 64 × 18 square elements [8]. The element pitch was 160 μm, and the center frequency was in the range 5-6 MHz. For channel count reduction, we implemented 1D micro-beamforming in the elevation direction. Additionally, to achieve a high frame rate while covering a volume of 70° × 70° × 10 cm, we employed a technique of transmitting fan-shaped diverging beams steered across seven elevation angles, with a 20° divergence in elevation and 70° in azimuth. In

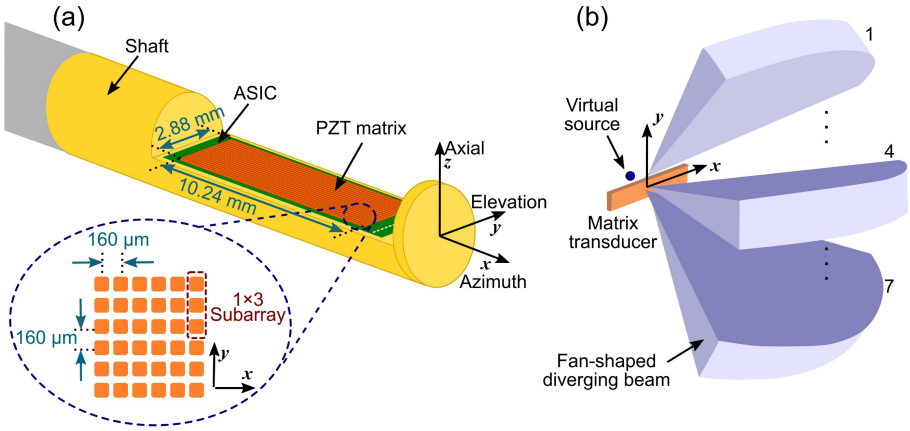

Figure 9.1: (a) Schematic representation of the proposed intracardiac echocardiography transducer. (b) Transmit scheme using fan-shaped beams.

simulations, the proposed method outperformed the current state of the art on 3D ICE in terms of frame rate. The currently reported prototype transducer fits such an imaging scheme.

Here we describe the development of a side-looking ICE prototype transducer that uses an array of piezoelectric elements with a pitch of 160 µm × 160 µm integrated with a pitch-matched ASIC. Details on the circuit implementation of the building blocks of this ASIC have been reported in Hopf et al. [26]. The primary objective of this work is to determine the feasibility of this prototype for high-frame-rate 3D ICE imaging. We provide a comprehensive analysis of the design, technical details, characterization, and performance of the prototype. To our knowledge, this is the first study to report an ICE probe that is capable of generating high-frame-rate 3D images with a wide field of view and having a digital output.

9.2. MATERIALS AND METHODS

9.2.1. DESIGN CHOICES

The process of designing ICE transducers is very challenging and complex, as the size of the catheter poses significant physical limitations on both the transducer aperture and channel count. The prototype transducer herein presented is designed to fit within a 10-French catheter, which has an outer diameter of 3.3 mm. This limits the transducer aperture to approximately 3 mm in the elevation direction, while the number of cables that can be accommodated within the catheter shaft is limited to ~100 [6], [9]. In our simulations [8], we have opted to use a rectangular aperture of about 10 mm × 3 mm (azimuth × elevation). The matrix array consisted of square elements with a pitch of 160 µm in both directions, resulting in a total of 64 × 18 elements. To achieve a penetration depth of up to 10 cm, we have selected a center

frequency of 6 MHz. A schematic representation of the proposed side-looking ICE transducer is shown in Figure 9.1(a).

To achieve optimal 3D imaging, precise control of transmit and receive time delays, as well as apodization for every element, is crucial. This requires addressing each element of the array individually [32]. As maintenance of an element pitch that is below or close to half the wavelength is desirable to avoid grating lobes [33], the resulting matrix array consists of more than a thousand elements, exceeding by far the cable limit imposed by the catheter shaft. Therefore, it is necessary to reduce the number of channels of the probe significantly.

Several techniques have been proposed to reduce the complexity of fully populated matrix arrays, including sparse matrix arrays [34], [35] and row-column addressed matrix arrays [36], [37]. However, these techniques have inherent limitations. Sparse matrix arrays suffer from lower SNR and higher clutter levels [38] while, while row-column addressed matrix arrays have more complex read-out sequences and reduced flexibility in transmit beamforming, severely complicating the implementation of a diverging wave transmission scheme as is required to insonify the full imaging volume with a small number of transmissions for high-frame-rate imaging [39]. One of the most effective ways to achieve channel reduction is by using the "micro-beamforming" technique, also known as "subarray/sub-aperture beamforming", or "pre-steering" [21]. This technique performs the first step of beamforming at the probe tip using an ASIC, by dividing the array into subarrays and combining the RF signals within each subarray by means of a delay-and-sum operation. This partial beamforming reduces the number of signals that need to be transmitted through the cables and processed in the ultrasound system. The remaining beamforming and image reconstruction are performed in the ultrasound system [22], [32]. In our design, we have opted to use micro-beamforming for channel reduction. Our approach involves dividing the array into small subarrays consisting of 1 × 3 elements, as this size offered a good balance between channel reduction and image quality according to earlier simulations [8]. With this, the number of cables was reduced by a factor of 3. Yet, a further on-chip reduction is still required to reduce the cable count sufficiently.

9.2.2. IMAGING SCHEME

In our earlier work [8], we introduced a novel imaging scheme that enables volumetric imaging with a sufficiently high frame rate and image quality for EWI, while also reducing the data rate to a practical level. Our objective was to achieve a frame rate of 1000 volumes/s, with a penetration depth of up to 10 cm and an opening angle of 70° × 70°. For a depth of 10 cm, the round-trip travel time of ultrasound waves requires approximately 130 µs, assuming the speed of sound of 1540 m/s. As a result, the pulse repetition frequency (PRF) is limited to 7.7 kHz to allow enough time for the echoes to return before sending out another pulse. For this PRF and depth, a maximum of seven ultrasound pulses can be transmitted per frame to cover the entire region of interest, leading to a frame rate of 1000 volumes/s. Because we are limited to only seven transmissions to cover the entire volume, a diverging wave transmission scheme is necessary.

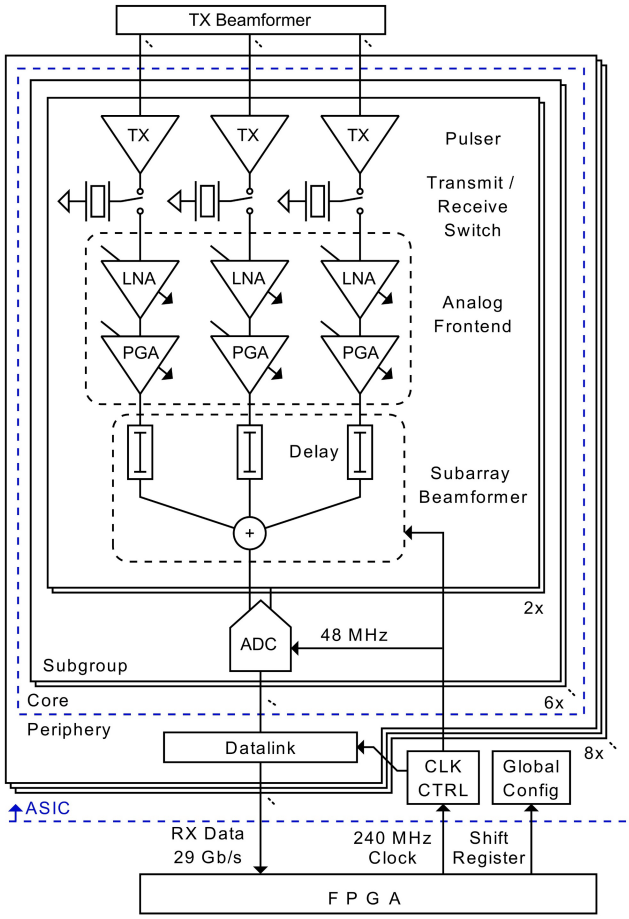

Figure 9.2: Block diagram of the application-specific integrated circuit architecture.

The proposed transmit scheme involves the use of seven fan-shaped diverging beams. These beams are steered in different directions in elevation, as illustrated in Figure 9.1(b), and employ a 20° divergence in elevation and 70° in azimuth. We use a single virtual source to generate the desired fan-shaped diverging beam. In receive, the subarray beamformers are capable of covering a pre-steering range of ±30° in the elevation direction. To reduce grating lobes and improve image quality, we use angular weighted coherent compounding. This technique accounts for transmit beam contours such that the noise and grating lobes from non-insonified regions are suppressed, while overlapping areas from neighboring transmissions are weighted and coherently compounded, resulting in a more accurate image [40].

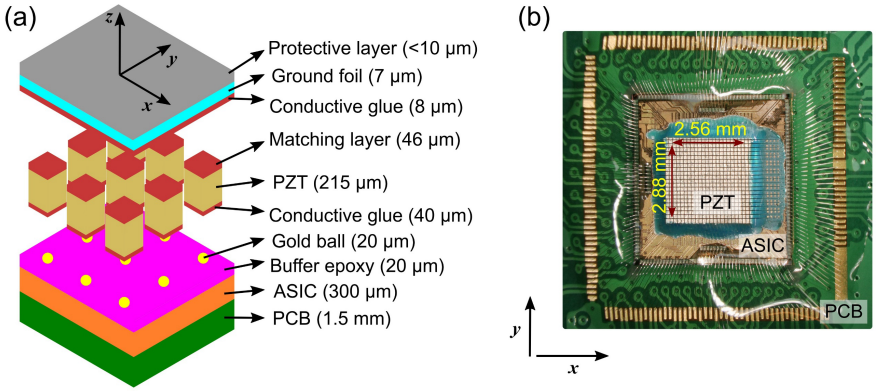

Figure 9.3: (a) Acoustic stack with the indication of the thickness of each layer (not drawn to scale). (b) Microscopic photo of the manufactured prototype.

9.2.3. ASIC IMPLEMENTATION

In Figure 9.2, the architecture overview of the designed ASIC is illustrated. It includes high-voltage transmitters, analog frontends, hybrid beamforming - analog-to-digital converters (ADCs), and data transmission to the imaging system [26]. The element-level circuitry is 160 µm × 160 µm in size and is pitch-matched with the matrix array.

The transmit (TX) part incorporates an on-chip unipolar pulser [41] that can generate pulses up to 30 V. In addition to diverging waves, the implemented TX beamformer can produce other commonly used delay patterns, such as angled plane waves or focused waves.

In receive (RX), the signal from each element is connected to a low-noise amplifier (LNA), followed by a second-stage programmable gain amplifier (PGA) [26]. The LNA can be switched in discrete steps of 18 dB ranging from -12 to 24 dB, while the second stage can be configured in 6 dB steps ranging from 6 dB to 24 dB. Together, this enables the implementation of time-gain compensation (TGC) with a range of 54 dB. This is achieved through the use of 10 discrete steps of 6 dB, spanning from -6 to 48 dB. The outputs of three individual element-level circuits are merged using a 1 × 3-element subarray beamformer. Two of these subarrays are then combined to form a 2 × 3-element subgroup. Following this, the merged signals are digitized by an ADC at the rate of 24 MS/s with a resolution of 10 bits. The outputs are received by a periphery-level block, which provides a datalink to process the received data. To further reduce cable count in receive, a channel that combines time-division multiplexing (TDM) and four-level pulse amplitude modulation (PAM) data transmission has been implemented [42], [43]. This approach, together with the subarray beamforming, results in an 18-fold reduction in cable count.

9.2.4. TRANSDUCER FABRICATION

To simplify the fabrication process of the prototype transducer, we made two key decisions. First, we chose to mount the probe onto a custom daughterboard printed

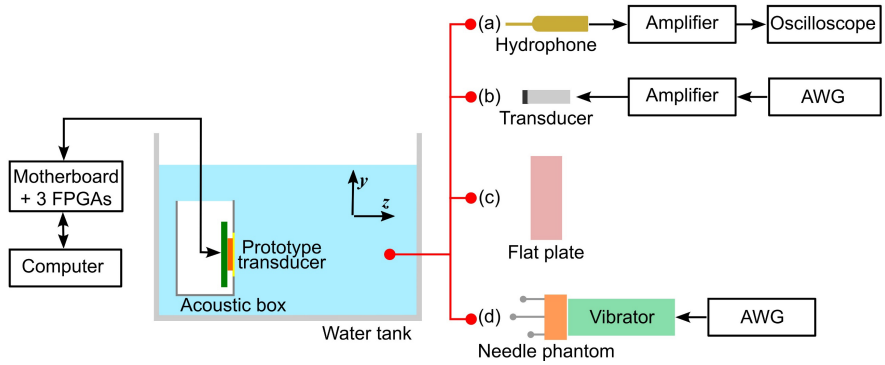

Figure 9.4: Measurement setup. (a) Transmit characterization. (b) Receive characterization. (c) Pulse–echo measurements. (d) Imaging.

circuit board (PCB) rather than assembling it into a catheter at this stage. Second, instead of building the full size of the proposed ICE transducer (a 64 × 18 matrix array), we opted to build one-quarter of the aperture in the azimuth direction, resulting in a 16 × 18 matrix array. Building a smaller aperture at this stage of prototype development reduces cost and complexity while all of the functionality can still be tested.

Figure 9.3(a) illustrates the proposed acoustic stack, which includes a matrix array made of lead zirconate titanate (PZT) piezoelectric material, the ASIC, a buffer layer, a matching layer, an aluminum ground foil, and a protective top layer. This stack design is similar to those we have described in our previous articles [24], [32], [44]. To determine the thickness of each layer within the stack, we conducted simulations using finite-element analysis software (PzFlex, Weidlinger Associates, Inc., Mountain View, CA, USA). To fabricate the acoustic stack, gold balls are first deposited onto the transducer bond pads of the ASIC. The gaps between the balls are filled with an electrically isolating epoxy material, which is then ground down until the gold balls are exposed again. A conductive glue matching layer is applied on top of the piezoelectric material (3203HD, CTS Corporation, Lisle, IL, USA), followed by gluing of the PZT and matching layer stack onto the gold balls. The acoustical stack is then diced using a 20 µm dicing saw. To create a common ground electrode, a 7-µm-thick aluminum foil is glued on top of the entire matrix array. Finally, to prevent moisture and damage, a thin layer of encapsulation material (AptFlex F7, Precision Acoustics Ltd., Dorchester, UK) is placed on top of the stack. Figure 9.3(b) displays a photograph of the acoustic stack mounted on top of the ASIC and PCB before the ground foil is deposited.

9.2.5. ACOUSTIC CHARACTERIZATION

For the acoustic characterization and tests, the prototype was placed in a watertight box with a 25-µm-thick polyimide acoustic window and submerged in a water tank filled with deionized water. A custom motherboard was used to interface the

prototype with a computer for data processing through commercial field programmable gate arrays (FPGAs), as illustrated in Figure 9.4.

To assess the transmit performance (Figure 9.4(a)), we evaluated the time and frequency responses of individual transducer elements. For this, we applied 30 V pulses to the element under test and measured the resulting acoustic pressure generated by it using a calibrated 1 mm needle hydrophone (SN2082, Precision Acoustics Ltd., Dorchester, UK) placed at a distance of 5 cm from the transducer. The hydrophone output was then amplified by a 60 dB amplifier (AU-1519, Miteq, Inc., Hauppauge, NY, USA) and digitized by an oscilloscope (DSO-X 4024A, Agilent Technologies, Santa Clara, CA, USA). Next, we characterized the directivity pattern of specific transducer elements using hydrophone scans with a calibrated 0.2 mm needle hydrophone (SN3800, Precision Acoustics Ltd.). We performed rotational scans ranging from -60° to 60° at a distance of 5 cm from the transducer. Using the same setup, we evaluated the directivity pattern of the entire transducer when transmitting diverging waves steered at seven different angles in elevation. To provide a comprehensive assessment, we compared the measured directivity patterns with simulations performed using the ultrasound simulator FOCUS [45].

To assess the receive performance (Figure 9.4(b)), we used a pre-calibrated 1 mm circular single-element transducer (PA865, Precision Acoustics Ltd., Dorchester, UK) as a transmitter placed 5 mm away from the prototype. We drove the single-element transducer with an 8-cycle sine wave generated by an arbitrary waveform generator (AWG; 33250A, Agilent Technologies, Santa Clara, CA, USA) and measured the response at each individual element of the prototype to evaluate the sensitivity variation and element yield. With the same setup, we evaluated the dynamic range of the prototype, which is defined as the difference between the highest and lowest detectable pressures. Hence, we varied the surface pressure applied to the prototype between 1 Pa and 100 kPa while varying the gain setting of the ASIC from -6 to 48 dB. Lastly, we measured the directivity pattern of one subarray when pre-steering it at seven different angles in the elevation direction. For this, the prototype was rotated from -60° to 60° in increments of 1°. At each angle, the received data was transferred to the computer for processing. For pulse-echo measurements (Figure 9.4 (c)), we positioned a quartz flat plate 5 cm from the prototype. A plane wave was transmitted with all elements excited with three cycles of 30 V, and the resulting echoes were received by each individual element.

9.2.6. HIGH FRAME RATE 3D IMAGING

To assess the high-frame-rate 3D imaging capability, we used a custom phantom consisting of three needles. The phantom was positioned at a distance of about 4 cm from the prototype transducer (Figure 9.4(d)). To introduce motion into the system, we attached the phantom to a mechanical shaker (Type 4810, Brüel & Kjær, Nærum, Denmark) and applied a low-frequency sine vibration of 20 Hz. To capture the dynamic movement of the needles in 3D, we acquired 280 pulse-echo cycles at a PRF of 7 kHz. As seven pulse-echo cycles are required to generate each 3D volume image, a total of 40 volumetric images were obtained from the 280 pulse-echo cycles at 1 kHz volumetric frame rate.

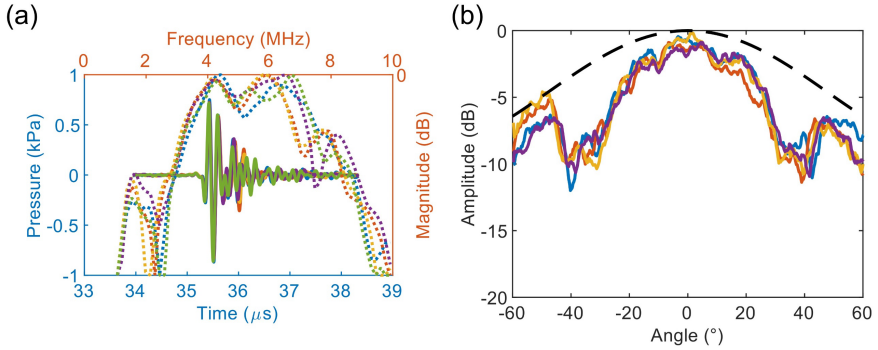

Figure 9.5: (a) Time and frequency responses of individual elements. (b) Measured and simulated directivity pattern of individual elements.

The received data were first digitized by the ADCs and subsequently transferred to the FPGA boards. After data acquisition, it was downloaded to the computer for processing, as detailed in Hopf et al. [43]. The reconstruction of the 3D volume image was performed offline using conventional delay-and-sum operations with angular-weighted coherent compounding, as described in Soozande et al. [8].

To provide a comparison to the high-frame-rate 3D imaging results, we used a commercial diagnostic ultrasound machine (Aplio Artida, Toshiba Medical Systems, Otawara, Japan) with a linear probe (PLT-704SBT, Toshiba Medical Systems, Otawara, Japan) to measure the displacement of the needles using M-mode imaging.

9.3. RESULTS

9.3.1. TRANSMIT CHARACTERIZATION

Figure 9.5(a) shows the time and frequency responses of five transducer elements recorded with the hydrophone. At 5 cm, the average peak pressure for a single element is about 0.85 kPa. In the frequency domain, the center frequency is about 5.5 MHz and the average -6 dB bandwidth is about 60%. In Figure 9.5(b), the directivity pattern of five elements together with the simulated curve along the elevation direction is shown. The experimental observations reveal a -6 dB beam width of approximately 55°, while the simulated result is about 112°. This deviation is due to the dips seen at approximately ± 40° in the measured directivity. Similar results were observed along the azimuth direction since the element has a square geometry.

Figure 9.6 depicts the locally normalized directivity pattern of the entire matrix array transmitting diverging waves steered at seven different angles ranging from -30° to 30° in the elevation direction. The measured and simulated profiles are in good agreement, with a -6 dB beam width of approximately 20° observed in both cases. This confirms the effectiveness of the prototype in generating and steering diverging beams. In Figure 9.7, the directivity pattern along the azimuth direction is displayed for the current prototype and the full-size aperture. As seen, there is an excellent agreement between the measured and simulated profiles, with the -6 dB

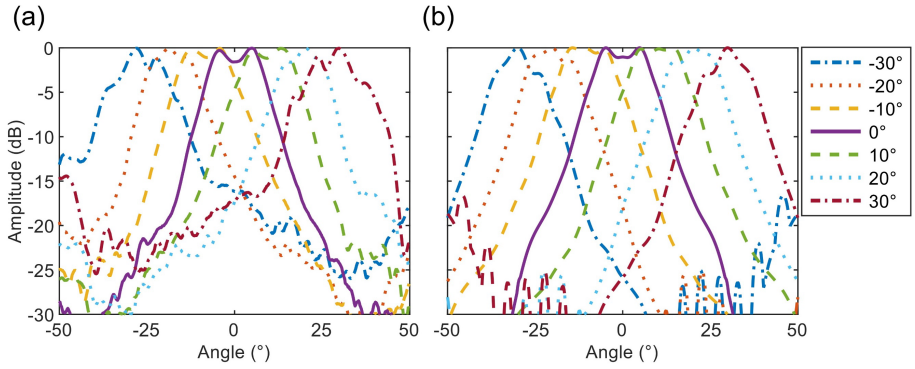

Figure 9.6: Directivity pattern of the transducer transmitting steered diverging waves in elevation. (a) Measured. (b) Simulated.

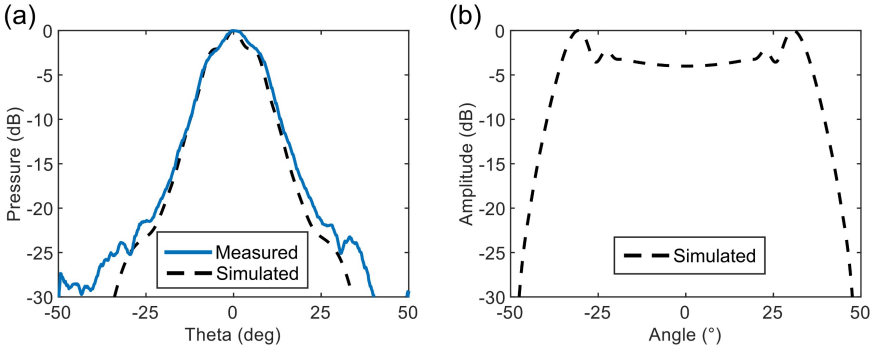

Figure 9.7: Directivity pattern of the transducer transmitting a diverging wave in azimuth. (a) Current aperture. (b) Full-size aperture.

beam width of about 20° for the current aperture. For the full-size aperture, we observe a -6 dB beam width of about 70°, which is according to our design goal.

9.3.2. RECEIVE CHARACTERIZATION

Figure 9.8(a) illustrates the sensitivity variation in receive across all elements of the prototype transducer. The results indicate a high yield, with 282 out of 288 elements (i.e., 98 %) falling within the range of 0 to -6 dB range. Only one element, indicated in dark blue, exhibits no signal and is considered defective in receive. Figure 9.8(b) illustrates the relationship between the received pressure at the surface of the prototype and the corresponding normalized ADC output for all gain levels. To reduce measurement time, the measurements were conducted using one-third of the array, that is, 96 elements. The plotted values represent the average across these 96 elements. The lowest detectable pressure is around 10 Pa, which was measured

when the ASIC gain was set to 48 dB. The highest detectable pressure was about 100 kPa, which was measured for a gain of -6 dB. An overall dynamic range of about 80 dB is obtained between the 0 dB SNR point of the highest gain and the 1 dB compression point of the lowest gain setting.

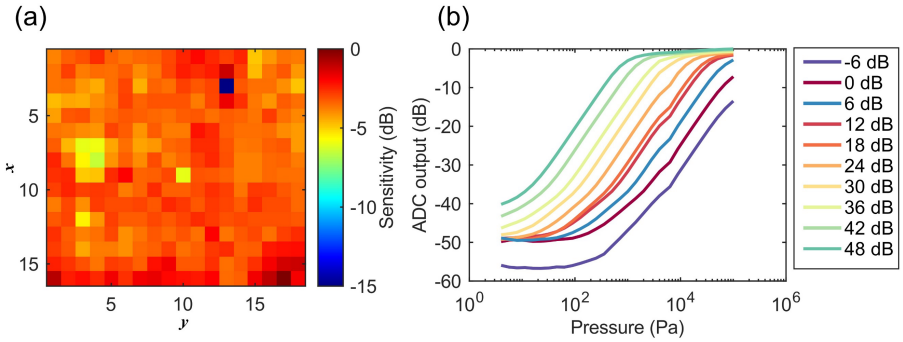

Figure 9.8: (a) Sensitivity variation in receive. (b) Relation between received pressure and ADC output for all ASIC gains.

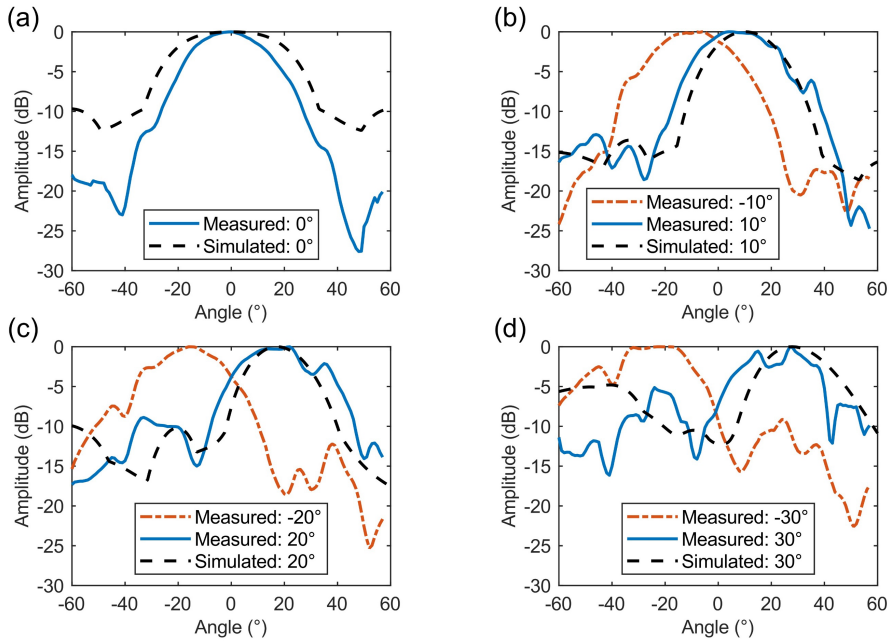

Figure 9.9: Measured and simulated directivity pattern of a 1 × 3 subarray pre-steered at (a) 0°, (b) ±10 °, (c) ±20° and (d) ±30° in the elevation direction.

Figure 9.9 illustrates the measured and simulated directivity patterns of a 1 × 3 subarray pre-steering at seven different angles, ranging from -30° to 30° in the elevation direction. The measured and simulated profiles exhibit good agreement, which indicates that the designed ASIC can efficiently generate the necessary delays to steer the subarrays toward the intended directions. The measured -6 dB beam width is approximately 40° for all steering angles, except for -30° steering, which has a beam width of about 50°. In simulations, the -6 dB beam width is 56° when there is no steering and about 35° for the other steering angles. Note that as the steering angle increases, the side lobe levels tend to rise too.

9.3.3. PULSE-ECHO MEASUREMENTS

Figure 9.10 shows the pulse-echo measurements obtained by transmitting three cycles with all elements (no steering) and receiving the echo with individual elements without applying micro-beamforming. The measurements were conducted using five arbitrarily selected elements as receivers. All measured elements exhibit a comparable amplitude response and a center frequency of about 6.1 MHz. Note that a dip around 6 MHz causes the -6 dB bandwidth to narrow to roughly 10%.

9.3.4. IMAGING

Figure 9.11 shows one of the 40 volumetric images of the needle phantom captured by our prototype transducer at a frame rate of 1000 volumes/s. After the acquisition, the data were transferred from the motherboard to a computer for offline image processing. The reconstructed image clearly distinguishes the needles in 3D space, and the positions of the point scatterers closely match the position of the needles in the photograph of the phantom. Note, however, that each imaged needle exhibits one main lobe accompanied by secondary lobes in both the azimuth and elevation directions.

We used the data set consisting of 40 images to track the axial motion of a single needle to show the high-frame-rate imaging capability of the ASIC. Figure 9.12(a)

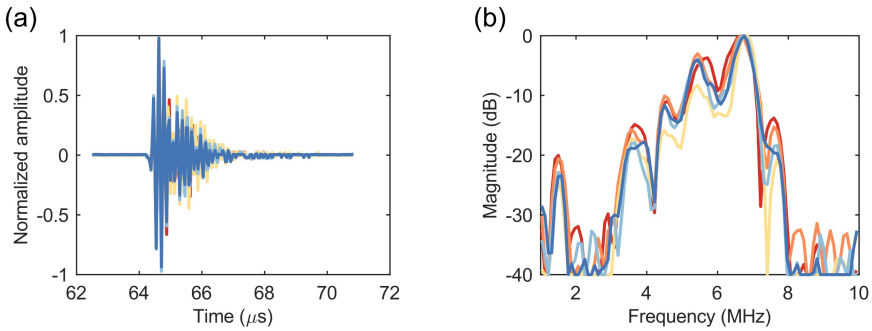

Figure 9.10: Pulse–echo responses obtained from 3-cycle transmissions using all elements and a single-element receiver. (a) Time domain. (b) Frequency domain..

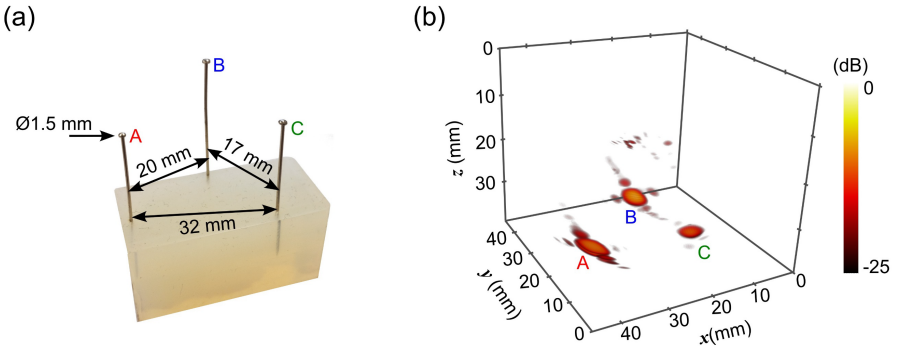

Figure 9.11: (a) Photograph of the needle phantom. (b) Reconstructed 3D image acquired with the prototype at a frame rate of 1000 volumes/s.

illustrates the resulting displacement of one needle, and Figure 9.12(b), its instantaneous velocity derived by pulsed-wave Doppler processing of the high-frame-rate images. The 20 Hz vibration of the needle is clearly visible, and we were able to capture about 80% of its sinusoidal motion within the 40 ms acquisition time. We observed a peak-to-peak displacement of approximately 1.5 mm, with a maximum measured velocity of around 5 cm/s.

In Figure 9.13(a), we present the B-mode image of the needle phantom acquired with the commercial imaging system, which was used for validation. To track the motion of one of the needles, we drew a line on it and performed M-mode imaging, as depicted in Figure 9.13(b). The 20 Hz vibration of the needle is also evident, and we measured the same peak-to-peak displacement of about 1.5 mm. This agreement highlights our capability to achieve high-frame-rate 3D imaging.

9.4. DISCUSSION

We have described the development of a high-frame-rate 3D imaging prototype ICE transducer. This involved constructing a PZT matrix array with 16 × 18 elements interfaced with a pitch-matched ASIC. To address the challenge of cable count reduction, we implemented subarray beamforming in receive and on-chip digitization, and used a combination of TDM and PAM data transmission. This allowed us to reduce the total cable count by 18-fold lower than the acoustic element number, resulting in a feasible number of cables for practical implementation. Because of complexity and cost constraints, we built a prototype that corresponds to a quarter of the full-size aperture design (64 × 18) and the transducer was mounted on a PCB for convenience. Despite these modifications, we were able to conduct comprehensive tests to examine the prototype's performance and verify its functionality.

As depicted in Figure 9.5(a), the responses of the five individual elements exhibit similar behavior in transmit. At a distance of 5 cm, each element has a transmit efficiency of around 28 Pa/V, which is consistent with previous designs

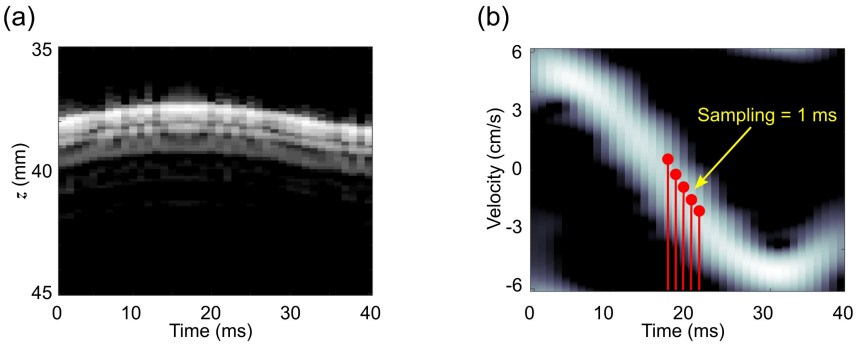

Figure 9.12: Motion of a single needle extracted from high-frame-rate 3-D images acquired with the prototype transducer. (a) Needle displacement. (b) Needle velocity.

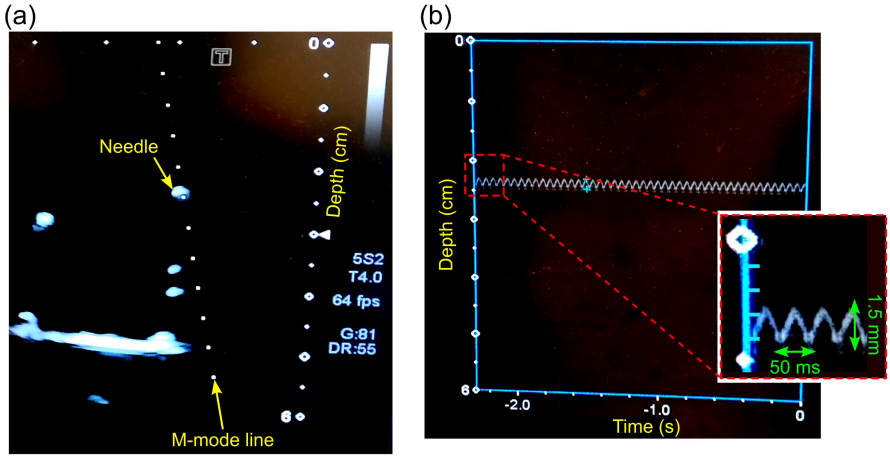

Figure 9.13: Images of the needle phantom acquired with the Toshiba system. (a) B-mode image. (b) M-mode image.

[32], [44]. On average, the center frequency of the elements is 5.5 MHz, and the -6 dB bandwidth is 60% in transmit. Note that the frequency spectrum exhibits a dip at approximately the center frequency, which decreases the overall bandwidth. This dip is also observed in the pulse-echo response, illustrated in Figure 9.10, and is likely the result of reflections and standing waves from the ASIC, as we have previously investigated through simulations [44], [46]. To mitigate this effect, an interposer layer between the PZT and the ASIC could be used [6], [44], [47]. We may explore this option in future designs.

The directivity pattern of the single elements, as shown in Figure 9.5(b), generally follows the trend of the simulated directivity. However, we observed dips at ±40°, which is likely caused by acoustic crosstalk [48], [49], as we have previously reported [44], [46] Note that the measured electric crosstalk for this probe is about -75 dB between channels, as determined in our previous work [26]. The directivity

pattern of the entire transducer, as illustrated in Figure 9.6 and Figure 9.7, aligns very well with simulations and demonstrates that the prototype is capable of steering from -30° to 30° in the elevation direction. Considering that the azimuth aperture is extended as originally designed (i.e., with 64 elements), our prototype is expected to provide a coverage of 70° × 70°. In receive, the directivity pattern of the 1 × 3 subarrays (Figure 9.9) also exhibits the expected behavior, albeit with an increase in degradation and artifacts at higher steering angles [50]. Overall, the directivity pattern measurements confirm that the ASIC is effective in generating the desired delay patterns, as specified in our design.

The sensitivity map depicted in Figure 9.8(a) reveals that 282 out of 288 elements of the prototype are within the -6 dB range. This element yield of 98% indicates the efficacy of our fabrication process and encourages us to consider scaling up the aperture size to 64 × 18 elements in future developments. In Figure 9.8(b), we observed that the lowest detectable pressure of 10 Pa is limited by the ASIC's noise floor for a gain setting of 48 dB, whereas the highest detectable pressure of 100 kPa is limited by the ASIC's saturation level for a gain of -6 dB. This results in a total dynamic range of 80 dB, which is suitable for ICE. The measured peak SNR for the receive path is 52.2 dB [43]. Note that there seems to be an overlap in the gain step between 12 and 18 dB, which is not consistent with the expected 6 dB difference. This is likely due to a mismatch in the amplifier circuitry which can be easily corrected for in a future re-adjustment of design.

In the imaging experiment with the vibrating needle phantom, we successfully acquired 40 volumes within a 40 ms interval, achieving the intended frame rate of 1000 volumes/s. The reconstructed 3D image of the needles depicted in Figure 9.11 confirms the prototype's 3D imaging capabilities, even though some side lobes are present in the image. Nonetheless, it is worth noting that for the full-size array, the side lobes will be reduced and the overall imaging quality will be improved. By analyzing the 40 acquired volumetric images, we were able to extract the motion pattern of the needle and accurately estimate its velocity with retrospective pulsed-wave Doppler analysis, as shown in Figure 9.12. The clean Doppler spectrogram indicates proper internal timing and digitization of the signals. These results are very promising, as we were able to precisely validate them with a clinical ultrasound system as a reference (Figure 9.13).

As the ICE prototype transducer is currently mounted on a large PCB for testing purposes, it is not yet ready for (pre)clinical use. In future work, we plan to assemble a complete prototype and integrate it into a catheter for EWI validation.

9.5. CONCLUSIONS

In this study, we have presented the design, fabrication, and characterization of a prototype transducer with an integrated ASIC for high-frame-rate 3D ICE. By applying subarray beamforming alongside on-chip digitization time-division multiplexing and pulse amplitude modulation data transmission, we were able to significantly reduce the cable count to a realistic number that can fit within a catheter shaft. The acoustic performance of the prototype met the design requirements, allowing us to achieve 3D imaging with a large field of view and a

frame rate of 1000 volumes/s. This high frame rate outperforms current state-of-the-art ICE probes and paves the way toward the implementation of electromechanical wave imaging on future ICE catheters. Future work should focus on realizing a full aperture transducer inside a catheter to enable *in vivo* testing.

9.6. REFERENCES

[1] J. Jalife, "Mother rotors and fibrillatory conduction: a mechanism of atrial fibrillation," *Cardiovasc Res*, vol. 54, no. 2, pp. 204–216, May 2002, doi: 10.1016/S0008-6363(02)00223-7.

[2] A. S. Go *et al.*, "Prevalence of Diagnosed Atrial Fibrillation in Adults," *JAMA*, vol. 285, no. 18, p. 2370, May 2001, doi: 10.1001/jama.285.18.2370.

[3] B. P. Krijthe *et al.*, "Projections on the number of individuals with atrial fibrillation in the European Union, from 2000 to 2060," *Eur Heart J*, vol. 34, no. 35, pp. 2746–2751, Sep. 2013, doi: 10.1093/eurheartj/eht280.

[4] B. Kheiri *et al.*, "Ablation Versus Antiarrhythmic Drugs as First-Line Treatment of Paroxysmal Atrial Fibrillation: A Meta-Analysis of Randomized Trials," *Circ Arrhythm Electrophysiol*, vol. 14, no. 8, pp. 305–315, Aug. 2021, doi: 10.1161/CIRCEP.120.009692.

[5] G. Katritsis and H. Calkins, "Catheter Ablation of Atrial Fibrillation – Techniques and Technology," *Arrhythm Electrophysiol Rev*, vol. 1, p. 29, 2012, doi: 10.15420/aer.2012.1.29.

[6] D. Wildes *et al.*, "4-D ICE: A 2-D Array Transducer With Integrated ASIC in a 10-Fr Catheter for Real-Time 3-D Intracardiac Echocardiography," *IEEE Trans Ultrason Ferroelectr Freq Control*, vol. 63, no. 12, pp. 2159–2173, Dec. 2016, doi: 10.1109/TUFFC.2016.2615602.

[7] J. M. Cooper and L. M. Epstein, "Use of Intracardiac Echocardiography to Guide Ablation of Atrial Fibrillation," *Circulation*, vol. 104, no. 25, pp. 3010–3013, Dec. 2001, doi: 10.1161/hc5001.101503.

[8] M. Soozande *et al.*, "Imaging Scheme for 3-D High-Frame-Rate Intracardiac Echography: A Simulation Study," *IEEE Trans Ultrason Ferroelectr Freq Control*, vol. 69, no. 10, pp. 2862–2874, Oct. 2022, doi: 10.1109/TUFFC.2022.3186487.

[9] W. Lee, S. F. Idriss, P. D. Wolf, and S. W. Smith, "A miniaturized catheter 2-D array for real-time, 3-D intracardiac echocardiography," *IEEE Trans Ultrason Ferroelectr Freq Control*, vol. 51, no. 10, pp. 1334–1346, Oct. 2004, doi: 10.1109/TUFFC.2004.1350962.

[10] E. C. Pua, S. F. Idriss, P. D. Wolf, and S. W. Smith, "Real-time 3D transesophageal echocardiography," in *IEEE Ultrasonics Symposium, 2004*, IEEE, 2004, pp. 778–781. doi: 10.1109/ULTSYM.2004.1417837.

[11] C. La Greca, A. Cirasa, D. Di Modica, A. Sorgato, U. Simoncelli, and D. Pecora, "Advantages of the integration of ICE and 3D electroanatomical mapping and ultrasound-guided femoral venipuncture in catheter ablation of atrial fibrillation," *Journal of Interventional Cardiac Electrophysiology*, vol. 61, no. 3, pp. 559–566, Sep. 2021, doi: 10.1007/s10840-020-00835-6.

[12] J. Provost, W.-N. Lee, K. Fujikura, and E. E. Konofagou, "Imaging the electromechanical activity of the heart in vivo," *Proceedings of the National Academy of Sciences*, vol. 108, no. 21, pp. 8565–8570, May 2011, doi: 10.1073/pnas.1011688108.

[13] E. E. Konofagou and J. Provost, "Electromechanical wave imaging for noninvasive mapping of the 3D electrical activation sequence in canines and humans in vivo," *J Biomech*, vol. 45, no. 5, pp. 856–864, Mar. 2012, doi: 10.1016/j.jbiomech.2011.11.027.

[14] J. Provost *et al.*, "Electromechanical wave imaging for arrhythmias," *Phys Med Biol*, vol. 56, no. 22, pp. L1–L11, Nov. 2011, doi: 10.1088/0031-9155/56/22/F01.

[15] J. Provost, V. Gurev, N. Trayanova, and E. E. Konofagou, "Mapping of cardiac electrical activation with electromechanical wave imaging: An in silico–in vivo reciprocity study," *Heart Rhythm*, vol. 8, no. 5, pp. 752–759, May 2011, doi: 10.1016/j.hrthm.2010.12.034.

[16] J. Provost *et al.*, "Assessing the atrial electromechanical coupling during atrial focal tachycardia, flutter, and fibrillation using electromechanical wave imaging in humans," *Comput Biol Med*, vol. 65, pp. 161–167, Oct. 2015, doi: 10.1016/j.compbiomed.2015.08.005.

[17] A. Costet, E. Wan, E. Bunting, J. Grondin, H. Garan, and E. Konofagou, "Electromechanical wave imaging (EWI) validation in all four cardiac chambers with 3D electroanatomic mapping in canines in vivo," *Phys Med Biol*, vol. 61, no. 22, pp. 8105–8119, Nov. 2016, doi: 10.1088/0031-9155/61/22/8105.

[18] M. Allessie and N. de Groot, "CrossTalk opposing view: Rotors have not been demonstrated to be the drivers of atrial fibrillation," *J Physiol*, vol. 592, no. 15, pp. 3167–3170, Aug. 2014, doi: 10.1113/jphysiol.2014.271809.

[19] M. T. B. Pope *et al.*, "Spatial and temporal variability of rotational, focal, and irregular activity: Practical implications for mapping of atrial fibrillation," *J Cardiovasc Electrophysiol*, vol. 32, no. 9, pp. 2393–2403, Sep. 2021, doi: 10.1111/jce.15170.

[20] F. Bessiere *et al.*, "High frame rate ultrasounds for electromechanical wave imaging to characterize and differentiate endocardial from epicardial activation of ventricular arrhythmia: A proof of concept study," *Archives of Cardiovascular Diseases Supplements*, vol. 11, no. 2, p. 259, Apr. 2019, doi: 10.1016/j.acvdsp.2019.02.164.

[21] B. Savord and R. Solomon, "Fully sampled matrix transducer for real time 3D ultrasonic imaging," *Proceedings of the IEEE Ultrasonics Symposium*, vol. 1, no. c, pp. 945–953, 2003, doi: 10.1109/ultsym.2003.1293556.

[22] C. Chen *et al.*, "A Pitch-Matched Front-End ASIC With Integrated Subarray Beamforming ADC for Miniature 3-D Ultrasound Probes," *IEEE J Solid-State Circuits*, vol. 53, no. 11, pp. 3050–3064, Nov. 2018, doi: 10.1109/JSSC.2018.2864295.

[23] T. M. Carpenter, M. W. Rashid, M. Ghovanloo, D. M. J. Cowell, S. Freear, and F. L. Degertekin, "Direct Digital Demultiplexing of Analog TDM Signals for Cable Reduction in Ultrasound Imaging Catheters," *IEEE Trans Ultrason Ferroelectr Freq Control*, vol. 63, no. 8, pp. 1078–1085, Aug. 2016, doi: 10.1109/TUFFC.2016.2557622.

[24] E. Kang *et al.*, "A Reconfigurable Ultrasound Transceiver ASIC With 24 × 40 Elements for 3-D Carotid Artery Imaging," *IEEE J Solid-State Circuits*, vol. 53, no. 7, pp. 2065–2075, Jul. 2018, doi: 10.1109/JSSC.2018.2820156.

[25] C. Chen *et al.*, "A Front-End ASIC with Receive Sub-array Beamforming Integrated with a 32 × 32 PZT Matrix Transducer for 3-D Transesophageal Echocardiography," *IEEE J Solid-State Circuits*, vol. 52, no. 4, pp. 994–1006, Apr. 2017, doi: 10.1109/JSSC.2016.2638433.

[26] Y. M. Hopf *et al.*, "A Pitch-Matched Transceiver ASIC With Shared Hybrid Beamforming ADC for High-Frame-Rate 3-D Intracardiac Echocardiography," *IEEE J Solid-State Circuits*, vol. 57, no. 11, pp. 3228–3242, Nov. 2022, doi: 10.1109/JSSC.2022.3201758.

[27] J. Lee *et al.*, "A 36-Channel Auto-Calibrated Front-End ASIC for a pMUT-Based Miniaturized 3-D Ultrasound System," *IEEE J Solid-State Circuits*, vol. 56, no. 6, pp. 1910–1923, Jun. 2021, doi: 10.1109/JSSC.2021.3049560.

[28] J. Li *et al.*, "A 1.54mW/Element 150µm-Pitch-Matched Receiver ASIC with Element-Level SAR/Shared-Single-Slope Hybrid ADCs for Miniature 3D Ultrasound Probes," in *2019 Symposium on VLSI Circuits*, IEEE, Jun. 2019, pp. C220–C221. doi: 10.23919/VLSIC.2019.8778200.

[29] R. M. Kaplan *et al.*, "Use of a novel 4D intracardiac echocardiography catheter to guide interventional electrophysiology procedures," *J Cardiovasc Electrophysiol*, vol. 32, no. 12, pp. 3117–3124, Dec. 2021, doi: 10.1111/jce.15251.

[30] Y.-H. Kim *et al.*, "Automated catheter tip repositioning for intra-cardiac echocardiography," *Int J Comput Assist Radiol Surg*, vol. 17, no. 8, pp. 1409–1417, Aug. 2022, doi: 10.1007/s11548-022-02631-1.

[31] D. G. Della Rocca *et al.*, "PO-696-06 REAL-WORLD EXPERIENCE WITH A NOVEL 3D INTRACARDIAC ECHOCARDIOGRAPHY CATHETER," *Heart Rhythm*, vol. 19, no. 5, pp. S419–S420, May 2022, doi: 10.1016/j.hrthm.2022.03.997.

[32] V. Daeichin *et al.*, "Acoustic characterization of a miniature matrix transducer for pediatric 3D transesophageal echocardiography," *Ultrasound Med Biol*, vol. 44, no. 10, pp. 2143–2154, Oct. 2018, doi: 10.1016/j.ultrasmedbio.2018.06.009.

[33] N. de Jong, N. Bom, J. Souquet, and G. Faber, "Vibration modes, matching layers and grating lobes," *Ultrasonics*, vol. 23, no. 4, pp. 176–182, Jul. 1985, doi: 10.1016/0041-624X(85)90027-7.

[34] N. Ellens, A. Pulkkinen, J. Song, and K. Hynynen, "The utility of sparse 2D fully electronically steerable focused ultrasound phased arrays for thermal surgery: a simulation study," *Phys Med Biol*, vol. 56, no. 15, pp. 4913–4932, Aug. 2011, doi: 10.1088/0031-9155/56/15/017.

[35] A. Ramalli, E. Boni, A. S. Savoia, and P. Tortoli, "Density-tapered spiral arrays for ultrasound 3-D imaging," *IEEE Trans Ultrason Ferroelectr Freq Control*, vol. 62, no. 8, pp. 1580–1588, 2015, doi: 10.1109/TUFFC.2015.007035.

[36] K. Chen, H. S. Lee, and C. G. Sodini, "A Column-Row-Parallel ASIC Architecture for 3-D Portable Medical Ultrasonic Imaging," *IEEE J Solid-State Circuits*, vol. 51, no. 3, pp. 738–751, Mar. 2016, doi: 10.1109/JSSC.2015.2505714.

[37] M. Flesch *et al.*, "4D in vivo ultrafast ultrasound imaging using a row-column addressed matrix and coherently-compounded orthogonal plane waves," *Phys Med Biol*, vol. 62, no. 11, pp. 4571–4588, Jun. 2017, doi: 10.1088/1361-6560/aa63d9.

[38] L. Wei *et al.*, "High Frame Rate Volumetric Imaging of Microbubbles Using a Sparse Array and Spatial Coherence Beamforming," *IEEE Trans Ultrason Ferroelectr Freq Control*, vol. 68, no. 10, pp. 3069–3081, 2021, doi: 10.1109/TUFFC.2021.3086597.

[39] H. Bouzari *et al.*, "Curvilinear 3-D Imaging Using Row-Column-Addressed 2-D Arrays with a Diverging Lens: Phantom Study," *IEEE Trans Ultrason Ferroelectr Freq Control*, vol. 65, no. 7, pp. 1182–1192, 2018, doi: 10.1109/TUFFC.2018.2836384.

[40] C. Papadacci, M. Pernot, M. Couade, M. Fink, and M. Tanter, "High-contrast ultrafast imaging of the heart," *IEEE Trans Ultrason Ferroelectr Freq Control*, vol. 61, no. 2, pp. 288–301, Feb. 2014, doi: 10.1109/TUFFC.2014.6722614.

[41] Y. M. Hopf *et al.*, "A Compact Integrated High-Voltage Pulser Insensitive to Supply Transients for 3-D Miniature Ultrasound Probes," *IEEE Solid State Circuits Lett*, vol. 5, pp. 166–169, 2022, doi: 10.1109/LSSC.2022.3180071.

[42] Y. M. Hopf, "Integrated Circuits for 3D High-Frame-Rate Intracardiac Echocardiography Probes," PhD thesis, Delft University of Technology, 2023. doi: https://doi.org/10.4233/uuid:7016e74d-c7df-42a8-8257-11326940ad7f.

[43] Y. M. Hopf *et al.*, "A Pitch-Matched High-Frame-Rate Ultrasound Imaging ASIC for Catheter-Based 3-D Probes," *IEEE J Solid-State Circuits*, pp. 1–16, 2023, doi: 10.1109/JSSC.2023.3299749.

[44] D. S. dos Santos *et al.*, "A Tiled Ultrasound Matrix Transducer for Volumetric Imaging of the Carotid Artery," *Sensors*, vol. 22, no. 24, p. 9799, Dec. 2022, doi: 10.3390/s22249799.

[45] R. J. McGough, "Rapid calculations of time-harmonic nearfield pressures produced by rectangular pistons," *J Acoust Soc Am*, vol. 115, no. 5, pp. 1934–1941, May 2004, doi: 10.1121/1.1694991.

[46] M. Shabanimotlagh *et al.*, "Optimizing the directivity of piezoelectric matrix transducer elements mounted on an ASIC," *IEEE International Ultrasonics Symposium, IUS*, pp. 5–8, 2017, doi: 10.1109/ULTSYM.2017.8091752.

[47] R. Wodnicki *et al.*, "Co-Integrated PIN-PMN-PT 2-D Array and Transceiver Electronics by Direct Assembly Using a 3-D Printed Interposer Grid Frame," *IEEE Trans Ultrason Ferroelectr Freq Control*, vol. 67, no. 2, pp. 387–401, Feb. 2020, doi: 10.1109/TUFFC.2019.2944668.

[48] M. Celmer and K. J. Opieliński, "Research and Modeling of Mechanical Crosstalk in Linear Arrays of Ultrasonic Transducers," *Archives of Acoustics*, vol. 41, no. 3, pp. 599–612, Sep. 2016, doi: 10.1515/aoa-2016-0058.

[49] A. Bybi, D. Khouili, C. Granger, M. Garoum, A. Mzerd, and A.-C. Hladky-Hennion, "Experimental Characterization of A Piezoelectric Transducer Array Taking into Account Crosstalk Phenomenon," *International Journal of Engineering and Technology Innovation*, vol. 10, no. 1, pp. 01–14, Jan. 2020, doi: 10.46604/ijeti.2020.4348.

[50] S.-C. Wooh and Y. Shi, "Optimum beam steering of linear phased arrays," *Wave Motion*, vol. 29, no. 3, pp. 245–265, 1999, doi: 10.1016/S0165-2125(98)00039-0.

10

Design of a CMUT matrix transducer for high-frame-rate 3D imaging of the abdominal aorta

10.1. INTRODUCTION

STROKE and the rupture of abdominal aortic aneurysm (AAA) are among the leading causes of sudden death [1]. AAA refers to a localized enlargement of the abdominal aorta, characterized by a diameter exceeding 3 cm, or being 50% larger than its normal size, which is typically around 2.0 cm. Existing prevention strategies for these life-threatening and debilitating conditions rely on simplistic geometric measures such as percentage stenosis and aortic diameter [2], which often prove to be insufficient in predicting many acute events. Moreover, surgical intervention prevents stroke in only one out of six patients with carotid stenosis exceeding 70%. In contrast, patients with an aortic diameter greater than 5.5 cm may actually have a relatively low risk of rupture. Consequently, current screening practices are highly inadequate, leading to fatal events in untreated vulnerable arteries and unnecessary overtreatment in stable vessels [3].

Recent advancements in ultrasound technology enable the measurement of mechanical properties of tissues and blood velocity at high resolution. However, these ultrasound techniques provide only a limited 2D view [4], which is insufficient for a comprehensive analysis of the vessel vulnerability. Emerging ultrasound techniques such as 3D flow imaging and elastography have the potential to significantly improve cardiovascular disease diagnosis and treatment by allowing ultrafast 3D imaging and harmonic imaging, which is required for detailed spatial and temporal analysis of the abdominal aorta [5]. Therefore, the ultrasound probes utilized should be able to generate 3D images at an ultrafast rate (> 1000 volumes per second) with a wide field of view [6].

The most common approaches for 3D ultrasound imaging include mechanically moving a standard linear probe or electronically steering a focused transmit beam using a matrix transducer. However, these methods impede the achievement of higher frame rates [7], [8]. To achieve 3D high-frame-rate ultrasound imaging with a wide field of view, it is necessary to use a large matrix transducer (typically consisting of thousands of elements) and employ unfocused transmit beams, such as plane and diverging waves, along with parallel receive beamforming [5], [9], [10].

Building a matrix array with numerous small elements presents a significant challenge due to the need for thousands of electrical connections between the matrix array and the imaging system. To overcome this challenge, an application-specific integrated circuit (ASIC) can be integrated with the matrix array to reduce the number of electrical connections. This integration allows the utilization of transducers with a high element count to be used with conventional 128- to 256-channel systems and probe cables. Although this approach offers advantages such as channel reduction and signal amplification, it does involve a more complex and expensive development process [10], [11].

In this paper, we introduce the development of a capacitive micromachined ultrasonic transducer (CMUT) matrix probe designed for high-frame-rate 3D imaging of the abdominal aorta. To achieve a high frame rate while covering a large field of view, we employ four diverging transmit beams steered at four different angles to cover one quadrant of the volume at a time. The transducer operates at 2.6 MHz and features 2048 elements arranged in a 32 × 64 configuration with a pitch of 365 μm × 365 μm. The matrix array is integrated with a pitch-matched ASIC that

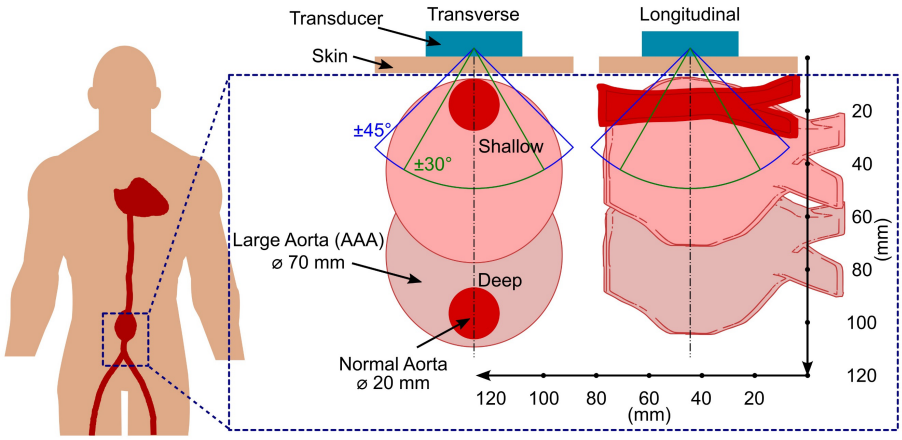

Figure 10.1: Abdominal aortic ultrasound imaging.

contains a pulser capable of generating 65V unipolar pulses, and a current-mode low-noise amplifier with 36 dB continuous time-gain compensation. In addition, the ASIC provides an 8-fold reduction in receive channel count through micro-beamforming and time-division multiplexing. We conduct acoustic simulations to define the main specifications of the prototype, discuss the fabrication and characterization process, and present initial experiments demonstrating the imaging capabilities of the prototype.

10.2. METHODS

10.2.1. DESIGN CHOICES

Here, we present the key features of the matrix transducer designed for abdominal aorta imaging (see Figure 10.1 and Table 10.1). We have opted for a CMUT array due to its distinct advantages over traditional piezoelectric transducers made of lead zirconate titanate (PZT). CMUTs, as vacuum-sealed capacitive components, exhibit reduced self-heating compared to PZT, known for their higher dielectric loss. Additionally, the thin plates of CMUTs, characterized by low acoustic impedance,

Table 10.1: Design parameters of the CMUT probe.

Parameter	Value
Center frequency	2.6 MHz
Aperture	23 mm × 46 mm
Number of elements	8192
Pitch	365 µm × 365 µm
SAP size	2 × 2
TDM	2
Number of Verasonics systems	4

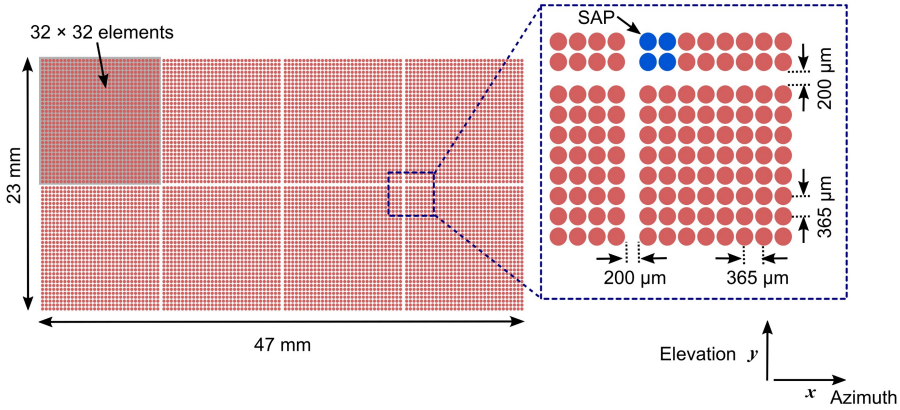

Figure 10.2: Layout of the designed CMUT matrix array.

eliminate the need for a matching layer—a contrast to PZT transducers [12]. Another advantage of CMUTs lies in their bandwidth. Despite our application's targeted center frequency (f_c) being 2.6 MHz, CMUTs exhibit a broad bandwidth, typically exceeding 100%. This characteristic enables them to operate effectively across a wide frequency range, offering versatility beyond the intended center frequency. Lastly, CMUTs offer the practical advantage of facilitating larger arrays and large-scale manufacturing [13]. This is in contrast to PZT transducers, which are labor-intensive and pose challenges in the manufacturing process.

Figure 10.2 illustrates the layout of the designed CMUT matrix array. This probe consists of 64 × 128 elements with a pitch of 365 µm × 365 µm, resulting in a total aperture of about 23 mm × 47 mm. Note that, due to the high element count of the probe (8192 elements), a significant degree of channel reduction is required in order to connect the probe to a conventional research ultrasound system, which contains up to 256 channels [14], [15].

To achieve the required channel reduction, we chose to integrate the CMUT array with an ASIC. However, note that manufacturing a single large ASIC is very expensive. Thus, we opted to tile eight identical smaller ASICs in a 2 × 4 array configuration [13], with a spacing of 200 µm between the tiles. ASICs provide flexibility in reducing channel count through various methods, such as channel multiplexing, "micro-beamforming" (also known as "sub-array/sub-aperture beamforming," or "pre-steering"), in-probe digitization, and time-division multiplexing [16], [17], [18]. In our design, we employed different strategies to reduce the number of channels in receive, starting with sub-aperture (SAP) beamforming.

In the SAP beamforming approach, the array elements are arranged into sub-groups, and the time delay required for beamforming includes two stages: a coarse delay, which is common for all elements of the SAP; and a fine delay, which might be distinct for each element within the SAP. The coarse delays are applied by the back-end console (i.e., external imaging system), while the fine delays are provided by the ASIC inside the probe. All received RF signals within the SAP are then summed into

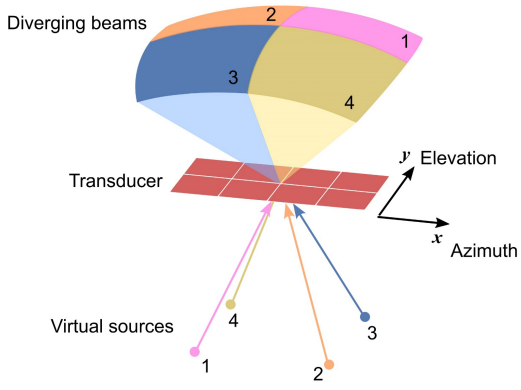

Figure 10.3: Imaging scheme using four diverging beams.

a single signal [19], [20]. In the proposed design, we divided the matrix array into small SAPs consisting of 2 × 2 elements, resulting in a fourfold reduction in the number of channels.

To further reduce channel count in receive, we implemented 2× time-division multiplexing (TDM) [21]. The combination of the 2× TDM together with 2 × 2 SAP resulted in an overall 8-fold reduction in the number of channels. In practical terms, this means that 1024 cables are required to connect the probe to the external imaging system. To interface the fully populated matrix, we plan to utilize four research imaging systems (Vantage, Verasonics, Inc., Kirkland, WA, USA), each equipped with 256 channels.

10.2.2. IMAGING SCHEME

In the context of abdominal aortic ultrasound imaging, we aim to achieve a volume rate of 2000 volumes/s while imaging a 3D volume of 60° × 60° (azimuth × elevation) with a penetration depth of up to 10 cm. For this depth and sound speed of 1540 m/s, the round-trip travel time of ultrasound waves is about 130 µs. Given this travel time, the pulse repetition frequency (PRF) is constrained to 7.7 kHz to allow enough time for the echoes to return before sending the next pulse. Consequently, with this PRF and depth, a maximum of four ultrasound pulses can be transmitted per frame to cover the entire region of interest, resulting in a frame rate of 2000 volumes/s.

In our design, we propose a transmit scheme utilizing four diverging beams steered in four different directions. As depicted in Figure 10.3, the beams are steered at (15°, 15°), (-15°, 15°), (15°, -15°), and (-15°, -15°) to sequentially cover one quadrant of the volume at a time. This is accomplished through the utilization of four distinct "virtual sources," defined as focal distances positioned behind the physical transducer [19], [22]. During the receive phase using parallel receive beamforming,

the SAPs can cover a pre-steering range of ±15° in both azimuth and elevation directions.

10.2.3. BEAM PROFILE SIMULATIONS

In conventional ultrasound imaging, where sweeping focused transmit beams are utilized, a single scan line is reconstructed from each transmit event. When SAP beamforming is applied during the receive phase, the pre-focusing and steering of the SAP can precisely align with the direction of the scan line. This alignment ensures that the two-stage beamforming process (involving coarse and fine delays) closely resembles a fully wired array, preserving image quality effectively. In contrast, in high-frame-rate ultrasound imaging employing diverging waves, multiple scan lines with significantly different directions must be reconstructed from the same transmit event and SAP channel data. Consequently, the global delays become substantially inaccurate for scan lines deviating from the pre-focusing direction. This inaccuracy leads to the occurrence of side and grating lobes, potentially degrading the overall image quality [19], [23].

To evaluate the performance of the beamforming of our probe, we conducted a simulation study using Field II, an ultrasound simulator based on the spatial impulse response method [24]. This study focused on assessing key parameters of the probe's beam profile in both transmit and receive operations. In transmit, we investigated the impact of the virtual focal distance on different aspects of the generated beam, including the amplitude of the main lobe, its opening angle, and the generation of secondary lobes. For this, we defined a virtual focus distance ranging from -10 mm to – 40 mm and recorded the resulting one-way beam profile generated by the transducer. Furthermore, we explored the influence of time delay quantization on the degradation of the transmitted beam. Due to the discrete nature of the applied time delays, the curves necessary for ideal focusing and steering are approximated in a quantized manner, which can give rise to grating lobes within the image field of view [25], [26]. Our investigation involved testing time delay increments of 96 ns ($T/4$), 48 ns ($T/8$), and 32 ns ($T/12$), where $T = 1/f_c$ is the period of the transmitted waveform (i.e., 384 ns).

To evaluate the receive phase, we conducted a two-way beam profile simulation [19]. First, we examined the impact of the beamforming on the generation of secondary lobes when the transmit beam, the back-end console, and the SAPs are steering in different directions within a range of 0° to 30° (note that, in all cases, the SAPs are set to follow the transmit direction). For the worst-case scenario, we assessed the effect of uniformizing the SAP delays, meaning that all SAPs are pre-steered to the same direction within an ASIC. Then, we investigated the effect of delay quantization in the SAPs. Similar to the approach used in transmit, we evaluated the time delay resolution with steps of $T/4$, $T/8$, and $T/12$.

In all simulations, we defined a region of 60° × 60° × 10 cm and recorded the beam profile across its surface area in increments of 1° in both azimuth and elevation. The parameters set for these simulations included a sampling frequency of 50 MHz, a medium sound speed of 1540 m/s, and an attenuation of 0.5 dB/cm.

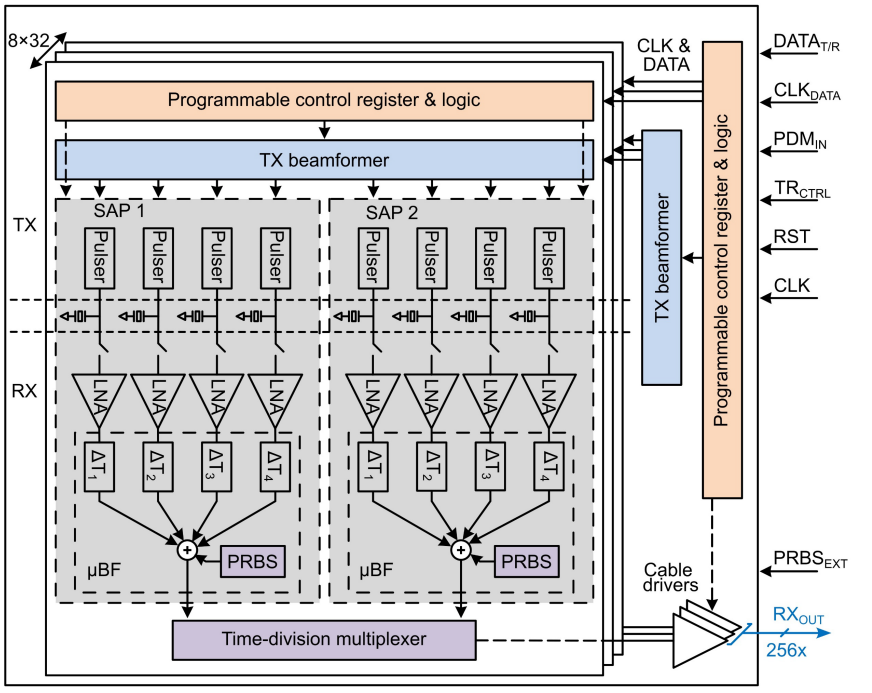

Figure 10.4: Block diagram of the architecture of a single ASIC.

The outcomes of the simulations were subsequently employed to refine the specifications of the probe and assist the design of the ASIC.

10.2.4. ASIC DESIGN

Figure 10.4 illustrates the architecture overview of the designed ASIC. As shown, each CMUT is connected to a pitch-matched front-end on the ASIC, consisting of a pulser capable of generating 65V unipolar pulses for transmit (TX), and a current-mode low-noise amplifier (LNA) with 36 dB continuous time-gain compensation (TGC) for receive (RX), isolated from the pulser by a TX/RX switch. For on-chip transmit beamforming, the pulsers are driven by a programmable digital pipeline routing a pulse-density modulated signal across the chip, providing high flexibility in both the transmit waveform and the delay pattern. Each ASIC is subdivided into subgroups of 2 × 4 elements, consisting of two 2 × 2 SAPs applying delay-and-sum beamforming, which are combined using TDM and fed to the imaging system via a cable driver.

In conjunction with the ASIC, we developed a custom motherboard that serves as the interface between the CMUT probe and the Verasonics system. This motherboard contains a field programmable gate array (FPGA), which is responsible for controlling the ASIC.

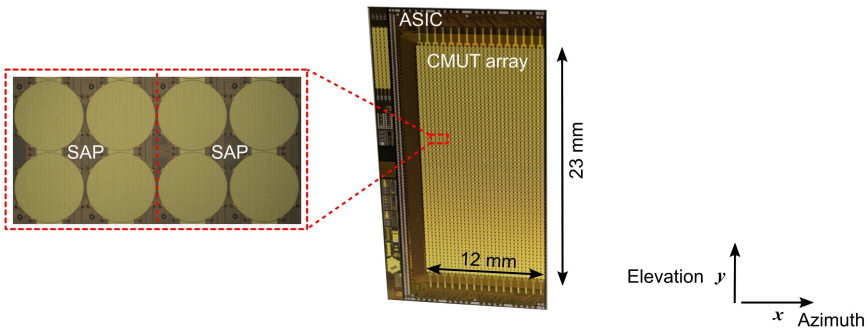

Figure 10.5: Die micrograph of the fabricated CMUT array.

10.2.5. FABRICATION

In general, there are two CMUT fabrication approaches: surface machining (i.e., sacrificial release) and wafer-to-wafer bonding. Our employed CMUT technology uses a sacrificial release process (CM5, Philips Engineering Solutions, Eindhoven, The Netherlands). In this approach, a vacuum gap is formed by etching a sacrificial layer positioned between the top plate and the substrate [27].

The CM5 device is biased at 120V and is specifically designed to operate in so-called collapse mode [28]. In collapse mode, the bias voltage consistently exceeds the collapse voltage, ensuring a part of the membrane is consistently in contact with the substrate. The operation in collapse mode results in high output pressure and receive sensitivity due to the high electric field and small effective gap [13].

To simplify the fabrication process of the first CMUT prototype, we made a key decision. Instead of building the full size of the proposed CMUT probe (a 64 × 128 matrix array), we opted to build one-half of the aperture in both directions, resulting in a 32 × 64 matrix array. Building a smaller aperture at this stage of prototype development reduces cost and complexity while all of the functionality of the probe can still be tested. A photograph of the fabricated CMUT array, which is monolithically integrated on an ASIC, is presented in Figure 10.5.

10.2.6. PRESSURE FIELD CHARACTERIZATION

We conducted a preliminary acoustic characterization of the CMUT prototype using the measurement setup depicted in Figure 10.6(a). This initial assessment focused on characterizing the acoustic beam profile of the prototype when transmitting a steered diverging wave. For this, hydrophone scans were executed on a plane parallel to the transducer surface, precisely positioned 60 mm away from the transducer. We utilized a calibrated 0.2 mm needle hydrophone (SN2385, Precision Acoustics Ltd., Dorchester, UK). The hydrophone output was digitized by an oscilloscope (DSO-X 4024A, Agilent Technologies, Santa Clara, CA, USA).

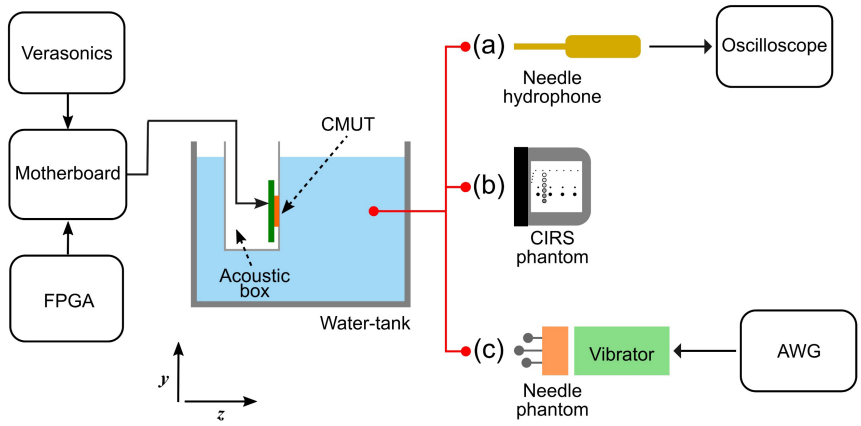

Figure 10.6: Experimental setup. (a) Hydrophone measurements. (b) Imaging of CIRS phantom. (c) Imaging of vibrating needles.

10.2.7. HIGH-FRAME-RATE 3D IMAGING

To evaluate the high-frame-rate 3D imaging capabilities of the designed probe, we conducted two imaging experiments. In the initial experiment (see Figure 10.6(b)), we utilized a multi-purpose ultrasound phantom that provides tissue-mimicking properties (model: 040GSE, CIRS, Inc., Norfolk, VA, USA). In the second experiment (see Figure 10.6(c)), we used a custom phantom consisting of three vibrating needles. To introduce motion into the system, we attached this needle phantom to a mechanical shaker (Type 4810, Brüel & Kjær, Nærum, Denmark) and applied a low-frequency sine vibration of 20 Hz using an arbitrary waveform generator (AWG; 33250A, Agilent Technologies, Santa Clara, CA, USA), as we described in our previous work [11]. In all imaging experiments, the digitized received data was transferred to a computer for processing. The reconstruction of the 3D volume image was performed offline using conventional delay-and-sum operations.

10.3. RESULTS AND DISCUSSION

10.3.1. SIMULATION RESULTS

Figure 10.7 illustrates simulations of the beam profile for the diverging transmit beam steered at (15°, 15°) under different virtual focus distances. Each beam profile has been normalized with respect to the maximum pressure observed in the main lobe of Figure 10.7(d). Through our observations, we identified a trade-off between the opening angle and the transmitted pressure. When the virtual source is positioned near the transducer surface, it leads to the insonification of a broad beam with a lower pressure level. Conversely, placing the virtual source farther behind the probe results in a higher emitted pressure but at the expense of a reduced opening

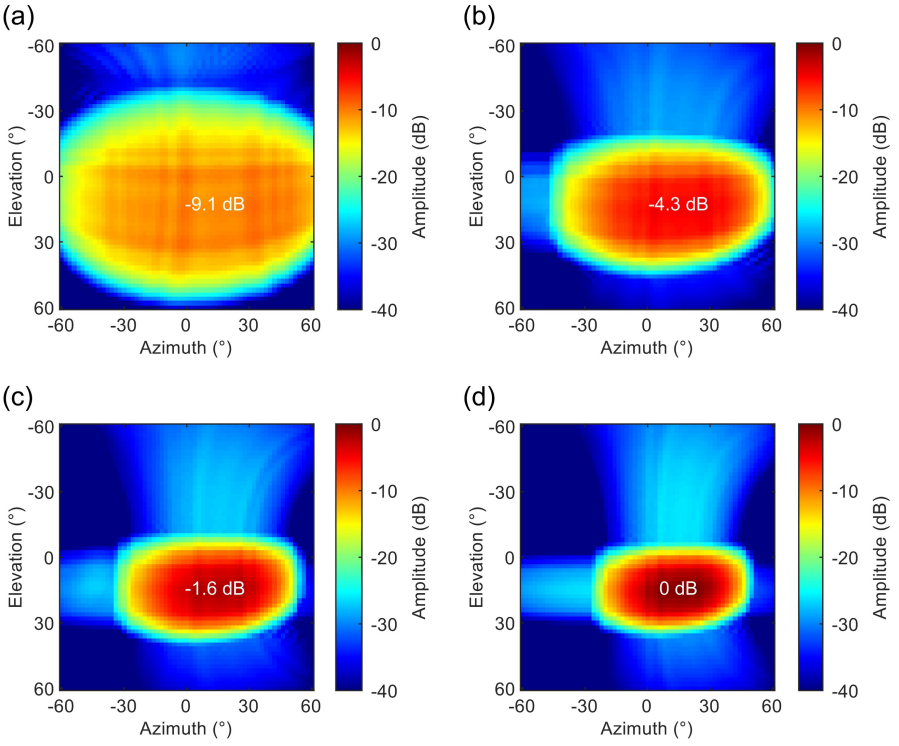

Figure 10.7: Simulated transmitted beams steered at (15°, 15°) with the virtual source focused at (a) -10 mm, (b) -20 mm, (c) -30 mm, and (d) -40 mm.

angle. After careful analysis, we determined that the optimal value for the virtual source focus distance is -30 mm. At this distance, we achieve a -6 dB opening angle of approximately 58° in azimuth and 30° in elevation, with a considerably higher amplitude compared to scenarios with wider beams.

In Figure 10.8, we illustrate the impact of time delay quantization on the transmit beam. It is evident that a finer quantization of the delays reduces artifacts, improving the overall quality of the beam profile. Our observations indicate that employing a delay step smaller than $T/12$ appears unnecessary, as it does not significantly enhance the beam quality further.

In Figure 10.9, we present the two-way beam profile for various steering configurations that were tested. Each beam profile has been independently normalized to improve the visibility of grating lobes. Upon observation, it is evident that when the pre-steering direction of the SAP beamformers aligns with the desired direction of the reconstructed scan line, grating lobes are absent, and all received energy originates from the main lobe. This phenomenon is observed when both the SAPs and the back-end console are steering at (0°, 0°), (15°, 15°), and (30°, 30°), as seen in Figure 10.9(a), (d), and (f), respectively. In these conditions, the receive beamformer operates as a fully wired array. Conversely, when the SAP and console are steering in different directions, a noticeable increase in grating lobes is observed,

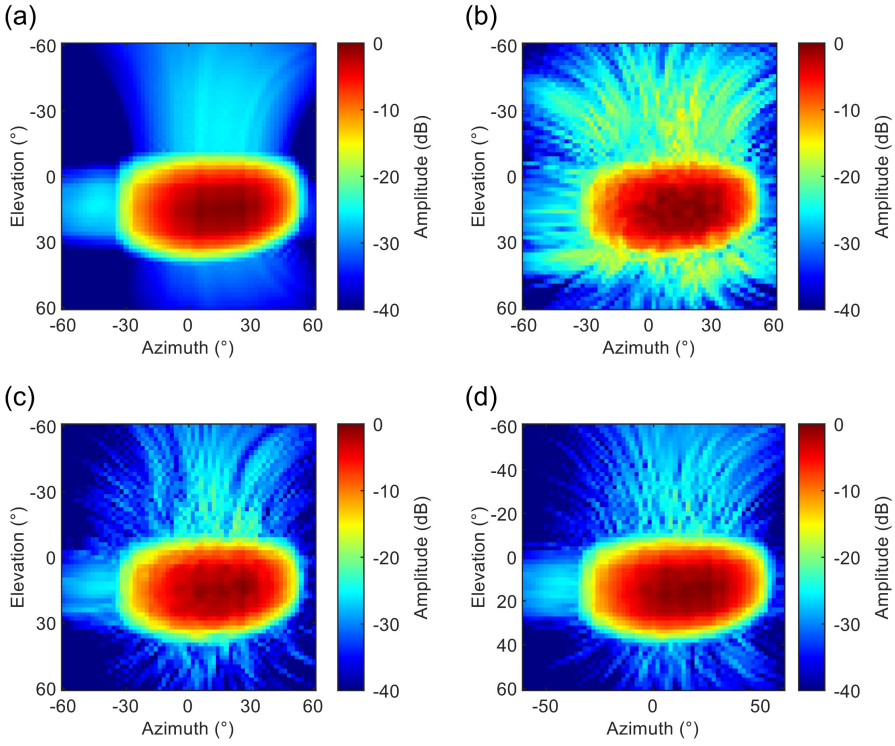

Figure 10.8: Effect of time delay quantization on the transmit beam. (a) No quantization. (b) $T/4$. (c) $T/8$. (d) $T/12$.

as seen in Figure 10.9(b), (c), and (e), respectively. This occurs because energy "leaks" from the desired direction to the pre-steering direction, leading to a partial loss of main lobe amplitude while preserving side/grating lobes in the SAP pre-steering direction [19], [23]. The worst-case scenario is visible in Figure 10.9(e), where the energy level of the secondary lobes closely approaches that of the main lobe. This specific case was chosen for the analysis of delay quantization and uniformization in the SAPs.

Figure 10.10 illustrates the implementation of uniform delays per ASICs, a strategy employed in our design to reduce complexity. In this approach, the delay pattern for all SAPs within a given ASIC is identical. These delays are computed using the central SAP of the ASIC as a reference. Thus, the delay pattern of the central SAP is extended to all SAPs within the same ASIC. It is important to note, however, that each ASIC can be individually programmed. This flexibility allows for distinct ASICs to have different delay patterns.

In Figure 10.11, we depict the influence of uniform SAP delays along with time delay quantization on the two-way beam profile. Similar to our observations in the transmit phase, a delay step smaller than $T/12$ seems unnecessary, as it does not bring a significant improvement in beam quality. Additionally, the uniformization of delays does not notably contribute to beam degradation. Consequently,

incorporating this feature is feasible and proves advantageous in simplifying the ASIC design.

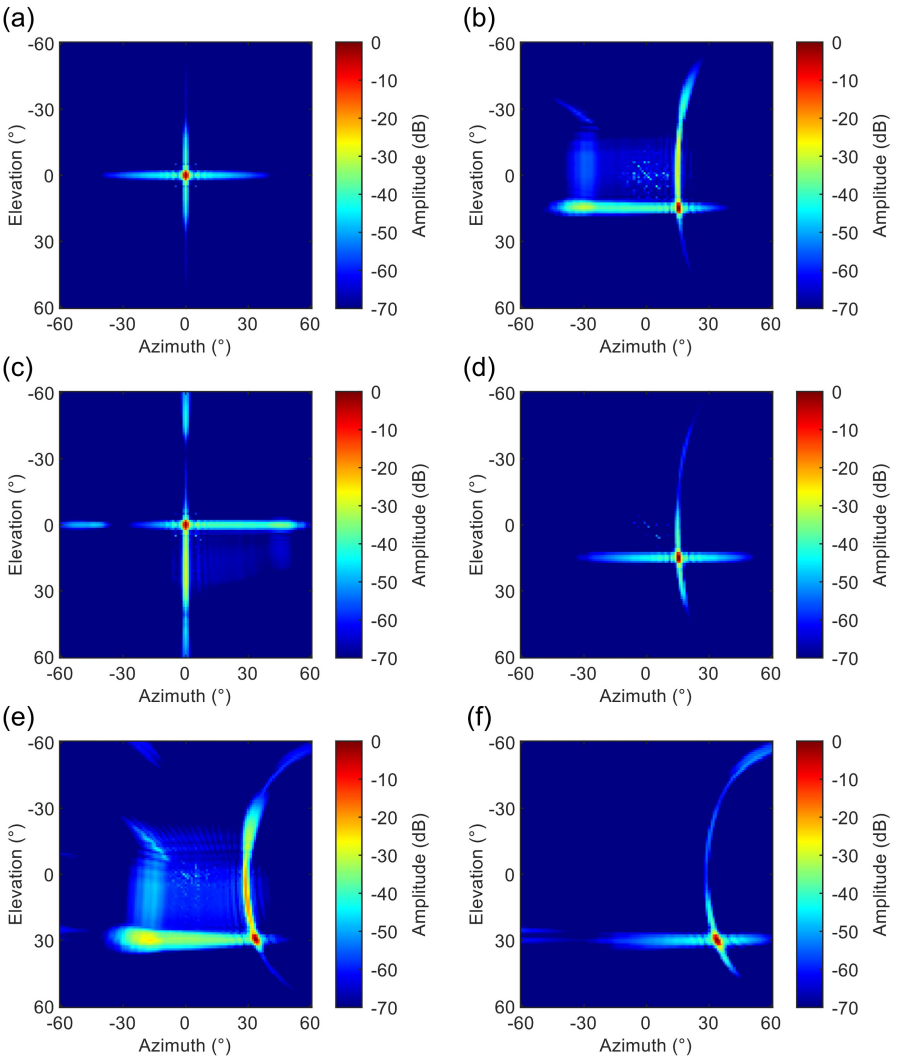

Figure 10.9: Two-way beam profile simulations for different steering directions.
(a) SAP=(0°,0°); console=(0°,0°). (b) SAP=(0°,0°); console=(15°,15°).
(c) SAP=(15°,15°); console=(0°,0°). (d) SAP=(15°,15°); console=(15°,15°).
(e) SAP=(15°,15°); console=(30°,30°). (f) SAP=(30°,30°); console=(30°,30°).

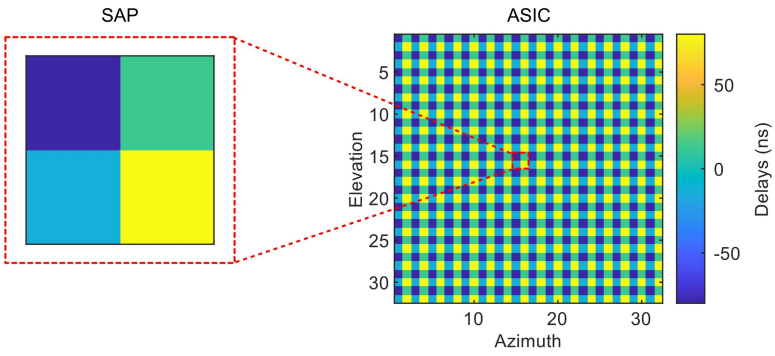

Figure 10.10: Single ASIC with uniform SAP delays.

10.3.2. EXPERIMENTAL RESULTS

Figure 10.12(a) and Figure 10.12(b) display, respectively, the simulated and measured pressure field of the CMUT prototype transmitting a diverging wave steered at (15°, 15°). The experimental beam profile closely aligns with the simulation, although slightly narrower. We attribute this variance in beam width to potential misalignment of the prototype during hydrophone scans. However, despite of this variance, these results indicate that the designed ASIC can accurately generate time delays for transmitting diverging beams and steering them in accordance with the proposed imaging scheme.

Figure 10.13 presents a slice of the reconstructed volumetric image of the tissue-mimicking phantom. The image reveals that all wire targets within the field of view (red dashed line in Figure 10.13(b)) are detectable up to a distance of 10 cm. Although the current aperture size does not provide the lateral resolution of the intended full aperture size (i.e., 64 × 128 elements), this result indicates that the full aperture probe should successfully capture images within the intended volume of 60° × 60° × 10 cm.

Figure 10.14(a) shows a volumetric image of the vibrating needles captured by our CMUT probe at a frame rate of 2000 volumes/s. The reconstructed image clearly distinguishes the three needles in the 3D space. In order to demonstrate the high-frame-rate imaging capability of our device, we tracked the vibrational motion of a single needle during a 60 ms acquisition. Figure 10.14(b) illustrates the resulting displacement of one needle, where the 20 Hz vibration is clearly visible. As seen, we successfully captured the entire sinusoidal motion within the acquisition with a temporal resolution of 0.5 ms, which indicates proper internal timing of the prototype. These results are consistent with our previous experiments using a different probe [11], confirming our capability to achieve high-frame-rate 3D imaging.

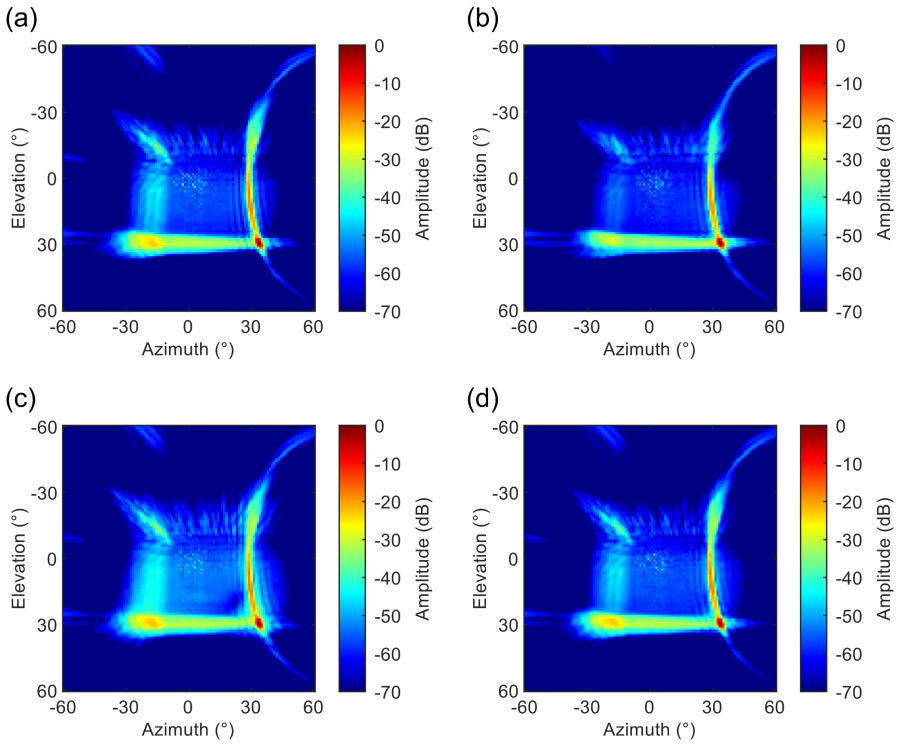

Figure 10.11: Effect of uniform SAP delays and delay quantization on the two-way beam profile. (a) No quantization. (b) $T/4$. (c) $T/8$. (d) $T/12$.

10.4. CONCLUSION

We have presented the design of a high-frame-rate 3D imaging CMUT matrix with a pitch of 365 µm × 365 µm, comprising 64 × 128 elements, and interfaced with a pitch-matched ASIC. To reduce the number of channels, we implemented 2 × 2 SAP beamforming and 2× TDM in receive, resulting in an overall 8-fold reduction.

To reduce complexity and cost during this stage of the development, we constructed a smaller aperture than originally intended. Despite the reduced size, we were able to conduct initial tests to assess the functionality of the probe. However, a more comprehensive acoustic characterization is still necessary.

In imaging experiments, we successfully obtained 3D images with a large field of view and at a rate of 2000 volumes/s. This outcome opens avenues for future ultrasound imaging applications, particularly in the context of the abdominal aorta.

Future efforts should concentrate on realizing a full-aperture probe. Additionally, we aim to construct an equivalent PZT matrix interfaced with the same ASIC to facilitate a comparative analysis between both PZT and CMUT technologies.

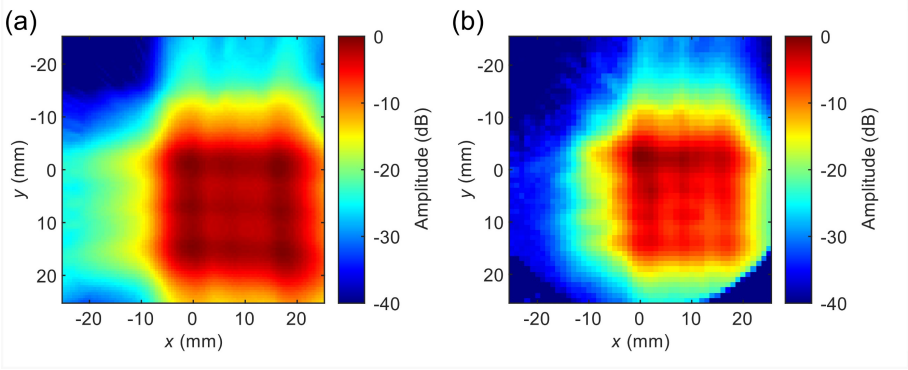

Figure 10.12: Pressured field generated by the CMUT prototype steered at (15°, 15°). (a) Simulated. (b) Measured.

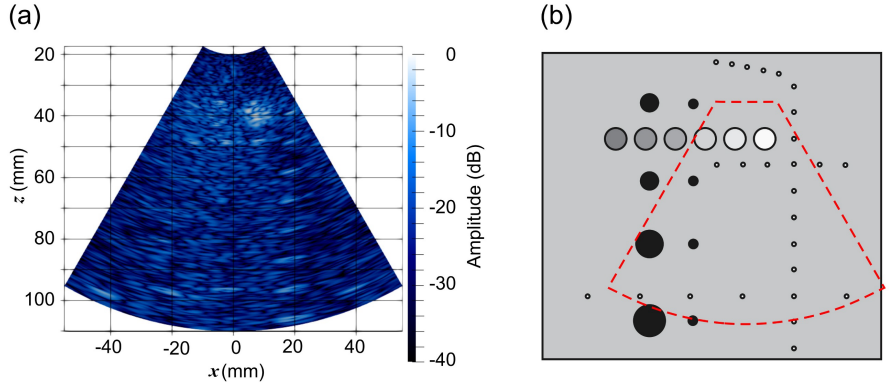

Figure 10.13: Imaging of the CIRS phantom. (a) Reconstructed 2D image. (b) Scheme of the phantom indicating the field of view of the probe.

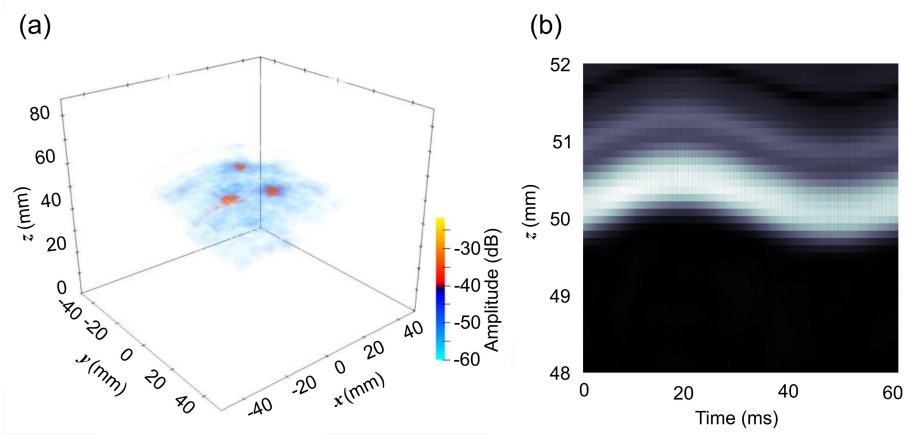

Figure 10.14: (a) 3D reconstructed image of the needle phantom. (b) Needle displacement.

10.5. REFERENCES

[1] D. Mozaffarian *et al.*, "Executive Summary: Heart Disease and Stroke Statistics—2016 Update," *Circulation*, vol. 133, no. 4, pp. 447–454, Jan. 2016, doi: 10.1161/CIR.0000000000000366.

[2] H. Baumgartner *et al.*, "Recommendations on the echocardiographic assessment of aortic valve stenosis: a focused update from the European Association of Cardiovascular Imaging and the American Society of Echocardiography," *Eur Heart J Cardiovasc Imaging*, vol. 18, no. 3, pp. 254–275, Mar. 2017, doi: 10.1093/ehjci/jew335.

[3] E. Kang *et al.*, "A Reconfigurable Ultrasound Transceiver ASIC With 24 × 40 Elements for 3-D Carotid Artery Imaging," *IEEE J Solid-State Circuits*, vol. 53, no. 7, pp. 2065–2075, Jul. 2018, doi: 10.1109/JSSC.2018.2820156.

[4] M. Couade *et al.*, "Ultrafast imaging of the arterial pulse wave," *IRBM*, vol. 32, no. 2, pp. 106–108, Apr. 2011, doi: 10.1016/j.irbm.2011.01.012.

[5] M. Cikes, L. Tong, G. R. Sutherland, and J. D'hooge, "Ultrafast Cardiac Ultrasound Imaging," *JACC Cardiovasc Imaging*, vol. 7, no. 8, pp. 812–823, Aug. 2014, doi: 10.1016/j.jcmg.2014.06.004.

[6] P. Kruizinga, F. Mastik, N. de Jong, A. F. W. van der Steen, and G. van Soest, "High frame rate ultrasound imaging of human carotid artery dynamics," in *2012 IEEE International Ultrasonics Symposium*, IEEE, Oct. 2012, pp. 1177–1180. doi: 10.1109/ULTSYM.2012.0293.

[7] Z. Guo and A. Fenster, "Three-dimensional power Doppler imaging: A phantom study to quantify vessel stenosis," *Ultrasound Med Biol*, vol. 22, no. 8, pp. 1059–1069, Jan. 1996, doi: 10.1016/S0301-5629(96)00125-1.

[8] J. N. Welch, J. A. Johnson, M. R. Bax, R. Badr, and R. Shahidi, "A real-time freehand 3D ultrasound system for image-guided surgery," in *2000 IEEE Ultrasonics Symposium. Proceedings. An International Symposium (Cat. No.00CH37121)*, IEEE, 2000, pp. 1601–1604. doi: 10.1109/ULTSYM.2000.921630.

[9] S. W. Smith, W. Lee, E. D. Light, J. T. Yen, P. Wolf, and S. Idriss, "Two dimensional arrays for 3-D ultrasound imaging," in *2002 IEEE Ultrasonics Symposium, 2002. Proceedings.*, IEEE, 2002, pp. 1545–1553. doi: 10.1109/ULTSYM.2002.1192590.

[10] D. S. dos Santos *et al.*, "A Tiled Ultrasound Matrix Transducer for Volumetric Imaging of the Carotid Artery," *Sensors*, vol. 22, no. 24, p. 9799, Dec. 2022, doi: 10.3390/s22249799.

[11] D. S. dos Santos *et al.*, "An Ultrasound Matrix Transducer for High-Frame-Rate 3-D Intra-cardiac Echocardiography," *Ultrasound Med Biol*, vol. 50, no. 2, pp. 285–294, Feb. 2024, doi: 10.1016/j.ultrasmedbio.2023.11.001.

[12] C. Seok, O. J. Adelegan, A. O. Biliroglu, F. Y. Yamaner, and O. Oralkan, "A Wearable Ultrasonic Neurostimulator—Part II: A 2D CMUT Phased Array System With a Flip-Chip Bonded ASIC," *IEEE Trans Biomed Circuits Syst*, vol. 15, no. 4, pp. 705–718, Aug. 2021, doi: 10.1109/TBCAS.2021.3105064.

[13] R. van Schaijk, M. in 't Zandt, P. Robaeys, M. Slotboom, J. Klootwijk, and P. Bekkers, "Reliability of collapse mode CMUT," in *2023 IEEE International Ultrasonics Symposium (IUS)*, IEEE, Sep. 2023, pp. 1–4. doi: 10.1109/IUS51837.2023.10307882.

[14] E. Boni *et al.*, "ULA-OP 256: A 256-Channel Open Scanner for Development and Real-Time Implementation of New Ultrasound Methods," *IEEE Trans Ultrason Ferroelectr Freq Control*, vol. 63, no. 10, pp. 1488–1495, 2016, doi: 10.1109/TUFFC.2016.2566920.

[15] "Verasonics. The Vantage System." Accessed: May 05, 2022. [Online]. Available: https://verasonics.com/the-vantage-advantage/

[16] B. Savord and R. Solomon, "Fully sampled matrix transducer for real time 3D ultrasonic imaging," in *IEEE Symposium on Ultrasonics, 2003*, IEEE, 2003, pp. 945–953. doi: 10.1109/ULTSYM.2003.1293556.

[17] C. Chen *et al.*, "A Pitch-Matched Front-End ASIC With Integrated Subarray Beamforming ADC for Miniature 3-D Ultrasound Probes," *IEEE J Solid-State Circuits*, vol. 53, no. 11, pp. 3050–3064, Nov. 2018, doi: 10.1109/JSSC.2018.2864295.

[18] T. M. Carpenter, M. W. Rashid, M. Ghovanloo, D. M. J. Cowell, S. Freear, and F. L. Degertekin, "Direct Digital Demultiplexing of Analog TDM Signals for Cable Reduction in Ultrasound Imaging Catheters," *IEEE Trans Ultrason Ferroelectr Freq Control*, vol. 63, no. 8, pp. 1078–1085, Aug. 2016, doi: 10.1109/TUFFC.2016.2557622.

[19] P. Santos, G. U. Haugen, L. Lovstakken, E. Samset, and J. D'Hooge, "Diverging Wave Volumetric Imaging Using Subaperture Beamforming," *IEEE Trans Ultrason Ferroelectr Freq Control*, vol. 63, no. 12, pp. 2114–2124, Dec. 2016, doi: 10.1109/TUFFC.2016.2616172.

[20] S. Blaak *et al.*, "Design of a micro-beamformer for a 2D piezoelectric ultrasound transducer," in *2009 IEEE International Ultrasonics Symposium*, IEEE, Sep. 2009, pp. 1338–1341. doi: 10.1109/ULTSYM.2009.5441534.

[21] Y. M. Hopf *et al.*, "A Pitch-Matched High-Frame-Rate Ultrasound Imaging ASIC for Catheter-Based 3-D Probes," *IEEE J Solid-State Circuits*, pp. 1–16, 2023, doi: 10.1109/JSSC.2023.3299749.

[22] H. Hasegawa and H. Kanai, "High-frame-rate echocardiography using diverging transmit beams and parallel receive beamforming," *Journal of Medical Ultrasonics*, vol. 38, no. 3, pp. 129–140, Jul. 2011, doi: 10.1007/s10396-011-0304-0.

[23] P. Santos, G. Haugen, L. Lovstakken, E. Samset, and J. D'hooge, "High frame rate 3D tissue velocity imaging using sub-aperture beamforming: A pilot study in vivo," in *2016 IEEE International Ultrasonics Symposium (IUS)*, IEEE, Sep. 2016, pp. 1–4. doi: 10.1109/ULTSYM.2016.7728385.

[24] J. A. Jensen and N. B. Svendsen, "Calculation of pressure fields from arbitrarily shaped, apodized, and excited ultrasound transducers," *IEEE Trans Ultrason Ferroelectr Freq Control*, vol. 39, no. 2, pp. 262–267, Mar. 1992, doi: 10.1109/58.139123.

[25] O. T. Von Ramm and S. W. Smith, "Beam Steering with Linear Arrays," *IEEE Trans Biomed Eng*, vol. BME-30, no. 8, pp. 438–452, Aug. 1983, doi: 10.1109/TBME.1983.325149.

[26] C. A. Samson, A. Bezanson, and J. A. Brown, "A Sub-Nyquist, Variable Sampling, High-Frequency Phased Array Beamformer," *IEEE Trans Ultrason Ferroelectr Freq Control*, vol. 64, no. 3, pp. 568–576, Mar. 2017, doi: 10.1109/TUFFC.2016.2646925.

[27] K. Brenner, A. Ergun, K. Firouzi, M. Rasmussen, Q. Stedman, and B. Khuri–Yakub, "Advances in Capacitive Micromachined Ultrasonic Transducers," *Micromachines (Basel)*, vol. 10, no. 2, p. 152, Feb. 2019, doi: 10.3390/mi10020152.

[28] Y. Huang *et al.*, "Comparison of conventional and collapsed region operation of capacitive micromachined ultrasonic transducers," *IEEE Trans Ultrason Ferroelectr Freq Control*, vol. 53, no. 10, pp. 1918–1933, Oct. 2006, doi: 10.1109/TUFFC.2006.125.

11

DISCUSSION AND CONCLUSION

11.1. OVERVIEW

THIS thesis detailed the development of dedicated ultrasound probes designed for three distinct cardiovascular applications: carotid artery imaging, intracardiac echocardiography utilizing electromechanical wave imaging, and abdominal aorta imaging. These applications all share a common need for high-frame-rate 3D imaging with a relatively large field of view. To meet this requirement, matrix transducers with thousands of elements are needed. However, practical challenges arise when accommodating such a high number of cables within the transducer housing and connecting them to imaging systems, which typically support no more than 256 channels. To overcome this limitation, we integrate the ultrasound probe with an application-specific integrated circuit (ASIC). The ASIC not only facilitates channel reduction through various techniques but also performs critical functions within the probe, such as amplification, beamforming, and digitization of the RF signals. While interfacing ultrasound probes with ASICs offers advantages, it also introduces complexity to the manufacturing process.

To evaluate the manufacturing process and probe performance, with the potential for design optimization, a comprehensive characterization process is crucial. This requires conducting a detailed element-level characterization in both transmit and receive operations. Given the impracticality of the manual execution of this extensive characterization, we stress the importance of automating the procedure. We outline specific strategies to address this characterization challenge and have incorporated them into our test routines.

11.1.1. TRANSDUCER EVALUATION: CALIBRATION, AUTOMATION, AND PERFORMANCE ENHANCEMENT

Chapter 2 presents a novel calibration method for ultrasound transducers using acoustic streaming. The evaluation involved comparing this method with established techniques, namely hydrophone and pulse-echo measurements. At the central frequency of 5 MHz, the transmit efficiency estimated from streaming measurements was 1.9 kPa/V. In comparison, hydrophone and pulse-echo measurements yielded transmit efficiencies of 2.1 kPa/V and 1.8 kPa/V, respectively. These results indicate that the proposed method for estimating the transfer function of ultrasound transducers achieves a satisfactory level of accuracy.

In **Chapter 3**, we present an automated procedure for the element-level acoustic characterization of an ultrasound matrix transducer in both transmit and receive operations. To evaluate its effectiveness, we applied the pipeline to characterize a lead zirconate titanate (PZT) matrix transducer featuring 960 elements. The results demonstrate that the proposed pipeline offers a rapid and convenient approach for characterizing ultrasound transducers.

Chapter 4 introduces an automated method for measuring pressure fields in ultrasound matrix transducers with a high element count. This approach significantly reduces measurement time compared to traditional methods, enabling an extensive assessment of transducer performance. Validation with a prototype matrix transducer consisting of 2880 elements demonstrates the effectiveness of the

procedure, revealing insights into beam profiles, sensitivity maps, and individual element time/frequency responses in a faster way.

In **Chapter 5**, we examined the transmit performance of a prototype PZT matrix transducer with both subdiced and non-subdiced elements. On average, subdicing led to a 25% increase in peak pressure, a 10% expansion in bandwidth, and a 25% reduction in ringing time. The findings indicate that subdicing improves the performance of ultrasound transducers with large elements (width-to-thickness ratio greater than 0.7).

11.1.2. ADVANCES IN TRANSDUCERS FOR HIGH-FRAME-RATE 3D IMAGING

Chapter 6 introduces an ultrasound transceiver ASIC designed for imaging of the carotid artery, featuring a switching artifact reduction technique. The improved switch controller effectively mitigates clock feedthrough and charge injection issues observed in the first-generation ASIC, resulting in a 20 dB reduction in imaging artifacts.

Chapter 7 presents the development of a PZT matrix transducer with integrated ASICs specifically designed for carotid artery imaging. During the fabrication process, the prototype, aimed at having 7680 elements on 8 × 1 tiled ASICs, faced challenges that resulted in damage to two ASICs. On average, individual transducer elements exhibited a transmit efficiency of 30 Pa/V at 200 mm and a −6 dB bandwidth of 45%. The receive dynamic range was 81 dB, with a minimum detectable pressure of 60 Pa and a maximum of 700 kPa.

In **Chapter 8**, we introduce a transceiver ASIC designed for catheter-based high-frame-rate 3D ultrasound imaging probes. By employing time-division multiplexing, subarray beamforming, and a load modulation multi-level data transmission channel, we achieved a cable-count reduction of 18-fold. The system can generate all required transmit patterns at up to 30 V, provides quick settling after the transmit phase, and has a power consumption of 1.12 mW/element in receive. The functionality and operation have been successfully demonstrated through electrical and acoustic imaging experiments, achieving a rate of up to 1000 volumes/s.

In **Chapter 9**, we detail the development of a matrix transducer for high-frame-rate 3D intracardiac echocardiography. The matrix consists of 16 × 18 PZT elements with a pitch of 160 µm × 160 µm and integrates with an ASIC. We measured a transmit efficiency of 28 Pa/V at 5 cm per element and a bandwidth of 60%. In receive, a dynamic range of 80 dB is measured with a minimum detectable pressure of 10 Pa per element. The probe is capable of imaging at a frame rate of up to 1000 volumes/s and is intended to cover a volume of 70° × 70° × 10 cm.

Chapter 10 presents the design of a high-frame-rate 3D imaging capacitive micromachined ultrasonic transducer (CMUT) matrix comprising 64 × 128 elements for abdominal aorta imaging. The matrix is interfaced with ASICs, and we employed subarray beamforming and time-division multiplexing to obtain an 8-fold reduction in channel count. To achieve the desired frame rate, we use four diverging transmit beams. We included initial imaging experiments conducted on tissue-mimicking and needle phantoms. These results demonstrate that we successfully captured 3D

images at a rate of 2000 volumes/s. The intended imaging volume is 60° × 60° × 10 cm.

11.2. RECOMMENDATIONS AND FUTURE WORK

11.2.1. CALIBRATION OF TRANSDUCERS USING ACOUSTIC STREAMING

To enhance the calibration of ultrasound transducers using acoustic streaming, we suggest integrating two cameras into the setup—one positioned above the water tank and another on the side. This can improve the tracking of the marker, ensuring alignment along the axial line of the transducer in both directions. Exploring alternative experimental conditions, such as those without ink injection, can minimize flow disturbances; for example, using starch is an interesting option [1], [2]. Additionally, conducting simulations to investigate the streaming patterns produced by transducer arrays would significantly contribute to the advancement of this technique.

11.2.2. AUTOMATED CHARACTERIZATION OF MATRIX TRANSDUCERS

To enhance the automated characterization process of ultrasound matrix transducers presented in this thesis, incorporating additional features and tests is crucial. One essential aspect is an automated process for measuring acoustic crosstalk between elements. This addition would contribute to a more comprehensive evaluation, enabling us to identify opportunities to refine the design and minimize crosstalk. Moreover, this feature is essential for validating our crosstalk simulations.

Consideration should also be given to the reusability and shareability of the software for different probes. Currently, the characterization protocol is limited to our designed prototypes. However, it would be beneficial to extend this capability to other transducers, including commercial ones. Therefore, efforts should be directed toward making the existing codes flexible and easy to adapt for alternative probe configurations and equipment. This facilitates the standardization of a characterization protocol across different devices and research groups.

11.2.3. FABRICATION PROCESS OF MATRIX TRANSDUCERS

The fabrication process of integrating large-aperture PZT matrix transducers with ASICs presents notable challenges, primarily in two domains: mechanical and electrical. The mechanical challenge arises from tiling multiple ASICs over a large area, making it difficult to ensure uniform flatness. This becomes crucial when constructing the PZT matrix on top of the ASICs, as any deviation in flatness may result in damage during the subsequent dicing or grinding processes. Electrical issues may arise due to electrostatic discharge (ESD) during the fabrication of our prototypes. Despite implementing safety measures, it remains challenging to

completely prevent ESD, which can potentially damage the ASICs at different stages of the manufacturing process.

The combination of these two challenges (mechanical and electrical) makes it very difficult to fabricate a matrix probe with a high element yield. To address this, we propose a modification to our fabrication process by incorporating the use of anisotropic conductive film (ACF) [3]. The use of ACF in transducer fabrication has been already investigated in the literature [4], [5]. A potential strategy involves initially fabricating the PZT matrix on either a printed circuit board (PCB) or a flex circuit board with vias. Subsequently, the ASICs would be tiled on a separate structure, such as a glass plate, and finally, the bonding of these two parts (PZT and ASICs) would be facilitated using ACF tape. This method offers the advantage of reducing mechanical damage since there is no need to dice or grind the PZT material on top of the ASICs. Regarding the ESD issue, it can be minimized through the effective grounding of leakage paths during the assembly of the ASICs. This could be realized by designing a flex circuit that incorporates grounding and connecting it to the ASICs. Once the fabrication process is completed, the ground should be removed by tearing up this flex circuit.

11.2.4. FURTHER EVALUATION AND IMAGING TESTS

Our primary focus for all presented ultrasound probes is to manufacture prototypes with the designated aperture size and element count specified in their designs. This translates to 9600 elements for the carotid artery probe (presented in **Chapter 7**), 1152 elements for the intracardiac echocardiography probe (discussed in **Chapter 9**), and 8192 elements for the abdominal aorta probe (detailed in **Chapter 10**). Once we achieve successful fabrication of fully populated matrix arrays with the intended aperture size, our next steps include conducting additional tests and more specific imaging experiments.

For the carotid artery imaging probe, the next step of the evaluation could be performing high-frame rate volumetric *in vivo* imaging experiments on the vasculature of a chicken embryo, similar to the work presented by Wei et al. [6]. Additionally, it would be interesting to explore the integration of graphical processing units (GPUs) and advanced postprocessing techniques to facilitate the acquisition and real-time display of 3D data. Once we achieve enhanced imaging performance and visualization, the probe could be utilized for preclinical studies and more advanced imaging experiments.

Regarding the intracardiac echocardiography probe, the next phase involves assembling the prototype within a 10-French catheter (i.e., 3.3 mm diameter). This process will likely require the design of a custom flex circuit to replace the current PCB [4], [7]. Furthermore, it is crucial to address the challenge of handling the significant output data bandwidth in the context of a full aperture size. For future iterations, it is recommended to explore the development of an application-specific receiver chip to effectively handle the output data and enable real-time visualization. Initial *in vivo* experiments can only be conducted after implementing these aforementioned features.

For the abdominal aorta probe, additional tests and characterization are necessary for our ongoing development. Before progressing to more advanced imaging experiments, the next steps should involve conducting extensive acoustic characterization to fully understand the probe's performance. Additionally, we aim to compare the sensitivity of the CMUT prototype with that of an equivalent PZT prototype. The manufacturing of the PZT version is currently in its final stages, and we anticipate conducting this comparison soon. Once we successfully develop and characterize a fully populated matrix array, efforts should be directed toward connecting multiple Verasonics systems to the setup to verify the functionality of the complete probe.

11.3. CONCLUSION

This thesis presents the development of dedicated ultrasound matrix arrays for high-frame-rate 3D cardiovascular imaging. It explores the specific requirements for different applications and explains the rationale behind the proposed probe design. The thesis provides detailed insights into the characterization and fabrication processes of the probes, addressing the challenges they present. Three distinct prototypes were successfully manufactured and tested for three specific imaging applications: carotid artery imaging, intracardiac echocardiography, and abdominal aorta imaging. However, the current prototypes have smaller aperture sizes than intended due to challenges in their fabrication process. With further improvements in both design and manufacturing, there is potential to translate the technology presented herein to clinical settings, promising a better assessment and treatment of cardiovascular diseases.

11.4. REFERENCES

[1] A. Nowicki, T. Kowalewski, W. Secomski, and J. Wójcik, "Estimation of acoustical streaming: theoretical model, Doppler measurements and optical visualisation," *European Journal of Ultrasound*, vol. 7, no. 1, pp. 73–81, Feb. 1998, doi: 10.1016/S0929-8266(98)00020-2.

[2] A. Nowicki, W. Secomski, and J. Wójcik, "Acoustic streaming: Comparison of low-amplitude linear model with streaming velocities measured by 32-MHz Doppler," *Ultrasound Med Biol*, vol. 23, no. 5, pp. 783–791, Jan. 1997, doi: 10.1016/S0301-5629(97)00005-7.

[3] M. J. Rizvi, Y. C. Chan, C. Bailey, H. Lu, and A. Sharif, "The effect of curing on the performance of ACF bonded chip-on-flex assemblies after thermal ageing," *Soldering & Surface Mount Technology*, vol. 17, no. 2, pp. 40–48, Jun. 2005, doi: 10.1108/09540910510597492.

[4] D. Wildes *et al.*, "4-D ICE: A 2-D Array Transducer With Integrated ASIC in a 10-Fr Catheter for Real-Time 3-D Intracardiac Echocardiography," *IEEE Trans Ultrason Ferroelectr Freq Control*, vol. 63, no. 12, pp. 2159–2173, Dec. 2016, doi: 10.1109/TUFFC.2016.2615602.

[5] H.-V. Nguyen, T. Eggen, B. Sten-Nilsen, K. Imenes, and K. E. Aasmundtveit, "Assembly of multiple chips on flexible substrate using anisotropie conductive film for medical imaging applications," in *2014 IEEE 64th Electronic Components and Technology Conference (ECTC)*, IEEE, May 2014, pp. 498–503. doi: 10.1109/ECTC.2014.6897330.

[6] L. Wei *et al.*, "High Frame Rate Volumetric Imaging of Microbubbles Using a Sparse Array and Spatial Coherence Beamforming," *IEEE Trans Ultrason Ferroelectr Freq Control*, vol. 68, no. 10, pp. 3069–3081, 2021, doi: 10.1109/TUFFC.2021.3086597.

[7] B. T. Khuri-Yakub *et al.*, "Miniaturized ultrasound imaging probes enabled by CMUT arrays with integrated frontend electronic circuits," in *2010 Annual International Conference of the IEEE*

Engineering in Medicine and Biology, IEEE, Aug. 2010, pp. 5987–5990. doi: 10.1109/IEMBS.2010.5627580.

ACKNOWLEDGMENTS

THE Huygens principle, named after the Dutch physicist Christiaan Huygens (1629–1695), states that the wavefront of a propagating wave at any instant is the sum of infinite point sources from the previous instant. Similarly, although this book bears my name on the front cover, it results from the contribution of many people who radiated support and guidance along my PhD journey. I would like to take a moment to thank each person who "constructively interfered" to bring this thesis to completion.

I want to start by expressing my gratitude to my promotors, **Nico** and **Martin**, for their trust in me and for providing me the opportunity to pursue a PhD. Their guidance over the past four years has been invaluable. **Nico**, thank you for always joining me in the lab to conduct experiments (or as you say, to do the "real work"), whether it was transducer characterization, performing ACF tests in the cleanroom, or calibrating the cameras of our pick-and-place machine. Your expertise across various fields has been truly inspiring. I appreciate how you kept me engaged with multiple projects and tasks, which sometimes felt overwhelming but ultimately helped me grow into a better researcher. I also enjoyed our conversations about non-work-related topics like family and football. **Martin**, thank you for the valuable discussions about the project and papers, and for involving me in supervising various student projects. Your sharp questions during meetings, though initially intimidating, have significantly improved my critical thinking and communication skills. I am especially grateful that you agreed to visit Brazil with me as part of the SPRINT program, even during a challenging time for you. I truly enjoyed our time in Ribeirão Preto.

I would also like to thank all the PIs who were directly involved with my research and made significant contributions to the work described in this thesis. **Rik**, thank you for the scientific discussions and your meticulous input on my manuscripts, which played a significant role in their smooth acceptance. Also, I appreciate you offering me a Postdoc position, and I look forward to a fruitful collaboration on the SOUND-CHECK project. **Paul**, thank you for your initiative in introducing acoustic streaming into our research practice, which became very popular among the students. Furthermore, I appreciate your guidance on signal processing and transducer calibration. **Michiel**, thank you for your valuable feedback on my papers and for the insightful meetings and discussions we had about different projects. **Hans**, thank you for your support across various aspects of the projects, including your assistance in designing a setup for high-frame-rate imaging and processing of the results. Additionally, many thanks for the car ride from Sint-Michielsgestel to Delft during the Ultra-X-Treme meeting. **Jason**, thank you for the interesting discussions regarding the design requirements of the CMUT probe. I appreciate your assistance in providing the codes for beam profile simulation and your support with phantom imaging. I am also thankful for the other PIs from the Medical Imaging group—**Frans**, **David**, **Guillaume**, **Sebastian**, and **Qian Tao**. Though not directly

involved in my research, they have contributed to my development and understanding of academia.

I could not have done my research without the help of our support staff, who keep things running smoothly behind the scenes. **Angela** and **Annelies**, thank you for your assistance with various administrative matters and for organizing enjoyable events for the group. **Ronald**, thank you for your technical support and our discussions about Bossa Nova, jazz, and music theory. **Zu-Yao**, thank you for your help with the heat camera. **Robert**, thank you for assisting me with electrical impedance measurements on ACF. **Henry**, thank you for all your help both in the office and in the lab. You always find solutions to any technical problem and are always happy to assist. **Emile**, thank you for the countless prototypes you built for my research. Your expertise in transducer manufacturing was crucial to the success of the projects. Additionally, I appreciate your efforts in developing our custom pick-and-place machine for ACF bonding, which will hopefully be operational soon.

I am also grateful for the collaboration with fellow PhD students and postdocs, who played a significant role in much of the work presented in my thesis. **Fabian**, we spent a lot of time together in the lab doing measurements and fixing bugs in our codes. Thank you for helping me with the Verasonics and PZFlex and for keeping our version control repositories organized whenever I messed things up. Also, thanks for the daily reminder that noon is lunchtime. **Boudewine**, I am grateful for the opportunity to join the end of your PhD project and co-author a paper with you. Thank you for explaining everything about the 3D-ICE probe to me. **Moein**, thank you for helping me with PZFlex and water tank measurements at the start of my PhD. Also, thank you for the imaging experiments on the PUMA probe. **Taehoon**, **Yannick**, and **Nuriel**, many thanks for your contributions to the electronics aspect of our projects and for your support in controlling the FPGAs during acoustic measurements. **Luxi**, thank you for sharing your codes for the spiral array. **Xiufeng**, I appreciate your support with MATLAB and MS Word, the Chinese snacks, and your genuine kindness in helping others. **Sabiju**, I thank you for your assistance with Comsol simulations and our discussions about the joys and challenges of parenthood during the PhD. Additionally, I would like to thank the students I supervised —**Kim**, **Leonardo**, and **Tigran**—, from whom I have learned a lot. Lastly, I want to thank **Lorenzo** for his great help in comparing PZFlex and Comsol simulations.

My office mates deserve special thanks for creating an enjoyable workspace. I value our engaging conversations, shared frustrations, and celebrations of PhD milestones together. **Agis**, thank you for helping me settle in and explaining how day-to-day things work here. I really enjoy our scientific discussions, which might begin with serious topics like the Navier–Stokes equations or Fourier transforms, but almost always end up with us laughing and wondering why we are not farming instead of solving integrals. Also, thank you for bringing your modern Greek philosophy to academia, reminding us that there is much more to life than just work. **Chih-Hsien**, I appreciate our discussions about our progress and the nice Taiwanese snacks you brought to the office every time you went home. **Martijn**, thank you for your help with translations, not only with the Dutch language but also in interpreting Dutch culture. Additionally, I appreciate your efforts in organizing various extra activities for PhD students.

Next, I would like to extend my gratitude to my old and new colleagues from the MI and CI groups for the discussions over lunches or during seminars: **Jack**, **Ulaş**, **Alberico**, **Elango**, **Verya**, **Dion**, **Alina**, **João**, **Kathleen**, **Eleonora**, **Baptiste**, **Yidong**, **Yi**, **Gabrielle**, **Hugues**, **Liam**, and **Min**.

Of course, I have to thank the wonderful "beach people". Your company has brought countless special moments to me over drinks, delicious food, gatherings, and unforgettable parties. A big thank you to **Agis**, **Chiara**, **Fabian**, **Jack**, **Eszter**, **Moein**, **Paulina**, **Victor**, **Ayda**, **Maša**, **Chih-Hsien**, **Xiufeng**, **Rick**, and **Martina**. I would also like to give a special mention to **Geraldi**, **Gonzalo**, and Agis's Greek friends. You made every shared beer a special occasion, and I am truly grateful for these memories.

Also, beyond the limits of the research group, I want to thank my friends from the Catholic community in Delft, especially those in the international choir. Playing piano with them over the past few years has helped me unwind and recharge during the weekends.

It is also important for me to acknowledge the support I have received from my family. I am grateful to my in-laws, **Tibor**, **Csilla**, **Nora**, and **Vincent**, for their efforts in arranging family reunions during holidays or long weekends in Hungary, Belgium, or The Netherlands. Also, I appreciate our discussions about life and career.

Aos meus pais **Nalva** e **Djalma**, muito obrigado por terem me dado a oportunidade de estudar e por todos os sacrifícios que fizeram pela nossa família. Vocês são minha fonte de inspiração. Aos meus irmãos **Denis**, **Denilson**, e **Nadja**, muito obrigado pelo apoio constante que sempre me deram e por estarem sempre presentes, mesmo à distância.

My wife and daughter, depicted in Figure 1.1 of this thesis, deserve my deepest gratitude. **Eszter**, thank you for your unconditional support over the years. Your belief in me has made all the difference. You were the one who encouraged me to apply for a PhD in Delft, and I am immensely grateful for that. Thank you for your patience and understanding, especially when I had to be absent due to work. Most importantly, thank you for the wonderful family we have built together. Szeretlek!

Jazmin, thanks for always sleeping for more than ten hours straight through the night. We are so lucky to have you. Papai te ama e vai passar muito mais tempo com você!

Finally, and above all, I want to thank **God** for granting me the strength to pursue my PhD degree. All glory belongs to Him!

List of publications

Journal papers

1. **dos Santos, D.S.**; Fool, F.; Vos, H.J.; Verweij, M.D.; de Jong, N. Characterization of pressure fields in high-element-count ultrasound matrix transducers. IEEE Open Journal of Instrumentation and Measurement (*in preparation*).

2. **dos Santos, D.S.**; Baldini, L.; Vos, H.J.; Verweij, M.D.; de Jong, N.; van Neer, P.L.M.J. Acoustic Streaming-Based Calibration of Ultrasound Transducers. Applied Acoustics 2024, 217, 109863, doi:10.1016/j.apacoust.2024.109863.

3. **dos Santos, D.S.**; Ossenkoppele, B.; Hopf, Y.M.; Soozande, M.; Noothout, E.; Vos, H.J.; Bosch, J.G.; Pertijs, M.A.P.; Verweij, M.D.; de Jong, N. An Ultrasound Matrix Transducer for High-Frame-Rate 3-D Intra-Cardiac Echocardiography. Ultrasound Med Biol 2024, 50, 285–294, doi:10.1016/j.ultrasmedbio.2023.11.001.

4. Hopf, Y.M.; **dos Santos, D.S.**; Ossenkoppele, B.W.; Soozande, M.; Noothout, E.; Chang, Z.-Y.; Chen, C.; Vos, H.J.; Bosch, J.G.; Verweij, M.D.; et al. A Pitch-Matched High-Frame-Rate Ultrasound Imaging ASIC for Catheter-Based 3-D Probes. IEEE J Solid-State Circuits 2024, 59, 476–491, doi:10.1109/JSSC.2023.3299749.

5. Rodrigues, E.P.; **dos Santos, D.S.**; Buiochi, F. Comparison of Three Linear Digital Filters Applied to Improve the Quality of the Measured Acoustic Field. Eng 2023, 4, 2582–2600, doi:10.3390/eng4040148.

6. **dos Santos, D.S.**; Fool, F.; Mozaffarzadeh, M.; Shabanimotlagh, M.; Noothout, E.; Kim, T.; Rozsa, N.; Vos, H.J.; Bosch, J.G.; Pertijs, M.A.P.; et al. A Tiled Ultrasound Matrix Transducer for Volumetric Imaging of the Carotid Artery. Sensors 2022, 22, 9799, doi:10.3390/s22249799.

7. Kim, T.; Fool, F.; **dos Santos, D.S.**; Chang, Z.-Y.; Noothout, E.; Vos, H.J.; Bosch, J.G.; Verweij, M.D.; de Jong, N.; Pertijs, M.A.P. Design of an Ultrasound Transceiver ASIC with a Switching-Artifact Reduction Technique for 3D Carotid Artery Imaging. Sensors 2020, 21, 150, doi:10.3390/s21010150.

8. **dos Santos, D.S.**; Cardoso, F.M.; Furuie, S.S. Two-Dimensional Ultrasonic Transducer Array for Shear Wave Elastography in Deep Tissues: A Preliminary Study. Research on Biomedical Engineering 2020, 36, 277–289, doi:10.1007/s42600-020-00068-6.

CONFERENCE PAPERS

1. **dos Santos, D.S.**; Fool, F.; Kim, T.; Noothout, E.; Rozsa, N.; Vos, H.J.; Bosch, J.G.; Pertijs, M.A.P.; Verweij, M.D.; de Jong, N. Automated Characterization of Matrix Transducer Arrays Using the Verasonics Imaging System. In Proceedings of the 2022 IEEE International Ultrasonics Symposium (IUS); IEEE, October 10 2022; Vol. 2022-Octob, pp. 1–4.

2. **dos Santos, D.S.**; Fool, F.; Kim, T.; Noothout, E.; Vos, H.J.; Bosch, J.G.; Pertijs, M.A.P.; Verweij, M.D.; de Jong, N. Experimental Investigation of the Effect of Subdicing on an Ultrasound Matrix Transducer. In Proceedings of the 2021 IEEE International Ultrasonics Symposium (IUS); IEEE, September 11 2021; pp. 1–3.

3. **dos Santos, D.S.**; Cardoso, F.M.; Furuie, S.S. Two-Dimensional Ultrasound Transducer Array for Acoustic Radiation Force Impulse Imaging. In Proceedings of the 24th ABCM International Congress of Mechanical Engineering; ABCM, December 3 2017; pp. 1–10.

4. **dos Santos, D.S.**; Cardoso, F.M.; Furuie, S.S. Development of a 2D Array Ultrasound Transducer for Acoustic Radiation Force Impulse Imaging in Deep Tissues. In Proceedings of the 23rd Congress of the European Society of Biomechanics (ESB); ESB, July 2 2017; pp. 1–2.

5. Cardoso, F.M.; **dos Santos, D.S.**; Furuie, S.S. Acoustic Radiation Force Impulse in Deep Tissues Using Matrix Array Transducers. In Proceedings of the XXV Brazilian Congress of Biomedical Engineering; SBEB, October 17 2016; pp. 1075–1078.

About the author

DJALMA Simões dos Santos, who is one of identical triplets, was born in São Paulo, Brazil. He attended vocational-technical schools for primary and secondary education, specializing as an electrician and electronics technician, respectively. In 2014, he received his BSc degree in electrical engineering, focusing on control systems, from the Federal Institute of São Paulo, São Paulo, Brazil. During his undergraduate studies, he worked on a hardware-in-the-loop test system to simulate the behavior of a combustion engine. Additionally, he participated in a scientific exchange program at the Budapest University of Technology and Economics, in Budapest, Hungary.

In 2018, he obtained his MSc degree in biomedical engineering from the University of São Paulo, São Paulo, Brazil, where he worked on the design and fabrication of ultrasound transducers for shear wave elastography, aiming to expand the capabilities of this technique to deeper tissues. Outside of academia, he has worked as an engineer in industry for over five years in diverse roles, including product design, technical support, and operational maintenance.

In 2020, Djalma relocated to Delft, the Netherlands, to join the Department of Imaging Physics at the Delft University of Technology as a PhD candidate, where he performed the work described in this thesis. His position was within the MATRIX project, which is part of the Ultrafast Ultrasound Imaging for Extended Diagnosis and Treatment of Vascular Disease (Ultra-X-Treme) consortium.

Upon completion of his PhD, he will become a postdoctoral researcher at the Delft University of Technology, where he will work on the development of ultrasound transducers for ultrasound and microbubbles treatment as well as real-time 3D monitoring of drug delivery.

In his spare time, he enjoys playing the piano, delving into music theory, and supporting his favorite football team, São Paulo FC.



Propositions

accompanying the dissertation

Ultrasound transducers for ultrafast 3D cardiovascular imaging

by

Djalma Simões dos Santos

1. High repeatability in the manufacturing of piezoelectric transducers can only be obtained by often repeating their manufacturing (this thesis).
2. You can only improve what you can measure (this thesis).
3. Keeping your computer screen visible to colleagues and supervisors avoids procrastination.
4. Caring for a baby is time-consuming but boosts productivity.
5. *How* you say it matters more than *what* you say.
6. Having faith implies being a believer, but being a believer does not imply having faith.
7. The quality of a public service improves dramatically when it is used by politicians.
8. Common sense is not so common in a multicultural society.
9. The Hungarian football team of 1954, the Dutch team of 1974, and the Brazilian team of 1982 were by far the best teams that failed to win the FIFA World Cup.
10. A PhD is like a jazz musician's journey: mastering theory, reviewing repertoire, refining aural and oral skills, practicing, and experimenting – all indispensable for improvisation.

These propositions are regarded as opposable and defendable, and have been approved as such by the promotors Prof. dr. ir. N. de Jong and Dr. ir. M. D. Verweij.